

Self-consistent approach to the dynamics of excitation energy transfer in multichromophoric systems

Cite as: J. Chem. Phys. 161, 204108 (2024); doi: 10.1063/5.0237483

Submitted: 5 September 2024 • Accepted: 12 November 2024 •

Published Online: 26 November 2024



View Online



Export Citation



CrossMark

Veljko Janković^{1,a)}  and Tomáš Mančal² 

AFFILIATIONS

¹Institute of Physics Belgrade, University of Belgrade, Pregrevica 118, 11080 Belgrade, Serbia

²Faculty of Mathematics and Physics, Charles University, Ke Karlovu 5, 121 16 Prague 2, Czech Republic

^{a)}Author to whom correspondence should be addressed: veljko.jankovic@ipb.ac.rs

ABSTRACT

Computationally tractable and reliable, albeit approximate, methods for studying exciton transport in molecular aggregates immersed in structured bosonic environments have been actively developed. Going beyond the lowest-order (Born) approximation for the memory kernel of the quantum master equation typically results in complicated and possibly divergent expressions. Starting from the memory kernel in the Born approximation, and recognizing the quantum master equation as the Dyson equation of Green's functions theory, we formulate the self-consistent Born approximation to resum the memory-kernel perturbation series in powers of the exciton–environment interaction. Our formulation is in the Liouville space and frequency domain and handles arbitrary exciton–environment spectral densities. In a molecular dimer coupled to an overdamped oscillator environment, we conclude that the self-consistent cycle significantly improves the Born-approximation energy-transfer dynamics. The dynamics in the self-consistent Born approximation agree well with the solutions of hierarchical equations of motion over a wide range of parameters, including the most challenging regimes of strong exciton–environment interactions, slow environments, and low temperatures. This is rationalized by the analytical considerations of coherence-dephasing dynamics in the pure-dephasing model. We find that the self-consistent Born approximation is good (poor) at describing energy transfer modulated by an underdamped vibration resonant (off-resonant) with the exciton energy gap. Nevertheless, it reasonably describes exciton dynamics in the seven-site model of the Fenna–Matthews–Olson complex in a realistic environment comprising both an overdamped continuum and underdamped vibrations.

Published under an exclusive license by AIP Publishing. <https://doi.org/10.1063/5.0237483>

I. INTRODUCTION

The light absorption and thus initiated excitation energy transfer (EET) in molecular aggregates constitute the first steps of solar-energy conversion in both natural^{1,2} and artificial^{3–6} systems. The EET takes place in a complex dynamic spatiotemporal landscape stemming from the competition of interactions promoting exciton delocalization (resonance coupling between molecules) and localization (static and dynamic disorder).⁷ As the energy scales of these counteracting interactions are typically comparable to one another,^{8,9} theoretical descriptions of EET dynamics are quite challenging.

When approached from the perspective of the theory of open quantum systems,^{10,11} the challenge transforms into describing

non-Markovian quantum dynamics of excitons interacting with their environment. As standard theories (such as Redfield¹² and Förster¹³ theories) do not meet this challenge,¹⁴ various numerically exact methods have been developed. Two most common foundations of these are (i) the Feynman–Vernon influence functional theory¹⁵ and (ii) the Nakajima–Zwanzig [time-convolution (TC)] quantum master equation (QME).^{16–18} The approaches rooted in (i) include the hierarchical equations of motion (HEOM)^{19–21} and a host of path-integral and process-tensor-based methods.^{22–29} Each of these approaches develops a different representation of the so-called exact reduced evolution superoperator (or the dynamical map) $\mathcal{U}(t)$, which becomes its central object. Meanwhile, the main aim of the approaches originating from (ii) is to evaluate the exact memory-kernel superoperator $\mathcal{K}(t)$.^{30–32} All the above-referenced

approaches are in general computationally intensive. Their applications to realistic EET models, which feature a larger number of chromophores and/or structured spectral densities (SDs) of the exciton–environment interaction extracted from experiments or atomistic simulations,^{33–38} can thus be impractical. A need for computationally less demanding and reliable, although approximate, approaches to study EET dynamics in realistic multichromophoric models cannot be overemphasized.

Recent years have witnessed the emergence of many such approaches, among others quantum–classical methods,^{39–44} and related quantum–chemical approaches to nonadiabatic dynamics (e.g., the surface hopping).^{45–47} One can also devise approximations to \mathcal{U} and \mathcal{K} starting from the formally exact expressions of (i) and (ii), respectively. For example, the former give rise to cumulant-expansion-based approaches,^{48–51} while the latter result in various approximations to the exact memory kernel.^{52,53} The authors of Ref. 54 noted that the second-order TC (TC2) QME, which retains only the lowest-order (second-order) term $\mathcal{K}^{(2)}(t)$ in the expansion of \mathcal{K} in powers of the exciton–environment interaction, can qualitatively reproduce the main features of EET dynamics in multichromophoric systems. The most obvious improvement over the TC2 QME, also known as the (second) Born approximation (BA),⁵⁵ is to retain some of the higher-order contributions to \mathcal{K} . Such a route generally leads to involved expressions that might not always be convergent and that can be practically evaluated only for the simplest models, where they show some improvements over the original theory.^{56–63} While already the lowest-order kernel of polaron-transformed QMEs^{64–67} can significantly improve over TC2 QME, decent results can also be obtained by partially resumming the perturbation expansion for \mathcal{K} using only low-order terms as the input. Partial resummations are most commonly performed in the frequency domain, and one usually applies Padé or Landau–Zener resummation schemes to $\mathcal{K}^{(2)}(\omega)$ and $\mathcal{K}^{(4)}(\omega)$.^{62,68} Another possibility, the self-consistent resummation schemes strongly rooted in condensed-matter physics,^{69–72} has received even less attention in this context.

Successful self-consistent improvements over the TC2 QME have been reported in the context of quantum theory of electronic transport through molecular junctions.^{73–76} These approaches have mainly considered purely electronic quantum transport, when the role of the bath is played by electronic leads. Their applications to the quantum transport in the presence of both electronic leads and molecular vibrations are much more recent and scarcer.⁷⁷ A proposal for a self-consistent description of the dynamics of a general open quantum system has been made only very recently.⁷⁸ It leans on a diagrammatic representation of the perturbation series for $\mathcal{U}(t)$, which has indeed appeared in the context of open quantum dynamics; see, for example, Refs. 79–81. The novelty of the approach by Scarlatella and Schirò⁷⁸ lies in the subsequent formulation of the perturbation series for $\mathcal{K}(t)$, which is related to $\mathcal{U}(t)$ via the TC QME. In the context of the theory of Green's functions in quantum many-body systems,^{71,72,82} the memory kernel $\mathcal{K}(t)$ is analogous to the self-energy, whereas the TC QME plays the role of the Dyson equation. Considering the zero-temperature dynamics of the spin–boson model, Scarlatella and Schirò⁷⁸ find that performing the self-consistent cycle starting from the BA memory kernel $\mathcal{K}^{(2)}$ produces promising results. However, they consider only the zero temperature and SDs commonly used when studying

the spin–boson model in its narrowest sense.⁸³ Moreover, their time-domain formulation of the self-consistent Born approximation (SCBA) involves solving an integrodifferential equation in each iteration of the cycle.

This study explores the applicability of the self-consistent memory-kernel resummation scheme introduced in Ref. 78 to EET dynamics in multichromophoric aggregates. For the sake of completeness, we first reconsider the theoretical developments of Ref. 78 and make them technically simpler by working in the Liouville space and replacing the above-mentioned integrodifferential equation in the time domain by a matrix equation in the frequency domain. In a molecular dimer coupled to an overdamped phonon environment, we find that the self-consistent cycle greatly improves the original BA (TC2 QME) over a wide range of dimer parameters. This success of the SCBA is rationalized by considering the analytically tractable example of coherence dephasing in the pure-dephasing model. Remarkably, we find that the SCBA remains reliable even in the generally difficult regimes of strong exciton–environment interactions and/or slow environments, when multiple environmentally assisted processes dominate the dynamics,^{84,85} as well as at low temperatures. Considering exciton dynamics modulated by a single underdamped vibrational mode, we conclude that the SCBA delivers good results only when the vibrational energy is resonant with the exciton–energy gap. Upon including overdamped phonon continuum on top of a number of underdamped modes, we find that the SCBA delivers decent results for EET dynamics in the seven-site model of the FMO complex interacting with the realistic environment extracted from atomistic simulations.

This paper is organized as follows. Section II introduces our theoretical framework, whose applicability to EET dynamics is assessed in Sec. III. Section IV summarizes our main findings and discusses prospects for future work.

II. THEORETICAL CONSIDERATIONS

A. Model

We model EET dynamics in an aggregate composed of N chromophores using the Frenkel–Holstein Hamiltonian,

$$H = H_S + H_B + H_{S-B}. \quad (1)$$

We take into account only the ground and one excited state on each chromophore so that the purely electronic part H_S reads as

$$H_S = \sum_n \varepsilon_n |n\rangle \langle n| + \sum_{m \neq n} J_{mn} |m\rangle \langle n|. \quad (2)$$

Here, $|n\rangle$ is the collective singly excited state residing on chromophore n (all the other chromophores are unexcited), ε_n is the energy of the vertical transition from the ground state to the excited state on chromophore n , while J_{mn} is the resonance (typically dipole–dipole) coupling between chromophores m and n . The aggregate is in contact with the environment modeled as collections of mutually independent harmonic oscillators associated with each chromophore,

$$H_B = \sum_{n\xi} \omega_{n\xi} b_{n\xi}^\dagger b_{n\xi}. \quad (3)$$

Here, $\omega_{n\xi}$ is the frequency of oscillator ξ on chromophore n , while bosonic operators $b_{n\xi}^\dagger$ ($b_{n\xi}$) create (annihilate) the corresponding oscillation quantum and obey $[b_{n\xi}, b_{m\xi'}] = 0$, $[b_{n\xi}, b_{m\xi'}^\dagger] = \delta_{nm}\delta_{\xi\xi'}$. The exciton–environment interaction is of the Holstein type, i.e., local and linear in oscillator displacements,

$$H_{S-B} = \sum_{n\xi} g_{n\xi} V_n (b_{n\xi} + b_{n\xi}^\dagger), \quad (4)$$

where $V_n = |n\rangle\langle n|$. Its strength, determined by the interaction constants $g_{n\xi}$, is more conveniently described using the reorganization energy on chromophore n ,

$$\lambda_n = \sum_{\xi} \frac{g_{n\xi}^2}{\omega_{n\xi}} = \int_{-\infty}^{+\infty} \frac{d\omega}{2\pi} \frac{\mathcal{J}_n(\omega)}{\omega}, \quad (5)$$

where the SD of the exciton–environment interaction

$$\mathcal{J}_n(\omega) = \pi \sum_{\xi} g_{n\xi}^2 [\delta(\omega - \omega_{n\xi}) - \delta(\omega + \omega_{n\xi})] \quad (6)$$

is typically a continuous function of ω . We focus on exciton dynamics starting from the factorized initial condition

$$W(0) = \rho(0)\rho_B^{\text{eq}}, \quad (7)$$

where $\rho(0)$ is the excitonic reduced density matrix (RDM) at the initial instant $t = 0$, while

$$\rho_B^{\text{eq}} = \frac{e^{-\beta H_B}}{\text{Tr}_B e^{-\beta H_B}} \quad (8)$$

represents the state of the environment (equilibrium at temperature $T = \beta^{-1}$) with no excitons present. Within the Condon approximation,⁸⁶ this choice of the initial condition leads to the dynamics that can be probed in ultrafast nonlinear spectroscopies.⁸⁷ As our formalism deals with Green's function, we can still reconstruct the dynamics under an arbitrary excitation condition as long as the light–matter interaction is weak and the Condon approximation is valid.^{87–89} The only environmental quantity influencing the reduced excitonic dynamics starting from Eq. (7) is the displacement autocorrelation function,¹⁵

$$\begin{aligned} C_n(t) &= \sum_{\xi} g_{n\xi}^2 \text{Tr}_B \left\{ [b_{n\xi}(t) + b_{n\xi}^\dagger(t)] (b_{n\xi} + b_{n\xi}^\dagger) \rho_B^{\text{eq}} \right\} \\ &= \int_{-\infty}^{+\infty} \frac{d\omega}{\pi} e^{-i\omega t} \frac{\mathcal{J}_n(\omega)}{1 - e^{-\beta\omega}}. \end{aligned} \quad (9)$$

The time dependence in Eq. (9) is taken with respect to H_B , i.e., $b_{n\xi}(t) = e^{-i\omega_{n\xi}t} b_{n\xi}$.

B. Real-time diagrammatic representation: Green's superoperator and self-energy superoperator

The assumption embodied in Eq. (7) permits us to define the exact reduced evolution superoperator (dynamical map) $\mathcal{U}(t)$ by

$$|\rho(t)\rangle\rangle = \mathcal{U}(t)|\rho(0)\rangle\rangle. \quad (10)$$

Equation (10) is formulated in the Liouville space,⁸⁶ in which the excitonic RDM at $t > 0$, represented by the operator $\rho(t)$ in

the Hilbert space, becomes the N^2 -component vector $|\rho(t)\rangle\rangle$. The reduced evolution superoperator is then a tetradic quantity comprising N^4 entries $\langle\langle e_2' e_1' | \mathcal{U}(t) | e_2 e_1 \rangle\rangle$, where $\{|e\rangle\}$ is an arbitrary basis in the single-exciton manifold. $\mathcal{U}(t)$ is formally expressed as (see, for example, Ref. 90 and references therein)

$$\mathcal{U}(t) = e^{-i\mathcal{L}_S t} \text{Tr}_B \left\{ \mathcal{T}_t e^{-i\int_0^t ds \mathcal{L}_{S-B}^{(I)}(s)} \rho_B^{\text{eq}} \right\}, \quad (11)$$

where the Liouvillian \mathcal{L}_a associated with the term H_a ($a = S, B, S - B$) in Eq. (1) is defined by its action on an arbitrary Liouville-space vector $|O\rangle\rangle$ corresponding to the Hilbert-space operator O , $\mathcal{L}_a|O\rangle\rangle \leftrightarrow [H_a, O]$, while the interaction-picture counterpart of \mathcal{L}_{S-B} is

$$\mathcal{L}_{S-B}^{(I)}(t) = e^{i(\mathcal{L}_S + \mathcal{L}_B)t} \mathcal{L}_{S-B} e^{-i(\mathcal{L}_S + \mathcal{L}_B)t}. \quad (12)$$

The time-ordering sign \mathcal{T}_t imposes the chronological order (latest to the left) among the Liouvillians in the expansion of Eq. (11) in powers of the exciton–environment interaction. The Liouville-space approach adopted here is somewhat different from standard real-time approaches to the RDM of a particle in an oscillator environment,^{78,91} which consider the forward and backward Hilbert-space evolution operators separately. Dealing with superoperators, we simplify the formalism, as we consider only the forward evolution in the Liouville space.⁹² The average in Eq. (11) can be performed term-by-term using Wick's theorem,⁹¹ and only even-order powers in \mathcal{L}_{S-B} remain. The order $2k$ ($k \geq 1$) consists of $(2k - 1)!!$ terms. Further manipulations usually proceed in two different manners.

The first possibility is to observe that, because of the \mathcal{T}_t sign, all the terms appearing in any given order are mutually identical.⁸¹ Retaining the \mathcal{T}_t sign, one obtains the well-known Feynman–Vernon expression,^{20,81}

$$\mathcal{U}(t) = e^{-i\mathcal{L}_S t} \mathcal{T}_t e^{-\Phi(t)}, \quad (13)$$

with

$$\begin{aligned} \Phi(t) &= \sum_n \int_0^t ds_2 \int_0^{s_2} ds_1 V_n^{(I)}(s_2)^\times \\ &\quad \times \left[C_n^r(s_2 - s_1) V_n^{(I)}(s_1)^\times + i C_n^i(s_2 - s_1) V_n^{(I)}(s_1)^\circ \right]. \end{aligned} \quad (14)$$

In Eq. (14), the superoperators V^\times and V° are defined by the correspondences $V^\times|O\rangle\rangle \leftrightarrow [V, O]$ and $V^\circ|O\rangle\rangle \leftrightarrow \{V, O\}$ (anticommutator), respectively. Assuming that $C_n(t)$ can be decomposed into a number of exponentially decaying terms, Eqs. (13) and (14) serve as the starting point for the HEOM method.

The possibility we opt for here is to make the time ordering explicit in each term, in which case the terms in any given order appear as different. Further developments are facilitated by considering the (retarded) evolution superoperator [the (retarded) Green's function or Green's superoperator]⁸⁶

$$\mathcal{G}(t) = -i\theta(t)\mathcal{U}(t) \quad (15)$$

instead of $\mathcal{U}(t)$. Each term in order $2k$ of the expansion of $\mathcal{G}(t)$ can be represented by a diagram [Fig. 1(d)] comprising a total of $2k + 2$ (2 terminal and $2k$ internal) instants,

$$s_{2k+1} = t \geq s_{2k} \geq \dots \geq s_1 \geq 0 = s_0,$$

and k chromophore indices n_k, \dots, n_1 associated with k pairs selected from the set $\{s_{2k}, \dots, s_1\}$ by the application of Wick's theorem. The consecutive instants s_{j+1} and s_j ($0 \leq j \leq 2k + 1$) of a diagram are connected by a straight line directed from s_j to s_{j+1} [Fig. 1(d)] and represent the (retarded) free-exciton Green's superoperator [Fig. 1(b)]

$$\mathcal{G}_S(t) = -i\theta(t)e^{-i\mathcal{L}_S t}. \quad (16)$$

The directed double-line represents $\mathcal{G}(t)$ [Fig. 1(a)]. The dashed circumferences connect the instants s_l and s_j ($s_l \geq s_j$) that are paired by Wick's theorem; see Fig. 1(c). These instants are accompanied by the same chromophore index n_{jl} [see Eq. (4)] and the following superoperators [cf. Eq. (14)]:

$$s_l \leftrightarrow V_{n_{jl}}^\times, \quad (17)$$

$$s_j \leftrightarrow C_{n_{jl}}^r(s_l - s_j)V_{n_{jl}}^\times + iC_{n_{jl}}^i(s_l - s_j)V_{n_{jl}}^\circ. \quad (18)$$

Having placed all the superoperators in a chronologically ordered string (reading diagrams from left to right), one performs integrations $\int_0^t ds_{2k} \dots \int_0^{s_2} ds_1$ over $2k$ internal instants and summations over k independent chromophore indices. Any diagram is either reducible or irreducible, depending on whether it can be cut into two by cutting a free Green's superoperator line or not.⁹³ Examples of irreducible diagrams in Fig. 1(d) are diagrams (2), (4.2), and (4.3), while the diagram (4.1) is reducible. Amputating the external lines corresponding to $\mathcal{G}_S(s_1)$ and $\mathcal{G}_S(t - s_{2k})$ of irreducible diagrams, one obtains the diagrammatic representation of the so-called (retarded) self-energy superoperator; see Fig. 1(f). The self-energy superoperator thus consists of all amputated diagrams that cannot be cut into two by cutting a free Green's superoperator line. One can then derive the following Dyson equation:⁹³

$$\mathcal{G}(t) = \mathcal{G}_S(t) + \int_{-\infty}^{+\infty} ds_2 \int_{-\infty}^{+\infty} ds_1 \mathcal{G}_S(t - s_2)\Sigma(s_2 - s_1)\mathcal{G}(s_1), \quad (19)$$

whose diagrammatic representation is shown in Fig. 1(e). All the superoperators in Eq. (19) are retarded, and the integrals in Eq. (19) can run from $-\infty$ to $+\infty$, which facilitates the transition to the frequency domain. Rewriting Eq. (19) as an equation for $\mathcal{U}(t)$,

inserting the result thus obtained into Eq. (10), and differentiating with respect to t , one obtains the QME,

$$\partial_t |\rho(t)\rangle\rangle = -i\mathcal{L}_S |\rho(t)\rangle\rangle - \int_0^t ds \mathcal{K}(t - s) |\rho(s)\rangle\rangle, \quad (20)$$

where the relation between the memory kernel \mathcal{K} and the retarded self-energy Σ is

$$\Sigma(t) = -i\theta(t)\mathcal{K}(t). \quad (21)$$

Equation (20) differs from the standard QME only by the representation of the memory kernel. The memory kernel is commonly expressed in terms of projection superoperators \mathcal{P} and $\mathcal{Q} = \mathbb{1} - \mathcal{P}$, and its perturbation expansion in the exciton–environment interaction is most often hidden in the propagator of the irrelevant part $\mathcal{Q}\mathcal{L}_{S-B}\mathcal{Q}$ of the interaction Liouvillian; see, for example, Refs. 10 and 18. Choosing $\mathcal{P}|O\rangle\rangle \leftrightarrow \text{Tr}_B\{O\rho_B^{\text{eq}}\}$ ^{94,95} and expanding the aforementioned irrelevant propagator in power series, one obtains the perturbation expansion of the memory kernel in terms of the so-called partial cumulants of the interaction Liouvillian.⁹⁶ The results of Ref. 95 suggest that the same final result is obtained using the more conventional Agyres–Kelley⁹⁷ projection superoperator $\mathcal{P}|O\rangle\rangle \leftrightarrow \rho_B^{\text{eq}}\text{Tr}_B\{O\}$. One can convince themselves that the partial cumulants in Ref. 96 simply restate that the memory-kernel (or self-energy) perturbation series does not contain disconnected diagrams, as in Fig. 1(f). To that end, the general expressions of Ref. 96 have to be transformed by applying Wick's theorem and diagrammatically representing the resulting series according to the above-stated rules. These two steps, which were not considered in Ref. 96, are vital to the formulation of the self-consistent resummation scheme in Sec. II E.

C. Frequency-domain description

Resummation techniques usually require transferring to the frequency space. This is most conveniently done starting from Eq. (19) and forming the dynamical equation for $\mathcal{G}(t)$,

$$\partial_t \mathcal{G}(t) = -i\delta(t) - i\mathcal{L}_S \mathcal{G}(t) - i \int_{-\infty}^{+\infty} ds \Sigma(t - s)\mathcal{G}(s). \quad (22)$$

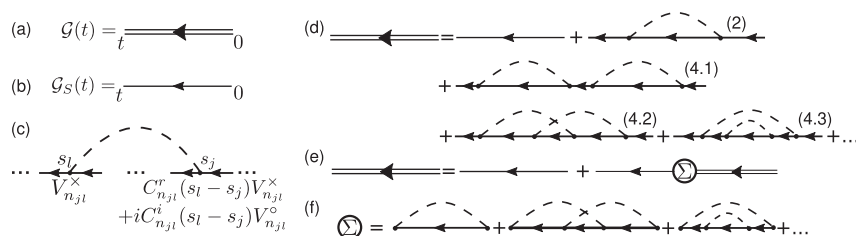


FIG. 1. Diagrammatic representation of (a) the interacting Green's superoperator and (b) the free-exciton Green's superoperator. (c) In an arbitrary diagram, the environmental assistance starting at s_j , ending at s_l ($t \geq s_l \geq s_j \geq 0$), and involving the environment that surrounds chromophore n_{jl} is represented by a dashed circumference connecting s_j and s_l . The connections of the circumference with free-exciton lines, represented by full dots, correspond to the superoperators in Eqs. (17) and (18). Diagrammatic representation of (d) the perturbation expansion for $\mathcal{G}(t)$ up to the fourth order in the exciton–environment interaction, (e) the Dyson equation [Eq. (19)], and (f) the self-energy superoperator up to the fourth order in the exciton–environment interaction.

With the standard definition of the frequency-dependent quantities,

$$\mathcal{G}(t) = \int_{-\infty}^{+\infty} \frac{d\omega}{2\pi} e^{-i\omega t} \mathcal{G}(\omega). \quad (23)$$

Equation (22) becomes the following algebraic equation:

$$\mathcal{G}(\omega) = [\omega - \mathcal{L}_S - \Sigma(\omega)]^{-1}. \quad (24)$$

The Hermitian property of the RDM implies that $\mathcal{G}(\omega)$ satisfies

$$\langle\langle e_2' e_1' | \mathcal{G}(\omega) | e_2 e_1 \rangle\rangle = -\langle\langle e_1' e_2' | \mathcal{G}(-\omega) | e_1 e_2 \rangle\rangle^*. \quad (25)$$

This property shows that it is sufficient to compute $\mathcal{G}(\omega)$ only for $\omega \geq 0$, while the values for negative frequencies follow from this symmetry property. We additionally note that the same symmetry property also characterizes the inverse Green's superoperator $\mathcal{G}^{-1}(\omega)$, as well as the self-energy superoperator $\Sigma(\omega)$, which now carries the dimension of energy.

The frequency-domain diagrammatic representations of $\mathcal{G}(\omega)$ and $\Sigma(\omega)$ appear the same as the time-domain representations in Figs. 1(d) and 1(f), respectively. The general rules for translating diagrams into formulas can be inferred from the discussion in Sec. II D.

D. Born and Redfield approximations

The lowest, second-order approximation to Σ is known as the (second) BA.⁵⁵ The corresponding self-energy superoperator, shown in Fig. 2(a1), reads as (see also Refs. 84 and 85)

$$\Sigma_{\text{BA}}(t) = \sum_n V_n^\times \mathcal{G}_S(t) [C_n^r(t) V_n^\times + i C_n^i(t) V_n^\circ], \quad (26)$$

while its frequency-domain counterpart is

$$\Sigma_{\text{BA}}(\omega) = \sum_n \int_{-\infty}^{+\infty} \frac{d\nu}{2\pi} \mathcal{J}_n(\omega - \nu) \times \left\{ \coth\left(\frac{\beta(\omega - \nu)}{2}\right) V_n^\times \mathcal{G}_S(\nu) V_n^\times + V_n^\times \mathcal{G}_S(\nu) V_n^\circ \right\}. \quad (27)$$

Upon inserting $\mathcal{K}_{\text{BA}}(t) = i\Sigma_{\text{BA}}(t)$ into Eq. (20), we obtain the well-known TC2 QME,⁵⁴

$$\begin{aligned} \partial_t \rho(t) = & -i[H_S, \rho(t)] \\ & - \sum_n \left[V_n, \int_0^t ds C_n(t-s) e^{-iH_S(t-s)} V_n \rho(s) e^{iH_S(t-s)} \right] \\ & + \sum_n \left[V_n, \int_0^t ds C_n(t-s)^* e^{-iH_S(t-s)} \rho(s) V_n e^{iH_S(t-s)} \right]. \end{aligned} \quad (28)$$

For delta-correlated noise characterized by the dephasing rate Γ , $C_n(t) = \Gamma\delta(t)$, Eq. (28) assumes the Lindblad form,

$$\partial_t \rho(t) = -i[H_S, \rho(t)] - \Gamma \sum_n \left(\frac{1}{2} \{ V_n^2, \rho(t) \} - V_n \rho(t) V_n \right). \quad (29)$$

We will use this result in Sec. III B 3.

The time-independent and nonsecular Redfield theory (see, for example, Sec. 3.8.2 of Ref. 55 or Sec. 11.2 of Ref. 98),

$$\partial_t |\rho(t)\rangle\rangle = -i\mathcal{L}_S |\rho(t)\rangle\rangle - \mathcal{R} |\rho(t)\rangle\rangle, \quad (30)$$

is obtained by inserting Eq. (26) into Eq. (22) and then performing the Markovian and adiabatic approximations. These approximations result in the delta-like self-energy in the time domain, $\Sigma_{\text{Red}}(t) = \Sigma_{\text{Red}}\delta(t)$, the frequency-independent self-energy $\Sigma_{\text{Red}}(\omega) = \Sigma_{\text{Red}}$, and the Redfield tensor $\mathcal{R} = i\Sigma_{\text{Red}}$ [see Eq. (21)], where

$$\Sigma_{\text{Red}} = \int_{-\infty}^{+\infty} ds \Sigma_{\text{BA}}(s) e^{i\mathcal{L}_S s}. \quad (31)$$

The Redfield theory is formulated in the exciton basis $\{|x\rangle\}$ defined through $H_S|x\rangle = \omega_x|x\rangle$. Equation (31) then implies that the Redfield-tensor matrix elements read

$$\langle\langle x_2' x_1' | \mathcal{R} | x_2 x_1 \rangle\rangle = i \langle\langle x_2' x_1' | \Sigma_{\text{BA}}(\omega_{x_2} - \omega_{x_1}) | x_2 x_1 \rangle\rangle. \quad (32)$$

For delta-correlated noise, $C_n(t) = \Gamma\delta(t)$, the Redfield equation [Eq. (30)] also assumes the Lindblad form [Eq. (29)].⁹⁸

E. Self-consistent Born approximation

In this work, we improve upon the BA by replacing the free-exciton Green's superoperator \mathcal{G}_S in Fig. 2(a1) or Eq. (27) with the interacting Green's superoperator \mathcal{G} ; see Fig. 2(b1). The resultant equation for the self-energy superoperator

$$\Sigma(\omega) = \sum_n \int_{-\infty}^{+\infty} \frac{d\nu}{2\pi} \mathcal{J}_n(\omega - \nu) \times \left\{ \coth\left(\frac{\beta(\omega - \nu)}{2}\right) V_n^\times \mathcal{G}(\nu) V_n^\times + V_n^\times \mathcal{G}(\nu) V_n^\circ \right\} \quad (33)$$

is to be solved together with the Dyson equation [Eq. (24)] in a self-consistent loop. Namely, one starts from the free-exciton case, $\Sigma^{(0)}(\omega) = 0$, when Eq. (24) gives the free-exciton Green's function ($\eta \rightarrow +0$),

$$\mathcal{G}^{(0)}(\omega) = \mathcal{G}_S(\omega) = [\omega + i\eta - \mathcal{L}_S]^{-1}. \quad (34)$$

$\mathcal{G}^{(0)}(\omega)$ is then inserted into Eq. (33) to yield $\Sigma^{(1)}(\omega) = \Sigma_{\text{BA}}(\omega)$, which is then inserted into Eq. (24) to yield $\mathcal{G}^{(1)}(\omega)$, etc. The

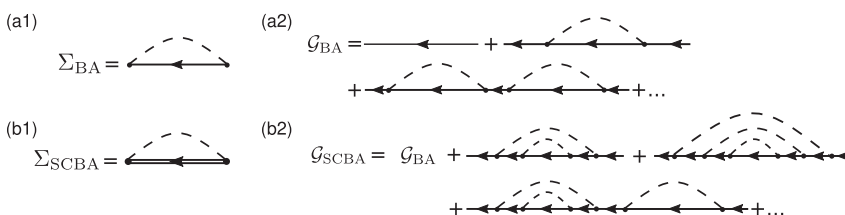


FIG. 2. Diagrammatic representation of (a1) the BA self-energy superoperator [Eq. (26) or Eq. (27)], (b1) the SCBA self-energy superoperator [Eq. (33)], (a2) Green's superoperator in the BA, and (b2) Green's superoperator in the SCBA.

above-described procedure is repeated until the difference between two consecutive iterations $\Sigma^{(k)}(\omega)$ and $\Sigma^{(k-1)}(\omega)$ for the self-energy ($k \geq 1$) becomes smaller than a prescribed numerical tolerance (see Sec. III A for more details).

Using either BA or SCBA for the self-energy superoperator, we do perform a partial resummation of the perturbation series for \mathcal{G} [Fig. 1(d)]. The resulting $\mathcal{G}_{(\text{SC})\text{BA}}$ contains contributions from all orders in the exciton–environment interaction constant. Nevertheless, the diagrammatic content of the SCBA is much richer than that of the BA, compare Fig. 2(b2) to Fig. 2(a2), suggesting that the SCBA is reliable in a much wider parameter range than the BA. Still, the SCBA retains only a very limited subset of all possible diagrams appearing in Figs. 1(d),⁹⁹ and its reliability is to be carefully checked.

III. RESULTS

A. Technical details

Equation (34) features an infinitesimally small frequency η , which ensures the causality, i.e., $\mathcal{G}_S(t) = 0$ for $t < 0$. We always shift $\omega \rightarrow \omega + i\eta$ on the right-hand side of the Dyson equation [Eq. (24)], which, apart from the causality, ensures that the matrix inversion in Eq. (24) is numerically stable. However, the numerical Fourier transformation of $\mathcal{G}(\omega)$ thus obtained produces the exponentially damped Green’s superoperator $\tilde{\mathcal{G}}(t) = e^{-\eta t} \mathcal{G}(t)$. The results for the true Green’s superoperator $\mathcal{G}(t) = e^{\eta t} \tilde{\mathcal{G}}(t)$ are thus the most reliable for $t \ll \eta^{-1}$. In all our computations, we set $\eta = 1 \text{ cm}^{-1}$, meaning that our results for exciton dynamics are bound to be reliable for $t \ll 5 \text{ ps}$. While we find that our results in the real-time domain are free of finite- η effects on timescales beyond η^{-1} , we always show only the initial 2–3 ps of exciton dynamics.

Generally, $\mathcal{G}(\omega)$ slowly decays toward zero as $|\omega| \rightarrow +\infty$. The dominant component of the high-frequency tail of $\mathcal{G}(\omega)$ can be inferred by performing one partial integration of $\mathcal{G}(\omega) = \int_0^{+\infty} dt e^{i(\omega+i\eta)t} \mathcal{G}(t)$, which results in

$$\mathcal{G}(\omega) = \frac{1}{\omega + i\eta} + \mathcal{O}(\omega^{-2}), \quad |\omega| \rightarrow +\infty. \quad (35)$$

Deriving Eq. (35), we use $\mathcal{G}(t=0) = -i\mathbb{1}$, where $\mathbb{1}$ denotes the unit operator in the Liouville space. The strongly pronounced high-frequency tail of $\mathcal{G}(\omega)$ means that we have to consider many values of ω in order for the discrete Fourier transform to produce decent results in the time domain. This is to be avoided as computing $\mathcal{G}(\omega)$ and $\Sigma(\omega)$ involves inversion of an $N^2 \times N^2$ matrix [Eq. (24)] and numerical integration [Eq. (33)], respectively. Defining $\mathcal{T}(\omega) = \frac{1}{\omega+i\eta}$ and $\mathcal{G}^{\text{nt}}(\omega) = \mathcal{G}(\omega) - \mathcal{T}(\omega)$,¹⁰⁰ the discrete (numerical) Fourier transformation of the non-tailed part $\mathcal{G}^{\text{nt}}(\omega)$ produces $\tilde{\mathcal{G}}^{\text{nt}}(t)$, while the Fourier transformation of the high-frequency tail $\mathcal{T}(\omega)$ can be performed analytically to yield $\tilde{\mathcal{T}}(t) = -i\theta(t)e^{-\eta t}\mathbb{1}$. Finally,

$$\mathcal{G}(t) = -i\theta(t)\mathbb{1} + e^{\eta t}\tilde{\mathcal{G}}^{\text{nt}}(t). \quad (36)$$

As we assume local exciton–environment interaction [Eq. (4)], $\mathcal{G}(\omega)$ and $\Sigma(\omega)$ are most conveniently represented in the site basis $\{|n\rangle\}$. In all the examples to be discussed, we assume for simplicity that the

environments of individual chromophores are identical. The integration in Eq. (33) expressing Σ in terms of \mathcal{G} is performed using the ordinary trapezoidal rule. Because of the symmetry property in Eq. (25), we perform a numerical integration of Eq. (33) from 0 to ω_{max} with frequency step $\Delta\omega$. The contribution around $\nu = \omega$ to the integral in Eq. (33) may be divergent for sub-Ohmic SDs, while it is finite (zero) for Ohmic (super-Ohmic) SDs. The correct treatment of the possible divergence when computing Eq. (33) for sub-Ohmic SDs is beyond the scope of this study. Importantly, the SDs that are most widely used in studying EET through multichromophoric aggregates are either super-Ohmic or Ohmic^{101,102} and can be handled in the manner presented here; see Sec. III C and Appendix C. We stop the self-consistent cycle once we achieve $\delta\Sigma^{(k)} \leq \epsilon_{\text{tol}}$, where ($k \geq 1$),

$$\delta\Sigma^{(k)} = \max_{\substack{n'_2 n'_1 \\ n_2 n_1}} \left| \frac{2\langle\langle n'_2 n'_1 | \Sigma^{(k)}(\omega) - \Sigma^{(k-1)}(\omega) | n_2 n_1 \rangle\rangle}{\langle\langle n'_2 n'_1 | \Sigma^{(k)}(\omega) + \Sigma^{(k-1)}(\omega) | n_2 n_1 \rangle\rangle} \right|, \quad (37)$$

while ϵ_{tol} is the desired (relative) accuracy. We summarize the values of adjustable numerical parameters ($\eta, \omega_{\text{max}}, \Delta\omega, \epsilon_{\text{tol}}$) involved in our computations in Table I.

The computational performance of the numerical integration of Eq. (33) mainly depends on the high-frequency rather than low-frequency behavior of the SD. In the examples analyzed in Sec. III B, $\mathcal{J}(\omega) \sim \omega^{-1}$ as $|\omega| \rightarrow +\infty$ so that the integrand in Eq. (33) falls off as ν^{-2} as $|\nu| \rightarrow +\infty$; see also Eq. (35). Other widely used SDs decrease even more rapidly in the high-frequency limit.^{101,102} This suggests that the bottleneck in the self-consistent cycle is the inversion of the $N^2 \times N^2$ matrix in Eq. (24).

Figures 3(a) and 3(b), respectively, show $\delta\Sigma^{(k)}$ as a function k when the SCBA is used on the dimer in the overdamped phonon continuum [the examples analyzed in Figs. 7(a)–7(d)] and on the seven-site FMO model in the realistic environment [the examples analyzed in Figs. 12(b1) and 12(b2)]. Notably, the convergence of the self-consistent algorithm is achieved in a couple of tens of steps, even in a multichromophoric system immersed in a structured environment. After its initial increase with k , starting from the value of 2 [see the text above Eq. (34)], $\delta\Sigma^{(k)}$ decreases in a power-law fashion for sufficiently large k .

In both BA and SCBA, the trace of the RDM is preserved because of the outermost commutator in self-energies in Eqs. (27) and (33). The RDM positivity is a much subtler issue, but we observe that, whenever SCBA improves over the BA, the results of both approximations conform to the positivity requirement on the timescales analyzed.

TABLE I. Summary of the adjustable numerical parameters needed to perform the self-consistent cycle and the values used in our computations.

Parameter (unit)	Value
η (cm^{-1})	1
ω_{max} (cm^{-1})	3000–5000
$\Delta\omega$ (cm^{-1})	0.5
ϵ_{tol} (–)	10^{-6}

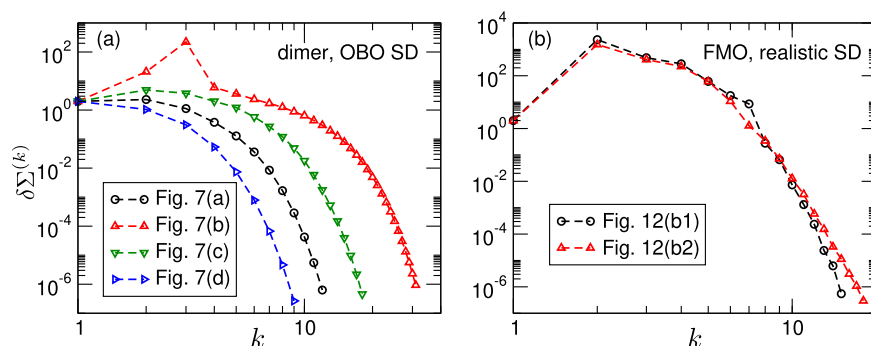


FIG. 3. Dependence of the quantity $\delta\Sigma^{(k)}$ [Eq. (37)] monitoring the convergence of the self-consistent algorithm on the iteration number k in the examples analyzed in (a) Figs. 7(a)–7(d) and (b) Figs. 12(b1) and 12(b2). Note the logarithmic scale on both axes.

As we are primarily interested in examining the reliability of the BA and SCBA, we use

$$|\rho(0)\rangle\rangle = \frac{1}{N} \sum_{n_2 n_1} |n_2 n_1\rangle\rangle \quad (38)$$

as the initial condition in all numerical computations. Apart from its simplicity, this initial condition provides a fairer assessment of the approximation performance than the widely used initial condition $|n_0 n_0\rangle\rangle$, in which the exciton is placed at chromophore n_0 . In more detail, exciton dynamics in an arbitrary basis $\{|e\rangle\}$ is

$$\langle\langle e_2 e_1 | \rho(t) \rangle\rangle = \sum_{\substack{n_2 n_1 \\ n'_2 n'_1}} \langle e_2 | n_2 \rangle \langle n_1 | e_1 \rangle \langle\langle n_2 n_1 | \mathcal{G}(t) | n'_2 n'_1 \rangle\rangle \langle\langle n'_2 n'_1 | \rho(0) \rangle\rangle. \quad (39)$$

If the exciton is initially placed at chromophore n_0 , its subsequent dynamics is determined by only N^2 matrix elements $\langle\langle n_2 n_1 | \mathcal{G}(t) | n_0 n_0 \rangle\rangle$ of \mathcal{G} out of the total of N^4 elements. Quite generally,¹⁰³ the quality of approximate dynamics is different for different matrix elements of \mathcal{G} , that is, for different starting chromophores n_0 . Inserting the initial condition of Eq. (38) into Eq. (39), we can assess the overall approximation performance, which is effectively “averaged” over different matrix elements of \mathcal{G} .

B. Reliability of the SCBA: Asymmetric dimer

The advantages and shortcomings of the SCBA are most transparently identified on the simplest model relevant for EET, the molecular dimer. In the site basis $\{|1_n\rangle, |2_n\rangle\}$, the exciton Hamiltonian H_S is represented by the matrix

$$H_S = \begin{pmatrix} \Delta\varepsilon & J \\ J & 0 \end{pmatrix}, \quad (40)$$

where $\Delta\varepsilon$ is the site-energy gap, while J is the resonance coupling. The exciton state of lower (higher) energy is denoted as $|1_x\rangle$ ($|2_x\rangle$).

In Secs. III B 1–III B 4, we consider exciton dynamics in the featureless phonon environment described by the overdamped Brownian oscillator (OBO) SD,⁸⁶

$$\mathcal{J}_{\text{ph}}(\omega) = 2\lambda_{\text{ph}} \frac{\omega\gamma_{\text{ph}}}{\omega^2 + \gamma_{\text{ph}}^2}, \quad (41)$$

TABLE II. Summary of the default values of excitonic ($\Delta\varepsilon, J$) and exciton–environment interaction ($\lambda_{\text{ph}}, \gamma_{\text{ph}}$) parameters used in Secs. III B 1–III B 4.

Parameter (unit)	Value
$\Delta\varepsilon$ (cm ⁻¹)	100
J (cm ⁻¹)	50
λ_{ph} (cm ⁻¹)	40
γ_{ph} (cm ⁻¹)	40
T (K)	300

where λ_{ph} is the reorganization energy, while γ_{ph}^{-1} determines the environment–reorganization timescale. Table II summarizes the default values of model parameters, which are broadly representative of photosynthetic aggregates. The performance of our approximations upon varying these parameters is studied in Secs. III B 1 and III B 3.

In Sec. III B 5, we assume that the exciton interacts with a single underdamped vibrational mode so that the interaction can be modeled by the underdamped Brownian oscillator SD,⁸⁶

$$\mathcal{J}_{\text{vib}}(\omega) = S_0 \omega_0 \left[\frac{\omega\gamma_0}{(\omega - \omega_0)^2 + \gamma_0^2} + \frac{\omega\gamma_0}{(\omega + \omega_0)^2 + \gamma_0^2} \right], \quad (42)$$

where ω_0 is the vibrational frequency, S_0 is the Huang–Rhys factor, while γ_0 is the relaxation rate. Quite generally, $\gamma_0 \ll \omega_0$ and $S_0 \ll 1$. The values used in benchmarks are taken from Ref. 50 and are listed in Sec. III B 5.

1. Overdamped phonon continuum: Variations in excitonic parameters

Here, we fix the exciton–environment interaction parameters λ_{ph} and γ_{ph} and study the quality of SCBA and BA for different excitonic parameters J and $\Delta\varepsilon$. Figure 4 provides an overall assessment of the performance of BA [Fig. 4(a)] and SCBA [Fig. 4(b)] and of the improvement of the SCBA over the BA introduced by the self-consistent cycle [Fig. 4(c)]. A convenient performance measure is the trace distance between the approximate $[\rho_{(\text{SCBA})}(t)]$ and numerically exact $[\rho_{\text{HEOM}}(t)]$ RDM. As the trace distance is time-dependent, while we also limit ourselves to the short-time dynamics

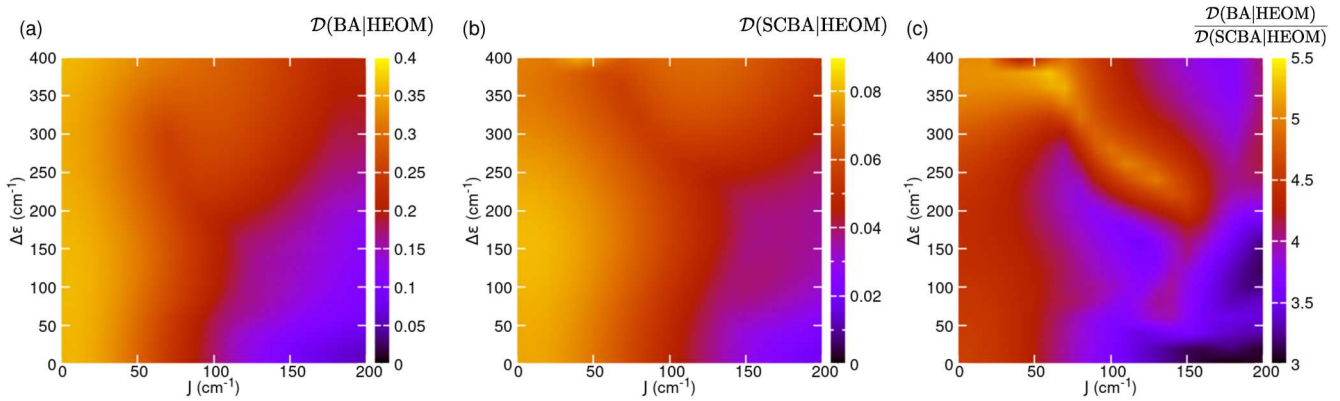


FIG. 4. (a) and (b) Heat maps of the maximum trace distance $\mathcal{D}((\text{SC})\text{BA}|\text{HEOM})$ [Eq. (43)] between the numerically exact and BA [(a)] or SCBA [(b)] excitonic RDM over the interval $[0, t_{\max}]$. (c) Heat map of the ratio $\frac{\mathcal{D}(\text{BA}|\text{HEOM})}{\mathcal{D}(\text{SCBA}|\text{HEOM})}$ between the performance metrics used in (a) and (b). All quantities are computed for different values of the resonance coupling J and the site-energy gap $\Delta\epsilon$, the remaining parameters assume their default values listed in Table II, the initial condition is specified in Eq. (38), while $t_{\max} = 2$ ps.

(see Sec. III A), we quantify the performance of our approximations using the maximum trace distance over the time window $[0, t_{\max}]$,

$$\mathcal{D}((\text{SC})\text{BA}|\text{HEOM}) = \max_{0 \leq t \leq t_{\max}} \frac{1}{2} \sum_{k=1}^2 |r_k^{(\text{SC})\text{BA}-\text{HEOM}}(t)|, \quad (43)$$

where $r_k^{(\text{SC})\text{BA}-\text{HEOM}}(t)$ is the k th eigenvalue of the operator $\rho_{(\text{SC})\text{BA}}(t) - \rho_{\text{HEOM}}(t)$. We set $t_{\max} = 2$ ps in Eq. (43). The colorbar ranges in Figs. 4(a) and 4(b) suggest that the SCBA is generally a better approximation to the exact dynamics than the BA. To quantify the improvement of the SCBA over the BA, in Fig. 4(c), we plot the ratio $\frac{\mathcal{D}(\text{BA}|\text{HEOM})}{\mathcal{D}(\text{SCBA}|\text{HEOM})}$, which we find to be greater than or equal to unity for all the pairs $(J, \Delta\epsilon)$ examined. The larger the ratio, the more pronounced the improvement of the SCBA over the BA.

Figures 4(a) and 4(b) show that the reliability of both BA and SCBA generally improves with increasing J and/or decreasing $\Delta\epsilon$. This suggests that the approximations are best suited for relatively delocalized excitons, when the mixing angle $\theta \in [0, \pi/4]$, defined as $\tan(2\theta) = 2J/\Delta\epsilon$, significantly deviates from zero. Still, for $\Delta\epsilon = 0$, when excitons are perfectly delocalized, the quality of both BA and SCBA increases with increasing J , i.e., decreasing λ_{ph}/J . The impact of the exciton–environment interaction on the approximation reliability will be analyzed in detail in Sec. III B 3. Figure 4(c) reveals that the improvement of SCBA over BA is the most pronounced in the region of moderate resonance coupling $50 \text{ cm}^{-1} \lesssim J \lesssim 150 \text{ cm}^{-1}$ and large site-energy gap $\Delta\epsilon \gtrsim 200 \text{ cm}^{-1}$. The improvement is also appreciable for small resonance coupling, irrespective of the value of $\Delta\epsilon$, when both BA and SCBA perform relatively poorly; see Figs. 4(a) and 4(b).

2. Overdamped phonon continuum: Analytical insights into the pure-dephasing model

For $J = 0$, the model reduces to the pure-dephasing model, in which there is no population dynamics, but only dephasing

of the initially present interexciton coherences. The superoperators entering Eq. (14) are then time independent, and combining Eqs. (13)–(15), we readily obtain the following exact expression for the reduced evolution superoperator:

$$\langle\langle n'_2 n'_1 | \mathcal{G}(t) | n_2 n_1 \rangle\rangle = -i\theta(t) \delta_{n'_2 n_2} \delta_{n'_1 n_1} \times \left\{ \delta_{n_2 n_1} + (1 - \delta_{n_2 n_1}) e^{-i\epsilon_{n_2 n_1} t} e^{-2g^r(t)} \right\}, \quad (44)$$

where $g^r(t) = \int_0^t ds_2 \int_0^{s_2} ds_1 C^r(s_1)$ is the real part of the line shape function, whereas $\epsilon_{n_2 n_1} = \epsilon_{n_2} - \epsilon_{n_1}$ (for the dimer, $\epsilon_{n_2 n_1} = \pm\Delta\epsilon$). The derivation of Eq. (44), in which only g^r appears, crucially relies on our assumption that individual-chromophore environments are identical. While the exact coherence dynamics, which follows from Eqs. (38), (39), and (44), can be recovered from the time-convolutionless second-order QME,¹⁰⁴ the corresponding BA and SCBA results remain only approximations to the exact solution, as both involve an explicit convolution in the time domain. Still, relevant analytical insights concerning the (SC)BA can be obtained for the pure-dephasing model in the high-temperature limit $2\pi T \gg \gamma_{\text{ph}}$. In Appendix A, we derive that the matrix elements of the exact self-energy superoperator $\langle\langle n_2 n_1 | \Sigma(\omega) | n_2 n_1 \rangle\rangle$ for $n_2 \neq n_1$ have the following continued-fraction expansion (CFE):

$$\begin{aligned} \langle\langle n_2 n_1 | \Sigma(\omega) | n_2 n_1 \rangle\rangle &= \frac{4\lambda_{\text{ph}} T}{\omega - \epsilon_{n_2 n_1} + i\gamma_{\text{ph}} - \frac{2 \cdot 4\lambda_{\text{ph}} T}{\omega - \epsilon_{n_2 n_1} + 2i\gamma_{\text{ph}} - \frac{3 \cdot 4\lambda_{\text{ph}} T}{\omega - \epsilon_{n_2 n_1} + 3i\gamma_{\text{ph}} - \dots}}}. \end{aligned} \quad (45)$$

Truncating the CFE in the first layer, we obtain the BA result ($n_2 \neq n_1$),

$$\langle\langle n_2 n_1 | \Sigma_{\text{BA}}(\omega) | n_2 n_1 \rangle\rangle = \frac{4\lambda_{\text{ph}} T}{\omega - \epsilon_{n_2 n_1} + i\gamma_{\text{ph}}}. \quad (46)$$

The same result follows from Eq. (27) upon approximating $\coth\left(\frac{\beta(\omega-\nu)}{2}\right) \approx \frac{2T}{\omega-\nu}$, as appropriate in the high-temperature limit, and performing a contour integration by closing the contour in the upper half-plane. In the pure-dephasing model, we can use Eqs. (32) and (46) to obtain the matrix elements of the self-energy superoperator in the Redfield theory,

$$\langle\langle n_2 n_1 | \Sigma_{\text{Red}} | n_2 n_1 \rangle\rangle = -i \frac{4\lambda_{\text{ph}} T}{\gamma_{\text{ph}}}. \quad (47)$$

Appendix A also demonstrates that the CFE of the SCBA self-energy reads

$$\langle\langle n_2 n_1 | \Sigma_{\text{SCBA}}(\omega) | n_2 n_1 \rangle\rangle = \frac{4\lambda_{\text{ph}} T}{\omega - \varepsilon_{n_2 n_1} + i\gamma_{\text{ph}} - \frac{4\lambda_{\text{ph}} T}{\omega - \varepsilon_{n_2 n_1} + 2i\gamma_{\text{ph}} - \frac{4\lambda_{\text{ph}} T}{\omega - \varepsilon_{n_2 n_1} + 3i\gamma_{\text{ph}} - \dots}}. \quad (48)$$

Comparing Eq. (45) to Eq. (48), we find that the CFE of the SCBA result can be obtained from the exact result by changing all the coefficients multiplying $4\lambda_{\text{ph}} T$ in the CFE numerators to unity. While this could suggest that the SCBA is, in general, a poor approximation to the exact solution,^{99,105} we note that the broadening factors are the same at each CFE denominator in both the SCBA and exact self-energy. One can then expect that the SCBA is superior to both the BA and the Redfield theory at reproducing the timescale of coherence dephasing. This expectation is confirmed in Fig. 5(a) comparing different approximations to the coherence dynamics in a symmetric ($\Delta\varepsilon = 0$) pure-dephasing dimer. The Redfield theory predicts an excessively fast coherence dephasing whose analytical form reads as [see Appendix A and the circles in Fig. 5(a)]

$$\langle\langle 1_n 2_n | \rho_{\text{Red}}(t) \rangle\rangle = \frac{1}{2} \exp\left(-\frac{4\lambda_{\text{ph}} T}{\gamma_{\text{ph}}} t\right). \quad (49)$$

On the contrary, the BA predicts an excessively slow coherence dephasing that can be reasonably described by [see Appendix A and the down-triangles in Fig. 5(a)]

$$\langle\langle 1_n 2_n | \rho_{\text{BA}}(t) \rangle\rangle \approx \frac{1}{2} \cos\left(2\sqrt{\lambda_{\text{ph}} T} t\right) e^{-\gamma_{\text{ph}} t/2}. \quad (50)$$

The exact coherence-dephasing timescale is in between the results of the Redfield theory and BA, while the corresponding exact dynamics can be reasonably approximated by [see Appendix A and the up-triangles in Fig. 5(a)]

$$\langle\langle 1_n 2_n | \rho(t) \rangle\rangle \approx \frac{1}{2} \exp(-2\lambda_{\text{ph}} T t^2). \quad (51)$$

The SCBA indeed reproduces the correct order of magnitude of the dephasing timescale, although it displays oscillations similar to that predicted by Eq. (50). The performance of different approximations can also be inferred from (the imaginary part of) the corresponding self-energy profile presented in Fig. 5(b). The self-energy within the Redfield theory [Eq. (47)] does not bear even a qualitative resemblance to the exact result. The BA, SCBA, and the exact result all display a peak centered around $\omega = 0$. The BA peak is the narrowest and highest and has a Lorentzian shape whose full width at half-maximum is determined by γ_{ph} only; see Eq. (46). The exact peak

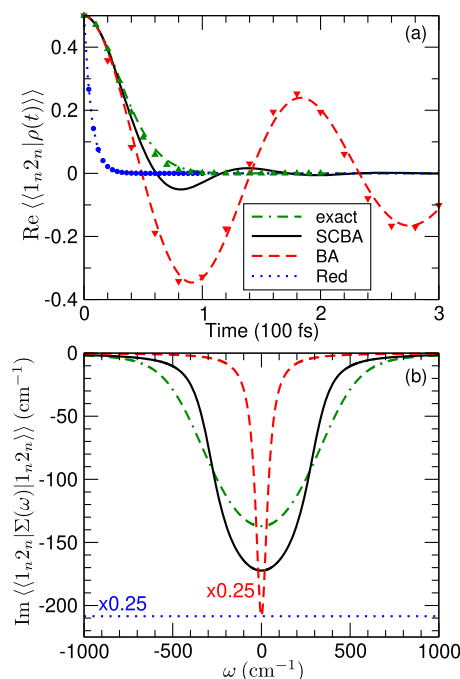


FIG. 5. (a) Time dependence of the real part of the coherence in a symmetric ($\Delta\varepsilon = 0$) pure-dephasing dimer. (b) Frequency profile of the imaginary part of the matrix element of the self-energy superoperator describing coherence dephasing in a symmetric pure-dephasing dimer. We compare the results of the SCBA (solid lines), BA (dashed lines), and Redfield theory (dotted lines) to the exact result (double dashed-dotted lines). The lines in (a) display Fourier-transformed frequency-domain results using the self-energies given in Eq. (45) (label "exact"), Eq. (48) (label "SCBA"), Eq. (46) (label "BA"), and Eq. (47) (label "Red"). Full symbols in (a) display the analytical results given by Eq. (49) (circles), Eq. (50) (down-triangles), and Eq. (51) (up-triangles). For visual clarity, the BA and Redfield self-energies in (b) are scaled down by a factor of 4.

[Eq. (45)] is much broader than the BA peak, while the width of the SCBA peak [Eq. (48)] is somewhat smaller than, yet comparable to, the width of the exact peak.

3. Overdamped phonon continuum: Variations in exciton-environment interaction parameters and temperature

Here, we fix exciton parameters $\Delta\varepsilon$ and J and vary λ_{ph} and γ_{ph} to examine the reliability of BA [Fig. 6(a)] and SCBA [Fig. 6(b)], as well as the improvement over the BA brought about by the self-consistent cycle [Fig. 6(c)]. Overall, we find that the quality of both BA and SCBA improves with decreasing the reorganization energy and/or shortening the environment-reorganization timescale; see Figs. 6(a) and 6(b). Figure 6(c) shows that the SCBA is always better at approximating the exact dynamics than the BA. Within the range of values of λ_{ph} and γ_{ph}^{-1} typically used in models of photosynthetic EET ($25 \text{ cm}^{-1} \lesssim \lambda_{\text{ph}} \lesssim 250 \text{ cm}^{-1}$ and $50 \text{ fs} \lesssim \gamma_{\text{ph}}^{-1} \lesssim 200 \text{ fs}$),¹ the self-consistent cycle significantly improves the BA results; see the dashed-line rectangle in Fig. 6(c). Notably, for very fast environments ($\gamma_{\text{ph}}^{-1} \lesssim 10 \text{ fs}$), we find that the quality of BA and SCBA

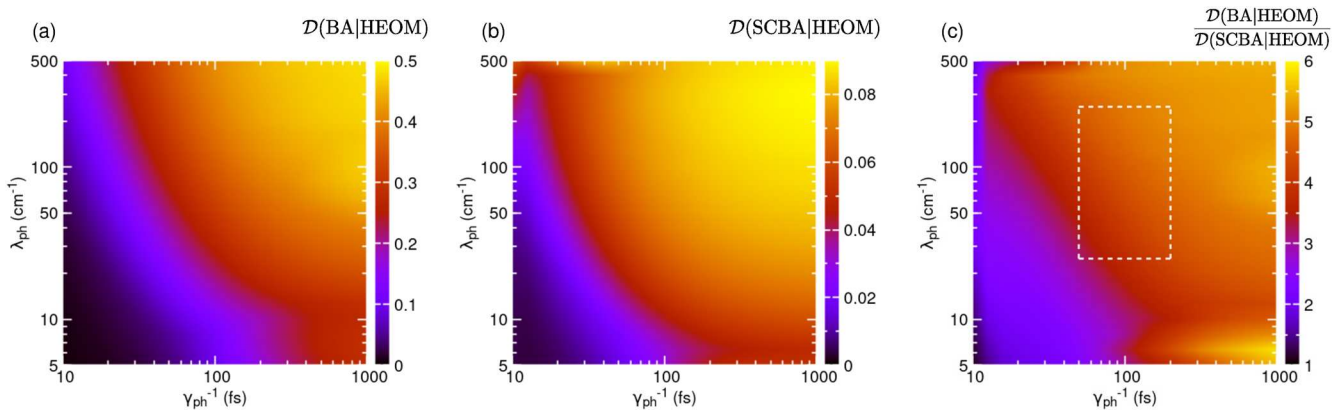


FIG. 6. (a) and (b) Heat maps of the maximum trace distance $\mathcal{D}((\text{SC})\text{BA}|\text{HEOM})$ between the numerically exact and BA [(a)] or SCBA [(b)] excitonic RDM over the interval $[0, t_{\max}]$ [Eq. (43)]. (c) Heat map of the ratio $\frac{\mathcal{D}(\text{BA}|\text{HEOM})}{\mathcal{D}(\text{SCBA}|\text{HEOM})}$ between the performance metrics used in (a) and (b). All quantities are computed for different values of the reorganization energy λ_{ph} and the environment–reorganization timescale γ_{ph}^{-1} , the remaining parameters assume their default values listed in Table II, the initial condition is specified in Eq. (38), while $t_{\max} = 2$ ps. The dashed-line rectangle in (c) delimits the range of values of γ_{ph}^{-1} and λ_{ph} typically used in modeling photosynthetic EET.

is virtually the same, i.e., $\mathcal{D}(\text{SCBA}|\text{HEOM}) \approx \mathcal{D}(\text{BA}|\text{HEOM})$, for all reorganization energies examined. To understand this, we observe that when $\gamma_{\text{ph}} \rightarrow \infty$ and $T \rightarrow \infty$ so that $\gamma_{\text{ph}}/T \rightarrow 0$, our model reduces to the well-known Haken–Strobl–Reineker white-noise model,^{106,107} within which $C_n(t) = \Gamma\delta(t)$, with $\Gamma = 2\lambda_{\text{ph}}T/\gamma_{\text{ph}}$. Inserting this $C_n(t)$ into Eq. (14) for the exact evolution superoperator $\mathcal{U}(t)$, we conclude that the exact equation of motion for $\rho(t)$ coincides with the Lindblad-like equation (29). To reach this

conclusion, we use that the white-noise assumption renders the time-ordering sign upon differentiating Eq. (14) effective only on the superoperator $e^{-\Phi(t)}$ and ineffective on the superoperator $\partial_t\Phi(t)$. Our discussion in Sec. II D then implies that the BA, and even the Redfield theory, becomes exact in the white-noise limit. The exactness of the BA implies that the self-consistent cycle cannot improve on BA any further, meaning that the SCBA result is also exact in the white-noise limit.

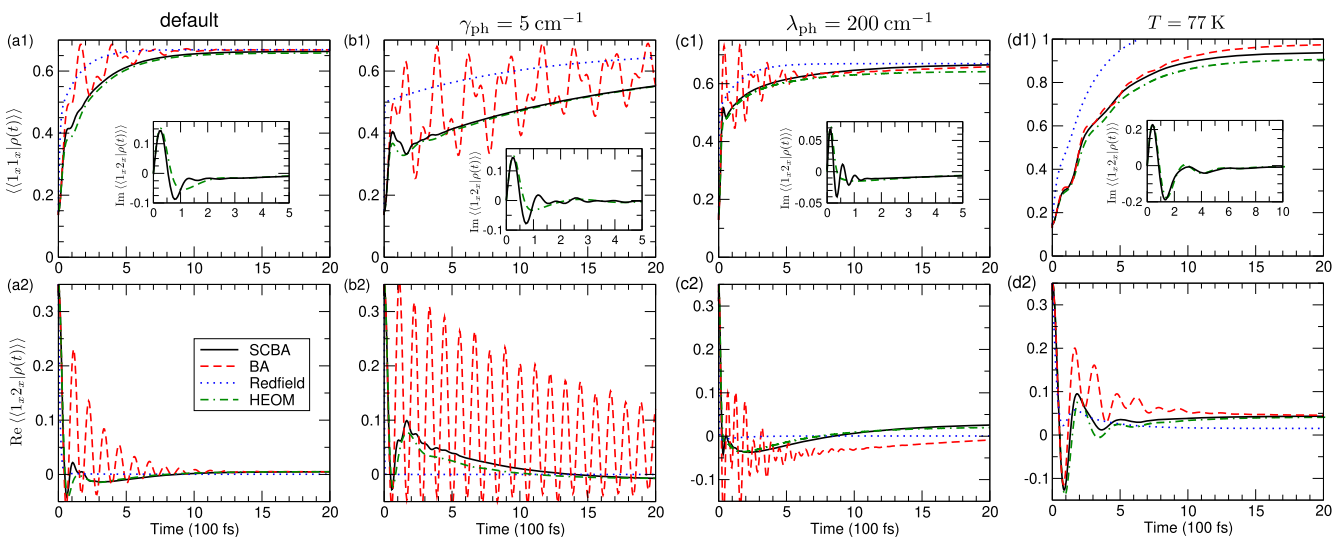


FIG. 7. Dynamics of the population of the lower-energy exciton state $|1_x\rangle$ [(a1)–(d1)] and the real part of the interexciton coherence [(a2)–(d2)] computed using SCBA (solid lines), BA (dashed lines), Redfield theory (dotted lines), and HEOM (double dashed-dotted lines). The insets in (a1)–(d1) present the very initial dynamics of the imaginary part of the interexciton coherence (BA and Redfield results are omitted for visual clarity). The parameters λ_{ph} , γ_{ph} , T , and λ_{ph} assume their default values in (a1) and (a2), while we change $\gamma_{\text{ph}} = 5 \text{ cm}^{-1}$ in (b1) and (b2), $T = 77 \text{ K}$ in (c1) and (c2), and $\lambda_{\text{ph}} = 200 \text{ cm}^{-1}$ in (d1) and (d2).

Figure 6(c) shows that the improvement of SCBA over BA is the most pronounced for sluggish environments or large reorganization energies. Both observations are ultimately rooted in the richer diagrammatic content of the SCBA compared to that of the BA, see Fig. 2, and are remarkable as computing exciton dynamics modulated by strong exciton–environment interactions and/or slow environments has to take into account higher-order environmentally assisted processes.^{84,85} Similar challenges are encountered when studying exciton dynamics at low temperatures. Additional insights into the quality of different approximations can be gained from Fig. 7, which compares approximate and numerically exact exciton dynamics for the default values of model parameters [Figs. 7(a1) and 7(a2)], slow environment [$\gamma_{\text{ph}} = 5 \text{ cm}^{-1}$, Figs. 7(b1) and 7(b2)], strong exciton–environment interaction [$\lambda_{\text{ph}} = 200 \text{ cm}^{-1}$, Figs. 7(c1) and 7(c2)], and low temperature [$T = 77 \text{ K}$, Figs. 7(d1) and 7(d2)]. The overall performance of approximate methods is essentially as discussed in Sec. III B 2. The Redfield theory shows pronounced deviations from the exact result already on shortest timescales, whereas the BA and SCBA reproduce the very initial stages ($t \lesssim 50 \text{ fs}$) of the exact dynamics quite well. While the subsequent dynamics within the BA generally exhibits oscillatory features that are damped relatively slowly, cf. Fig. 5(a), the SCBA dynamics of exciton populations and the interexciton coherence follows the corresponding HEOM results very reasonably. The SCBA approximates the true exciton-population dynamics in both realistically slow [Fig. 7(a1)] and excessively slow [Fig. 7(b1)] environments quite well, both on subpicosecond and on somewhat longer timescales. Meanwhile, Figs. 7(a2) and 7(b2), as well as the insets of Figs. 7(a1) and 7(b1), suggest that the SCBA is not that good at reproducing the true interexciton-coherence dynamics. Still, it does capture the correct long-time behavior (the imaginary part of the interexciton coherence tends to zero, and the real part tends to a non-zero value). For strong interactions and at low temperatures, the subpicosecond dynamics of exciton populations within the SCBA is quite close to

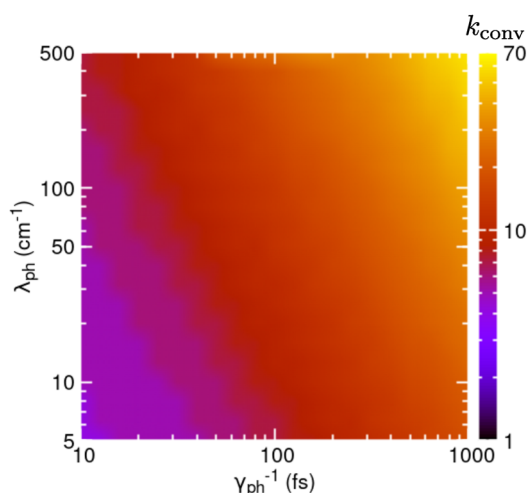


FIG. 8. Heat map of the number of steps k_{conv} needed to achieve the convergence of the SCBA [$\delta\Sigma^{(k)} \leq \epsilon_{\text{tol}}$ for $k \geq k_{\text{conv}}$] for different values of the reorganization energy λ_{ph} and the environment–reorganization timescale γ_{ph}^{-1} .

the true dynamics, see Figs. 7(c1) and 7(d1), while some quantitative differences between them appear on longer timescales (these are more pronounced for the higher-energy exciton state). Meanwhile, the SCBA dynamics of the interexciton coherence agrees well with the corresponding numerically exact dynamics, especially at lower temperatures; see Figs. 7(c2) and 7(d2) and the insets of Figs. 7(c1) and 7(d1).

Figure 3(a) suggests that the convergence of the SCBA slows down with increasing the reorganization energy or the environment–reorganization timescale. This is corroborated in Fig. 8, which shows the heat map of the number of iterations k_{conv} the SCBA needs to converge [$\delta\Sigma^{(k)} \leq \epsilon_{\text{tol}}$ for $k \geq k_{\text{conv}}$] for different values of λ_{ph} and γ_{ph}^{-1} . Even in the regime of strong interaction ($\lambda_{\text{ph}} = 500 \text{ cm}^{-1}$) with slow environment ($\gamma_{\text{ph}}^{-1} = 1 \text{ ps}$), the convergence is achieved in around 70 iterations. Interestingly, we find that k_{conv} remains essentially unaffected by variations in the excitonic parameters J and $\Delta\epsilon$ for fixed λ_{ph} and γ_{ph} . For all parameter combinations in Fig. 4, the SCBA converges in 10–13 iterations. The pace of the convergence appears to be relatively weakly affected by temperature variations; see Fig. 3(a). Figure 3(b) suggests that this holds true even in larger aggregates interacting with structured environments [Figs. 12(b1) and 12(b2)].

4. Overdamped phonon continuum: Self-energy superoperator

We formulate our approximate approaches in the frequency domain, with the self-energy (memory-kernel) superoperator as their central quantity, and Figs. 9(a)–9(d) discuss the reflections of the above-summarized time-domain observations on the frequency domain. We choose the slow-environment regime analyzed in Fig. 7(b) and concentrate on the matrix elements $\langle\langle 2_x 2_x | \Sigma(\omega) | 2_x 2_x \rangle\rangle$ and $\langle\langle 1_x 2_x | \Sigma(\omega) | 2_x 2_x \rangle\rangle$ describing, respectively, the population flux out of the higher-energy exciton state and the population-to-coherence transfer from that state. The results in Figs. 9(a)–9(d) are obtained setting the artificial-broadening parameter to $\eta = 1 \text{ cm}^{-1}$, and we have checked that varying η over the range $[0.5, 5] \text{ cm}^{-1}$ does not qualitatively (and to a large extent quantitatively) affect the results presented here. Within the BA, the imaginary parts of both self-energy matrix elements display very narrow peaks centered around the exciton energy gap (at $\omega = \pm\Delta\epsilon_X$), see Figs. 9(a) and 9(c), which is compatible with the oscillatory features of the BA in Fig. 7(b). Meanwhile, the peaks of the numerically exact profiles are much wider, and their centers are somewhat shifted from $\Delta\epsilon_X$. While the SCBA profiles overall reasonably reproduce the numerically exact ones in terms of both peak positions and shapes, we note the tendency of the SCBA toward somewhat excessive peak shifting and narrowing. The relative advantage of the SCBA over the BA is the most obvious for the population-to-coherence transfer, when the BA completely misses the peak appearing somewhat below $\Delta\epsilon_X$ in both HEOM and SCBA profiles; see Fig. 9(c).

In Figs. 9(e) and 9(f), we compare the BA and SCBA results for the self-energy superoperator in the time domain to the corresponding numerically exact result. As discussed in Sec. III A, these time-domain results do not depend on η . The general tendencies observed in the exciton dynamics in Fig. 7(b) are also seen on the level of the time-dependent memory kernel. Namely, the

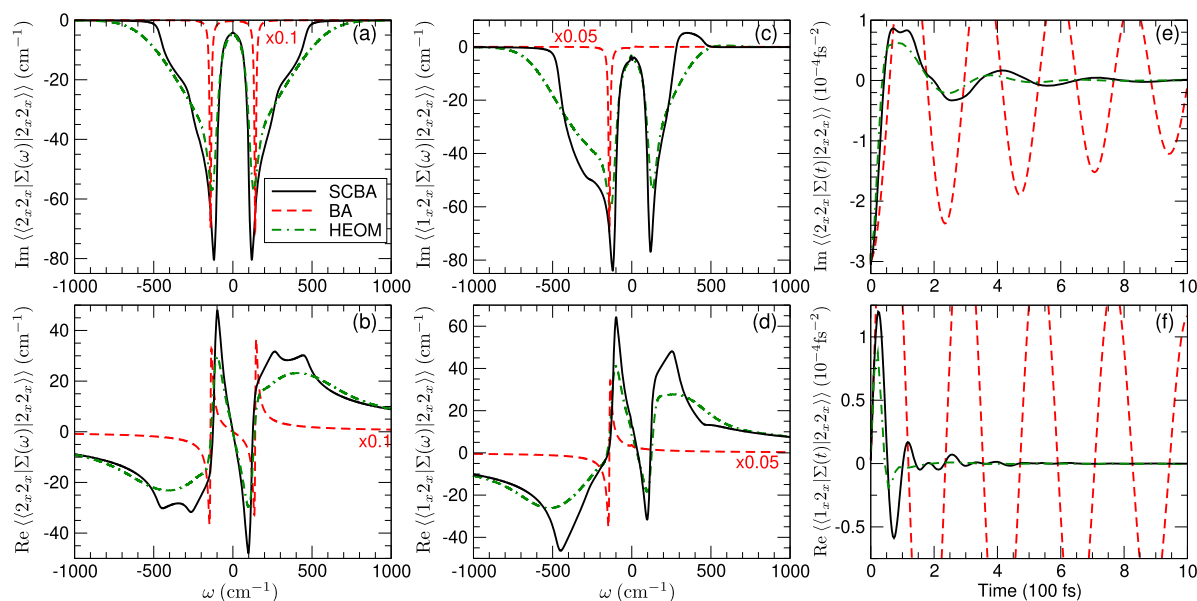


FIG. 9. (a)–(d) Frequency dependence of the imaginary [(a) and (c)] and real [(b) and (d)] parts of the matrix elements of the self-energy superoperator $\Sigma(\omega)$ computed using SCBA (solid lines), BA (dashed lines), and HEOM (double dashed-dotted lines). We show matrix elements describing the population flux out of the higher-energy exciton state $|2_x\rangle$ [(a) and (b)] and the population-to-coherence transfer from the higher-energy exciton state [(c) and (d)]. For visual clarity, the BA results are multiplied by a factor of (a) and (b) 0.1 and (c) and (d) 0.05. In panels (a)–(d), we use $\eta = 1 \text{ cm}^{-1}$. (e) and (f) Time dependence of the matrix elements of the self-energy superoperator $\Sigma(t)$ computed using SCBA, BA, and HEOM. The time-domain results on the timescales shown in (e) and (f) do not depend on η ; see Sec. III A. Model parameters assume the same values as in Figs. 7(b1) and 7(b2).

BA result for the time-dependent memory kernel displays pronounced weakly damped oscillatory features, while the SCBA reproduces the exact result reasonably well. The quantitative agreement between the SCBA and HEOM results for the matrix element connected to population-to-population transfer is somewhat better than in the case of population-to-coherence transfer; compare Fig. 9(e) to Fig. 9(f). We finally note that obtaining the memory-kernel superoperator in the time domain is generally difficult.¹⁰⁸ On the contrary, our time-domain results are readily obtained by the numerical Fourier transformation of the corresponding frequency-domain self-energies.

5. A single underdamped vibrational mode

Here, using the values of J , $\Delta\epsilon$, and T summarized in Table II, we benchmark the (SC)BA when the SD of the exciton–environment interaction is modeled using Eq. (42). We set $\gamma_0 = 3 \text{ cm}^{-1}$, corresponding to the relaxation timescale of $\gamma_0^{-1} = 1.77 \text{ ps}$. Keeping in mind that the interaction with an individual intrachromophore mode is, in general, relatively weak ($S_0 \sim 0.01$, irrespective of the vibrational frequency ω_0),¹⁰⁹ one could expect that already the BA recovers the numerically exact exciton dynamics. Figures 10(a) and 10(b) reveal that this is indeed the case when the vibrational mode is not resonant with the excitonic energy gap ($\omega_0 \neq \Delta\epsilon_X$). The true dynamics then exhibits weakly damped oscillations in both exciton populations and interexciton coherence, which reflect the relatively slow and inefficient interchromophore population transfer

discussed in the literature.¹¹⁰ While the BA reproduces the oscillatory behavior fairly well on the timescales we focus on, the SCBA produces an excessively fast oscillation damping and an overall incorrect dynamics of exciton populations. One may then expect that the general tendency of the self-consistent cycle toward the fast equilibration of the excitonic subsystem could render the SCBA a reliable approximation when the vibrational frequency is nearly resonant with the exciton-energy gap ($\omega_0 \approx \Delta\epsilon_X$). At resonance, the existing results show that the damping of the interexciton coherence and the concomitant interchromophore population transfer are particularly fast.¹¹⁰ Figures 11(a) and 11(b) show that the SCBA is indeed sufficiently good at reproducing this rapid equilibration of both exciton populations and coherences.

In the off-resonant case, the exciton populations and interexciton coherence predominantly oscillate at frequencies $|\omega_0 - \Delta\epsilon_X|$ and $\Delta\epsilon_X$, respectively; see the most pronounced features of the spectra in Figs. 10(c) and 10(d). The spectra in Figs. 10(c), 10(d), 11(c), and 11(d) originate from our frequency-domain computations so that they are broadened with the parameter η . The incorrect SCBA population dynamics in Fig. 10(a) is reflected on the frequency domain as the spurious low-frequency feature in Fig. 10(c). In the resonant case, the dynamics of interexciton coherence displays beats most probably stemming from oscillations at two similar frequencies; see the most intensive features in Fig. 11(d). In contrast to the off-resonant case, the relation of the beating frequency or the frequency of population oscillations in Fig. 11(c) to the inherent energy scales of the problem ($\Delta\epsilon, J, \omega_0$) is not obvious. To establish such

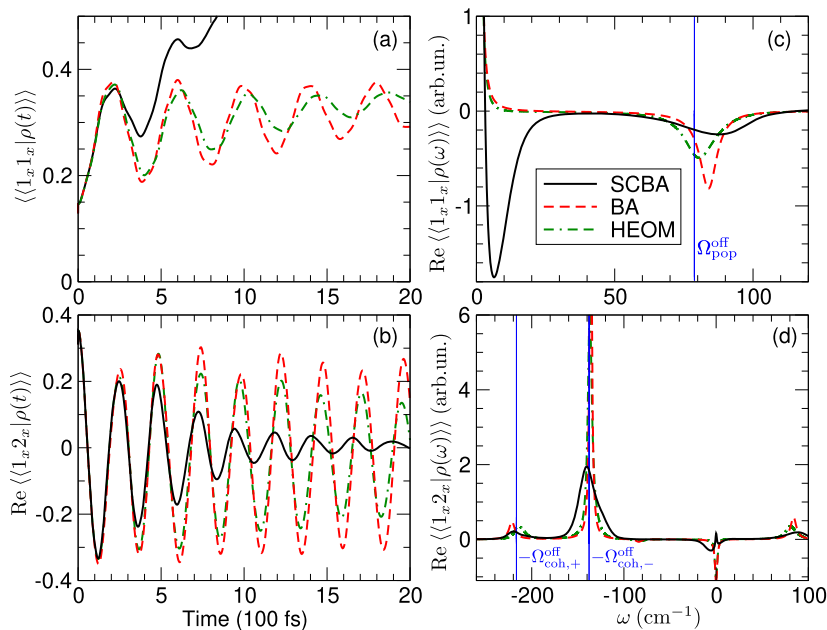


FIG. 10. Time dependence of (a) the population of the lower-energy exciton state $|1_x\rangle$ and (b) the real part of the interexciton coherence computed using SCBA (solid lines), BA (dashed lines), and HEOM (double dashed-dotted lines). (c) and (d) The real part of the Fourier transformation of the quantities displayed in (a) and (b), respectively. The dimer is coupled to an underdamped vibrational mode characterized by $\omega_0 = 213 \text{ cm}^{-1}$, $S_0 = 0.024$, and $\gamma_0 = 3 \text{ cm}^{-1}$. The vertical lines in (c) [(d)] show the frequencies of oscillatory features in exciton-population (interexciton-coherence) dynamics obtained using the weak-interaction vibronic-exciton model; see Eqs. (54)–(56).

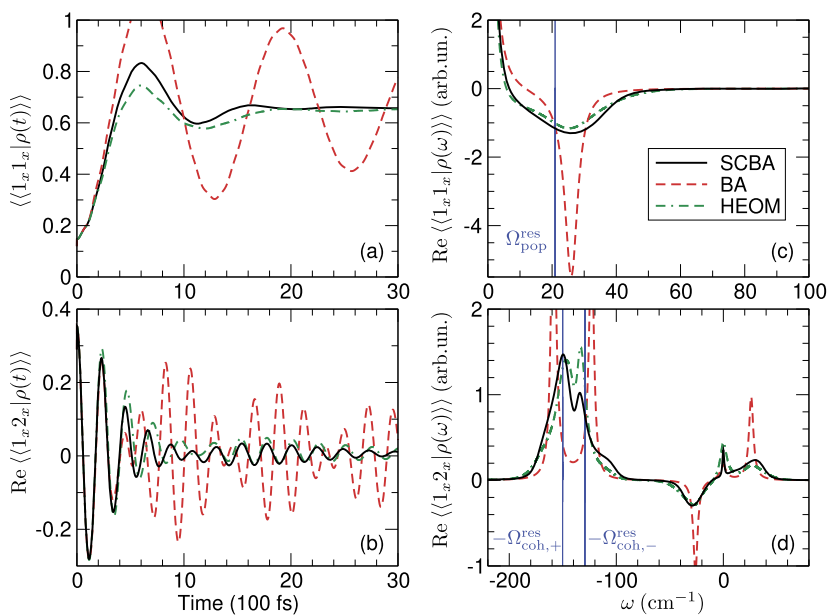


FIG. 11. Time dependence of (a) the population of the lower-energy exciton state $|1_x\rangle$ and (b) the real part of the interexciton coherence computed using SCBA (solid lines), BA (dashed lines), and BA (double dashed-dotted lines). (c) and (d) The real part of the Fourier transformation of the quantities displayed in (a) and (b), respectively. The dimer is coupled to an underdamped vibrational mode characterized by $\omega_0 = 138 \text{ cm}^{-1}$, $S_0 = 0.023$, and $\gamma_0 = 3 \text{ cm}^{-1}$. The vertical lines in (c) [(d)] show the frequencies of oscillatory features in exciton-population (interexciton-coherence) dynamics obtained using the weak-interaction vibronic-exciton model; see Eqs. (52) and (53).

a relation, we note that even the weak exciton–vibration interaction can induce appreciable mixing of the vibrational and excitonic levels and thus render the description in terms of vibronic–exciton states more appropriate. To discuss our observations in terms of these hybrid states, we assume, for simplicity, that the vibrational mode is undamped, i.e., $\gamma_0 = 0$. Then, the Hamiltonian is analogous to the Jaynes–Cummings Hamiltonian of quantum optics.¹¹¹ When $S_0 \ll 1$, it is sufficient to consider at most a single vibrational quantum,¹¹² and in Appendix B, we conclude that the first two states above the lowest-lying vibronic–exciton state $|1_x, v_0 = 0\rangle$

are linear combinations of the states $|1_x, v_0 = 1\rangle$ and $|2_x, v_0 = 0\rangle$. In the nearly resonant case ($\Delta\epsilon_X \approx \omega_0$), the energies corresponding to the oscillatory features in exciton populations,

$$\Omega_{\text{pop}}^{\text{res}} \approx \omega_0 \sqrt{2S_0} |\sin(2\theta)|, \quad (52)$$

and the interexciton coherence,

$$\Omega_{\text{coh},\pm}^{\text{res}} \approx \Delta\epsilon_X \pm \omega_0 \sqrt{\frac{S_0}{2}} |\sin(2\theta)|, \quad (53)$$

are proportional to $\sqrt{S_0}$ and agree reasonably well with the corresponding numerically exact and SCBA results; see Figs. 11(c) and 11(d). Interestingly, the frequency of the beats in the interexciton-coherence dynamics virtually coincides with the frequency of population oscillations, i.e., $\Omega_{\text{pop}}^{\text{res}} \approx \Omega_{\text{coh,+}}^{\text{res}} - \Omega_{\text{coh,-}}^{\text{res}}$. In the off-resonant case $\Delta\epsilon_X \neq \omega_0$, we find that the frequency of population oscillations is shifted from $|\Delta\epsilon_X - \omega_0|$ by an amount proportional to S_0 , i.e.,

$$\Omega_{\text{pop}}^{\text{off}} - |\Delta\epsilon_X - \omega_0| \approx S_0 \sin^2(2\theta) \frac{\omega_0^2}{|\Delta\epsilon_X - \omega_0|}, \quad (54)$$

which agrees very well with the HEOM result, and not so well with the BA and SCBA results; see Fig. 10(c). The frequency shift of the most pronounced component of exciton-coherence oscillations from $\Delta\epsilon_X$ is also linear in S_0 ,

$$\Omega_{\text{coh,-}}^{\text{off}} - \Delta\epsilon_X \approx -\frac{1}{2} S_0 \sin^2(2\theta) \frac{\omega_0^2}{|\Delta\epsilon_X - \omega_0|}, \quad (55)$$

in good agreement with the HEOM and BA results in Fig. 10(d). We mention that the much less intensive feature of the coherence-oscillation spectrum appearing around the vibration energy is shifted from ω_0 by

$$\Omega_{\text{coh,+}}^{\text{off}} - \omega_0 \approx \frac{1}{2} S_0 \sin^2(2\theta) \frac{\omega_0^2}{|\Delta\epsilon_X - \omega_0|}. \quad (56)$$

C. Reliability of the SCBA: Seven-site model of the FMO complex

In Figs. 12 and 13, we benchmark the SCBA and BA on the widely studied seven-site model of the FMO complex found in green sulfur bacteria. Detailed benchmarks of our approximations

for chromophore populations (Fig. 12) and interchromophore coherences (Fig. 13) against numerically exact results are possible for the OBO SD [Eq. (41)]. In Figs. 12(a1), 12(b1), 13(a1), and 13(b1), we use $\lambda_{\text{ph}} = 35 \text{ cm}^{-1}$ and $\gamma_{\text{ph}}^{-1} = 50 \text{ fs}$ ($\gamma_{\text{ph}} = 106.2 \text{ cm}^{-1}$). To explore the viability of our methodology, we also apply it to the model using the structured SD emerging from atomistic simulations performed in Ref. 34. As we are not aware of any numerically exact results for the dynamics modulated by this structured bath, Figs. 12(a2), 12(b2), 13(a2), and 13(b2) compare the SCBA and BA results. Details on the excitonic Hamiltonian H_S and the structured SD used are summarized in Appendix C.

Using the OBO SD, the BA already provides a good approximation to the subpicosecond dynamics of chromophore populations [Figs. 12(a1) and 12(b1)], in agreement with the findings of Ref. 54. Nevertheless, on a picosecond timescale, the BA overestimates (underestimates) populations of low-energy (high-energy) states, and this effect becomes more pronounced with decreasing the temperature; compare Fig. 12(a1) to Fig. 12(b1). While the SCBA suffers from the same deficiency, its predictions for chromophore populations are systematically closer to the numerically exact results throughout the time window examined. At higher temperatures, Figs. 12(a1) and 13(a1) suggest that the SCBA is better at approximating population dynamics than coherence dynamics. Meanwhile, Figs. 12(b1) and 13(b1) suggest that the reverse is true at lower temperatures. Figures 13(a1) and 13(b1) do not show BA results, which, at all temperatures, display oscillatory features lasting much longer than the numerically exact method predicts.

Comparing panels (a2) and (a1) [(b2) and (b1)] in Figs. 12 and 13, we conclude that our approximations deliver reasonable results for exciton dynamics in the structured environment, as it is overall similar to the dynamics in the featureless environment. The problems with longer-time population dynamics of extremal-energy

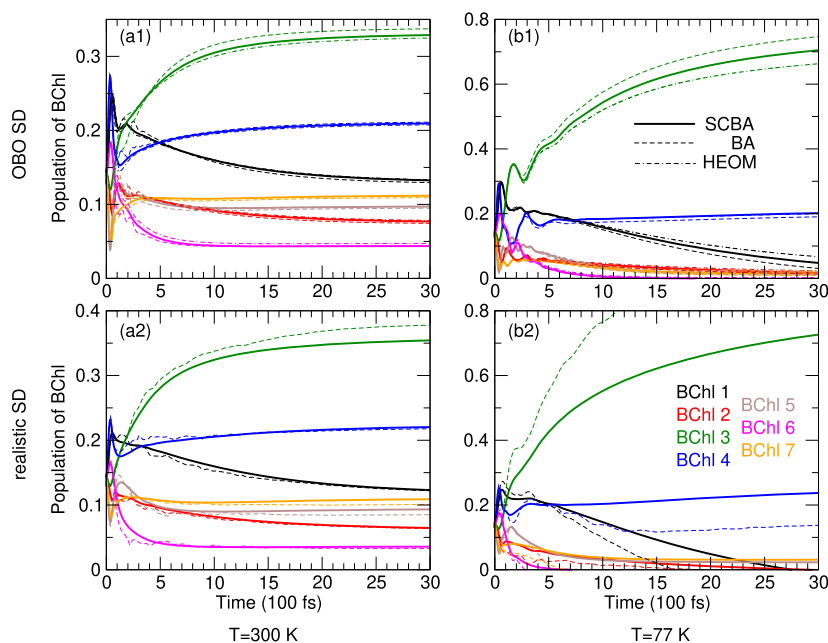


FIG. 12. Comparison of SCBA (solid), BA (dashed), and HEOM (double dashed-dotted) dynamics of BChl populations within the seven-site model of the FMO complex. Computations are performed at $T = 300 \text{ K}$ [(a1) and (a2)] and $T = 77 \text{ K}$ [(b1) and (b2)] using the OBO [(a1) and (b1)] and realistic [(a2) and (b2)] SDs of the exciton–environment interaction. As the numerically exact dynamics are not available for the realistic SD, panels (a2) and (b2) compare the SCBA and BA dynamics.

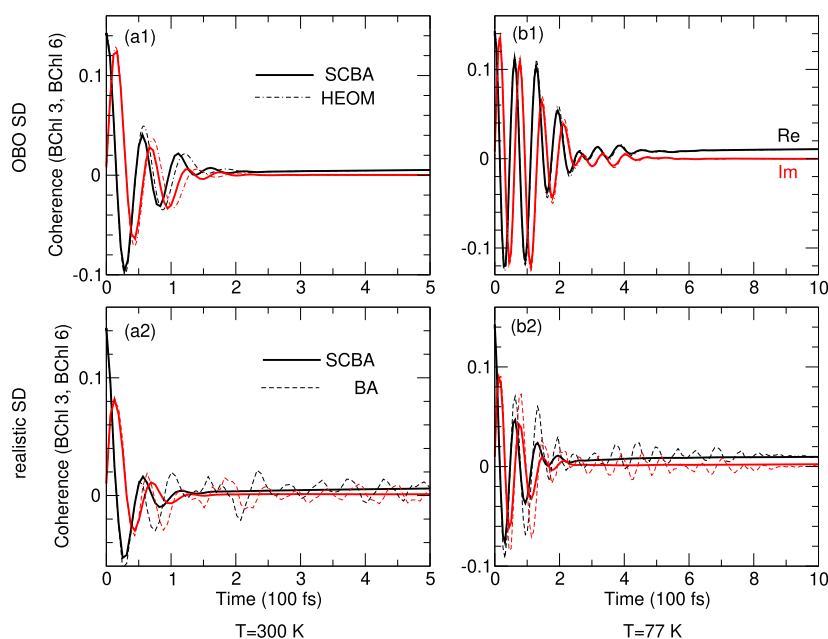


FIG. 13. Comparison of SCBA (solid), BA (dashed), and HEOM (double dashed-dotted) dynamics of the interchromophore coherence between BChl 3 and BChl 6 within the seven-site model of the FMO complex. Computations are performed at $T = 300$ K [(a1) and (a2)] and $T = 77$ K [(b1) and (b2)] using the OBO [(a1) and (b1)] and realistic [(a2) and (b2)] SDs of the exciton–environment interaction. In (a1) and (b1), we omit BA dynamics for visual clarity. As the numerically exact dynamics are not available for the realistic SD, panels (a2) and (b2) compare the SCBA and BA dynamics.

states are exacerbated in the structured environment at lower temperatures, when SCBA (and also BA) predicts nonphysical (greater than 1 or negative) populations of such states; see Fig. 12(b2). A possible origin of these problems can be understood from our analysis of the dynamics modulated by an underdamped vibrational mode; see Sec. III B 5. There, we find that the resonance condition between the exciton–energy gap and the vibrational energy quantum is crucial to the success of the SCBA. Here, exciton–energy gaps fluctuate due to low-frequency phonon modes, their fluctuations becoming more pronounced with increasing temperature. Therefore, at higher temperatures, satisfying resonance conditions between exciton–energy gaps and weakly damped vibrational modes is more probable than at lower temperatures. In other words, the SCBA is expected to work better at higher temperatures. The SCBA coherence dynamics in Figs. 13(a2) and 13(b2) is physically sensible, while the lifetime of interchromophore coherences in the structured environment is somewhat shorter than in the featureless environment at both temperatures examined.

IV. SUMMARY AND OUTLOOK

We have developed and benchmarked the self-consistent Born approximation for studying the dynamics of EET through a multichromophoric aggregate linearly interacting with a bosonic environment. We start from the lowest-order approximation for the memory kernel of the QME and improve it in the self-consistent cycle based on the QME represented in the Liouville space. We find that the SCBA reproduces the exact exciton dynamics modulated by an overdamped phonon continuum very well, even in the generally difficult regimes of strong exciton–environment interaction, slow environmental reorganization, and low temperature. This success of the SCBA can be understood from the analytically tractable

example—coherence-dephasing dynamics in the pure-dephasing model. We conclude that the reliability of the SCBA when the dynamics is modulated by an underdamped vibrational mode leans on the resonance between the mode frequency and the exciton–energy gap. Nevertheless, in a structured environment comprising both an overdamped phonon continuum and a number of underdamped vibrational modes, the SCBA reasonably describes exciton dynamics through the seven-site model of the FMO complex.

Importantly, our method does not introduce any assumptions on the form of the exciton–environment SD, making it a strong candidate for studying exciton dynamics modulated by structured environments whose properties are extracted from experiments or atomistic simulations. Although the method sometimes leads to unphysical results [see, for example, Fig. 12(b2)], it can, in principle, be improved by enlarging the set of the diagrams included in Green’s superoperator beyond that in Fig. 2(b2). Namely, Fig. 12(b2) shows that the onset of the unphysical behavior in the SCBA result is shifted toward later times with respect to the BA result so that including additional diagrams can be expected to further improve the SCBA result. Systematic improvements are possible by performing the self-consistent cycle starting from a higher-order approximation for the memory kernel. The next member of the family of self-consistent approximations thus obtained is the so-called one-crossing approximation, in which the starting memory kernel is the sum of the first two diagrams in Fig. 1(f). The final memory kernel then contains all diagrams in which the lines representing the environmental assistance cross at most once. However, the one-crossing approximation is computationally much more demanding than the SCBA, as each iteration involves a double integral over frequency. The practical applicability of the one-crossing approximation is thus determined by the balance between its computational requirements and the improvements it offers over the SCBA.

Remarkably, it may happen that the good results obtained in the lowest-order Born approximation are deteriorated by including the higher-order diagrams captured by the SCBA; see, for example, Fig. 10(a). Such situations typically feature underdamped (or undamped) environments, whose SDs are narrow (the corresponding bath correlation functions decay very slowly). Then, we have to recall that the perturbation series in Fig. 1(d) is actually an asymptotic series, which in general does not converge. Nevertheless, in realistic environments, overdamped contributions may be considered to come to rescue the convergence of the perturbation series, as these effectively hide the unphysical features caused by underdamped contributions alone.

Finally, our Liouville-space frequency-domain formulation of the SCBA suggests that it might be used as a computationally efficient and reasonably accurate approach to compute experimentally accessible nonlinear response functions. To test such a possibility, one should generalize the present formulation so that memory kernels in different excited-state sectors can be computed.

ACKNOWLEDGMENTS

The work in Prague was funded by the Czech Science Foundation (GAČR), Grant No. 22-26376S. The work in Belgrade was supported by the Institute of Physics Belgrade, through the grant by the Ministry of Science, Technological Development, and Innovation of the Republic of Serbia. Numerical computations were performed on the PARADOX-IV supercomputing facility in the Scientific Computing Laboratory, National Center of Excellence for the Study of Complex Systems, Institute of Physics Belgrade.

AUTHOR DECLARATIONS

Conflict of Interest

The authors have no conflicts to disclose.

Author Contributions

V.J. developed the method and performed all analytical derivations. V.J. and T.M. numerically implemented the method and conceived the examples on which the method was tested. V.J. performed all numerical computations and prepared the initial version of the manuscript. Both authors contributed to the final version of the manuscript.

Veljko Janković: Conceptualization (lead); Data curation (lead); Formal analysis (lead); Investigation (lead); Methodology (lead); Resources (equal); Software (lead); Validation (equal); Visualization (lead); Writing – original draft (lead); Writing – review & editing (equal). **Tomáš Mančal:** Funding acquisition (lead); Project administration (lead); Resources (equal); Software (supporting); Validation (equal); Writing – review & editing (equal).

DATA AVAILABILITY

The data that support the findings of this study are available from the corresponding author upon reasonable request.

APPENDIX A: COHERENCE DEPHASING IN THE PURE-DEPHASING MODEL (OBO SD AND HIGH-TEMPERATURE LIMIT)

We first show that the CFE of the exact $\Sigma(\omega)$ is given by Eq. (45). In the high-temperature limit, the real part of the line shape function can be approximated as⁸⁶

$$g^r(t) = \frac{2\lambda_{\text{ph}}T}{\gamma_{\text{ph}}^2} (e^{-\gamma_{\text{ph}}t} + \gamma_{\text{ph}}t - 1). \quad (\text{A1})$$

Inserting Eq. (A1) into Eq. (44) and performing the Fourier transformation of the latter gives ($n_2 \neq n_1$)

$$\begin{aligned} & \langle \langle n_2 n_1 | \mathcal{G}(\omega) | n_2 n_1 \rangle \rangle \\ &= e^{\Lambda_{\text{ph}}} \sum_{k=0}^{+\infty} \frac{(-\Lambda_{\text{ph}})^k}{k!} \frac{1}{\omega - \varepsilon_{n_2 n_1} + i\Lambda_{\text{ph}}\gamma_{\text{ph}} + ik\gamma_{\text{ph}}}, \end{aligned} \quad (\text{A2})$$

where we introduce the dimensionless parameter $\Lambda_{\text{ph}} = \frac{4\lambda_{\text{ph}}T}{\gamma_{\text{ph}}}$. It is known that the zero-temperature absorption line shape (the excitation-addition spectral function) of a two-level system whose energy gap ε_{eg} between the ground and excited states is modulated by an undamped vibrational mode (frequency ω_0 and HR factor S_0) is proportional to the negative imaginary part of the retarded Green's function (see, for example, Chap. 8 of Ref. 86 or Chap. 4 of Ref. 82),

$$G^R(\omega) = e^{-S_0} \sum_{k=0}^{+\infty} \frac{S_0^k}{k!} \frac{1}{\omega - \varepsilon_{eg} + S_0\omega_0 - k\omega_0 + i\eta}. \quad (\text{A3})$$

The CFE of Eq. (A3) reads as^{99,105}

$$G^R(\omega) = \frac{1}{\omega - \varepsilon_{eg} - \frac{S_0\omega_0^2}{\omega - \varepsilon_{eg} - \omega_0 - \frac{2S_0\omega_0^2}{\omega - \varepsilon_{eg} - 2\omega_0 - \dots}}}. \quad (\text{A4})$$

The CFE of $\langle \langle n_2 n_1 | \mathcal{G}(\omega) | n_2 n_1 \rangle \rangle$ is then obtained by substituting $\omega - \varepsilon_{eg} \rightarrow \omega - \varepsilon_{n_2 n_1}$, $S_0 \rightarrow -\Lambda_{\text{ph}}$, and $\omega_0 \rightarrow -i\gamma_{\text{ph}}$ in Eq. (A4), which follows from comparing Eq. (A2) with Eq. (A3), and reads

$$\begin{aligned} & \langle \langle n_2 n_1 | \mathcal{G}(\omega) | n_2 n_1 \rangle \rangle \\ &= \frac{1}{\omega - \varepsilon_{n_2 n_1} - \frac{4\lambda_{\text{ph}}T}{\omega - \varepsilon_{n_2 n_1} + i\gamma_{\text{ph}} - \frac{2 \cdot 4\lambda_{\text{ph}}T}{\omega - \varepsilon_{n_2 n_1} + 2i\gamma_{\text{ph}} - \dots}}}. \end{aligned} \quad (\text{A5})$$

Keeping in mind that $\langle \langle n_2 n_1 | \Sigma(\omega) | n_2 n_1 \rangle \rangle = \omega - \varepsilon_{n_2 n_1} - \langle \langle n_2 n_1 | \mathcal{G}(\omega) | n_2 n_1 \rangle \rangle^{-1}$, see Eq. (24), one immediately obtains Eq. (45).

Working in the high-temperature limit, Tanimura and Kubo obtained an expression very similar to Eq. (A5); see Appendix B of Ref. 113. They considered a single two-level chromophore (labeled n_1) and its optical coherence, whose time evolution is governed by $e^{-i\varepsilon_{n_1}t} e^{-g(t)}$.¹¹⁴ The numerators of their CFE feature nonzero imaginary parts originating from $g^r(t)$. Here, however, we consider the interchromophore coherence between excitonically uncoupled chromophores n_2 and n_1 and assume that their environments are identical and uncorrelated. In the time domain, the coherence involves the de-excitation of chromophore n_1 and

excitation of chromophore n_2 so that it evolves according to $e^{-i\varepsilon_{n_2}t}e^{-g(t)}[e^{-i\varepsilon_{n_1}t}e^{-g(t)}]^* = e^{-i\varepsilon_{n_2n_1}t}e^{-2g'(t)}$. The imaginary parts of the line shape functions cancel out, in agreement with Eq. (44), rendering the numerators of the CFE in Eqs. (A5) and (45) purely real.

We now argue that the CFE of the SCBA self-energy is given by Eq. (48). Our starting point is the BA propagator in the frequency domain ($n_2 \neq n_1$),

$$\langle\langle n_2n_1 | \mathcal{G}_{BA}(\omega) | n_2n_1 \rangle\rangle = \frac{1}{\omega - \varepsilon_{n_2n_1} - \frac{4\lambda_{ph}T}{\omega - \varepsilon_{n_2n_1} + i\gamma_{ph}}}, \quad (A6)$$

which is obtained by inserting the BA self-energy [Eq. (46)] into the Dyson equation [Eq. (24)]. The BA propagator is then inserted into Eq. (33) to obtain the following self-energy $\Sigma^{(2)}$ in the next iteration:

$$\langle\langle n_2n_1 | \Sigma^{(2)}(\omega) | n_2n_1 \rangle\rangle = \int_{-\infty}^{+\infty} \frac{dv}{2\pi} \frac{4\lambda_{ph}\gamma_{ph}T}{(\omega - v)^2 + \gamma_{ph}^2} \times \langle\langle n_2n_1 | \mathcal{G}_{BA}(\omega) | n_2n_1 \rangle\rangle. \quad (A7)$$

Here, we have approximated $\coth\left(\frac{\beta(\omega-v)}{2}\right) \approx \frac{2T}{\omega-v}$. The last integral is solved by integrating along a contour that is closed in the upper half-plane to ensure causality. As the poles of the BA propagator are in the lower half-plane by construction, the only pole of the integrand in the upper half-plane is at $v = \omega + i\gamma_{ph}$. Evaluating the corresponding residue, we obtain

$$\langle\langle n_2n_1 | \Sigma^{(2)}(\omega) | n_2n_1 \rangle\rangle = \frac{4\lambda_{ph}T}{\omega - \varepsilon_{n_2n_1} + i\gamma_{ph} - \frac{4\lambda_{ph}T}{\omega - \varepsilon_{n_2n_1} + 2i\gamma_{ph}}}. \quad (A8)$$

Repeating the above-described procedure *ad infinitum*, we obtain Eq. (48).

We end this section by presenting analytical results for the matrix elements of Green's superoperator that determine the dynamics of coherence dephasing within the BA and the Redfield theory; see Eqs. (49) and (50). Equation (A6) implies that the BA propagator in the time domain can be expressed as

$$\langle\langle n_2n_1 | \mathcal{G}_{BA}(t) | n_2n_1 \rangle\rangle = e^{-i\varepsilon_{n_2n_1}t} \int_{-\infty}^{+\infty} \frac{d\Omega}{2\pi} e^{-i\Omega t} \frac{\Omega + i\gamma_{ph}}{(\Omega - \Omega_+)(\Omega - \Omega_-)}, \quad (A9)$$

where

$$\Omega_{\pm} = \frac{\gamma_{ph}}{2} \left[\pm \sqrt{\frac{16\lambda_{ph}T}{\gamma_{ph}^2} - 1} - i \right] \approx \pm 2\sqrt{\lambda_{ph}T} - i\frac{\gamma_{ph}}{2} \quad (A10)$$

are the roots of the quadratic equation $\Omega^2 + i\gamma_{ph}\Omega - 4\lambda_{ph}T = 0$, of which both lie in the lower half-plane. We use $2\pi T/\gamma_{ph} \gg 1$ to obtain Ω_{\pm} in the high-temperature limit. The integral in Eq. (A9) is solved using the contour integration with the final result,

$$\langle\langle n_2n_1 | \mathcal{G}_{BA}(t) | n_2n_1 \rangle\rangle = -i\theta(t) \left[\frac{\Omega_+ + i\gamma_{ph}}{\Omega_+ - \Omega_-} e^{-i\Omega_+t} - \frac{\Omega_- + i\gamma_{ph}}{\Omega_+ - \Omega_-} e^{-i\Omega_-t} \right]. \quad (A11)$$

Retaining the contributions that are the most dominant in the high-temperature limit $2\pi T/\gamma_{ph} \gg 1$, Eq. (A11) can be further simplified to

$$\langle\langle n_2n_1 | \mathcal{G}_{BA}(t) | n_2n_1 \rangle\rangle = -i\theta(t) e^{-i\varepsilon_{n_2n_1}t} \cos\left(2\sqrt{\lambda_{ph}T}t\right) e^{-\gamma_{ph}t/2}. \quad (A12)$$

Equation (32) implies that the Redfield propagator in the time domain can be expressed as

$$\begin{aligned} \langle\langle n_2n_1 | \mathcal{G}_{Red}(t) | n_2n_1 \rangle\rangle &= e^{-i\varepsilon_{n_2n_1}t} \int_{-\infty}^{+\infty} \frac{d\Omega}{2\pi} \frac{e^{-i\Omega t}}{\Omega + i\frac{4\lambda_{ph}T}{\gamma_{ph}}} \\ &= -i\theta(t) e^{-i\varepsilon_{n_2n_1}t} \exp\left(-\frac{4\lambda_{ph}T}{\gamma_{ph}}t\right). \end{aligned} \quad (A13)$$

The approximation to the exact coherence-dephasing dynamics embodied in Eq. (51) is obtained by inserting the short-time approximation $g^r(t) \approx \lambda_{ph}Tt^2$ to the line shape function [Eq. (A1)] into Eq. (44).

APPENDIX B: VIBRONIC-EXCITON MODEL

We consider the model dimer, Eq. (40), in which the excitons interact with an undamped vibrational mode of frequency ω_0 and HR factor S_0 [we set $\gamma_0 = 0$ in Eq. (42)]. We assume that $S_0 \ll 1$ so that the reorganization energy $S_0\omega_0$ is much smaller than all the other energy scales in the problem ($\Delta\varepsilon, J$). It is known that the center-of-mass motion of the intrachromophore vibrations, described by $B_+ = (b_1 + b_2)/\sqrt{2}$, does not affect the single-exciton dynamics.^{109,115} The energies of the exciton states, as well as transitions between them, are then modulated by the relative motion of intrachromophore vibrations, which is described by $B_- = (b_1 - b_2)/\sqrt{2}$. The single-exciton dynamics is governed by the Hamiltonian $H = H_X + H_{B_-} + H_{X-B_-}$, where

$$H_X = \sum_{k=1}^2 |k_x\rangle \left[\varepsilon_{k_x} + (-1)^k \cos(2\theta)\omega_0 \sqrt{\frac{S_0}{2}} (B_-^\dagger + B_-) \right] \langle k_x|, \quad (B1)$$

$$H_{B_-} = \omega_0 B_-^\dagger B_-, \quad (B2)$$

$$H_{X-B_-} = -\sin(2\theta)\omega_0 \sqrt{\frac{S_0}{2}} (|2_x\rangle\langle 1_x| + |1_x\rangle\langle 2_x|)(B_-^\dagger + B_-). \quad (B3)$$

The energy of the bare exciton state $k = 1, 2$ is $\varepsilon_{k_x} = \frac{\Delta\varepsilon}{2} \left[1 + (-1)^k \sqrt{1 + \tan^2(2\theta)} \right]$. The dynamic modulation of the exciton energy can be taken into account exactly by transferring to the polaron frame, $\tilde{H} = UH U^\dagger$, using the polaron transformation,

$$U = \sum_{k=1}^2 |k_x\rangle \langle k_x| e^{(-1)^k S_\theta}, \quad S_\theta = \cos(2\theta) \sqrt{\frac{S_0}{2}} (B_-^\dagger - B_-). \quad (B4)$$

The bare exciton energies ε_{k_x} are then shifted to $\tilde{\varepsilon}_{k_x} = \varepsilon_{k_x} - \frac{S_0\omega_0}{2} \cos^2(2\theta)$, while the eigenstates $|k_x, v_0\rangle$ of the transformed Hamiltonian $\tilde{H}_X + \tilde{H}_{B_-}$ are enumerated by the exciton number

k and the number $v_0 = 0, 1, \dots$ of excited vibrational quanta. In more detail,

$$|k_x, v_0\rangle = |k_x\rangle \frac{(B_-^\dagger)^{v_0}}{\sqrt{v_0!}} |\emptyset\rangle, \quad \tilde{\varepsilon}_{k,v_0} = \varepsilon_{k_x} - \frac{S_0 \omega_0}{2} \cos^2(2\theta) + v_0 \omega_0. \quad (\text{B5})$$

As we assume that $S_0 \ll 1$, the leading contribution (proportional to $\sqrt{S_0}$) to the transformed interaction term \tilde{H}_{X-B_-} in powers of S_0 is identical to H_{X-B_-} . To proceed further, we additionally perform the rotating-wave approximation, which amounts to

$$\tilde{H}_{X-B_-} \approx -\omega_0 \sqrt{\frac{S_0}{2}} (|2_x\rangle \langle 1_x|_{B_-} + |1_x\rangle \langle 2_x|_{B_-}^\dagger). \quad (\text{B6})$$

We now limit ourselves to the subspace containing at most a single vibrational excitation, where we find that \tilde{H}_{X-B_-} mixes the states $|1_x, v_0 = 1\rangle$ and $|2_x, v_0 = 0\rangle$. In the resonant case $\omega_0 \approx \Delta\varepsilon_X$, these two states are nearly degenerate, and \tilde{H}_{X-B_-} lifts this degeneracy. While there is no degeneracy in the off-resonant case $\omega_0 \neq \Delta\varepsilon_X$, the vibronic mixing still affects the energy difference between these two states. The energies of vibronically mixed states measured with respect to the energy of the lowest-lying state $|1_x, v_0 = 0\rangle$ then read as

$$E_{v_0=1,\pm} - E_{v_0=0} = \frac{1}{2} \left[\Delta\varepsilon_X + \omega_0 \pm \sqrt{(\Delta\varepsilon_X - \omega_0)^2 + 2S_0\omega_0^2 \sin^2(2\theta)} \right]. \quad (\text{B7})$$

The exciton populations then exhibit oscillatory features of frequency,

$$\Omega_{\text{pop}} = E_{v_0=1,+} - E_{v_0=1,-} = \sqrt{(\Delta\varepsilon_X - \omega_0)^2 + 2S_0\omega_0^2 \sin^2(2\theta)}, \quad (\text{B8})$$

while the oscillations in interexciton coherence have the frequencies

$$\Omega_{\text{coh},\pm} = E_{v_0=1,\pm} - E_{v_0=0}. \quad (\text{B9})$$

In the nearly resonant case ($\Delta\varepsilon_X - \omega_0 \approx 0$), the frequencies of oscillatory features in exciton-population and interexciton-coherence dynamics are given by Eqs. (52) and (53), respectively. To be consistent with the simplifications made up to now, our considerations in the off-resonant case have to keep only the lowest-order term in small S_0 so that

$$\Omega_{\text{pop}}^{\text{off}} \approx |\Delta\varepsilon_X - \omega_0| \left[1 + S_0 \sin^2(2\theta) \frac{\omega_0^2}{(\Delta\varepsilon_X - \omega_0)^2} \right], \quad (\text{B10})$$

$$\Omega_{\text{coh},\pm}^{\text{off}} = \frac{1}{2} \left[\Delta\varepsilon_X + \omega_0 \pm |\Delta\varepsilon_X - \omega_0| \pm S_0 \sin^2(2\theta) \frac{\omega_0^2}{|\Delta\varepsilon_X - \omega_0|} \right]. \quad (\text{B11})$$

Equations (54)–(56) are then readily obtained from Eqs. (B10) and (B11).

APPENDIX C: COMPUTATIONS ON THE SEVEN-SITE MODEL OF THE FMO COMPLEX

The excitonic Hamiltonian H_S is taken from Ref. 116, and the values of interchromophore couplings and average chromophore energies are summarized in Table III.

We take the structured SD of the exciton–environment interaction from the spreadsheet `jz6b01440_si_002.xlsx` appearing

TABLE III. Interchromophore couplings and average chromophore energies (in cm^{-1}) within the seven-site model of the FMO complex considered in Ref. 116. We subtract the energy of the lowest-lying BChl3 ($12\,210 \text{ cm}^{-1}$) from the diagonal entries.

BChl	1	2	3	4	5	6	7
1	200	−87.7	5.5	−5.9	6.7	−13.7	−9.9
2		320	30.8	8.2	0.7	11.8	4.3
3			0	−53.5	−2.2	−9.6	6.0
4				110	−70.7	−17.0	−63.3
5					270	81.1	−1.3
6						420	39.7
7							230

in the supplementary material of Ref. 34. More specifically, we use the data from the sheet `PBE0-FMO_subunitA-J`, which reports the total SD (comprising both the interchromophore and intra-chromophore contributions) for individual BChls in one of the FMO subunits. In our computations, we assume that the SDs for all BChls are identical and thus use the arithmetic average of the SD data for BChl1, \dots , BChl7. The SD thus obtained is plotted in Fig. 14. The frequency grid is equidistant, with spacing $\Delta\omega = 0.53 \text{ cm}^{-1}$, which we find sufficiently fine for the numerical integration of Eq. (33) using the ordinary trapezoidal rule. The SD is Ohmic, and we obtain its linear behavior around $\omega = 0$ by fitting the points $(0, 0), (\Delta\omega, \mathcal{J}(\Delta\omega)), \dots, (5\Delta\omega, \mathcal{J}(5\Delta\omega))$ to a straight line. As the SD is available up to $\omega_{\text{avail}} = 2650.8 \text{ cm}^{-1}$, our numerical computations use $\omega_{\text{max}} = 2\omega_{\text{avail}}$ and assume $\mathcal{J}(\omega) = 0$ for $\omega_{\text{avail}} < \omega < \omega_{\text{max}}$.

While we take the excitonic and the exciton–environment interaction parameters from different studies and different (seven-site¹¹⁶ and eight-site³⁴) FMO models, we emphasize that our main goal is to examine the applicability of our approximate methods to a relatively realistic model of a multichromophoric complex. The results in Figs. 12 and 13 indeed suggest that our approximate methods can provide decent results on exciton dynamics in realistic models.

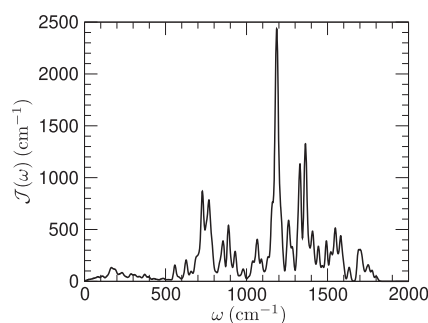


FIG. 14. Spectral density of the exciton–environment interaction used to obtain the results presented in Figs. 12 and 13. The SD is extracted from the data accompanying Ref. 34.

REFERENCES

- ¹S. J. Jang and B. Mennucci, "Delocalized excitons in natural light-harvesting complexes," *Rev. Mod. Phys.* **90**, 035003 (2018).
- ²J. Cao, R. J. Cogdell, D. F. Coker, H.-G. Duan, J. Hauer, U. Kleinekathöfer, T. L. C. Jansen, T. Mančal, R. J. D. Miller, J. P. Ogilvie, V. I. Prokhorenko, T. Renger, H.-S. Tan, R. Tempelaar, M. Thorwart, E. Thyraug, S. Westenhoff, and D. Zigmantas, "Quantum biology revisited," *Sci. Adv.* **6**, eaaz4888 (2020).
- ³T. Brixner, R. Hildner, J. Köhler, C. Lambert, and F. Würthner, "Exciton transport in molecular aggregates—from natural antennas to synthetic chromophore systems," *Adv. Energy Mater.* **7**, 1700236 (2017).
- ⁴O. Ostroverkhova, "Organic optoelectronic materials: Mechanisms and applications," *Chem. Rev.* **116**, 13279–13412 (2016).
- ⁵A. J. Sneyd, T. Fukui, D. Paleček, S. Prodhan, I. Wagner, Y. Zhang, J. Sung, S. M. Collins, T. J. A. Slater, Z. Andaji-Garmaroudi, L. R. MacFarlane, J. D. Garcia-Hernandez, L. Wang, G. R. Whittell, J. M. Hodgkiss, K. Chen, D. Beljonne, I. Manners, R. H. Friend, and A. Rao, "Efficient energy transport in an organic semiconductor mediated by transient exciton delocalization," *Sci. Adv.* **7**, eabh4232 (2021).
- ⁶V. Sláma, S. Rajabi, and T. Mančal, "Fluorographene with impurities as a biomimetic light-harvesting medium," *J. Chem. Phys.* **156**, 185102 (2022).
- ⁷P. Malý and R. van Grondelle, "Interplay of disorder and delocalization in photosynthetic light harvesting," *Curr. Opin. Chem. Biol.* **47**, 1–6 (2018).
- ⁸A. Ishizaki and G. R. Fleming, "Quantum coherence in photosynthetic light harvesting," *Annu. Rev. Condens. Matter Phys.* **3**, 333–361 (2012).
- ⁹A. Chenu and G. D. Scholes, "Coherence in energy transfer and photosynthesis," *Annu. Rev. Phys. Chem.* **66**, 69–96 (2015).
- ¹⁰H.-P. Breuer and F. Petruccione, *The Theory of Open Quantum Systems* (Oxford University Press, 2002).
- ¹¹U. Weiss, *Quantum Dissipative Systems*, 3rd ed. (World Scientific, 2008).
- ¹²A. G. Redfield, "The theory of relaxation processes," in *Advances in Magnetic Resonance, Advances in Magnetic and Optical Resonance*, edited by J. S. Waugh (Academic Press, 1965), Vol. 1, pp. 1–32.
- ¹³T. Förster, "Delocalized excitation and excitation transfer. Bulletin no. 18," Technical Report No. FSU-2690-18, Florida State University, Tallahassee, Department of Chemistry, 1964.
- ¹⁴A. Ishizaki and G. R. Fleming, "On the adequacy of the Redfield equation and related approaches to the study of quantum dynamics in electronic energy transfer," *J. Chem. Phys.* **130**, 234110 (2009).
- ¹⁵R. Feynman and F. Vernon, "The theory of a general quantum system interacting with a linear dissipative system," *Ann. Phys.* **24**, 118–173 (1963).
- ¹⁶R. Zwanzig, "Ensemble method in the theory of irreversibility," *J. Chem. Phys.* **33**, 1338–1341 (1960).
- ¹⁷S. Nakajima, "On quantum theory of transport phenomena: Steady diffusion," *Prog. Theor. Phys.* **20**, 948–959 (1958).
- ¹⁸D. Brian and X. Sun, "Generalized quantum master equation: A tutorial review and recent advances," *Chin. J. Chem. Phys.* **34**, 497–524 (2021).
- ¹⁹R.-X. Xu and Y. J. Yan, "Dynamics of quantum dissipation systems interacting with bosonic canonical bath: Hierarchical equations of motion approach," *Phys. Rev. E* **75**, 031107 (2007).
- ²⁰A. Ishizaki and G. R. Fleming, "Unified treatment of quantum coherent and incoherent hopping dynamics in electronic energy transfer: Reduced hierarchy equation approach," *J. Chem. Phys.* **130**, 234111 (2009).
- ²¹Y. Tanimura, "Numerically 'exact' approach to open quantum dynamics: The hierarchical equations of motion (HEOM)," *J. Chem. Phys.* **153**, 020901 (2020).
- ²²N. Makri and D. E. Makarov, "Tensor propagator for iterative quantum time evolution of reduced density matrices. I. Theory," *J. Chem. Phys.* **102**, 4600–4610 (1995).
- ²³M. Thorwart, J. Eckel, J. Reina, P. Nalbach, and S. Weiss, "Enhanced quantum entanglement in the non-Markovian dynamics of biomolecular excitons," *Chem. Phys. Lett.* **478**, 234–237 (2009).
- ²⁴N. Makri, "Modular path integral methodology for real-time quantum dynamics," *J. Chem. Phys.* **149**, 214108 (2018).
- ²⁵N. Makri, "Small matrix disentanglement of the path integral: Overcoming the exponential tensor scaling with memory length," *J. Chem. Phys.* **152**, 041104 (2020).
- ²⁶L. Simine and D. Segal, "Path-integral simulations with fermionic and bosonic reservoirs: Transport and dissipation in molecular electronic junctions," *J. Chem. Phys.* **138**, 214111 (2013).
- ²⁷A. Strathearn, P. Kirton, D. Kilda, J. Keeling, and B. W. Lovett, "Efficient non-Markovian quantum dynamics using time-evolving matrix product operators," *Nat. Commun.* **9**, 3322 (2018).
- ²⁸D. Gribben, D. M. Rouse, J. Iles-Smith, A. Strathearn, H. Maguire, P. Kirton, A. Nazir, E. M. Gauger, and B. W. Lovett, "Exact dynamics of nonadditive environments in non-Markovian open quantum systems," *PRX Quantum* **3**, 010321 (2022).
- ²⁹M. Cygorek, M. Cosacchi, A. Vagov, V. M. Axt, B. W. Lovett, J. Keeling, and E. M. Gauger, "Simulation of open quantum systems by automated compression of arbitrary environments," *Nat. Phys.* **18**, 662–668 (2022).
- ³⁰Q. Shi and E. Geva, "A new approach to calculating the memory kernel of the generalized quantum master equation for an arbitrary system–bath coupling," *J. Chem. Phys.* **119**, 12063–12076 (2003).
- ³¹M.-L. Zhang, B. J. Ka, and E. Geva, "Nonequilibrium quantum dynamics in the condensed phase via the generalized quantum master equation," *J. Chem. Phys.* **125**, 044106 (2006).
- ³²E. Mulvihill and E. Geva, "A road map to various pathways for calculating the memory kernel of the generalized quantum master equation," *J. Phys. Chem. B* **125**, 9834–9852 (2021).
- ³³X. Wang, G. Ritschel, S. Wüster, and A. Eisfeld, "Open quantum system parameters for light harvesting complexes from molecular dynamics," *Phys. Chem. Chem. Phys.* **17**, 25629–25641 (2015).
- ³⁴M. K. Lee and D. F. Coker, "Modeling electronic-nuclear interactions for excitation energy transfer processes in light-harvesting complexes," *J. Phys. Chem. Lett.* **7**, 3171–3178 (2016).
- ³⁵C. W. Kim, B. Choi, and Y. M. Rhee, "Excited state energy fluctuations in the Fenna–Matthews–Olson complex from molecular dynamics simulations with interpolated chromophore potentials," *Phys. Chem. Chem. Phys.* **20**, 3310–3319 (2018).
- ³⁶D. Padula, M. H. Lee, K. Claridge, and A. Troisi, "Chromophore-dependent intramolecular exciton–vibrational coupling in the FMO complex: Quantification and importance for exciton dynamics," *J. Phys. Chem. B* **121**, 10026–10035 (2017).
- ³⁷E. Cignoni, V. Sláma, L. Cupellini, and B. Mennucci, "The atomistic modeling of light-harvesting complexes from the physical models to the computational protocol," *J. Chem. Phys.* **156**, 120901 (2022).
- ³⁸S. Maity and U. Kleinekathöfer, "Recent progress in atomistic modeling of light-harvesting complexes: A mini review," *Photosynth. Res.* **156**, 147–162 (2023).
- ³⁹R. Kapral, "Quantum dynamics in open quantum-classical systems," *J. Phys.: Condens. Matter* **27**, 073201 (2015).
- ⁴⁰C. W. Kim, W.-G. Lee, I. Kim, and Y. M. Rhee, "Effect of underdamped vibration on excitation energy transfer: Direct comparison between two different partitioning schemes," *J. Chem. Phys. A* **123**, 1186–1197 (2019).
- ⁴¹Z. Gong and J. Wu, "Absorption matrix of multi-site systems calculated by a hybrid quantum-classical Liouville equation," *J. Chem. Phys.* **151**, 224109 (2019).
- ⁴²C. W. Kim and Y. M. Rhee, "Toward monitoring the dissipative vibrational energy flows in open quantum systems by mixed quantum–classical simulations," *J. Chem. Phys.* **152**, 244109 (2020).
- ⁴³K. H. Cho and Y. M. Rhee, "Cooperation between excitation energy transfer and antisynchronously coupled vibrations," *J. Phys. Chem. B* **125**, 5601–5610 (2021).
- ⁴⁴Y. Braver, L. Valkunas, and A. Gelzinis, "Quantum–classical approach for calculations of absorption and fluorescence: Principles and applications," *J. Chem. Theory Comput.* **17**, 7157–7168 (2021).
- ⁴⁵A. Kelly and T. E. Markland, "Efficient and accurate surface hopping for long time nonadiabatic quantum dynamics," *J. Chem. Phys.* **139**, 014104 (2013).
- ⁴⁶J. R. Mannouch and J. O. Richardson, "A mapping approach to surface hopping," *J. Chem. Phys.* **158**, 104111 (2023).
- ⁴⁷J. E. Runeson, T. P. Fay, and D. E. Manolopoulos, "Exciton dynamics from the mapping approach to surface hopping: Comparison with Förster and Redfield theories," *Phys. Chem. Chem. Phys.* **26**, 4929–4938 (2024).
- ⁴⁸J. Ma and J. Cao, "Förster resonance energy transfer, absorption and emission spectra in multichromophoric systems. I. Full cumulant expansions and system-bath entanglement," *J. Chem. Phys.* **142**, 094106 (2015).

- ⁴⁹L. Cupellini, F. Lipparini, and J. Cao, "Absorption and circular dichroism spectra of molecular aggregates with the full cumulant expansion," *J. Phys. Chem. B* **124**, 8610–8617 (2020).
- ⁵⁰J. A. Nöthling, T. Mančal, and T. P. J. Krüger, "Accuracy of approximate methods for the calculation of absorption-type linear spectra with a complex system–bath coupling," *J. Chem. Phys.* **157**, 095103 (2022).
- ⁵¹R. Borrelli and A. Peluso, "Quantum dynamics of radiationless electronic transitions including normal modes displacements and Duschinsky rotations: A second-order cumulant approach," *J. Chem. Theory Comput.* **11**, 415–422 (2015).
- ⁵²E. Mulvihill, A. Schubert, X. Sun, B. D. Dunietz, and E. Geva, "A modified approach for simulating electronically nonadiabatic dynamics via the generalized quantum master equation," *J. Chem. Phys.* **150**, 034101 (2019).
- ⁵³E. Mulvihill, K. M. Lenn, X. Gao, A. Schubert, B. D. Dunietz, and E. Geva, "Simulating energy transfer dynamics in the Fenna–Matthews–Olson complex via the modified generalized quantum master equation," *J. Chem. Phys.* **154**, 204109 (2021).
- ⁵⁴A. Shabani, M. Mohseni, H. Rabitz, and S. Lloyd, "Efficient estimation of energy transfer efficiency in light-harvesting complexes," *Phys. Rev. E* **86**, 011915 (2012).
- ⁵⁵V. May and O. Kühn, *Charge and Energy Transfer Dynamics in Molecular Systems*, 3rd ed. (WILEY-VCH Verlag GmbH & Co. KGaA, Weinheim, 2011).
- ⁵⁶B. B. Laird, J. Budimir, and J. L. Skinner, "Quantum-mechanical derivation of the Bloch equations: Beyond the weak-coupling limit," *J. Chem. Phys.* **94**, 4391–4404 (1991).
- ⁵⁷M. Aihara, H. M. Seviran, and J. L. Skinner, "Non-Markovian relaxation of a spin-1/2 particle in a fluctuating transverse field: Cumulant expansion and stochastic simulation results," *Phys. Rev. A* **41**, 6596–6601 (1990).
- ⁵⁸D. R. Reichman, F. L. H. Brown, and P. Neu, "Cumulant expansions and the spin-boson problem," *Phys. Rev. E* **55**, 2328–2337 (1997).
- ⁵⁹H.-P. Breuer, B. Kappler, and F. Petruccione, "Stochastic wave-function method for non-Markovian quantum master equations," *Phys. Rev. A* **59**, 1633–1643 (1999).
- ⁶⁰S. Jang, J. Cao, and R. J. Silbey, "Fourth-order quantum master equation and its Markovian bath limit," *J. Chem. Phys.* **116**, 2705–2717 (2002).
- ⁶¹J. Wu and J. Cao, "Higher-order kinetic expansion of quantum dissipative dynamics: Mapping quantum networks to kinetic networks," *J. Chem. Phys.* **139**, 044102 (2013).
- ⁶²M. Xu, Y. Yan, Y. Liu, and Q. Shi, "Convergence of high order memory kernels in the Nakajima–Zwanzig generalized master equation and rate constants: Case study of the spin-boson model," *J. Chem. Phys.* **148**, 164101 (2018).
- ⁶³S. J. Jang, "Fourth order expressions for the electronic absorption lineshape of molecular excitons," *J. Chem. Phys.* **151**, 044110 (2019).
- ⁶⁴S. Jang, Y.-C. Cheng, D. R. Reichman, and J. D. Eaves, "Theory of coherent resonance energy transfer," *J. Chem. Phys.* **129**, 101104 (2008).
- ⁶⁵S. Jang, "Theory of multichromophoric coherent resonance energy transfer: A polaronic quantum master equation approach," *J. Chem. Phys.* **135**, 034105 (2011).
- ⁶⁶D. P. S. McCutcheon and A. Nazir, "Consistent treatment of coherent and incoherent energy transfer dynamics using a variational master equation," *J. Chem. Phys.* **135**, 114501 (2011).
- ⁶⁷S. J. Jang, "Partially polaron-transformed quantum master equation for exciton and charge transport dynamics," *J. Chem. Phys.* **157**, 104107 (2022).
- ⁶⁸M. G. Mavros and T. Van Voorhis, "Resummed memory kernels in generalized system-bath master equations," *J. Chem. Phys.* **141**, 054112 (2014).
- ⁶⁹D. Pines, "Electron, phonon and polaron propagators," in *Polarons and Excitons*, edited by C. G. Kuper and G. D. Whitfield (Plenum Press, New York, 1963).
- ⁷⁰R. Puff and G. D. Whitfield, "Application of Green's function techniques to the polaron problem," in *Polarons and Excitons*, edited by C. G. Kuper and G. D. Whitfield (Plenum Press, New York, 1963).
- ⁷¹H. Bruus and K. Flensberg, *Many-Body Quantum Theory in Condensed Matter Physics: An Introduction* (Oxford University Press, 2004).
- ⁷²M. V. Sadovskii, *Diagrammatics: Lectures on Selected Problems in Condensed Matter Theory* (World Scientific Publishing Co. Pte. Ltd., Singapore, 2006).
- ⁷³P. Cui, X.-Q. Li, J. Shao, and Y. Yan, "Quantum transport from the perspective of quantum open systems," *Phys. Lett. A* **357**, 449–453 (2006).
- ⁷⁴M. Esposito and M. Galperin, "Self-consistent quantum master equation approach to molecular transport," *J. Phys. Chem. C* **114**, 20362–20369 (2010).
- ⁷⁵J. Jin, J. Li, Y. Liu, X.-Q. Li, and Y. Yan, "Improved master equation approach to quantum transport: From Born to self-consistent Born approximation," *J. Chem. Phys.* **140**, 244111 (2014).
- ⁷⁶X.-Q. Li, "Number-resolved master equation approach to quantum measurement and quantum transport," *Front. Phys.* **11**, 110307 (2016).
- ⁷⁷J. K. Sowa, N. Lambert, T. Seideman, and E. M. Gauger, "Beyond Marcus theory and the Landauer–Büttiker approach in molecular junctions. II. A self-consistent Born approach," *J. Chem. Phys.* **152**, 064103 (2020).
- ⁷⁸O. Scarlatella and M. Schirò, "Self-consistent dynamical maps for open quantum systems," *SciPost Phys.* **16**, 026 (2024).
- ⁷⁹Y. Tanimura, "Nonperturbative expansion method for a quantum system coupled to a harmonic-oscillator bath," *Phys. Rev. A* **41**, 6676–6687 (1990).
- ⁸⁰A. Ishizaki and Y. Tanimura, "Nonperturbative non-Markovian quantum master equation: Validity and limitation to calculate nonlinear response functions," *Chem. Phys.* **347**, 185–193 (2008).
- ⁸¹V. Janković and T. Mančal, "Exact description of excitonic dynamics in molecular aggregates weakly driven by light," *J. Chem. Phys.* **153**, 244122 (2020).
- ⁸²G. Mahan, *Many-Particle Physics* (Kluwer Academic, New York, 2000).
- ⁸³A. J. Leggett, S. Chakravarty, A. T. Dorsey, M. P. A. Fisher, A. Garg, and W. Zwerger, "Dynamics of the dissipative two-state system," *Rev. Mod. Phys.* **59**, 1–85 (1987).
- ⁸⁴P. Nalbach and M. Thorwart, "Multiphonon transitions in the biomolecular energy transfer dynamics," *J. Chem. Phys.* **132**, 194111 (2010).
- ⁸⁵T. Palm and P. Nalbach, "Nonperturbative environmental influence on dephasing," *Phys. Rev. A* **96**, 032105 (2017).
- ⁸⁶S. Mukamel, *Principles of Nonlinear Optical Spectroscopy* (Oxford University Press, Inc., New York, 1995).
- ⁸⁷T. Mančal, "A decade with quantum coherence: How our past became classical and the future turned quantum," *Chem. Phys.* **532**, 110663 (2020).
- ⁸⁸T. Mančal and L. Valkunas, "Exciton dynamics in photosynthetic complexes: Excitation by coherent and incoherent light," *New J. Phys.* **12**, 065044 (2010).
- ⁸⁹A. Chenu, P. Malý, and T. Mančal, "Dynamic coherence in excitonic molecular complexes under various excitation conditions," *Chem. Phys.* **439**, 100–110 (2014).
- ⁹⁰S. Koller, M. Grifoni, M. Leijnse, and M. R. Wegewijs, "Density-operator approaches to transport through interacting quantum dots: Simplifications in fourth-order perturbation theory," *Phys. Rev. B* **82**, 235307 (2010).
- ⁹¹J. Rammer, *Quantum Transport Theory* (Perseus Books, 1998).
- ⁹²U. Harbola and S. Mukamel, "Superoperator nonequilibrium Green's function theory of many-body systems; applications to charge transfer and transport in open junctions," *Phys. Rep.* **465**, 191–222 (2008).
- ⁹³J. Rammer, *Quantum Field Theory of Non-equilibrium States* (Cambridge University Press, 2007).
- ⁹⁴J. Albers and J. M. Deutch, "Redfield–Langevin equation for nuclear spin relaxation," *J. Chem. Phys.* **55**, 2613–2619 (1971).
- ⁹⁵B. Yoon, J. M. Deutch, and J. H. Freed, "A comparison of generalized cumulant and projection operator methods in spin-relaxation theory," *J. Chem. Phys.* **62**, 4687–4696 (1975).
- ⁹⁶F. Shibata and T. Arimitsu, "Expansion formulas in nonequilibrium statistical mechanics," *J. Phys. Soc. Jpn.* **49**, 891–897 (1980).
- ⁹⁷P. N. Argyres and P. L. Kelley, "Theory of spin resonance and relaxation," *Phys. Rev.* **134**, A98–A111 (1964).
- ⁹⁸L. Valkunas, D. Abramavicius, and T. Mančal, *Molecular Excitation Dynamics and Relaxation* (Wiley-VCH Verlag GmbH & Co. KGaA, 2013).
- ⁹⁹G. L. Goodvin, M. Berciu, and G. A. Sawatzky, "Green's function of the Holstein polaron," *Phys. Rev. B* **74**, 245104 (2006).
- ¹⁰⁰P. Mitrić, "Spectral functions and mobility of the Holstein polaron," Ph.D. thesis, Faculty of Physics, University of Belgrade, Belgrade, Serbia, 2023.

- ¹⁰¹A. Kell, X. Feng, M. Reppert, and R. Jankowiak, "On the shape of the phonon spectral density in photosynthetic complexes," *J. Phys. Chem. B* **117**, 7317–7323 (2013).
- ¹⁰²G. Ritschel and A. Eisfeld, "Analytic representations of bath correlation functions for ohmic and superohmic spectral densities using simple poles," *J. Chem. Phys.* **141**, 094101 (2014).
- ¹⁰³A. Fruchtmann, N. Lambert, and E. M. Gauger, "When do perturbative approaches accurately capture the dynamics of complex quantum systems?," *Sci. Rep.* **6**, 28204 (2016).
- ¹⁰⁴R. Doll, D. Zueco, M. Wubs, S. Kohler, and P. Hänggi, "On the conundrum of deriving exact solutions from approximate master equations," *Chem. Phys.* **347**, 243–249 (2008).
- ¹⁰⁵S. Ciuchi, F. de Pasquale, S. Fratini, and D. Feinberg, "Dynamical mean-field theory of the small polaron," *Phys. Rev. B* **56**, 4494–4512 (1997).
- ¹⁰⁶H. Haken and G. Strobl, "An exactly solvable model for coherent and incoherent exciton motion," *Z. Phys. Hadrons Nuclei* **262**, 135–148 (1973).
- ¹⁰⁷H. Haken and P. Reineker, "The coupled coherent and incoherent motion of excitons and its influence on the line shape of optical absorption," *Z. Phys.* **249**, 253–268 (1972).
- ¹⁰⁸S. Jesenko and M. Žnidarič, "Excitation energy transfer efficiency: Equivalence of transient and stationary setting and the absence of non-Markovian effects," *J. Phys. Chem. Phys.* **138**, 174103 (2013).
- ¹⁰⁹F. Caycedo-Soler, A. Mattioni, J. Lim, T. Renger, S. F. Huelga, and M. B. Plenio, "Exact simulation of pigment-protein complexes unveils vibronic renormalization of electronic parameters in ultrafast spectroscopy," *Nat. Commun.* **13**, 2912 (2022).
- ¹¹⁰A. G. Dijkstra, C. Wang, J. Cao, and G. R. Fleming, "Coherent exciton dynamics in the presence of underdamped vibrations," *J. Phys. Chem. Lett.* **6**, 627–632 (2015).
- ¹¹¹A. Eisfeld, L. Braun, W. T. Strunz, J. S. Briggs, J. Beck, and V. Engel, "Vibronic energies and spectra of molecular dimers," *J. Chem. Phys.* **122**, 134103 (2005).
- ¹¹²A. Chenu, N. Christensson, H. F. Kauffmann, and T. Mančal, "Enhancement of vibronic and ground-state vibrational coherences in 2D spectra of photosynthetic complexes," *Sci. Rep.* **3**, 2029 (2013).
- ¹¹³Y. Tanimura and R. Kubo, "Time evolution of a quantum system in contact with a nearly Gaussian–Markoffian noise bath," *J. Phys. Soc. Jpn.* **58**, 101–114 (1989).
- ¹¹⁴T. Mančal, "Principles of multi-dimensional electronic spectroscopy," in *Quantum Effects in Biology*, edited by M. Mohseni, Y. Omar, G. S. Engel, and M. B. Plenio (Cambridge University Press, 2014), pp. 82–120.
- ¹¹⁵V. Tiwari, W. K. Peters, and D. M. Jonas, "Electronic resonance with anti-correlated pigment vibrations drives photosynthetic energy transfer outside the adiabatic framework," *Proc. Natl. Acad. Sci.* **110**, 1203–1208 (2013).
- ¹¹⁶J. Adolphs and T. Renger, "How proteins trigger excitation energy transfer in the FMO complex of green sulfur bacteria," *Biophys. J.* **91**, 2778–2797 (2006).

Vertex corrections to conductivity in the Holstein model: A numerical-analytical studyVeljko Janković ^{*}, Petar Mitrić [†], Darko Tanasković [‡], and Nenad Vukmirović [§]
Institute of Physics Belgrade, University of Belgrade, Pregrevica 118, 11080 Belgrade, Serbia

(Received 1 April 2024; accepted 5 June 2024; published 26 June 2024)

The optical-conductivity profile carries information on electronic dynamics in interacting quantum many-body systems. Its computation is a formidable task that is usually approached by invoking the single-particle (bubble) approximation and neglecting vertex corrections, the importance of which remains elusive even in model Hamiltonian calculations. Here, we combine analytical arguments with our recent breakthroughs in numerically exact and approximate calculations of finite-temperature real-time correlation functions to thoroughly assess the importance of vertex corrections in the one-dimensional Holstein polaron model. We find, both analytically and numerically, vanishing vertex corrections to optical conductivity in the limits of zero electron-phonon interaction, zero electronic bandwidth, and infinite temperature. Furthermore, our numerical results show that vertex corrections to the electron mobility also vanish in many parameter regimes between these limits. In some of these cases, the vertex corrections still introduce important qualitative changes to the optical-conductivity profile in comparison to the bubble approximation even though the self-energy remains approximately local. We trace these changes back to the bubble approximation not fully capturing a time-limited slowdown of the electron on intermediate timescales between ballistic and diffusive transport. We find that the vertex corrections are overall most pronounced for intermediate electron-phonon interaction and may increase or decrease the bubble-approximation mobility depending on the values of the model parameters.

DOI: [10.1103/PhysRevB.109.214312](https://doi.org/10.1103/PhysRevB.109.214312)**I. INTRODUCTION**

Charge carrier transport in semiconducting materials is the key physical process behind the operation of many semiconductor electronic and optoelectronic devices [1,2]. Under typical operating conditions, the carrier density is low, and their transport is limited by the interaction with phonons [3,4]. Quantifying the ability of a carrier to cover long distances, phonon-limited electron (dc) mobility is the primary factor determining device performance. On the other hand, the frequency profile of the dynamical (ac) mobility, which is proportional to the optical conductivity, carries information on charge dynamics on various time and length scales, thus providing fundamental insights into the mechanisms of carrier transport [5–7]. While the dc and ac mobility are nowadays experimentally accessible [5], reliable theoretical results for these quantities are rather scarce.

Within the linear-response theory [8], transport properties are encoded in the two-particle current-current correlation function, which is, however, seldom calculated exactly. One usually calculates it in the so-called independent-particle (single-particle or bubble) approximation [9,10], which expresses it entirely in terms of single-particle quantities (the so-called bubble term), and neglects two-particle correlations (commonly referred to as vertex corrections). The bubble term

is, in principle, much easier to evaluate than the vertex corrections, and the bubble approximation is commonly employed both in first-principles studies of transport properties [9,11,12] and in many model Hamiltonian calculations [13–17].

Understanding how the vertex corrections influence transport properties is an arduous task whose solution has been attempted in just a few instances. Historically, the first instance is impurity scattering in metals, where the Green's functions in the Born approximation are used for the calculation of the ladder diagrams, whose contribution to the dc conductivity is comparable to the bubble term [10,18]. These diagrams are responsible for the dominant contribution to dc resistivity from the large-angle scattering within the semiclassical Boltzmann approach in the presence of diluted impurities. Another well-studied case is the disorder scattering in two dimensions, where the maximally crossed diagrams give a divergent contribution to resistivity at low temperatures even in the presence of weak disorder [19,20]. Concerning the electron-phonon models, the contribution of vertex corrections to conductivity [21–25] has been studied so far only for weak interaction. In classic papers from the 1960s, vertex corrections to conductivity stemming from scattering on acoustic phonons were calculated by summing the ladder diagrams [25]. Within the Fröhlich model, vertex corrections originating from scattering on optical phonons were shown to be negligible at low temperatures and for weak electron-phonon coupling [24,25]. It is a challenge to determine the importance of vertex corrections outside the weak-coupling limit, and, to the best of our knowledge, this has not been done before either for the Fröhlich model or the Holstein model, on which we focus in this study.

^{*}Contact author: veljko.jankovic@ipb.ac.rs[†]Contact author: petar.mitric@ipb.ac.rs[‡]Contact author: darko.tanaskovic@ipb.ac.rs[§]Contact author: nenad.vukmirovic@ipb.ac.rs

Transport properties of interacting electron-phonon models have been commonly studied either by approximately calculating the current-current correlation function [26–34] or by starting from (possibly approximate) single-particle spectral functions [15,17,35–39] and using the bubble approximation [13–17]. However, elucidating the role of vertex corrections requires genuine numerically exact approaches that provide results on both single-particle and two-particle correlation functions at finite temperatures. While imaginary-axis quantum Monte Carlo (QMC) approaches are formulated directly in the thermodynamic limit [40–43], the uncertainties associated with the procedure of numerical analytical continuation [44–48] cast doubts on the reliability of real-axis results thus obtained. It is therefore of paramount importance that numerically exact methods used to study vertex corrections be formulated directly on the real-time or real-frequency axis [49]. Calculations of the dc mobility are particularly challenging for such methods because of finite-size effects (e.g., Lanczos diagonalization-based methods [50–52]) or maximum simulation time that is not sufficiently long to fully capture the carrier’s diffusive motion (e.g., real-time QMC [53] or density matrix renormalization group [54,55]).

There have been three very recent advances that facilitate our present study. First, we developed the numerically exact momentum-space hierarchical equations of motion (HEOM) method for calculating both single- and two-particle correlation functions [56,57]. This method provides dc mobilities whose uncertainties due to finite-size effects are controllable and can be suppressed in a wide range of model parameters. Second, we developed the real-axis path integral QMC method, which can provide a real-time current-current correlation function for weak and intermediate electron-phonon coupling at elevated temperatures [53,56]. For lower temperatures or stronger coupling, valuable information can still be obtained for short time correlations, before the sign problem sets in. Finally, we also have at our disposal the dynamical mean-field theory (DMFT), a computationally inexpensive method producing close-to-exact results for the spectral functions of the Holstein polaron in the thermodynamic limit, even in one dimension, in the whole parameter space [39]. This can be used for reliable calculations of conductivity without vertex corrections, as all the results to be presented demonstrate that the DMFT ac mobility practically coincides with the one calculated in the bubble approximation within the HEOM method.

In this study, we first develop analytical arguments demonstrating that the vertex corrections vanish in the limits of vanishing electron-phonon interaction, vanishing electronic bandwidth (the atomic limit), and infinite temperature. We then proceed to numerically analyze their importance in parameter regimes between these limits for three values of phonon energy (intermediate, low, and high with respect to the bare electron’s kinetic energy) and at temperatures that are not too low for HEOM (to minimize finite-size effects) and QMC (to avoid severe sign problem) calculations. For intermediate phonon frequency and moderate electron-phonon coupling, the numerically exact dynamical mobility assumes a two-peak structure: the Drude-like peak is accompanied by another peak at finite frequency. At higher temperatures, this peak is centered away from ω_0 , and it can be ascribed to a temporally

limited slowdown of the carrier during the crossover between the ballistic and diffusive transport regimes. This slowdown is not fully captured by the bubble approximation, and the corresponding dynamical-mobility profile features only the Drude-like peak. On the other hand, at low temperatures, the finite-frequency peak is positioned exactly at ω_0 , and it is recovered also within the bubble approximation because it corresponds to the optical transitions between the quasi-particle and the satellite peaks in a single-particle spectral function. In all these cases, the numerically exact dc mobility is somewhat larger than that in the bubble approximation. For low phonon frequency and moderate interaction, we find that the dynamical-mobility profile bears qualitative similarities to that for intermediate phonon frequency. Interestingly, the peak at zero frequency persists, and the numerically exact dc mobility is somewhat smaller than, yet comparable to, the one in the bubble approximation. Only as ω_0 is further decreased is the dc mobility expected to decrease to the values much below the bubble-approximation result. For high phonon frequency, available HEOM results do not indicate a large discrepancy in comparison to DMFT.

The paper is structured as follows. Section II provides an overview of the Holstein model and methods we use to study its transport properties. Section III exposes the readers to the analytical results and illustrative numerical examples demonstrating vanishing vertex corrections in the above-listed limiting cases. The in-depth analytical arguments are deferred to Appendixes B–D. We analyze our numerical results and present our main findings on the importance of vertex corrections in Sec. IV. Section V summarizes our results.

II. MODEL AND METHODS

A. Formalism: Holstein model and its transport properties

We examine the Holstein model on a one-dimensional (1D) lattice composed of N sites with periodic boundary conditions. In momentum space, its Hamiltonian reads

$$\begin{aligned}
 H &= H_e + H_{\text{ph}} + H_{\text{e-ph}} \\
 &= \sum_k \varepsilon_k c_k^\dagger c_k + \omega_0 \sum_q b_q^\dagger b_q + \frac{g}{\sqrt{N}} \sum_{kq} c_{k+q}^\dagger c_k (b_q + b_{-q}^\dagger).
 \end{aligned}
 \tag{1}$$

The electronic and phononic wave numbers k and q may assume any of the N allowed values $2\pi n/N$ (n is an integer) in the first Brillouin zone $(-\pi, \pi]$. The free-electron Hamiltonian H_e describes electrons in a band whose dispersion $\varepsilon_k = -2t_0 \cos k$ originates from the nearest-neighbor hopping of amplitude t_0 . The operator c_k^\dagger (c_k) creates (annihilates) an electron in the state with wave number k . The free-phonon Hamiltonian H_{ph} describes dispersionless optical phonons of frequency ω_0 , with b_q^\dagger (b_q) creating (annihilating) a phonon of momentum q . The interaction term $H_{\text{e-ph}}$ is characterized by its strength g . In the following, we set the lattice constant a_l , the elementary charge e_0 , and the physical constants \hbar and k_B to unity. As a convenient measure of the electron-phonon interaction strength, we use the dimensionless parameter

$$\lambda = \frac{g^2}{2t_0\omega_0}.
 \tag{2}$$

We consider the dynamics of a single spinless electron in the band, which is determined by the current-current correlation function (normalized to the electron number)

$$C_{jj}(t) = \frac{\langle j(t)j(0) \rangle_K}{\langle N_e \rangle_K}. \quad (3)$$

In Eq. (3), $N_e = \sum_k c_k^\dagger c_k$ denotes the electron-number operator, and the expectation values are evaluated in the grand-canonical ensemble defined by temperature $T = \beta^{-1}$ and chemical potential μ_F ($K = H - \mu_F N_e$),

$$\langle A \rangle_K = \frac{\text{Tr}\{A e^{-\beta K}\}}{\text{Tr} e^{-\beta K}}. \quad (4)$$

The current operator reads

$$j = \sum_k j_k c_k^\dagger c_k, \quad (5)$$

with

$$j_k = -2t_0 \sin k. \quad (6)$$

We assume that μ_F lies far below the bottom of the band (formally, $\mu_F \rightarrow -\infty$), i.e., the electron density is low. A reasoning analogous to that in Refs. [37,39,58] shows that the dominant contributions to the expectation values entering Eq. (3) as $\mu_F \rightarrow -\infty$ read

$$\langle j(t)j(0) \rangle_K = e^{\beta\mu_F} \frac{\text{Tr}_{1e}\{e^{iHt} j e^{-iHt} j e^{-\beta H}\}}{Z_{\text{ph}}}, \quad (7)$$

$$\langle N_e \rangle_K = e^{\beta\mu_F} \frac{Z}{Z_{\text{ph}}}, \quad (8)$$

where $Z_{\text{ph}} = \text{Tr}_{\text{ph}} e^{-\beta H_{\text{ph}}}$ denotes the free-phonon partition sum, the trace Tr_{1e} is taken over states containing a single electron (and an arbitrary number of phonons), while

$$Z = \text{Tr}_{1e} e^{-\beta H} \quad (9)$$

is the corresponding partition sum. Equation (3) is then recast as

$$C_{jj}(t) = \langle j(t)j(0) \rangle_{H,1} = \frac{\text{Tr}_{1e}\{e^{iHt} j e^{-iHt} j e^{-\beta H}\}}{Z}. \quad (10)$$

The real part of the frequency-dependent mobility (for $\omega \neq 0$) is [10]

$$\text{Re} \mu(\omega) = \frac{1 - e^{-\beta\omega}}{2\omega} \int_{-\infty}^{+\infty} dt e^{i\omega t} C_{jj}(t), \quad (11)$$

and the corresponding dc mobility is

$$\begin{aligned} \mu_{\text{dc}} &= \frac{1}{T} \int_0^{+\infty} dt \text{Re} C_{jj}(t) \\ &= -2 \int_0^{+\infty} dt t \text{Im} C_{jj}(t). \end{aligned} \quad (12)$$

While the dynamical-mobility profile encodes information on carrier dynamics on all time and length scales, a more intuitive understanding of carrier transport can be gained from the evolution of the carrier's spread,

$$\Delta x(t) = \sqrt{\langle [x(t) - x(0)]^2 \rangle_{H,1}}, \quad (13)$$

where x is the carrier position operator. The growth rate of the spread is determined by the time-dependent diffusion constant

$$\mathcal{D}(t) = \frac{1}{2} \frac{d}{dt} [\Delta x(t)]^2 = \int_0^t ds \text{Re} C_{jj}(s), \quad (14)$$

which varies from 0 at short times to its long-time limit \mathcal{D}_∞ , for which the Einstein relation $\mathcal{D}_\infty = \mu_{\text{dc}} T$ holds. The carrier's dynamics then changes from short-time ballistic dynamics, when $\Delta x(t) \propto t$, to long-time diffusive dynamics, when $\Delta x(t) \propto \sqrt{t}$.

B. Single-particle (bubble) approximation

$C_{jj}(t)$ is a four-point (two-particle) correlation function, which can be expressed as [combine Eqs. (3) and (5)]

$$C_{jj}(t) = \frac{\sum_{k'k} j_{k'} j_k \langle c_{k'}^\dagger(t) c_{k'}(t) c_k^\dagger(0) c_k(0) \rangle_K}{\langle N_e \rangle_K}. \quad (15)$$

Its evaluation in the most general many-body setup is a formidable task. This remains true even when we limit ourselves to a single electron in the system [Eq. (10)], which represents an important case that has been successfully solved only very recently using the HEOM formalism [57,59].

Quite generally [60], the two-particle correlation function in Eq. (15) can be formally decomposed into the sum of products of two single-particle correlation functions plus a remainder containing genuine two-particle correlations (denoted as Δ_2):

$$\begin{aligned} C_{jj}(t) &= \frac{1}{\langle N_e \rangle_K} \sum_{k'k} j_{k'} j_k \{ \langle c_{k'}^\dagger(t) c_{k'}(t) \rangle_K \langle c_k^\dagger(0) c_k(0) \rangle_K \\ &\quad + \delta_{k'k} \langle c_k^\dagger(t) c_k(0) \rangle_K \langle c_k(t) c_k^\dagger(0) \rangle_K \\ &\quad + \Delta_2 [\langle c_{k'}^\dagger(t) c_{k'}(t) c_k^\dagger(0) c_k(0) \rangle_K] \}. \end{aligned} \quad (16)$$

The Kronecker δ in the second term on the right-hand side of Eq. (16) comes from momentum conservation. The first term on the right-hand side of Eq. (16) is $O(e^{\beta\mu_F})$, and is thus negligible in the $\mu_F \rightarrow -\infty$ limit with respect to the remaining two terms, which are both $O(1)$. The single-particle (or bubble) approximation additionally neglects the Δ_2 term, so that the current-current correlation function in this approximation reads

$$C_{jj}^{\text{bbl}}(t) = -\frac{1}{\langle N_e \rangle_K} \sum_k j_k^2 \mathcal{G}^>(k, t) \mathcal{G}^<(k, t)^*. \quad (17)$$

Here, the greater and lesser single-particle Green's functions read

$$\begin{aligned} \mathcal{G}^>(k, t) &= -i \langle c_k(t) c_k^\dagger(0) \rangle_K \\ &= -i \int_{-\infty}^{+\infty} d\omega e^{-i\omega t} \frac{\mathcal{A}(k, \omega)}{1 + e^{-\beta\omega}}, \end{aligned} \quad (18)$$

$$\begin{aligned} \mathcal{G}^<(k, t) &= i \langle c_k^\dagger(0) c_k(t) \rangle_K \\ &= i \int_{-\infty}^{+\infty} d\omega e^{-i\omega t} \frac{\mathcal{A}(k, \omega)}{e^{\beta\omega} + 1}. \end{aligned} \quad (19)$$

The first equalities in Eqs. (18) and (19) are the textbook definitions, while the second equalities use the fluctuation-dissipation theorem [18] to express $\mathcal{G}^>/<$ in terms of the

spectral function $\mathcal{A}(k, \omega)$, which is normalized so that $\int_{-\infty}^{+\infty} d\omega \mathcal{A}(k, \omega) = 1$. In the limit $\mu_F \rightarrow -\infty$, we can ensure that the spectral weight occurs at finite frequencies by defining $A(k, \omega) = \mathcal{A}(k, \omega - \mu_F)$; see the supplemental material of Ref. [39]. Equations (18) and (19) then become (we exploit $\mu_F \rightarrow -\infty$)

$$\mathcal{G}^>(k, t) = -ie^{i\mu_F t} \int_{-\infty}^{+\infty} d\omega e^{-i\omega t} A(k, \omega), \quad (20)$$

$$\mathcal{G}^<(k, t) = ie^{\beta\mu_F} e^{i\mu_F t} \int_{-\infty}^{+\infty} d\omega e^{-i\omega t} e^{-\beta\omega} A(k, \omega). \quad (21)$$

Remembering that $\langle N_e \rangle_K = -i \sum_k \mathcal{G}^<(k, t=0)$, and performing the Fourier transformation of Eq. (17), we obtain the well-known results [10,13,17] for the dynamical mobility,

$$\begin{aligned} \text{Re } \mu^{\text{bbl}}(\omega) &= 4\pi t_0^2 \frac{1 - e^{-\beta\omega}}{\omega} \\ &\times \frac{\sum_k \sin^2 k \int_{-\infty}^{+\infty} dv e^{-\beta v} A(k, \omega + v) A(k, v)}{\sum_k \int_{-\infty}^{+\infty} dv e^{-\beta v} A(k, v)}, \end{aligned} \quad (22)$$

and the dc mobility

$$\mu_{\text{dc}}^{\text{bbl}} = \frac{4\pi t_0^2}{T} \frac{\sum_k \sin^2 k \int_{-\infty}^{+\infty} dv e^{-\beta v} A(k, v)^2}{\sum_k \int_{-\infty}^{+\infty} dv e^{-\beta v} A(k, v)} \quad (23)$$

in the bubble approximation. The computation of transport properties in the bubble approximation thus reduces to the computation of the carrier's spectral function $A(k, \omega)$.

C. Hierarchical equations of motion

The HEOM method is a numerically exact density-matrix technique providing access to the dynamics of the system of interest (here, electrons) that is linearly coupled to a collection of harmonic oscillators (here, phonons) [61,62]. The method has been recently extended to computations of various real-time finite-temperature correlation functions of the operators acting on the system of interest [31,59,63–65]. The method is ultimately based on the formally exact results of the Feynman-Vernon influence functional theory [66] (though the details do depend on the correlation function). In Appendix A, we summarize such formally exact results for the current-current correlation function [Eq. (10)] [57] and the Green's function [Eqs. (20) and (21)] [56] of the Holstein model. These results can serve as a convenient starting point for analytical studies in various limits; see Sec. III. The actual computations are, however, performed numerically by recasting the formally exact result as a hierarchy of dynamical equations for the correlation function we consider (the hierarchy root) and auxiliary quantities needed to fully take the interactions into account (deeper hierarchy layers). The hierarchy is, in principle, infinite, and it has to be truncated at a certain maximum depth D .

The applications of the HEOM method to the Holstein model featuring a single oscillator per site [67] have been hindered by the numerical instabilities of the truncated hierarchy [68,69], which ultimately stem from the finite number of oscillators on a finite lattice. Within our recently developed momentum-space HEOM [56], we have resolved this issue

in a wide range of the model's parameter space by devising a physically motivated hierarchy closing [57]. At the same time, we have lowered the computational requirements with respect to the commonly used real-space HEOM by exploiting the model's translational symmetry. We summarize the momentum-space HEOM for the current-current correlation function [Eq. (10)] [57] and the Green's function [Eqs. (20) and (21)] [56] in Sec. SI of Ref. [70].

Numerical uncertainties in HEOM results can be due to the finite chain length N , finite maximum depth D , and finite maximum propagation time t_{max} . We found [57] that finite-size effects can be controlled by following the relative accuracy with which the optical sum rule $\int_{-\infty}^{+\infty} d\omega \text{Re } \mu(\omega) = -\pi \langle H_c \rangle_{H,1}$ is satisfied. We concluded [57] that the convergence with respect to D can be enhanced by taking the arithmetic average of HEOM results for two consecutive depths $D-1$ and D (provided that D is sufficiently large, so that the relative accuracies with which the optical sum rule is satisfied at the two depths almost coincide). The time t_{max} should be sufficiently long, so that the integrals $T^{-1} \int_0^{t_{\text{max}}} ds \text{Re } C_{jj}(s)$ and $-2 \int_0^{t_{\text{max}}} ds s \text{Im } C_{jj}(s)$, whose $t_{\text{max}} \rightarrow +\infty$ limit defines μ_{dc} [Eq. (12)], have entered into saturation as a function of t_{max} . In practice, we always choose N , D , and t_{max} that are sufficiently large so that (i) the optical sum rule is satisfied with relative accuracy $\lesssim 10^{-4}$, and (ii) the relative difference between the values of μ_{dc} obtained using the two expressions in Eq. (12) is $\lesssim 0.1$. Based on (ii), we estimate that the relative uncertainty of HEOM results for the dc mobility is $\lesssim 10\%$.

For stronger g or at higher T , we generally need smaller N , shorter t_{max} , and larger D . However, it is difficult to give an *a priori* estimate of N , D , and t_{max} based on the values of model parameters. As an illustration, we typically use $N \sim 100$, $D = 2-3$, and $\omega_0 t_{\text{max}} \gtrsim 500$ for small g and T , $N \sim 10$, $D \sim 7$, and $\omega_0 t_{\text{max}} \simeq 300$ at intermediate g and T , and $N \leq 7$, $D \geq 12$, and $\omega_0 t_{\text{max}} \lesssim 100$ for large g and T . The HEOM results to be presented are publicly available as a data set [71].

D. Real-time quantum Monte Carlo

We also employ path-integral QMC to evaluate the numerically exact current-current correlation function $C_{jj}(t)$, and the same quantity within the bubble approximation $C_{jj}^{\text{bbl}}(t)$. This method can produce reliable results for imaginary times and for real times that are not too long. For longer real times, the statistical error of the Monte Carlo procedure becomes very large due to the dynamical sign problem, and the results could not be obtained. The results obtained using QMC are used to cross-check the results obtained using HEOM, for model parameters and times when both methods give results, as well as to complement HEOM results for some cases in which the results could not be obtained using HEOM.

The path-integral QMC method used in this work is in many aspects the same as the methods that we employed in Refs. [53,56]. It is based on a path-integral representation of the correlation function, where the Suzuki-Trotter expansion is used to decompose the (real- or imaginary-time) evolution operator (e^{iHt} or $e^{-\beta H}$) into evolution operators over small time intervals. Unlike in Ref. [53], where the decomposition is performed to the operators $e^{-\beta H}$, e^{iHt} , and e^{-iHt} , here we

apply it to the operators $e^{-(\beta-it)H}$ and e^{-iHt} , which allows us to perform either real- or imaginary-time calculations using the same computational code. As in Ref. [53], in the path-integral representation, we make use of either the momentum or site representation for electronic single-particle states. An appropriate choice of the representation reduces the sign problem and enables the calculations for longer real time. For weaker electron-phonon interaction, the momentum representation of electronic states is more convenient in that respect, while the site representation is more convenient for stronger electron-phonon interaction.

We use QMC to calculate the quantities $C_{jj}(t)$ [as defined in Eq. (3)], $\mathcal{G}^>(k, t)$ [as defined in Eq. (18)], $\mathcal{G}^<(k, t)$ [see Eq. (19)], and $\langle N_e \rangle_K$ [see Eq. (8)]. With these quantities at hand, we can then also evaluate $C_{jj}^{\text{bbl}}(t)$ using Eq. (17).

E. Dynamical mean-field theory

The DMFT is an approximate yet nonperturbative method that can treat the models with local interactions [72]. The DMFT establishes a mapping between the lattice problem and the impurity problem, supplemented with a self-consistency condition. For the Holstein model, the polaron impurity model can be efficiently solved in a form of the continued fraction expansion [35]. While this mapping is exact in the infinite-dimensional limit, it remains applicable in the finite-dimensional case as well, yielding approximate results characterized by momentum-independent self-energy. It was recently shown that this method yields remarkably accurate single-particle properties of the Holstein polaron, regardless of the dimensionality of the system, while demanding minimal computational resources [39]. Therefore, it can also be used for the calculation of the optical conductivity within the bubble approximation.

III. ANALYTICAL INSIGHTS INTO THE LIMITS WITH VANISHING VERTEX CORRECTIONS

Using different analytical arguments, this section identifies the limits in which vertex corrections to conductivity vanish. The main analytical results accompanied with numerical examples are briefly summarized in Secs. III A–III C, while the corresponding technical details are provided in Appendixes B–D.

A. Limit of vanishing electron-phonon interaction ($g \rightarrow 0$)

In Appendix B, we first demonstrate that the lowest-order terms in the expansions of $C_{jj}(t)$ [Eq. (10)] and $C_{jj}^{\text{bbl}}(t)$ [Eq. (17)] in powers of small g are identical. We then use these terms to partially resum the perturbation series for $C_{jj}^{\text{bbl}}(t)$ in the $g \rightarrow 0$ limit by employing the second-order cumulant expansion approach [17,37,73], which becomes exact in this limit. The final expressions needed to evaluate the weak-coupling second-order cumulant result are provided in Eqs. (B17) and (B19)–(B23).

Figures 1(a) and 1(b) present a numerical example supporting our analytical conclusion that the vertex corrections vanish in the $g \rightarrow 0$ limit. We compare $C_{jj}(t)$ computed using HEOM, DMFT (in the thermodynamic limit), and the weak-coupling second-order cumulant expansion (label

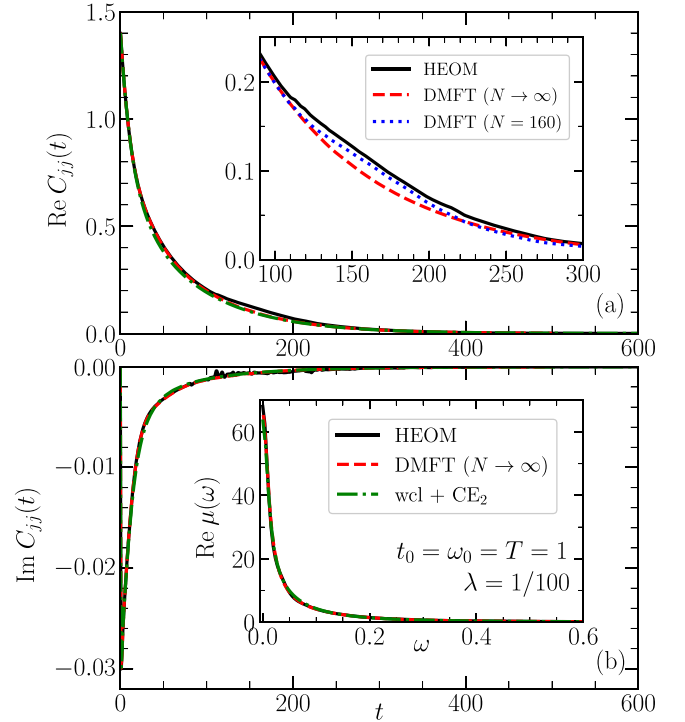


FIG. 1. Time dependence of the (a) real and (b) imaginary part of C_{jj} computed using HEOM (solid line), DMFT (dashed line), and Eqs. (B17) and (B19) (dash-dotted line, label “wcl + CE₂”). HEOM computations use $N = 160$ and $D = 2$, wcl + CE₂ computations use $N = 1009$, whereas the DMFT results are in the thermodynamic limit ($N \rightarrow \infty$). The inset of panel (b) shows the dynamical mobility obtained using the above approaches. The inset of panel (a) compares the DMFT result for $N \rightarrow \infty$ with the HEOM and finite-chain DMFT results, both of which use $N = 160$. The model parameters are $t_0 = 1$, $\omega_0 = 1$, $\lambda = 1/100$, and $T = 1$.

“wcl + CE₂,” obtained on a long but finite chain). While the dynamics predicted by the cumulant method almost perfectly agrees with the DMFT result, a small hump in the HEOM result for $\text{Re } C_{jj}(t)$ appearing around $t_0 t \sim 150$ suggests that it exhibits weak finite-size effects. This is further corroborated by the inset of Fig. 1(a), which shows that HEOM and DMFT results on a finite chain (as implemented in Ref. [39]) exhibit qualitatively (and also quantitatively) similar deviations from the infinite-chain DMFT result for $150 < t_0 t < 200$. The HEOM, DMFT ($N \rightarrow \infty$), and cumulant dynamical-mobility profiles virtually coincide and assume a Drude-like shape; see the inset of Fig. 1(b).

B. Limit of vanishing electronic coupling ($t_0 \rightarrow 0$)

One can demonstrate that the vertex corrections vanish in the limit $t_0 \rightarrow 0$ by establishing the equality of the first nonzero terms in expansions of $C_{jj}(t)$ and $C_{jj}^{\text{bbl}}(t)$ in powers of small t_0 . Since the current operator itself is linear in t_0 [Eqs. (5) and (6)], the lowest-order term in expansions of both $C_{jj}(t)$ and $C_{jj}^{\text{bbl}}(t)$ as $t_0 \rightarrow 0$ is of the order of t_0^2 . As a starting point, one can again take the formally exact expressions from which the HEOM are derived (Appendix A), in which all operators $e^{-\alpha H_c}$ ($\alpha = \beta, \pm it$) are replaced by the unit operator.

The procedure summarized in Sec. SII of Ref. [70] leads to $[n_{\text{ph}} = (e^{\beta\omega_0} - 1)^{-1}]$

$$C_{jj}(t) = C_{jj}^{\text{bbI}}(t) \approx 2t_0^2 \exp \left\{ -2 \frac{g^2}{\omega_0^2} [(2n_{\text{ph}} + 1) - (n_{\text{ph}} + 1)e^{-i\omega_0 t} - n_{\text{ph}} e^{i\omega_0 t}] \right\}. \quad (24)$$

While this proves that the vertex corrections vanish in the limit $t_0 \rightarrow 0$, the expression in Eq. (24) is periodic in real time with period $2\pi/\omega_0$. Thus, the current-current correlation function does not decay to zero as real time goes to infinity. Hence, one would obtain infinite dc mobility by integrating Eq. (24) over t . This issue has been recognized in the literature [74–77]. To circumvent it, we find it convenient to perform the polaronic (Lang-Firsov) unitary transformation [78] of the Holstein Hamiltonian and evaluate the current-current correlation function in the $t_0 \rightarrow 0$ limit in the polaronic frame. Using the Matsubara Green's function formalism [10], we eventually obtain an expression for $C_{jj}(t)$ that decays as t^{-3} at long times t , which is sufficiently fast to render the time integral of $C_{jj}(t)$, and thus the dc mobility, finite. While we defer all the details to Appendix C, here we only present the final result for the current-current correlation function,

$$C_{jj}(t) = C_{jj}^{\text{bbI}}(t) \approx 2t_0^2 \frac{\beta}{t(\beta - it)\sqrt{c_0}} \frac{I_1[-2(\beta - it)\sqrt{c_0}]J_1(2t\sqrt{c_0})}{I_1(-2\beta\sqrt{c_0})} \times \exp \left\{ -2 \frac{g^2}{\omega_0^2} [2n_{\text{ph}} + 1 - (n_{\text{ph}} + 1)e^{-i\omega_0 t} - n_{\text{ph}} e^{i\omega_0 t}] \right\}, \quad (25)$$

where c_0 is defined in Eq. (C35), while I_1 (J_1) is the (modified) Bessel function of the first kind of order 1.

In Figs. 2(a)–2(c) we present a numerical example that supports our analytical proof that vertex corrections vanish in the limit $t_0 \rightarrow 0$. We present $\text{Re}C_{jj}(t)$ for $g = 1$, $\omega_0 = 1$, $T = 1$, and different values of t_0 calculated using QMC, QMC within the bubble approximation, and using the analytical formula given in Eq. (25). The results clearly demonstrate that the analytical formula and the bubble-approximation results converge towards numerically exact QMC results as t_0 decreases towards zero.

C. Limit of infinite temperature ($\beta \rightarrow 0$)

In the limit of infinite temperature, it is permissible to treat phonons as classical harmonic oscillators. Furthermore, at sufficiently high temperatures, single-particle correlation functions become local (Fig. 3 provides illustrative examples), and their dynamics becomes primarily determined by local (on-site) processes. In Appendix D, we derive that the exact and bubble-approximation correlation functions are identical in the $\beta \rightarrow 0$ limit:

$$C_{jj}(t) = C_{jj}^{\text{bbI}}(t) \approx 2t_0^2 e^{-\sigma^2 t^2 - i\sigma^2 \beta t}. \quad (26)$$

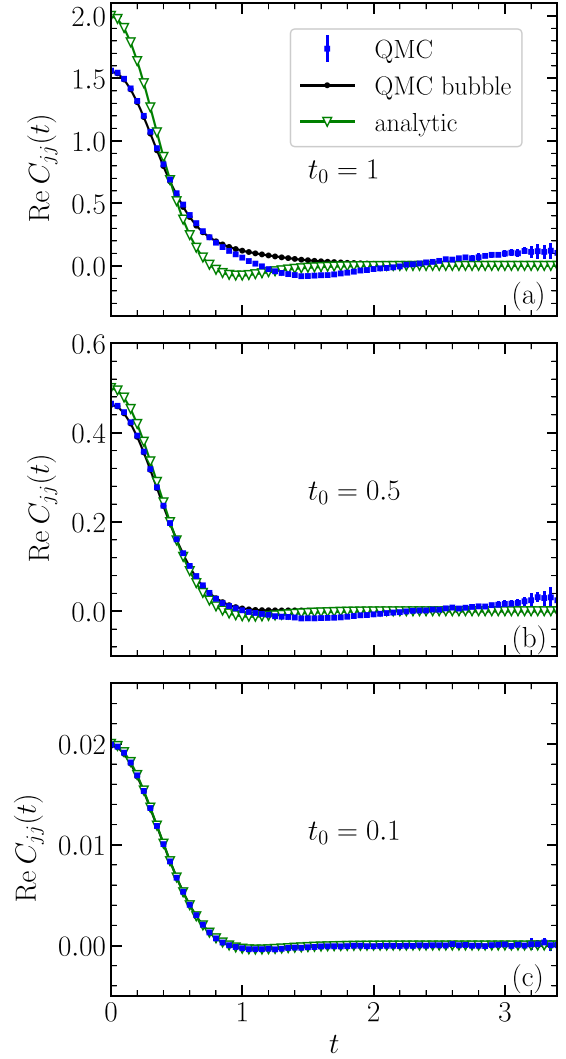


FIG. 2. (a)–(c) Real part of the real-time current-current correlation function for the Holstein model for different values of the parameter t_0 . Other parameters are set to $g = 1$, $\omega_0 = 1$, $T = 1$. The results labeled as “QMC” were obtained using QMC simulations, the results labeled as “bubble QMC” were obtained from QMC simulations within the bubble approximation, while the results labeled as “analytic” were obtained using Eq. (25).

Here,

$$\sigma^2 = g^2 \coth(\beta\omega_0/2) \approx 2g^2/(\beta\omega_0) \quad (27)$$

is the variance of the thermal fluctuations in the on-site energy $\varepsilon = g(b^\dagger + b)$ evaluated in the equilibrium state $\frac{e^{-\beta H_{\text{ph}}}}{Z_{\text{ph}}}$ of free phonons.

We support these analytical results with a numerical example, obtained from QMC simulations, presented in Figs. 3(a1)–3(c2). The results presented in Figs. 3(a1)–3(c1) show that the bubble-approximation result and the analytical result given by Eq. (26) converge towards the numerically exact result as T increases. In Figs. 3(a2)–3(c2) we present the absolute value of the quantity $s_{nm}(t) = \langle c_n(t)c_m^\dagger \rangle_K$, where c_n (c_m^\dagger) is the annihilation (creation) operator for an electron at site n (m). This quantity was obtained from Fourier transform to real space of the quantity $\mathcal{G}^>(k, t)$ [see Eq. (18)] and can be

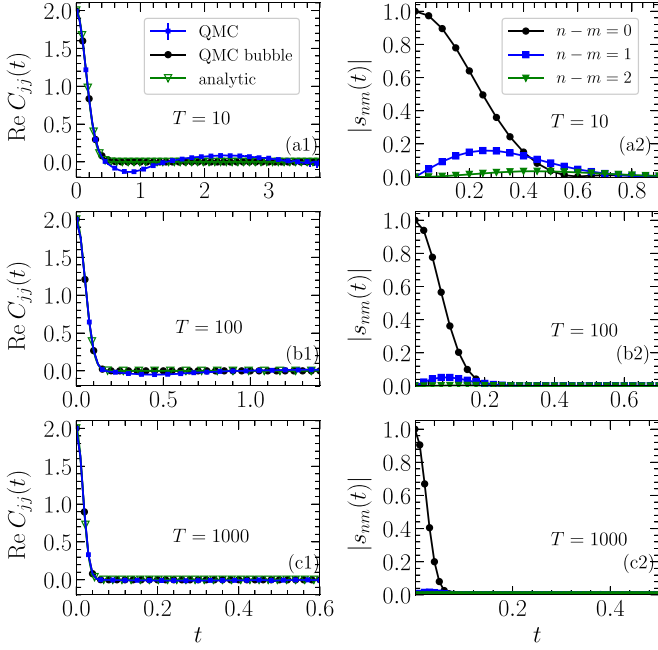


FIG. 3. (a1)–(c1) Real part of the real-time current-current correlation function for the Holstein model for different values of the temperature T . Other parameters are set to $g = 1$, $\omega_0 = 1$, $t_0 = 1$. The results labeled as “QMC” were obtained using QMC simulations, the results labeled as “QMC bubble” were obtained from QMC simulations within the bubble approximation, while the results labeled as “analytic” were obtained using Eq. (26). (a2)–(c2) Time dependence of the absolute value of the quantity $s_{nm}(t)$ (defined in the text) that describes correlations between annihilation and creation operators at lattice sites n and m . The results are presented for the same model parameters as in (a1)–(c1).

used as a measure of spatial correlations in the system. It can be seen from Figs. 3(a2)–3(c2) that at higher temperatures, the spatial correlations for $n - m \neq 0$ become smaller and eventually practically negligible. This confirms the assumption of locality of the correlations used in our analytical derivation. One should nevertheless note that unrealistically high temperatures (which would be certainly above the melting point in a real material) are needed for full vanishing of spatial correlations.

IV. IMPORTANCE OF VERTEX CORRECTIONS: ANALYSIS OF NUMERICAL RESULTS

Having identified the limiting cases in which the vertex corrections vanish, here we combine numerical results emerging from different methods at our disposal to analyze the importance of vertex corrections in parameter regimes between these limits. A detailed summary of the parameter regimes examined is provided in Table S1 of Ref. [70].

The numerically exact dynamics on short time scales can be computed using QMC in essentially any parameter regime. On the other hand, the crossover from the short-time ballistic to the long-time diffusive dynamics, and thus the dynamical-mobility profile down to $\omega = 0$, can be captured using the HEOM method, which in practice works best when the

hierarchy closing strategy developed in Ref. [57] is effective. This is the case for not too strong interaction ($\lambda \lesssim 1$), at moderate temperatures ($1 \lesssim T/t_0 \lesssim 10$), and for $\omega_0/t_0 \leq 2$. The results of the two numerically exact methods (HEOM and QMC) will be compared to the results stemming from the bubble approximation, which, in principle, needs numerically exact single-particle properties. While these are available from appropriate HEOM-method computations [56], we have recently demonstrated that the DMFT, which is formulated directly in the thermodynamic limit, provides close-to-exact single-particle properties of the Holstein model in the whole parameter space at a much smaller computational cost [39]. The very good agreement between HEOM and DMFT spectral functions translates into the very good agreement between the current-current correlation functions and dynamical-mobility profiles computed using HEOM (within bubble approximation) and DMFT, as shown in Figs. 4(a)–4(c) for different phonon frequencies ω_0 . We have checked that a similar level of agreement persists for all parameters where HEOM bubble computations are performed. We thus conclude that the DMFT results can be practically taken as the exact bubble-approximation results, which are available in the whole parameter space.

A. Comparison of typical features of numerically exact and bubble-approximation results in time and frequency domains

In Figs. 5(a1)–5(c3) we compare the numerically exact and bubble-approximation dynamics of $\text{Re } C_{jj}$, the carrier spread Δx , and the diffusion constant \mathcal{D} , as well as the corresponding dynamical-mobility profiles. We perform the comparison in three representative cases spanning the range from slow-phonon [$\omega_0/t_0 = 1/3$ in (b1)–(b3)] to intermediate-phonon [$\omega_0/t_0 = 1$ in (a1)–(a3)] and fast-phonon [$\omega_0/t_0 = 3$ in (c1)–(c3)] regimes. We choose the intermediate electron-phonon interaction ($\lambda = 1/2$), which unveils the most commonly observed differences between the numerically exact and bubble-approximation results. Figures S1–S3 of Ref. [70] summarize similar comparisons in other parameter regimes examined (see also Table S1).

In Appendix A, we prove that the exact and bubble-approximation current-current correlation functions are identical at $t = 0$ in all parameter regimes. Figures 5(a1)–5(c1) additionally demonstrate that their short-time dynamics are also identical. The very good agreement between the two dynamics persists beyond the very initial time scales, when the dynamics is ballistic so that $C_{jj,\text{bal}}(t) = C_{jj}(0)$, $\Delta x_{\text{bal}}(t) = \sqrt{C_{jj}(0)t}$, and $\mathcal{D}_{\text{bal}}(t) = C_{jj}(0)t$. Figures 5(a2)–5(c2) suggest that the numerically exact and bubble-approximation dynamics closely follow one another as long as $\Delta x(t) \lesssim 1$, i.e., the carrier spread is smaller than the lattice constant. In parameter regimes analyzed in Fig. 5, the agreement is good for $t_0 t \lesssim 1$, which is the timescale characteristic for the transfer of a free electron between neighboring sites. This translates into the very good agreement between the two dynamical-mobility profiles in the high-frequency region $\omega/t_0 \gtrsim 2\pi$; see the insets of Figs. 5(a1)–5(c1).

On intermediate time scales, the numerically exact results in Figs. 5(a) and 5(b) predict a time-limited slowdown of the carrier [negative values of $\text{Re } C_{jj}(t)$, decrease of $\mathcal{D}(t)$]

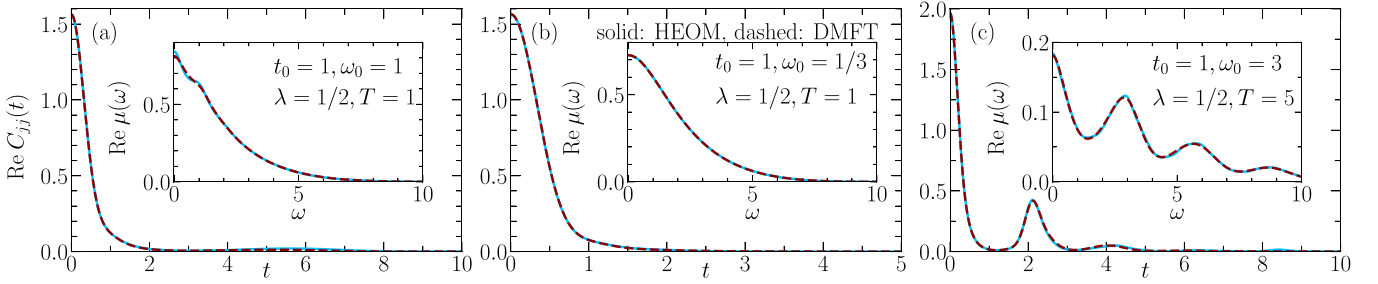


FIG. 4. Time dependence of $\text{Re } C_{jj}$ computed within the bubble approximation using numerically exact HEOM spectral functions (solid blue lines) and approximate DMFT spectral functions (dashed brown lines) for $t_0 = 1$ and (a) $\omega_0 = 1, T = 1$; (b) $\omega_0 = 1/3, T = 1$; (c) $\omega_0 = 3, T = 5$. The electron-phonon interaction strength in all three panels is $\lambda = 1/2$. The insets display the corresponding dynamical-mobility profiles computed within the bubble approximation using HEOM and DMFT spectral functions. HEOM spectral functions are computed using (a) $N = 10, D = 6$; (b) $N = 10, D = 8$; and (c) $N = 7, D = 12$.

that is followed by a steady increase in the diffusion constant until it saturates to its long-time limit. On the other hand, in the regimes analyzed here, the results in the bubble approximation do not display any transient slowdown of the carrier, and the diffusion constant is a monotonically increasing function of time. As a consequence, the dynamical-mobility profile in the bubble approximation has only the

Drude-like peak centered at $\omega = 0$ (qualitatively similar to that in the $g \rightarrow 0$ limit analyzed in Sec. III A), while the numerically exact dynamical-mobility profile additionally develops a finite-frequency peak. In the regimes analyzed here, the numerically exact dynamical-mobility profile still has a local maximum at $\omega = 0$. Namely, rewriting Eq. (11) as $\text{Re } \mu(\omega) = 2 \frac{\tanh(\beta\omega/2)}{\omega} \int_0^{+\infty} dt \cos(\omega t) \text{Re } C_{jj}(t)$, one realizes

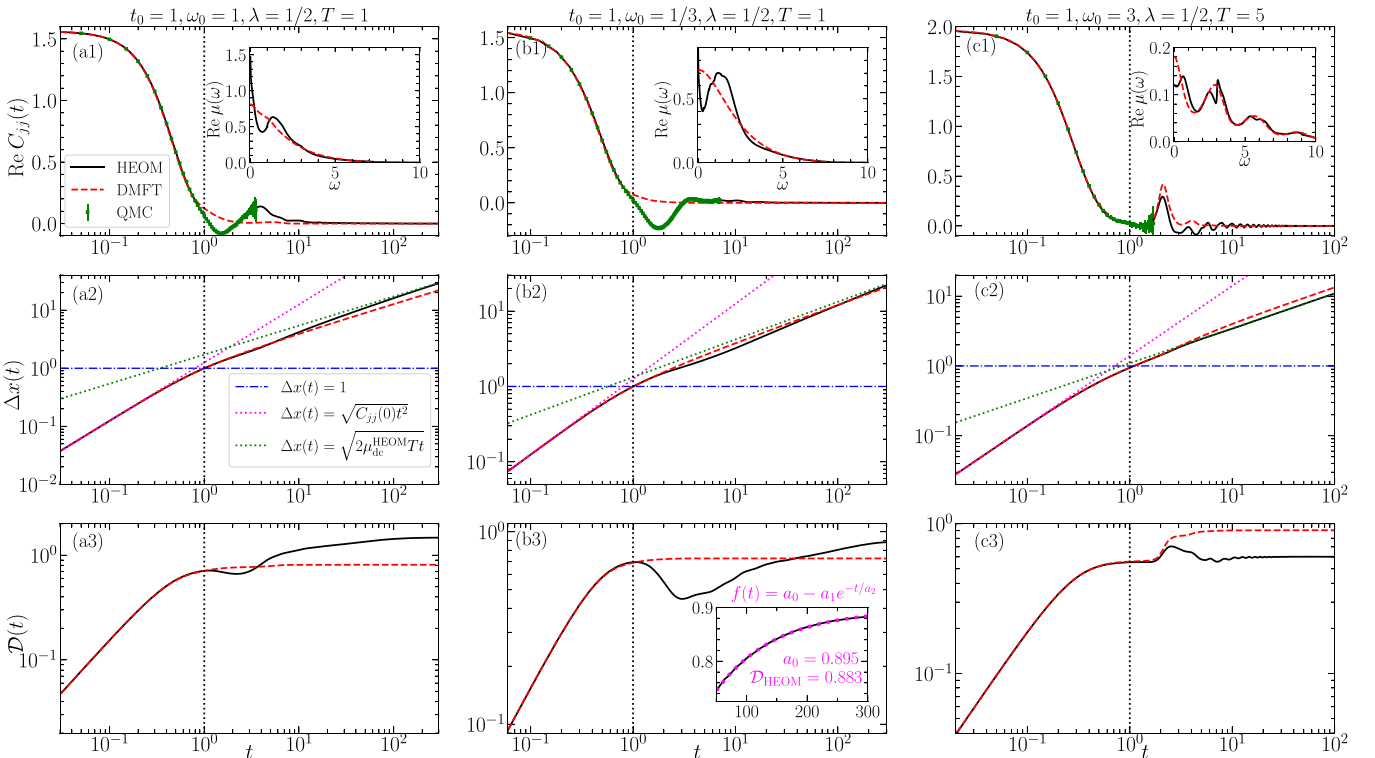


FIG. 5. Comparison of numerically exact (labels “HEOM” and “QMC”) and bubble-approximation (label “DMFT”) results for time evolution of (a1)–(c1) $\text{Re } C_{jj}$, (a2)–(c2) Δx , and (a3)–(c3) $\mathcal{D}(t)$. In all panels, $t_0 = 1, \lambda = 1/2$, while the remaining model parameters are (a1)–(a3) $\omega_0 = 1, T = 1$; (b1)–(b3) $\omega_0 = 1/3, T = 1$; and (c1)–(c3) $\omega_0 = 3, T = 5$. Vertical dotted lines indicate time $t = 1$. The insets of (a1)–(c1) compare dynamical-mobility profiles in the numerically exact approach and in the bubble approximation. Dotted lines in (a2)–(c2) show the carrier spread in the short-time ballistic [$\Delta x_{\text{bal}}(t) = \sqrt{C_{jj}(0)t^2}$] and long-time diffusive [$\Delta x_{\text{diff}}(t) = \sqrt{2\mu_{\text{dc}}^{\text{HEOM}} T t}$] regimes, while double dash-dotted lines show $\Delta x(t) = 1$. The inset of panel (b3) shows the fit of $\mathcal{D}_{\text{HEOM}}(t)$ to the exponentially decaying function $f(t) = a_0 - a_1 e^{-t/a_2}$ (magenta dots) for $50 \leq t \leq 300$. Fitting parameters are $a_0 = 0.895, a_1 = 0.251, a_2 = 97.1$. HEOM results in (a1)–(a3) are obtained using $N = 13, D = 6$, while the results displayed in (b1)–(b3) [(c1)–(c3)] are obtained by performing the arithmetic average of HEOM results for $N = 10, D = 7$ and $N = 10, D = 8$ [$N = 7, D = 11$ and $N = 7, D = 12$]. QMC results are displayed with the associated statistical error bars and are obtained using $N = 10$ in (a1), $N = 7$ in (b1), and $N = 10$ in (c1).

that $\omega = 0$ is a stationary point of the dynamical-mobility profile [$\text{Re } \mu(\omega) \propto \omega^2$ as $\omega \rightarrow 0$]. The convexity of $\text{Re } \mu(\omega)$ around $\omega = 0$ then follows from the sign of the corresponding second derivative that reads [79]

$$\begin{aligned} & \left(\frac{d^2}{d\omega^2} \text{Re } \mu(\omega) \right)_{\omega=0} \\ &= -\beta \left\{ \frac{\mathcal{D}_\infty \beta^2}{6} + 2 \int_0^{+\infty} dt t [\mathcal{D}_\infty - \mathcal{D}(t)] \right\}. \end{aligned} \quad (28)$$

In Figs. 5(a) and 5(b), the function $\mathcal{D}_\infty - \mathcal{D}(t)$ is non-negative for $t \geq 0$, and $\omega = 0$ is a local maximum. In general, the sign of $\mathcal{D}_\infty - \mathcal{D}(t)$ can change with t , and direct analytical arguments based on Eq. (28) cannot be developed. It is then notable that our HEOM results suggest that $\omega = 0$ remains a local maximum of $\text{Re } \mu(\omega)$ in all parameter regimes amenable to HEOM computations; see Figs. S1–S3 of Ref. [70].

While the long-time saturation of $\mathcal{D}_{\text{HEOM}}(t)$ is apparent in Fig. 5(a3), Fig. 5(b3) might suggest that the corresponding t_{max} is not sufficiently long to guarantee that the relative uncertainty of $\mathcal{D}_{\text{HEOM}}$ (or $\mu_{\text{dc}}^{\text{HEOM}} = \mathcal{D}_{\text{HEOM}}/T$) is below or of the order of the target 10% accuracy (Sec. II C). To exclude this possibility, we fit $\mathcal{D}_{\text{HEOM}}(t)$ in Fig. 5(b3) for $t \geq 50$ (when all the transients have certainly vanished) to the exponentially saturating function $f(t) = a_0 - a_1 e^{-t/a_2}$. The high quality of the fit is apparent from the inset of Fig. 5(b3), and the relative difference between $\mathcal{D}_{\text{HEOM}}$ and a_0 is well below 10%.

Differently from the situation in Figs. 5(a) and 5(b), in Fig. 5(c) the bubble-approximation dynamical-mobility profile qualitatively resembles its numerically exact counterpart. Both profiles display relatively broad peaks at integer multiples of ω_0 that originate from peaks in $\text{Re } C_{jj}(t)$ at integer multiples of $2\pi/\omega_0$. The bubble approximation predicts peaks without internal structure, whereas numerically exact results predict structured peaks. Such peaks may be ascribed to a more complicated dynamics of $\text{Re } C_{jj}$, which becomes negative after the first peak. A word of caution is in order here as we have established [57] that our HEOM results for $\omega_0/t_0 = 3$ may not be entirely reliable due to possible problems with the HEOM closing strategy for $\omega_0/t_0 \geq 2$.

Finally, in contrast to the regimes studied in Figs. 5(a) and 5(b), there are situations in which the bubble approximation partially captures the time-limited slowdown of the carrier. This typically happens for strong interaction and at not too high temperatures. One example ($\omega_0/t_0 = 1, \lambda = 2, T/t_0 = 1$) is analyzed in Fig. 6, whose inset shows the short-time dynamics of the carrier spread. While in Figs. 5(a) and 5(b) the carrier slows down having covered more than a lattice constant, the slowdown in Fig. 6 happens over the time interval in which Δx remains well below a single lattice constant. This suggests that the dynamics shown in Fig. 6 predominantly reflects on-site phonon-assisted processes. It is thus not surprising that the short-time bubble-approximation dynamics can be qualitatively (and to a large extent quantitatively) reproduced by the atomic-limit formula [Eq. (25)] corrected so

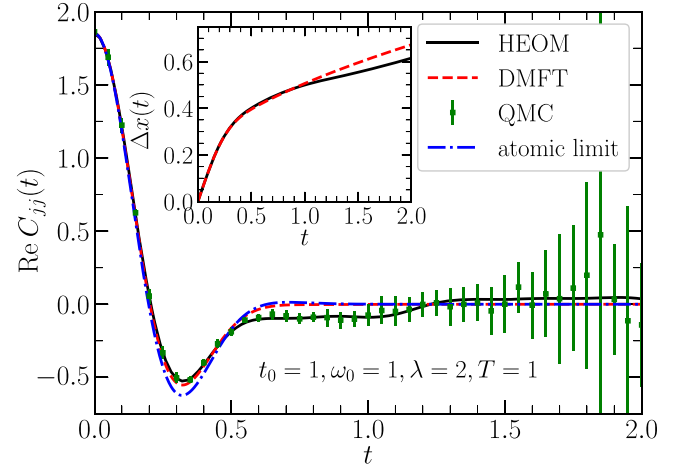


FIG. 6. Comparison of numerically exact (labels “HEOM” and “QMC”) and bubble-approximation (label “DMFT”) dynamics of $\text{Re } C_{jj}$ for $t_0 = 1, \omega_0 = 1, \lambda = 2$, and $T = 1$. The results labeled “atomic limit” are obtained using Eq. (29). The inset shows time-dependent carrier spread $\Delta x(t)$ computed numerically exactly and within the bubble approximation. HEOM computations use $N = 10, D = 8$. QMC results are displayed with the associated statistical error bars and are obtained for $N = 10$.

that it reproduces the value of $C_{jj}(t = 0)$:

$$\begin{aligned} C_{jj}(t) = C_{jj}(0) \exp \left\{ -2 \frac{g^2}{\omega_0^2} [(2n_{\text{ph}} + 1) - (n_{\text{ph}} + 1)e^{-i\omega_0 t}] \right. \\ \left. - n_{\text{ph}} e^{i\omega_0 t} \right\}, \end{aligned} \quad (29)$$

compare the lines labeled “DMFT” and “atomic limit” in Fig. 6. [We have checked that, on timescales analyzed in Fig. 6, the attenuating time-dependent prefactor entering Eq. (25) does not introduce any quantitative changes to the result of Eq. (29).] The numerically exact dynamics shows that the slowdown is prolonged with respect to the bubble-approximation results, meaning that the latter captures the temporal slowdown only partially.

B. Vertex corrections to the dc mobility

The importance of vertex corrections to the dc mobility will be quantified by the relative deviation of the dc mobility in the bubble approximation from the numerically exact result, i.e.,

$$\delta \mu_{\text{dc}}^{\text{vtx}} = \frac{\mu_{\text{dc}}^{\text{HEOM}} - \mu_{\text{dc}}^{\text{DMFT}}}{\mu_{\text{dc}}^{\text{HEOM}}}. \quad (30)$$

The results in the bubble approximation can be considered to carry no intrinsic numerical error because they follow from the DMFT equations formulated directly in the thermodynamic limit; see also Fig. 4. On the other hand, the relative uncertainty that should accompany HEOM results for the dc mobility does not surpass 10%, as discussed in Sec. II C and Ref. [57]. In other words, whenever $|\delta \mu_{\text{dc}}^{\text{vtx}}| \lesssim 0.1$, one can regard the vertex corrections to the dc mobility as unimportant.

Figures 7(a1)–7(c2) provide an overall picture of the importance of the vertex corrections to the dc mobility for

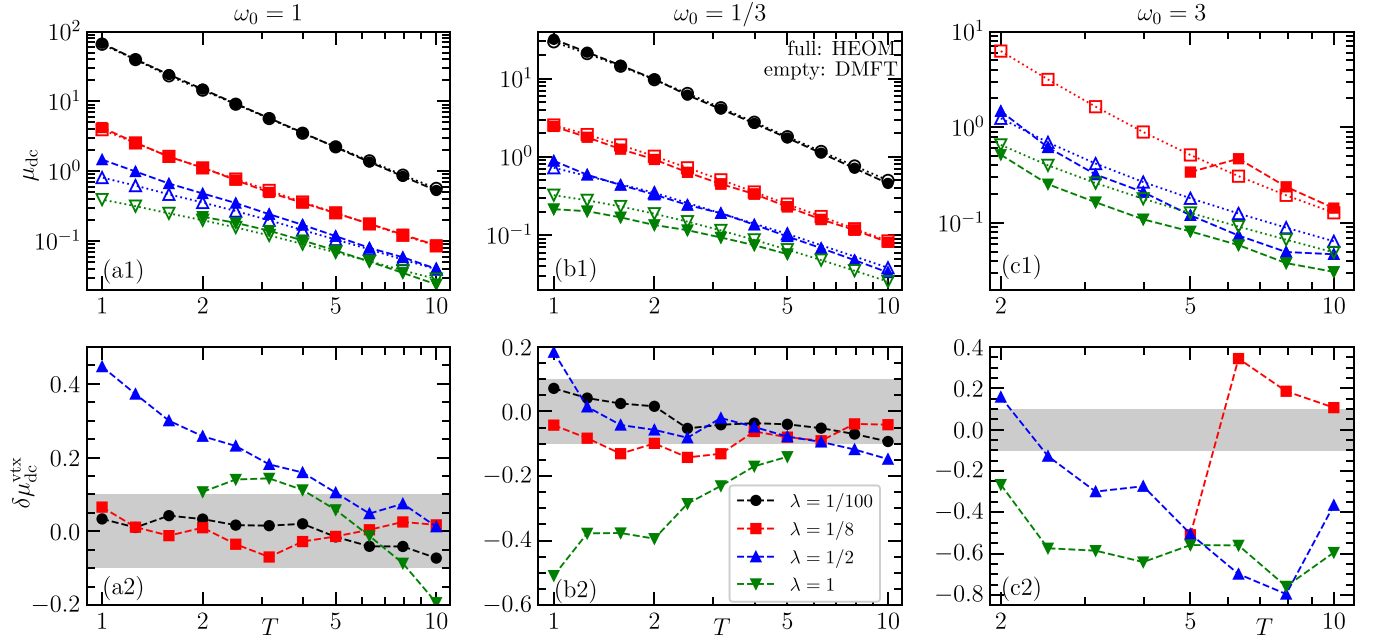


FIG. 7. (a1)–(c1) Temperature dependence of the dc mobility computed using the HEOM (full symbols connected by dashed lines) and DMFT (empty symbols connected by dotted lines) for different strengths of the electron-phonon interaction λ and fixed phonon frequency ω_0 . (a2)–(c2) Temperature dependence of the quantity $\delta\mu_{\text{dc}}^{\text{vtx}}$ [Eq. (30)], which quantifies the importance of vertex corrections to the dc mobility, for different values of λ and fixed ω_0 . Gray regions in (a2)–(c2) delimit the range $\delta\mu_{\text{dc}}^{\text{vtx}} \in [-0.1, 0.1]$ in which the vertex corrections to the dc mobility can be considered as vanishing. ω_0 is equal to 1 in (a1) and (a2), $1/3$ in (b1) and (b2), and 3 in (c1) and (c2), while $t_0 = 1$ in all panels.

different values of ω_0/t_0 , λ , and T/t_0 . Interestingly, in most of the parameter regimes examined for $\omega_0/t_0 = 1$ and $1/3$, $\delta\mu_{\text{dc}}^{\text{vtx}}$ falls in the gray-shaded regions delimiting the aforementioned range $|\delta\mu_{\text{dc}}^{\text{vtx}}| \lesssim 0.1$, in which the vertex corrections to the dc mobility can be regarded as vanishing. Our scarce results for $\omega_0/t_0 = 3$ might suggest that the vertex corrections to the dc mobility are more important than in the other two cases analyzed in Fig. 7. However, possible problems with HEOM results for $\omega_0/t_0 \geq 2$ [57] prevent us from giving a definite statement on the importance of the vertex corrections to the dc mobility in the case of fast phonons.

In the parameter regimes analyzed in Figs. 5(a) and 5(b), the vertex corrections to the dc mobility can be deemed important as $\delta\mu_{\text{dc}}^{\text{vtx}}$ is around 0.5 and 0.2, respectively. On the other hand, while $\delta\mu_{\text{dc}}^{\text{vtx}} \approx -0.4$ points towards significant vertex corrections to the dc mobility for parameters in Fig. 5(c), the overall shape of the dynamical-mobility profile suggests that their importance may be much smaller for the ac mobility. The vertex corrections in Figs. 5(a) and 5(b) are positive, i.e., $\mu_{\text{dc}}^{\text{HEOM}} > \mu_{\text{dc}}^{\text{DMFT}}$. The dominant contribution to $\mu_{\text{dc}}^{\text{DMFT}}$ comes from the dynamics on short time scales $t_0 t \lesssim 1$, on which the approximate and numerically exact results agree quite well [see also Eq. (12)]. This is most conveniently seen from Figs. 5(a3)–5(c3) showing the dynamics of \mathcal{D} . The subsequent slowdown of the carrier is fully compensated by the speedup of the carrier [$\text{Re } C_{jj}(t) > 0$, $\mathcal{D}(t)$ increases with t] on somewhat longer time scales. Ultimately, the effects of the transient slowdown are overpowered by the speedup, so that the numerically exact dc mobility becomes larger than the approximate one.

Our results for $\lambda = 1/2$ in Fig. 7(a2) and for $\lambda = 1$ in Fig. 7(b2) suggest that the vertex corrections to the dc mobility decrease with temperature for the parameters studied. However, even at the highest temperatures accessible in these two cases, the numerically exact results (and the bubble-approximation results, too) are not close to the results in the infinite-temperature limit analyzed in Sec. III C. Also, one should keep in mind that even when the vertex corrections to the dc mobility can be considered as vanishing [e.g., for $\lambda = 1/8$ in Figs. 7(a2) and 7(b2)], there may be important differences between the numerically exact and bubble-approximation dynamical-mobility profiles (see also Figs. S1 and S2 of Ref. [70]).

Considering all these things, in the following three sections we discuss in more detail specific results related to the importance of vertex corrections for the three values of ω_0/t_0 studied.

C. Intermediate-frequency phonons ($\omega_0/t_0 = 1$)

For $\lambda = 1/100$ and at all temperatures examined, our numerical results show vanishing vertex corrections to the dc mobility, as demonstrated both numerically in Fig. 7(a2) and analytically in Sec. III A. The small nonzero values of $\delta\mu_{\text{dc}}^{\text{vtx}}$ can be attributed to the weakly pronounced finite-size effects in the HEOM results; see also Fig. 1. The vertex corrections to dc mobility are also small for $\lambda = 1/8$. However, as the temperature is increased, the dynamical-mobility profile develops a finite-frequency peak qualitatively similar to that discussed in Fig. 5(a); see Fig. S1 of Ref. [70].

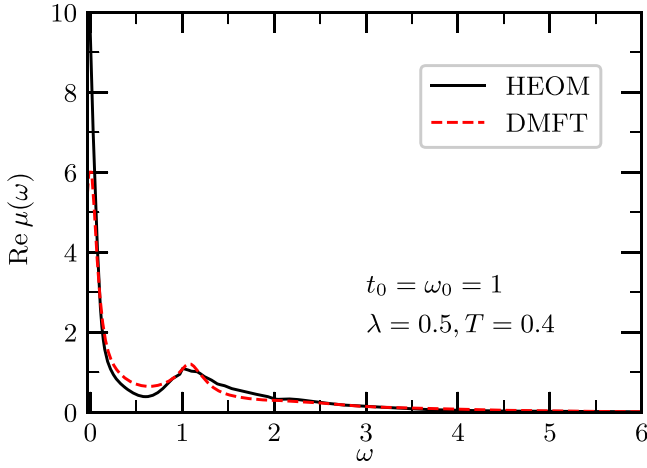


FIG. 8. Dynamical-mobility profile computed using HEOM and DMFT for $t_0 = \omega_0 = 1$, $\lambda = 1/2$, and $T = 0.4$. HEOM computations use $N = 29$, $D = 4$.

Although the vertex corrections to the dc mobility for $\lambda = 1/2$ become insignificant at the highest temperatures considered, see Fig. 7(a2), the differences between the numerically exact and bubble-approximation dynamics of $\text{Re } C_{jj}$ and dynamical-mobility profiles persist, as shown in Fig. 5(a) and Fig. S1 of Ref. [70]. Figure S1 additionally suggests that the carrier slowdown becomes less pronounced and shifts towards later times as the temperature is decreased, meaning that the finite-frequency peak in the numerically exact $\text{Re } \mu(\omega)$ then shifts towards lower frequencies. Also, in the inset of Fig. 4(a), we observe a nascent atomic-limit-like peak in the bubble-approximation optical response at ω_0 , indicating the presence of a more pronounced peak at ω_0 at even lower temperatures ($T/t_0 < 1$). These expectations are confirmed in Fig. 8, which compares the numerically exact and bubble-approximation dynamical-mobility profiles at $T/t_0 = 0.4$. Both HEOM and DMFT results show that the finite-frequency peak is centered exactly around ω_0 . This peak can be associated with the transitions between the quasiparticle and the satellite peak in the single-particle spectral function. While Fig. 8 indicates that the vertex corrections to the dc mobility remain important at lower temperatures, we note that reaching lower temperatures is problematic for the HEOM method here, mainly because of the system size necessary to minimize finite-size effects.

Figure 7(a2) suggests that the vertex corrections to the dc mobility for $\lambda = 1$ are overall smaller than for $\lambda = 1/2$. The numerically exact dynamics of $\text{Re } C_{jj}$ displays similar features to those in Figs. 5(a1) ($\lambda = 1/2$) and 6 ($\lambda = 2$); see also Fig. S1 of Ref. [70]. Setting $\lambda = 1$ and increasing T , the overall decrease of $\text{Re } C_{jj}$ towards zero becomes generally faster, so that the difference between μ_{dc} and $\mu_{\text{dc}}^{\text{DMFT}}$ stemming from the carrier slowdown becomes more pronounced than that caused by the subsequent speedup. This argument can explain positive (negative) vertex corrections at the lower (upper) end of the temperature range considered for $\lambda = 1$ in Fig. 7(a2). In a similar vein, we argue that the vertex corrections to the dc mobility are not substantial for $\lambda = 2$. Namely, at a fixed temperature T , the overall decrease of

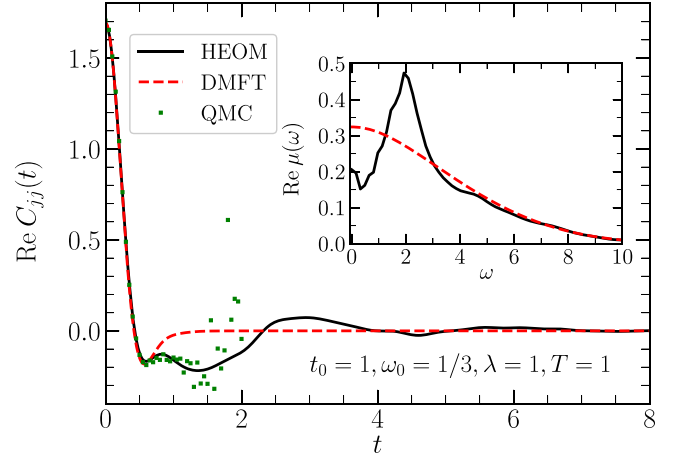


FIG. 9. Time dependence of $\text{Re } C_{jj}$ computed within the HEOM, DMFT, and QMC for $t_0 = 1$, $\omega_0 = 1/3$, $\lambda = 1$, and $T = 1$. The QMC results are displayed without the associated statistical error bars for visual clarity. The inset compares the corresponding dynamical-mobility profiles computed within HEOM and DMFT. HEOM computations use $N = 7$, $D = 11$ and 12 (arithmetic average). QMC simulations use $N = 7$.

$\text{Re } C_{jj}$ towards zero is faster for stronger interaction. Therefore, for sufficiently strong g , we may expect that the features specific to the numerically exact result will not appreciably affect μ_{dc} , which is then primarily determined by $\text{Re } C_{jj}(t)$ up to times at which the corresponding bubble-approximation and numerically exact results agree well; see also Fig. 6.

D. Slow phonons ($\omega_0/t_0 = 1/3$)

For $\lambda = 1/100$, the vertex corrections are negligible. For $\lambda = 1/8$, the vertex corrections are very small at $T/t_0 = 1$, but with increasing temperature, a characteristic two-peak structure emerges in the numerically exact dynamical-mobility profile; see Fig. S2 of Ref. [70]. Intermediate interactions $\lambda = 1/2$ [Fig. 5(b1)] and $\lambda = 1$ (Fig. 9) bring about the appearance of the two-peak structure also at $T/t_0 = 1$. For $\lambda = 1$, the finite-frequency peak is centered around $\omega = 2t_0$, in agreement with earlier numerically exact studies in the slow-phonon regime [80]. While the bubble approximation partially captures the time-limited carrier slowdown at $T/t_0 = 1$, compare Fig. 9 with Fig. 6, it does not capture the finite-frequency absorption feature; see the inset of Fig. 9 and Sec. IV C of Ref. [15]. To elucidate the origin of this feature, the assumption of strictly on-site phonon dynamics underlying the atomic-limit-like Eq. (29) (which reproduces the bubble-approximation result reasonably well, similarly to Fig. 6) has to be relaxed, as has been done by Schubert *et al.* [80]. Their analysis attributes the $2t_0$ absorption feature to the optical transition between the symmetric and antisymmetric states of the electron residing on two neighboring sites, over which phonon dynamics is considered. Figure S2 of Ref. [70] shows that the finite-frequency peak remains around $2t_0$ also at higher temperatures, in agreement with earlier results [80].

Despite important differences in the overall dynamics of C_{jj} , see Fig. 9, the results summarized in Fig. 7 show that the bubble approximation correctly predicts the order of

magnitude of the dc mobility. However, as we approach the adiabatic limit $\omega_0 \rightarrow 0$, the exact result for the dc mobility tends to zero (phonon motion is effectively frozen and an electron experiences a random potential in one dimension where it cannot move over a large distance due to the effect of Anderson localization), while the bubble-approximation result keeps a finite value [18]. Therefore, in this limit, vertex corrections are most pronounced. They give a negative contribution to dc mobility, which completely cancels out the bubble-approximation result (so that $\delta\mu_{\text{dc}}^{\text{vx}} \rightarrow -\infty$). The fact that the results presented in Fig. 7 show positive or somewhat negative vertex corrections implies that the system is still relatively far from the adiabatic limit in these cases. We illustrate this in Fig. S4 of Ref. [70], where we compare $C_{jj}(t)$ and $\mathcal{D}(t)$ for certain parameter values with the adiabatic-limit result for these quantities. The figure confirms that these quantities are far from their adiabatic-limit values. Adiabatic-limit results are obtained using a very computationally efficient Monte Carlo procedure that exploits the fact that phonon momentum is negligible in the adiabatic limit. This procedure is described in detail in Sec. SV of Ref. [70].

In the strong-interaction regime $\lambda = 2$, and at $T/t_0 = 1$, the DMFT captures the time-limited slowdown observed in QMC data quite well; see Fig. 10(a) and compare to Fig. 9. The short-time dynamics of $\text{Re } C_{jj}$ is also very well reproduced by the atomic-limit-like Eq. (29). The DMFT dynamical-mobility profile displays atomic-limit-like peaks at integer multiples of ω_0 . As the temperature is increased from $T/t_0 = 1$ to 10, the peaks become smoothed out, and their envelope changes from a function displaying a finite-frequency local maximum and a zero-frequency local minimum to a function displaying only a zero-frequency local maximum; see the insets of Figs. 10(a) and 10(b). This finite-frequency peak of the envelope, appearing at sufficiently low temperatures, is the well-known polaron peak because the shape of the envelope of the dynamical-mobility profile compares reasonably well with the high-temperature (small- ω_0) limit of the Reik formula [Eq. (29) of Ref. [77] in which $\sinh x \approx \tanh x \approx x$, with $x = \text{const} \times \beta\omega_0 \ll 1$], which reads

$$\text{Re } \mu(\omega) = \frac{\sqrt{\pi}t_0^2}{\sigma\omega} \left[\exp\left(-\frac{(\omega - 2\varepsilon_{\text{pol}})^2}{4\sigma^2}\right) - \exp\left(-\frac{(\omega + 2\varepsilon_{\text{pol}})^2}{4\sigma^2}\right) \right]. \quad (31)$$

Here, $\varepsilon_{\text{pol}} = g^2/\omega_0$ is the polaron binding energy, and σ is defined in Eq. (27). Even at the highest temperatures studied, QMC results predict a protracted temporally limited slowdown of the electron, pointing towards possibly nontrivial negative vertex corrections to the dc mobility (because the intensity of the possible atomic-limit-like features appearing at integer multiples of $2\pi/\omega_0$ decreases quickly with time, which is compatible with the rather wide DMFT optical response).

E. Fast phonons ($\omega_0/t_0 = 3$)

HEOM results are available only in a limited portion of the parameter space, characterized by sufficiently but not excessively high temperatures and interaction strengths.

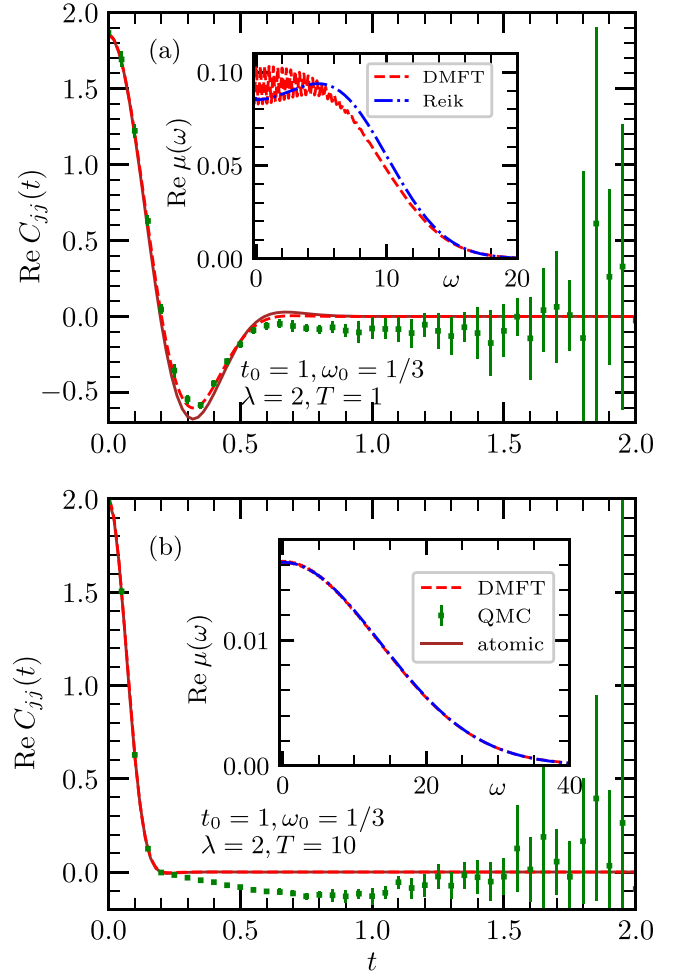


FIG. 10. Time dependence of $\text{Re } C_{jj}$ computed within DMFT and QMC for $t_0 = 1$, $\omega_0 = 1/3$, $\lambda = 2$, and (a) $T = 1$, (b) $T = 10$. Solid brown lines represent the results of the atomic-limit Eq. (29). The insets compare the corresponding dynamical-mobility profiles with those evaluated using the Reik formula [Eq. (31)]. QMC simulations use $N = 7$.

We first compare numerically exact and bubble-approximation results in the weak-coupling regime $\lambda = 1/8$ and $T/t_0 = 10$; see Fig. 11(a). While the bubble-approximation result predicts a monotonically increasing diffusion constant [$\text{Re } C_{jj}(t) > 0$], the numerically exact result predicts a time-limited slowdown of the carrier motion after it has covered a single lattice constant (for $1 \leq t_0 \leq 2$, when $\Delta x \gtrsim 1$), similarly to what we observed in Figs. 5(a) and 5(b) for smaller values of ω_0/t_0 . Interestingly, both numerically exact and approximate results predict a local maximum in $\text{Re } C_{jj}(t)$ around $2\pi/\omega_0$, which is typical for the atomic limit. With this in mind, the reasonable overall agreement between the numerically exact and approximate dynamical-mobility profiles, similar to our observations in Fig. 5(c), is not surprising; see Fig. S3 of Ref. [70]. The vertex corrections to the dc mobility may be considered as vanishing, see Fig. 7(c), as expected in the limit of weak electron-phonon coupling. The potential problems with our HEOM closing are exacerbated at a lower temperature ($T/t_0 = 5$), where our results predict significant vertex corrections, contrary to expectations for small λ .

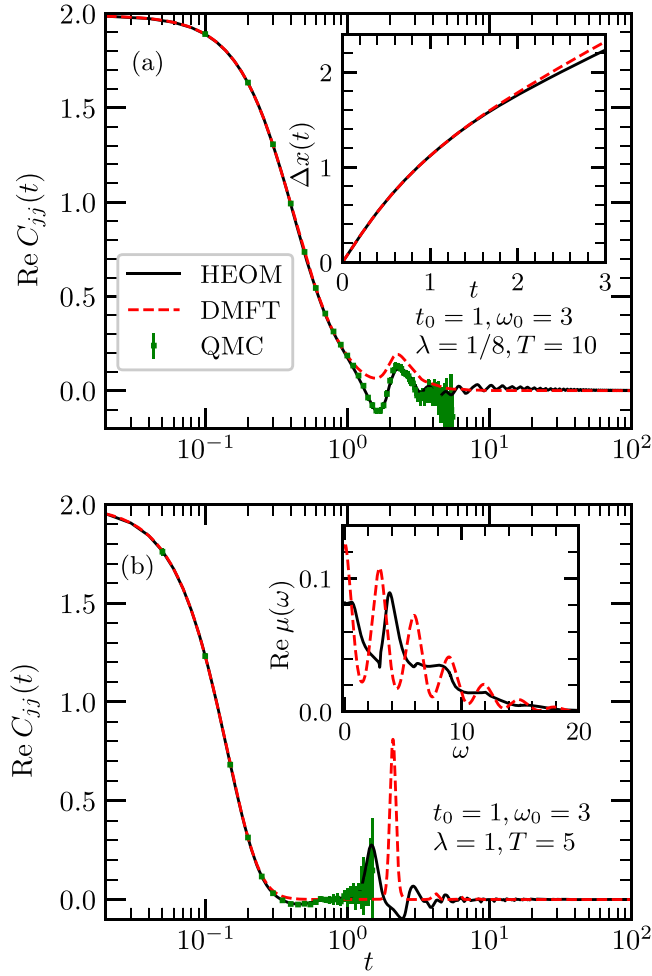


FIG. 11. Time dependence of $\text{Re } C_{jj}$ computed using HEOM (solid black lines), DMFT (dashed red lines), and QMC (full circles) for $t_0 = 1$, $\omega_0 = 3$ and (a) $\lambda = 1/8$, $T = 10$, and (b) $\lambda = 1$, $T = 5$. QMC results are accompanied with their statistical error bars. The insets show (a) the carrier spread and (b) the dynamical-mobility profile computed using HEOM and DMFT. HEOM computations use (a) $N = 10$, $D = 8$; (b) $N = 5$, $D = 20$ and 21 (arithmetic average). QMC simulations use (a) $N = 10$, (b) $N = 7$.

For $\lambda = 1$ and $T/t_0 = 5$, see Fig. 11(b), the bubble approximation again predicts strictly non-negative $\text{Re } C_{jj}(t)$ with peaks at integer multiples of $2\pi/\omega_0$. On the other hand, numerically exact results show that the peaks' centers are generally shifted towards somewhat earlier times, while $\text{Re } C_{jj}(t)$ may assume negative values. This is clearly observed for the first peak, whose intensity within the numerically exact framework is smaller than the intensity of its bubble-approximation counterpart. As a consequence, the numerically exact dynamical-mobility spectrum is qualitatively different from its bubble-approximation counterpart, which has equidistant peaks at integer multiples of ω_0 .

F. Insights from the imaginary-time domain

It is known that the extraction of transport properties from imaginary-axis data for the current-current correlation

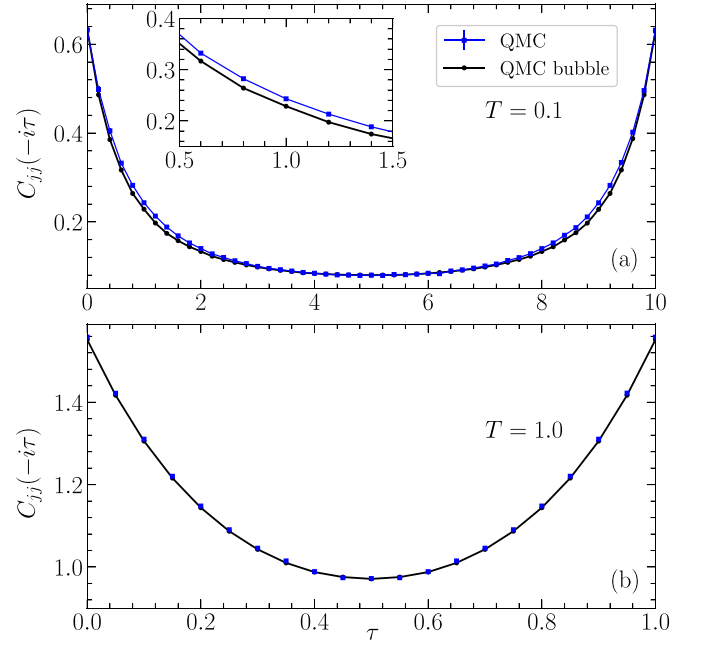


FIG. 12. Imaginary-time current-current correlation function for $t_0 = 1$, $\omega_0 = 1/3$, and $\lambda = 1/2$ at temperatures (a) $T = 0.1$ and (b) $T = 1$. The QMC results obtained from a full calculation and by making use of the bubble approximation are presented. The inset of the top panel shows a zoom to the region where the difference between numerically exact and bubble approximation results is most pronounced.

function can often be unreliable as it relies on procedures for numerical analytical continuation. In Fig. S5 of Ref. [70], we compare some of our results for dc mobility, which entirely follow from real-axis data, to the corresponding results of Ref. [41], which follow from imaginary-axis QMC data. Nevertheless, one may hope to gain insights into the importance of vertex corrections by comparing the imaginary-time current-current correlation functions computed numerically exactly and within the bubble approximation. We have done this by computing, on the one hand, the quantity $C_{jj}(-i\tau)$ [see Eq. (3)] for $0 \leq \tau \leq \beta$, and, on the other hand, the quantities $\mathcal{G}^>(k, -i\tau)$ [see Eq. (18)] and $\mathcal{G}^<(k, -i\tau)$ [see Eq. (19)], which are needed to obtain $C_{jj}^{\text{bbl}}(-i\tau)$ in accordance with Eq. (17). The computations were performed using QMC. It is easier to obtain these quantities in imaginary time than in real time because the dynamical sign problem occurs only for real times.

For the investigated values of parameters when $T/t_0 \geq 1$ we find that the differences between $C_{jj}(-i\tau)$ and $C_{jj}^{\text{bbl}}(-i\tau)$ are very small. They typically differ by less than 1%, and this difference is typically below or comparable to the statistical error of QMC results. One such example is presented in Fig. 12(b). These results should be contrasted with our conclusions reached by analyzing real-time results in the very same parameter regime; see Figs. 5(b) and 7(b2). We can thus conclude that good agreement between numerically exact and bubble approximation results in imaginary time does not imply that the same level of agreement will be present in real time.

When the temperature is lowered to $T/t_0 = 0.1$, the differences between numerically exact and bubble approximation results become noticeable; see Fig. 12(a). The inset of that panel shows a zoom to the region where this difference is most significant. In this region, the difference is above 5%, while the statistical error of QMC results is on the order of 0.5%, hence we are confident that the difference observed is above the level of statistical noise. While these data point towards non-negligible vertex corrections, a definitive conclusion could be reached only if we had access to the corresponding real-time data.

V. SUMMARY AND OUTLOOK

In summary, we presented a detailed analysis of the importance of vertex corrections for charge transport in the one-dimensional Holstein model. Our analytical results demonstrate that the vertex corrections vanish in the weak-interaction, atomic, and infinite-temperature limits, which is supported by numerical results. The numerically exact HEOM calculations were performed for three phonon frequencies: intermediate $\omega_0/t_0 = 1$, low $\omega_0/t_0 = 1/3$, and high $\omega_0/t_0 = 3$.

For $\omega_0/t_0 = 1$, as the electron-phonon coupling is increased, a characteristic two-peak profile of the numerically exact optical conductivity emerges instead of a single Drude peak. At low temperatures, the other peak is centered precisely at $\omega = \omega_0$ and is also captured within the bubble approximation because it corresponds to the transitions between the quasiparticle and the first satellite peak in the single-particle spectral density. At higher temperatures, the peak shifts to $\omega > \omega_0$. Then, the two-peak structure in optical conductivity, which cannot be reproduced in the bubble approximation, is traced back to a downturn in the time-dependent diffusion constant $\mathcal{D}(t)$ at intermediate timescales. Interestingly, for strong interactions, such a slowdown of charge carrier is observed also in the bubble approximation, but at shorter times. In this case, it is primarily governed by the on-site phonon-assisted processes and not by the vertex corrections. This observation is compatible with the absence of vertex corrections in the atomic limit. Both at low and high temperatures, we find that the vertex corrections either do not affect or increase the dc mobility by a few tens of percent in comparison to the bubble term.

Interestingly, for $\omega_0/t_0 = 1/3$ and for moderate electron-phonon interaction, the optical-conductivity profile looks qualitatively similar to that for $\omega_0/t_0 = 1$. We find that the peak at zero frequency persists, giving the dc mobility that is somewhat smaller, but still comparable to the one obtained in the bubble approximation. The height of this peak is expected to diminish as the frequency is lowered further, approaching the adiabatic limit. However, this calculation is not feasible within our implementation of the HEOM method, and is generally challenging for numerically exact methods on the market.

The HEOM solution in the bubble approximation almost coincides with the DMFT solution for optical conductivity for all available parameter values. Hence, our results demonstrate that the vertex corrections can be substantial also in the cases in which the single-particle correlations are almost local, in agreement with previous findings on the Hubbard model [49].

Our results also illustrate the challenges in numerical analytical continuation of the imaginary axis data: in all parameter regimes, the difference between the full and bubble correlation functions in imaginary time is minuscule, and yet the difference in optical conductivity can be large.

To our knowledge, in this work we have presented the most comprehensive study so far of vertex corrections to conductivity on a specific model of the electron-phonon interaction. However, there are several challenges left for future work. It would be interesting to calculate the charge transport in higher dimensions and make a comparison to the one-dimensional case. Also, microscopic calculations for lower phonon frequencies and for models with nonlocal electron-phonon interactions are highly desirable, especially in connection with real-world materials.

ACKNOWLEDGMENTS

This research was supported by the Science Fund of the Republic of Serbia, Grant No. 5468, Polaron Mobility in Model Systems and Real Materials–PolMoReMa. The authors acknowledge funding provided by the Institute of Physics Belgrade through a grant from the Ministry of Science, Technological Development, and Innovation of the Republic of Serbia. Numerical computations were performed on the PARADOX-IV supercomputing facility at the Scientific Computing Laboratory, National Center of Excellence for the Study of Complex Systems, Institute of Physics Belgrade. V.J. and N.V. also acknowledge computational time on the ARIS supercomputing facility (GRNET, Athens, Greece) that was granted by the NI4OS-Europe network under the CoNTraSt project (Open Call 2022, Project No. ni4os002).

V.J. and N.V. performed analytical work. V.J. performed HEOM calculations. P.M. performed DMFT calculations with guidance of D.T. QMC calculations were performed by N.V. The first version of the manuscript was prepared by V.J. All authors discussed the results and contributed to the final manuscript.

APPENDIX A: FORMALLY EXACT EXPRESSIONS FOR THE ELECTRONIC DYNAMICS

It is convenient to switch from the electronic creation and annihilation operators, which act in the Fock space for the electrons, to their counterparts acting in the subspaces containing at most one electron. The corresponding replacements $c_k^\dagger \rightarrow |k\rangle\langle\text{vac}|$ and $c_k \rightarrow |\text{vac}\rangle\langle k|$, where the state $|\text{vac}\rangle$ contains no electrons, are appropriate in the limit of low carrier concentration in which we are interested.

We first summarize the formally exact result for the dynamics of the current-current correlation function in Eq. (10), which can be expressed as

$$C_{jj}(t) = \text{Tr}_{1e}\{j\iota(t)\} = \sum_k j_k \langle k|\iota^{(I)}(t)|k\rangle, \quad (\text{A1})$$

where

$$\iota(t) = \frac{1}{Z} \text{Tr}_{\text{ph}}\{e^{-iHt} j e^{-\beta H} e^{iHt}\}. \quad (\text{A2})$$

In Ref. [57], we derived that the interaction-picture counterpart of the purely electronic operator $\iota(t)$ reads

$$\iota^{(I)}(t) = \mathcal{T} e^{-[\Phi_1(t) + \Phi_2(\beta) + \Phi_3(t, \beta)]} j \frac{e^{-\beta H_e}}{Z_e}. \quad (\text{A3})$$

The corresponding influence phases are given as

$$\begin{aligned} \Phi_1(t) &= \sum_{qm} \int_0^t ds_2 \int_0^{s_2} ds_1 V_q^{(I)}(s_2)^\times e^{-\mu_m(s_2 - s_1)} \\ &\quad \times \left[\frac{c_m + c_{\bar{m}}}{2} V_{-q}^{(I)}(s_1)^\times + \frac{c_m - c_{\bar{m}}}{2} V_{-q}^{(I)}(s_1)^\circ \right], \end{aligned} \quad (\text{A4})$$

$$\begin{aligned} \Phi_2(\beta) &= - \sum_{qm} \int_0^\beta d\tau_2 \int_0^{\tau_2} d\tau_1 {}^C \bar{V}_{-q}(\tau_1) \\ &\quad \times e^{i\mu_m(\tau_2 - \tau_1)} c_m {}^C \bar{V}_{-q}(\tau_2), \end{aligned} \quad (\text{A5})$$

$$\begin{aligned} \Phi_3(t, \beta) &= -i \sum_{qm} \int_0^t ds \int_0^\beta d\tau V_q^{(I)}(s)^\times \\ &\quad \times e^{-\mu_m s} e^{i\mu_m(\beta - \tau)} c_m {}^C \bar{V}_{-q}(\tau), \end{aligned} \quad (\text{A6})$$

where the purely electronic operator V_q reads

$$V_q = \sum_k |k+q\rangle \langle k|, \quad (\text{A7})$$

while the coefficients c_m and μ_m ($m = 0, 1$) are

$$c_0 = \left(\frac{g}{\sqrt{N}} \right)^2 (1 + n_{\text{ph}}), \quad \mu_0 = +i\omega_0, \quad n_{\text{ph}} = \frac{1}{e^{\beta\omega_0} - 1}, \quad (\text{A8})$$

$$c_1 = \left(\frac{g}{\sqrt{N}} \right)^2 n_{\text{ph}}, \quad \mu_1 = -i\omega_0. \quad (\text{A9})$$

For later use, we introduce the index \bar{m} defined by $\mu_{\bar{m}} = \mu_m^*$. In other words, $\bar{0} = 1$ and *vice versa*. The hyperoperators entering Eqs. (A4)–(A6) are defined by their action on an arbitrary operator O , which is as follows:

$$V^C O = VO, \quad (\text{A10a})$$

$${}^C V O = OV, \quad (\text{A10b})$$

$$V^\times O = VO - OV, \quad (\text{A10c})$$

$$V^\circ O = VO + OV. \quad (\text{A10d})$$

The operators V_q in the real-time and imaginary-time interaction picture are defined as

$$V_q^{(I)}(t) = e^{iH_e t} V_q e^{-iH_e t}, \quad \bar{V}_q(\tau) = e^{H_e \tau} V_q e^{-H_e \tau}. \quad (\text{A11})$$

The time-ordering sign \mathcal{T} in Eq. (A3) orders the hyperoperators so that one first applies imaginary time-dependent hyperoperators that are mutually antichronologically ordered (descending imaginary-time instants) and subsequently applies real time-dependent hyperoperators that are mutually chronologically ordered (ascending real-time instants). The so-called electronic partition sum entering Eq. (A3) is defined as

$$Z_e = \frac{Z}{Z_{\text{ph}}} = \text{Tr}_{1e} \{ \mathcal{T} e^{-\Phi_2(\beta)} e^{-\beta H_e} \}, \quad (\text{A12})$$

where $Z_{\text{ph}} = \text{Tr}_{\text{ph}} e^{-\beta H_{\text{ph}}}$ is the free-phonon partition sum.

Concerning single-particle quantities, it is convenient to redefine them as follows:

$$\begin{aligned} G^>(k, t) &= \mathcal{G}^>(k, t) e^{-i\mu_{\text{F}} t} \\ &= -i \frac{\text{Tr}_{0e} \{ e^{iH_t} | \text{vac} \rangle \langle k | e^{-iH_t} | k \rangle \langle \text{vac} | e^{-\beta H} \}}{Z_{\text{ph}}} \\ &= -i \frac{\text{Tr}_{\text{ph}} \{ e^{iH_{\text{ph}} t} \langle k | e^{-iH_t} | k \rangle e^{-\beta H_{\text{ph}}} \}}{Z_{\text{ph}}} \\ &= -i e^{-i\varepsilon_k t} \langle k | \mathcal{T} e^{-\varphi_1(t)} \mathbb{1}_e | k \rangle, \end{aligned} \quad (\text{A13})$$

$$\begin{aligned} G^<(k, t) &= \frac{\mathcal{G}^<(k, t) e^{-i\mu_{\text{F}} t}}{\langle N_e \rangle_K} \\ &= i \frac{\text{Tr}_{1e} \{ |k\rangle \langle \text{vac} | e^{iH_t} | \text{vac} \rangle \langle k | e^{-iH_t} e^{-\beta H} \}}{Z} \\ &= i \frac{\text{Tr}_{\text{ph}} \{ e^{iH_{\text{ph}} t} \langle k | e^{-iH_t} e^{-\beta H} | k \rangle \}}{Z} \\ &= i e^{-i\varepsilon_k t} \langle k | \mathcal{T} e^{-[\varphi_1(t) + \varphi_2(\beta) + \varphi_3(t, \beta)]} \frac{e^{-\beta H_e}}{Z_e} | k \rangle. \end{aligned} \quad (\text{A14})$$

The redefinition embodied in the first equalities of Eqs. (A13) and (A14) is fully compatible with the frequency shift used to transform Eqs. (18) and (19) into Eqs. (20) and (21), respectively. It also introduces a different normalization for $G^<$, $-i \sum_k G^<(k, t=0) = 1$, which explicitly shows that we consider a single electron, while the current-current correlation function in the bubble approximation is expressed as [cf. Eq. (17)]

$$C_{jj}^{\text{bbl}}(t) = - \sum_k j_k^2 G^>(k, t) G^<(k, t)^*. \quad (\text{A15})$$

In Ref. [56], we derived that the influence phases for single-particle quantities read

$$\varphi_1(t) = \sum_{qm} \int_0^t ds_2 \int_0^{s_2} ds_1 V_q^{(I)}(s_2) {}^C e^{-\mu_m(s_2 - s_1)} c_m V_{-q}^{(I)}(s_1) {}^C, \quad (\text{A16})$$

$$\varphi_2(\beta) = \Phi_2(\beta), \quad (\text{A17})$$

$$\begin{aligned} \varphi_3(t, \beta) &= -i \sum_{qm} \int_0^t ds \int_0^\beta d\tau V_q^{(I)}(s) {}^C \\ &\quad \times e^{-\mu_m s} e^{i\mu_m(\beta - \tau)} c_m {}^C \bar{V}_{-q}(\tau). \end{aligned} \quad (\text{A18})$$

As the first illustration of the utility of these formally exact results, we prove the equality $C_{jj}(t=0) = C_{jj}^{\text{bbl}}(t=0)$. Because of $\Phi_1(t=0) = \Phi_3(t=0, \beta) = 0$, see Eqs. (A4) and (A6), Eqs. (A1) and (A3) imply that

$$\begin{aligned} C_{jj}(t=0) &= \sum_k j_k \langle k | \mathcal{T} e^{-\Phi_2(\beta)} j \frac{e^{-\beta H_e}}{Z_e} | k \rangle \\ &= \sum_k j_k \langle k | j \mathcal{T} e^{-\Phi_2(\beta)} \frac{e^{-\beta H_e}}{Z_e} | k \rangle \\ &= \sum_k j_k^2 \langle k | \mathcal{T} e^{-\Phi_2(\beta)} \frac{e^{-\beta H_e}}{Z_e} | k \rangle. \end{aligned} \quad (\text{A19})$$

Since the hyperoperators in $\Phi_2(\beta)$ act on the operator $j e^{-\beta H_c} / Z_e$ from the right-hand side, see Eq. (A5), the current operator can be moved in front of $\mathcal{T} e^{-\Phi_2(\beta)}$. Because of $\varphi_1(t=0) = \varphi_3(t=0, \beta) = 0$ [see Eqs. (A16) and (A18)], Eqs. (A15), (A13), and (A14) imply that

$$C_{jj}^{\text{bbl}}(t=0) = \sum_k j_k^2 \langle k | \mathcal{T} e^{-\varphi_2(\beta)} \frac{e^{-\beta H_c}}{Z_e} | k \rangle. \quad (\text{A20})$$

The right-hand sides of Eqs. (A19) and (A20) are identical because of Eq. (A17).

APPENDIX B: EVALUATION OF $C_{jj}(t)$ AND $C_{jj}^{\text{bbl}}(t)$ IN THE $g \rightarrow 0$ LIMIT

1. Equality of the lowest-order terms

Let us start from the lowest-order term in the bubble result [Eq. (A15)], which we derive by separately considering $G^>(k, t)$ [Eq. (A13)] and $G^<(k, t)$ [Eq. (A14)] in the lowest-order approximation. Up to the second order in g , we have

$$[G^>(k, t)]_2 = -i e^{-i\epsilon_k t} [1 - \langle k | \varphi_1(t) \mathbb{1}_e | k \rangle], \quad (\text{B1})$$

$$\begin{aligned} [G^<(k, t)]_2 &= i e^{-i\epsilon_k t} \frac{e^{-\beta \epsilon_k}}{Z_e} [1 - \langle k | \varphi_1(t) \mathbb{1}_e | k \rangle \\ &\quad - \langle k | \varphi_2(\beta) \mathbb{1}_e | k \rangle - \langle k | \varphi_3(t, \beta) e^{-\beta(H_c - \epsilon_k)} | k \rangle], \end{aligned} \quad (\text{B2})$$

where we have used the relation

$$\langle k | \varphi_2(\beta) e^{-\beta(H_c - \epsilon_k)} | k \rangle = \langle k | \varphi_2(\beta) \mathbb{1}_e | k \rangle \quad (\text{B3})$$

and a similar relation for $\langle k | \varphi_1(t) e^{-\beta(H_c - \epsilon_k)} | k \rangle$. The time-ordering sign can be safely omitted because the hyperoperators entering Eqs. (B1) and (B2) are already properly ordered. Therefore, up to the second order in g , the current-current correlation function in the bubble approximation reads

$$\begin{aligned} [C_{jj}^{\text{bbl}}(t)]_2 &= \sum_k j_k^2 \frac{e^{-\beta \epsilon_k}}{Z_e} [1 - \langle k | \varphi_2(\beta) \mathbb{1}_e | k \rangle \\ &\quad - 2 \text{Re} \langle k | \varphi_1(t) \mathbb{1}_e | k \rangle \\ &\quad - \langle k | \varphi_3(t, \beta) e^{-\beta(H_c - \epsilon_k)} | k \rangle^*], \end{aligned} \quad (\text{B4})$$

where we have observed that the matrix element $\langle k | \varphi_2(\beta) \mathbb{1}_e | k \rangle$ is purely real.

We proceed to find the expression for the full current-current correlation function [Eq. (A1)] up to the second order in g . Because of Eqs. (A17) and (B3), together with $[j, H_c] = 0$, we can start from

$$\begin{aligned} [C_{jj}(t)]_2 &= \sum_k j_k^2 \frac{e^{-\beta H_c}}{Z_e} [1 - \langle k | \varphi_2(\beta) \mathbb{1}_e | k \rangle \\ &\quad - \langle k | \Phi_1(t) j_k^{-1} j e^{-\beta(H_c - \epsilon_k)} | k \rangle \\ &\quad - \langle k | \Phi_3(t, \beta) j_k^{-1} j e^{-\beta(H_c - \epsilon_k)} | k \rangle]. \end{aligned} \quad (\text{B5})$$

In the following two paragraphs, we demonstrate that

$$\begin{aligned} \Delta_1(k, t) &= \langle k | \Phi_1(t) j_k^{-1} j e^{-\beta(H_c - \epsilon_k)} | k \rangle - 2 \text{Re} \langle k | \varphi_1(t) \mathbb{1}_e | k \rangle \\ &= 0 \end{aligned} \quad (\text{B6})$$

and

$$\Delta_3(k, t) = \langle k | \Phi_3(t, \beta) j_k^{-1} j e^{-\beta(H_c - \epsilon_k)} | k \rangle - \langle k | \varphi_3(t, \beta) e^{-\beta(H_c - \epsilon_k)} | k \rangle^* = 0. \quad (\text{B7})$$

Collectively, Eqs. (B4), (B5), (B6), and (B7) show that, in the lowest order in the electron-phonon coupling g , the expressions for the full and bubble current-current correlation function coincide. Since these terms are the most important ones in the limit $g \rightarrow 0$, we can conclude that there are no vertex corrections in the limit of vanishing g .

We first prove that $\Delta_1(k, t) = 0$. We start from

$$\begin{aligned} \langle k | \Phi_1(t) j_k^{-1} j e^{-\beta(H_c - \epsilon_k)} | k \rangle &= \sum_{qm} \int_0^t ds_2 \int_0^{s_2} ds_1 e^{-\mu_m(s_2 - s_1)} [c_m \langle k | V_q^{(I)}(s_2) V_{-q}^{(I)}(s_1) | k \rangle + c_{\bar{m}} \langle k | V_{-q}^{(I)}(s_1) V_q^{(I)}(s_2) | k \rangle \\ &\quad - c_m \langle k | V_{-q}^{(I)}(s_1) j_k^{-1} j e^{-\beta(H_c - \epsilon_k)} V_q^{(I)}(s_2) | k \rangle - c_{\bar{m}} \langle k | V_q^{(I)}(s_2) j_k^{-1} j e^{-\beta(H_c - \epsilon_k)} V_{-q}^{(I)}(s_1) | k \rangle]. \end{aligned} \quad (\text{B8})$$

Since $V_q^\dagger = V_{-q}$ [see Eq. (A7)], one observes that the first two summands within the square brackets in Eq. (B8) are complex conjugates of one another, and the same applies to the last two summands. On the other hand,

$$\langle k | \varphi_1(t) \mathbb{1}_e | k \rangle = \sum_{qm} \int_0^t ds_2 \int_0^{s_2} ds_1 c_m e^{-\mu_m(s_2 - s_1)} \langle k | V_q^{(I)}(s_2) V_{-q}^{(I)}(s_1) | k \rangle, \quad (\text{B9})$$

so that the following equation holds:

$$\begin{aligned} \Delta_1(k, t) &= \langle k | \Phi_1(t) j_k^{-1} j e^{-\beta(H_c - \epsilon_k)} | k \rangle - 2 \text{Re} \langle k | \varphi_1(t) \mathbb{1}_e | k \rangle = \\ &= -2 \text{Re} \sum_{qm} \int_0^t ds_2 \int_0^{s_2} ds_1 c_{\bar{m}} e^{-\mu_m(s_2 - s_1)} \langle k | V_q^{(I)}(s_2) j_k^{-1} j e^{-\beta(H_c - \epsilon_k)} V_{-q}^{(I)}(s_1) | k \rangle. \end{aligned} \quad (\text{B10})$$

An explicit calculation of the matrix element in Eq. (B10) gives

$$\Delta_1(k, t) = -2 \operatorname{Re} \sum_{qm} \int_0^t ds_2 \int_0^{s_2} ds_1 c_{\bar{m}} e^{i(\varepsilon_k - \varepsilon_{k-q} + i\mu_m)(s_2 - s_1)} \frac{j_{k-q}}{j_k} e^{-\beta(\varepsilon_{k-q} - \varepsilon_k)}. \quad (\text{B11})$$

The following sum over q should be performed (with $q' = k - q$):

$$\sum_q j_{k-q} e^{-(\beta + it)\varepsilon_{k-q}} = \sum_{q'} j_{q'} e^{-(\beta + it)\varepsilon_{q'}}. \quad (\text{B12})$$

The second sum in Eq. (B12) is equal to zero because $j_{-q} = -j_q$, while $\varepsilon_{-q} = \varepsilon_q$. This proves Eq. (B6).

Let us now prove that $\Delta_3(k, t) = 0$. We start from

$$\begin{aligned} \langle k | \Phi_3(t, \beta) j_k^{-1} j e^{-\beta(H_c - \varepsilon_k)} | k \rangle &= i \sum_{qm} \int_0^t ds \int_0^\beta d\tau c_m e^{-\mu_m s} e^{i\mu_m(\beta - \tau)} \\ &\times [\langle k | \bar{V}_{-q}(\tau) V_q^{(I)}(s) | k \rangle - \langle k | V_q^{(I)}(s) j_k^{-1} j e^{-\beta(H_c - \varepsilon_k)} \bar{V}_{-q}(\tau) | k \rangle]. \end{aligned} \quad (\text{B13})$$

On the other hand, using Eq. (A18), we find that

$$\begin{aligned} \langle k | \varphi_3(t, \beta) e^{-\beta(H_c - \varepsilon_k)} | k \rangle^* &= i \sum_{qm} \int_0^t ds \int_0^\beta d\tau c_m e^{-\mu_m s} e^{-i\mu_m(\beta - \tau)} \langle k | \bar{V}_q(-\tau) e^{-\beta(H_c - \varepsilon_k)} V_{-q}^{(I)}(s) | k \rangle \\ &= i \sum_{qm} \int_0^t ds \int_0^\beta d\tau c_{\bar{m}} e^{-\mu_m s} e^{-i\mu_m(\beta - \tau)} \langle k | \bar{V}_{-q}(\beta - \tau) V_q^{(I)}(s) | k \rangle \\ &= i \sum_{qm} \int_0^t ds \int_0^\beta d\tau c_{\bar{m}} e^{-\mu_m s} e^{-i\mu_m \tau} \langle k | \bar{V}_{-q}(\tau) V_q^{(I)}(s) | k \rangle \\ &= i \sum_{qm} \int_0^t ds \int_0^\beta d\tau c_m e^{-\mu_m s} e^{i\mu_m(\beta - \tau)} \langle k | \bar{V}_{-q}(\tau) V_q^{(I)}(s) | k \rangle. \end{aligned} \quad (\text{B14})$$

Writing the first equality in Eq. (B14), we used $\mu_m^* = \mu_{\bar{m}}$, as well as $\bar{V}_{-q}(\tau) = \bar{V}_q(-\tau)$. In going from the first to the second equality in Eq. (B14), we performed the dummy-index change $q \rightarrow -q$, $m \rightarrow \bar{m}$, and observed that $\bar{V}_{-q}(-\tau) e^{-\beta H_c} = e^{-\beta H_c} \bar{V}_{-q}(\beta - \tau)$. The third equality is obtained from the second by the integral variable change $\beta - \tau \rightarrow \tau$. The last equality in Eq. (B14) follows from the identity $c_{\bar{m}} e^{-i\mu_m \tau} = c_m e^{i\mu_m(\beta - \tau)}$, which can be checked by direct inspection. Equations (B13) and (B14) imply that

$$\begin{aligned} \Delta_3(k, t) &= \langle k | \Phi_3(t, \beta) j_k^{-1} j e^{-\beta(H_c - \varepsilon_k)} | k \rangle - \langle k | \varphi_3(t, \beta) e^{-\beta(H_c - \varepsilon_k)} | k \rangle^* \\ &= -i \sum_{qm} \int_0^t ds \int_0^\beta d\tau c_m e^{-\mu_m s} e^{i\mu_m(\beta - \tau)} \langle k | V_q^{(I)}(s) j_k^{-1} j e^{-\beta(H_c - \varepsilon_k)} \bar{V}_{-q}(\tau) | k \rangle. \end{aligned} \quad (\text{B15})$$

An explicit calculation of the matrix element in Eq. (B15) leads to

$$\Delta_3(k, t) = -i \sum_{qm} \int_0^t ds \int_0^\beta d\tau c_m e^{i(\varepsilon_k - \varepsilon_{k-q} + i\mu_m)s} e^{i\mu_m \beta} e^{(\varepsilon_{k-q} - \varepsilon_k - i\mu_m)\tau} \frac{j_{k-q}}{j_k} e^{-\beta(\varepsilon_{k-q} - \varepsilon_k)}. \quad (\text{B16})$$

The same reasoning as in Eq. (B12) proves that $\Delta_3(k, t) = 0$.

2. Second-order cumulant expansion

Still, Eqs. (B4) or (B5) do not suffice to obtain an expression for $C_{jj}(t)$ in the weak-coupling limit. To that end, the perturbation series for $C_{jj}(t)$ in powers of g has to be (at least partially) resummed. We [17] and other groups [37] have recently promoted the second-order cumulant expansion as a computationally viable and accurate approach to resum the perturbation series for time-dependent quantities in the limit $g \rightarrow 0$. The second-order cumulant expansion starts from Eq. (B4) and produces the following expression for $C_{jj}(t)$:

$$C_{jj}(t) = C_{jj}^{\text{bb1}}(t) \approx \sum_k j_k^2 \frac{e^{-\beta \varepsilon_k}}{Z_e} e^{-\langle k | \varphi_2(\beta) \mathbb{1}_c | k \rangle} e^{-2 \operatorname{Re} \langle k | \varphi_1(t) \mathbb{1}_c | k \rangle - \langle k | \varphi_3(t, \beta) e^{-\beta(H_c - \varepsilon_k)} | k \rangle^*}. \quad (\text{B17})$$

Up to now, we have not discussed the electronic partition sum Z_e , which has its own perturbation expansion in g that up to second order reads

$$Z_e = \sum_k e^{-\beta \varepsilon_k} [1 - \langle k | \varphi_2(\beta) \mathbb{1}_e | k \rangle]. \quad (\text{B18})$$

Performing the second-order cumulant resummation in Eq. (B18), we obtain the following expression for Z_e :

$$Z_e = \sum_k e^{-\beta \varepsilon_k} e^{-\langle k | \varphi_2(\beta) \mathbb{1}_e | k \rangle}. \quad (\text{B19})$$

We note that Eq. (B17) suggests that the unnormalized equilibrium occupation of state $|k\rangle$ is proportional to $e^{-\beta \varepsilon_k} e^{-\langle k | \varphi_2(\beta) \mathbb{1}_e | k \rangle}$, so that Z_e given in Eq. (B19) ensures the correct normalization of equilibrium occupations.

We finally list the explicit expressions for the matrix elements needed to evaluate Eqs. (B17) and (B19):

$$\langle k | \varphi_1(t) \mathbb{1}_e | k \rangle = \frac{g^2}{N} \sum_q \left[(1 + n_{\text{ph}}) \frac{-e^{i\Delta\varepsilon_-(k,q)t} + i\Delta\varepsilon_-(k,q)t + 1}{\Delta\varepsilon_-(k,q)^2} + n_{\text{ph}} \frac{-e^{i\Delta\varepsilon_+(k,q)t} + i\Delta\varepsilon_+(k,q)t + 1}{\Delta\varepsilon_+(k,q)^2} \right], \quad (\text{B20})$$

$$\langle k | \varphi_2(\beta) \mathbb{1}_e | k \rangle = \frac{g^2}{N} \sum_q \left[(1 + n_{\text{ph}}) \frac{-e^{\beta\Delta\varepsilon_-(k,q)} + \beta\Delta\varepsilon_-(k,q) + 1}{\Delta\varepsilon_-(k,q)^2} + n_{\text{ph}} \frac{-e^{\beta\Delta\varepsilon_+(k,q)} + \beta\Delta\varepsilon_+(k,q) + 1}{\Delta\varepsilon_+(k,q)^2} \right], \quad (\text{B21})$$

$$\langle k | \varphi_3(t, \beta) e^{-\beta(H_e - \varepsilon_k)} | k \rangle = \frac{g^2}{N} \sum_q \frac{e^{-\beta\varepsilon_{k-q}}}{e^{-\beta\varepsilon_k}} \left\{ n_{\text{ph}} \frac{[e^{i\Delta\varepsilon_-(k,q)t} - 1][e^{-\beta\Delta\varepsilon_-(k,q)} - 1]}{\Delta\varepsilon_-(k,q)^2} + (1 + n_{\text{ph}}) \frac{[e^{i\Delta\varepsilon_+(k,q)t} - 1][e^{-\beta\Delta\varepsilon_+(k,q)} - 1]}{\Delta\varepsilon_+(k,q)^2} \right\}, \quad (\text{B22})$$

where

$$\Delta\varepsilon_{\pm}(k, q) = \varepsilon_k - \varepsilon_{k-q} \pm \omega_0. \quad (\text{B23})$$

APPENDIX C: EVALUATION OF $C_{jj}(t)$ AND $C_{jj}^{\text{bh}}(t)$ IN THE $t_0 \rightarrow 0$ LIMIT

Here, we rewrite the Holstein Hamiltonian in the site representation and partition it into the zeroth-order term and the perturbation term as appropriate in the limit $t_0 \rightarrow 0$:

$$H = H_0 + H_1, \quad (\text{C1})$$

where (p enumerates lattice sites)

$$H_0 = \omega_0 \sum_p b_p^\dagger b_p + g \sum_p c_p^\dagger c_p (b_p + b_p^\dagger), \quad (\text{C2})$$

while

$$H_1 = -t_0 \sum_p \sum_{\gamma=\pm 1} c_{p+\gamma}^\dagger c_p. \quad (\text{C3})$$

We perform a unitary transformation of the Hamiltonian

$$\tilde{H} = e^S H e^{-S} \quad (\text{C4})$$

with

$$S = -\frac{g}{\omega_0} \sum_p c_p^\dagger c_p (b_p - b_p^\dagger). \quad (\text{C5})$$

The action of the unitary transformation on the electron operators is

$$e^S c_p e^{-S} = c_p X_p, \quad (\text{C6})$$

with

$$X_p = \exp \left[\frac{g}{\omega_0} (b_p - b_p^\dagger) \right], \quad (\text{C7})$$

while its action on the phonon operators is

$$e^S b_p e^{-S} = b_p - \frac{g}{\omega_0} c_p^\dagger c_p. \quad (\text{C8})$$

Limiting the discussion on the Hilbert space of states that contain one electron, the transformed Hamiltonian takes the form $\tilde{H} = \tilde{H}_0 + \tilde{H}_1$, with

$$\tilde{H}_0 = -\frac{g^2}{\omega_0} + \omega_0 \sum_p b_p^\dagger b_p, \quad (\text{C9})$$

$$\tilde{H}_1 = -t_0 \sum_{p\gamma} X_{p+\gamma, p} c_{p+\gamma}^\dagger c_p. \quad (\text{C10})$$

We introduced the notation

$$X_{p+\gamma, p} = X_{p+\gamma}^\dagger X_p = \exp \left[\frac{g}{\omega_0} (b_p - b_p^\dagger - b_{p+\gamma} + b_{p+\gamma}^\dagger) \right]. \quad (\text{C11})$$

The transformed current operator reads

$$\tilde{j} = e^S j e^{-S} = -it_0 \sum_{p\gamma} \gamma c_{p+\gamma}^\dagger c_p X_{p+\gamma, p}. \quad (\text{C12})$$

We denote by z the (real or imaginary) time (where $z = t$ for real time and $z = -i\tau$ for imaginary time). We make use of the identity

$$\langle j(z) j(0) \rangle_K = \langle \tilde{j}(z) \tilde{j}(0) \rangle_{\tilde{K}} \quad (\text{C13})$$

and we use Eq. (C12) to obtain

$$C_{jj}(z) = -\frac{1}{\langle N_e \rangle_{\tilde{K}}} t_0^2 \sum_{\gamma, \delta=\pm 1} \gamma \delta \langle c_p^\dagger(z) c_{p+\gamma}(z) \times X_{p, p+\gamma}(z) c_s^\dagger(0) c_{s+\delta}(0) X_{s, s+\delta}(0) \rangle_{\tilde{K}}. \quad (\text{C14})$$

All the averages and time evolutions in Eq. (C14) should in principle be taken with respect to the operator \tilde{K} . We are,

however, interested in the limit of small t_0 , and we would like to obtain the first nonzero term with respect to t_0 . We note that the factor in front of the sum gives us the $\sim t_0^2$ term. The expansion of the time evolution operator for real z (the situation is similar in other cases) is of the form

$$\begin{aligned} e^{-i\tilde{K}z} &= e^{-i\tilde{K}_0 z} T \exp \left[-i \int_0^z ds e^{i\tilde{K}_0 s} \tilde{H}_1 e^{-i\tilde{K}_0 s} \right] \\ &= e^{-i\tilde{K}_0 z} [1 + O(t_0)], \end{aligned} \quad (\text{C15})$$

that is, its first nonzero term is of order ~ 1 and the remaining terms are of order $\sim t_0$ and smaller. The same is true for the $e^{-\beta\tilde{K}}$ operator. Therefore, to obtain the first nonzero term in Eq. (C14), it is sufficient to take the terms of order ~ 1 in the expansion of all operators $e^{\pm i\tilde{K}z}$ and $e^{-\beta\tilde{K}}$. This is equivalent to replacing the \tilde{K} operator with the \tilde{K}_0 operator. All the averages in Eq. (C14) can then be obtained by applying Wick's theorem. We thus obtain

$$\begin{aligned} &\langle c_p^\dagger(z) c_{p+\gamma}(z) X_{p,p+\gamma}(z) c_s^\dagger(0) c_{s+\delta}(0) X_{s,s+\delta}(0) \rangle_{\tilde{K}} \\ &\approx \langle c_p^\dagger(z) c_{p+\gamma}(z) X_{p,p+\gamma}(z) c_s^\dagger(0) c_{s+\delta}(0) X_{s,s+\delta}(0) \rangle_{\tilde{K}_0} \\ &= \langle c_p^\dagger(z) c_{p+\gamma}(z) c_s^\dagger(0) c_{s+\delta}(0) \rangle_{\tilde{K}_0} \langle X_{p,p+\gamma}(z) X_{s,s+\delta}(0) \rangle_{\tilde{K}_0}. \end{aligned} \quad (\text{C16})$$

By applying Wick's theorem to the term with electronic operators, we obtain

$$\begin{aligned} &\langle c_p^\dagger(z) c_{p+\gamma}(z) c_s^\dagger(0) c_{s+\delta}(0) \rangle_{\tilde{K}_0} \\ &= \langle c_p^\dagger(z) c_{s+\delta}(0) \rangle_{\tilde{K}_0} \langle c_{p+\gamma}(z) c_s^\dagger(0) \rangle_{\tilde{K}_0} \\ &\quad + \langle c_p^\dagger(z) c_{p+\gamma}(z) \rangle_{\tilde{K}_0} \langle c_s^\dagger(0) c_{s+\delta}(0) \rangle_{\tilde{K}_0} \\ &\approx \delta_{p,s+\delta} \delta_{s,p+\gamma} \langle c_p^\dagger(z) c_p(0) \rangle_{\tilde{K}_0} \langle c_{p+\gamma}(z) c_{p+\gamma}^\dagger(0) \rangle_{\tilde{K}_0}. \end{aligned} \quad (\text{C17})$$

The first term on the right-hand side of the first equality is proportional to the number of carriers, while the second term is proportional to the square of the number of carriers. Hence, in the limit of small carrier concentration, it is the first term that dominates. Eventually,

$$\begin{aligned} C_{jj}(z) &= \frac{1}{\langle N_e \rangle_{\tilde{K}_0}} t_0^2 \sum_{p\gamma} \langle c_p^\dagger(z) c_p(0) \rangle_{\tilde{K}_0} \langle c_{p+\gamma}(z) c_{p+\gamma}^\dagger(0) \rangle_{\tilde{K}_0} \\ &\quad \times \langle X_{p,p+\gamma}(z) X_{p+\gamma,p}(0) \rangle_{\tilde{K}_0}. \end{aligned} \quad (\text{C18})$$

We now show that the result of Eq. (C18) is recovered in the bubble approximation in which, upon neglecting the term proportional to the square of carrier density, one obtains

$$\begin{aligned} C_{jj}^{\text{bbbl}}(z) &= -\frac{1}{\langle N_e \rangle_{\tilde{K}}} t_0^2 \sum_{ps} \gamma \delta \langle c_p^\dagger(z) c_{s+\delta}(0) \rangle_K \langle c_{p+\gamma}(z) c_s^\dagger(0) \rangle_K \\ &= -\frac{1}{\langle N_e \rangle_{\tilde{K}}} t_0^2 \sum_{ps} \gamma \delta \langle c_p^\dagger(z) c_{s+\delta}(0) X_p^\dagger(z) X_{s+\delta}(0) \rangle_{\tilde{K}} \\ &\quad \times \langle c_{p+\gamma}(z) c_s^\dagger(0) X_{p+\gamma}(z) X_s^\dagger(0) \rangle_{\tilde{K}}. \end{aligned} \quad (\text{C19})$$

Following the same reasoning as above, the leading term in the expansion of $C_{jj}^{\text{bbbl}}(z)$ in powers of $t_0 \rightarrow 0$ is obtained by replacing all averages and time evolutions with respect to \tilde{K} with those with respect to \tilde{K}_0 . Similarly as in Eq. (C17), we

obtain

$$\begin{aligned} C_{jj}^{\text{bbbl}}(z) &= \frac{1}{\langle N_e \rangle_{\tilde{K}_0}} t_0^2 \sum_{p\gamma} \langle c_p^\dagger(z) c_p(0) \rangle_{\tilde{K}_0} \langle c_{p+\gamma}(z) c_{p+\gamma}^\dagger(0) \rangle_{\tilde{K}_0} \\ &\quad \times \langle X_p^\dagger(z) X_p(0) \rangle_{\tilde{K}_0} \langle X_{p+\gamma}(z) X_{p+\gamma}^\dagger(0) \rangle_{\tilde{K}_0}. \end{aligned} \quad (\text{C20})$$

We finally note that

$$\begin{aligned} &\langle X_{p,p+\gamma}(z) X_{p+\gamma,p}(0) \rangle_{\tilde{K}_0} \\ &= \langle X_p^\dagger(z) X_{p+\gamma}(z) X_{p+\gamma}^\dagger(0) X_p(0) \rangle_{\tilde{K}_0} \\ &= \langle X_p^\dagger(z) X_p(0) \rangle_{\tilde{K}_0} \langle X_{p+\gamma}(z) X_{p+\gamma}^\dagger(0) \rangle_{\tilde{K}_0}, \end{aligned} \quad (\text{C21})$$

where the first equality stems from Eq. (C11), while the second equality follows from the fact that phonon operators acting on different sites p and $p+\gamma$ commute. From Eqs. (C18), (C20), and (C21), we conclude that $C_{jj}(z) = C_{jj}^{\text{bbbl}}(z)$ as $t_0 \rightarrow 0$.

In the remainder of this Appendix, we provide explicit expressions for $C_{jj}^{\text{bbbl}}(z)$ to show that the corresponding dc mobility is finite. The phonon term from Eq. (C21) is given as

$$\begin{aligned} \langle X_{p,p+\gamma}(z) X_{p+\gamma,p}(0) \rangle_{\tilde{K}_0} &= \exp \left\{ -2 \frac{g^2}{\omega_0^2} [2n_{\text{ph}} + 1 \right. \\ &\quad \left. - (n_{\text{ph}} + 1) e^{-i\omega_0 z} - n_{\text{ph}} e^{i\omega_0 z}] \right\}. \end{aligned} \quad (\text{C22})$$

In the limit of low carrier density, the electronic term from Eq. (C20) reads

$$\langle c_p^\dagger(z) c_p(0) \rangle_{\tilde{K}_0} \langle c_{p+\gamma}(z) c_{p+\gamma}^\dagger(0) \rangle_{\tilde{K}_0} = n_F, \quad (\text{C23})$$

where n_F is the occupation of single-particle electronic state given by the Fermi-Dirac function. It follows from Eqs. (C20), (C22), and (C23) that $C_{jj}^{\text{bbbl}}(z)$ does not decay to zero as real time goes to infinity. Hence, one would obtain infinite dc mobility by integrating $C_{jj}^{\text{bbbl}}(z)$. To circumvent this issue, we make use again of the fact that the leading term in the limit of small t_0 is approximately the same when all averages and time evolutions are taken either with respect to \tilde{K}_0 or \tilde{K} . Therefore, we now make use of

$$\begin{aligned} \langle c_p^\dagger(z) c_p(0) \rangle_{\tilde{K}_0} &\approx \langle c_p^\dagger(z) c_p(0) \rangle_{\tilde{K}}, \\ \langle c_p(z) c_p^\dagger(0) \rangle_{\tilde{K}_0} &\approx \langle c_p(z) c_p^\dagger(0) \rangle_{\tilde{K}}. \end{aligned} \quad (\text{C24})$$

To evaluate the terms $\langle c_p^\dagger(z) c_p(0) \rangle_{\tilde{K}}$ and $\langle c_p(z) c_p^\dagger(0) \rangle_{\tilde{K}}$ for the Hamiltonian given by Eqs. (C9) and (C10) (where the irrelevant shift $-g^2/\omega_0$ in \tilde{H}_0 is neglected), we make use of the Matsubara Green's function formalism to evaluate the self-energy stemming from the perturbation \tilde{H}_1 to the Hamiltonian \tilde{H}_0 . The overall approach is very similar to that developed in Ref. [33], see in particular its Appendix B. To first order in interaction, we obtain the self-energy

$$\Sigma_{p\pm 1,p}^{(1)}(\omega) = -t_0 e^{-\frac{g^2}{\omega_0^2} (2n_{\text{ph}}+1)}, \quad (\text{C25})$$

which in the momentum representation reads

$$\Sigma_k^{(1)}(\omega) = -2t_{\text{eff}} \cos(k) \quad (\text{C26})$$

with

$$t_{\text{eff}} = t_0 e^{-\frac{g^2}{\omega_0^2}(2n_{\text{ph}}+1)}. \quad (\text{C27})$$

It can be seen from Eq. (C26) that first-order self-energy describes the formation of bands due to renormalized electronic coupling t_{eff} . This term, however, does not have an imaginary part and therefore it does not lead to energy level broadening. Hence it is not expected that it will provide energy dissipation of electronic system, which is a requirement for finite dc mobility to occur. For this reason, we proceed to evaluate the self-energy term arising from second-order terms in interaction. We obtain that the dominant second-order term is the local term

$$\Sigma^{(2)}(\omega) = 2t_0^2 \frac{i}{2\pi} \int_{-\infty}^{+\infty} d\omega_1 X^>(\omega_1) G^R(\omega - \omega_1), \quad (\text{C28})$$

where G^R is the retarded Green's function, and $X^>(\omega) = \int dt e^{i\omega t} X^>(t)$ with

$$X^>(t) = -i \exp \left\{ -2 \frac{g^2}{\omega_0^2} [2n_{\text{ph}} + 1 - (n_{\text{ph}} + 1)e^{-i\omega_0 t}] - n_{\text{ph}} e^{i\omega_0 t} \right\}. \quad (\text{C29})$$

We can further transform Eq. (C28) into the form (we now omit superscripts R , 2 for brevity)

$$\Sigma(\omega) = 2t_0^2 \frac{i}{2\pi} \int_{-\infty}^{+\infty} d\omega_1 X^>(\omega_1) G(\omega - \omega_1) \quad (\text{C30})$$

that is amenable to the self-consistent treatment in conjunction with the Dyson equation

$$[\omega - \Sigma(\omega)]G(\omega) = 1. \quad (\text{C31})$$

Making use of the identities

$$e^{a \cos \theta} = \sum_{l=-\infty}^{+\infty} I_l(a) e^{il\theta}, \quad (\text{C32})$$

where I_l is the modified Bessel function of the first kind of order l and

$$\begin{aligned} & (n_{\text{ph}} + 1)e^{-i\omega_0 t} + n_{\text{ph}} e^{i\omega_0 t} \\ &= 2\sqrt{n_{\text{ph}}(n_{\text{ph}} + 1)} \cos \left[\omega_0 \left(t + i\frac{\beta}{2} \right) \right], \end{aligned} \quad (\text{C33})$$

we recast Eq. (C30) as

$$\Sigma(\omega) = \sum_{l=-\infty}^{+\infty} c_l G(\omega + l\omega_0), \quad (\text{C34})$$

with c_l given by

$$c_l = 2t_0^2 e^{-2\frac{g^2}{\omega_0^2}(2n_{\text{ph}}+1)} e^{-l\frac{\beta\omega_0}{2}} I_l \left[4\frac{g^2}{\omega_0^2} \sqrt{n_{\text{ph}}(n_{\text{ph}} + 1)} \right]. \quad (\text{C35})$$

Equations (C31) and (C34) can be solved using a self-consistent procedure. Alternatively, these equations can be solved analytically by introducing an additional approximation that the dominant term in the sum in Eq. (C34) is the $l = 0$ term. This is a reasonable assumption as one might expect that both $G(\omega)$ and $\Sigma(\omega)$ should have maximal values in the

region around $\omega = 0$. This assumption can always be checked by comparing the result with the self-consistent solution of Eqs. (C31) and (C34). Under this assumption, Eqs. (C31) and (C34) reduce to a single quadratic equation for $G(\omega)$ and we obtain the corresponding spectral function as

$$A(\omega) = -\frac{1}{\pi} \text{Im}G(\omega) = \frac{\sqrt{4c_0 - \omega^2}}{2\pi c_0} \theta(4c_0 - \omega^2). \quad (\text{C36})$$

From the relation between the spectral function and the correlation functions of creation and annihilation operators, we obtain

$$\begin{aligned} & \frac{1}{\langle N_e \rangle_{\tilde{K}}} \langle c_p^\dagger(z) c_p(0) \rangle_{\tilde{K}} \langle c_{p+\gamma}(z) c_{p+\gamma}^\dagger(0) \rangle_{\tilde{K}} \\ &= \frac{\int d\omega e^{-\beta(\omega-iz)} A(\omega)}{\int d\omega e^{-\beta\omega} A(\omega)} \int d\omega e^{-i\omega z} A(\omega). \end{aligned} \quad (\text{C37})$$

The integrals in the previous equation are all of the form

$$f(z) = \frac{2}{\pi a^2} \int_{-a}^a d\omega e^{-z\omega} \sqrt{a^2 - \omega^2} = -\frac{2}{az} I_1(-az), \quad (\text{C38})$$

with $a = 2\sqrt{c_0}$. The integral is solved by introducing the substitution $\omega = a \cos t$, by making use of $I_n(u) = \frac{1}{\pi} \int_0^\pi d\theta e^{u \cos \theta} \cos(n\theta)$, and by using the identity $I_\nu(z) - I_{\nu+2}(z) = 2\frac{\nu+1}{z} I_{\nu+1}(z)$. Combining Eqs. (C18), (C24), (C22), (C36), and (C37), we finally obtain the expression given in Eq. (25), where J_n denotes the Bessel function of the first kind of order n .

It is worth investigating the asymptotic behavior of the prefactor in front of the exponential term in Eq. (25) when real time t tends to infinity $z = t \rightarrow +\infty$. The time dependence of this prefactor is determined by the term

$$g(t) = \frac{I_1[-2(\beta - it)\sqrt{c_0}] J_1(2t\sqrt{c_0})}{t(\beta - it)}. \quad (\text{C39})$$

As $t \rightarrow +\infty$, making use of $J_1(x) = -iI_1(-ix)$, we have

$$g(t) \sim \frac{J_1(-2t\sqrt{c_0}) J_1(2t\sqrt{c_0})}{t^2}. \quad (\text{C40})$$

The asymptotic behavior of the Bessel function when $x \rightarrow +\infty$ is

$$J_1(x) \sim \sqrt{\frac{2}{\pi x}} \cos \left(x - \frac{3\pi}{4} \right). \quad (\text{C41})$$

Consequently, $g(t) \sim t^{-3}$ as $t \rightarrow +\infty$. This is sufficiently fast convergence to make the time integral of the $C_{jj}(t)$ finite, which then leads to finite dc mobility.

APPENDIX D: EVALUATION OF $C_{jj}(t)$ AND $C_{jj}^{\text{bb}}(t)$ IN THE $\beta \rightarrow 0$ LIMIT

To prove that there are no vertex corrections in the infinite-temperature limit, it is instrumental to first analyze in more detail the single-site limit of the Holstein Hamiltonian in which phonons can be treated as classical harmonic oscillators. The appropriate Hamiltonian reads (the oscillator mass

is set to unity)

$$h = \underbrace{\frac{p^2}{2} + \frac{\omega_0^2}{2}x^2}_{h_{\text{ph}}(x,p)} + Cxc^\dagger c, \quad (\text{D1})$$

where x and p are, respectively, the classical coordinate and momentum of the oscillator, while $C = g\sqrt{2\omega_0}$. The greater Green's function can be expressed as [see also Eq. (A13)]

$$\begin{aligned} \mathcal{G}^>(t) &= -ie^{i\mu_F t} \frac{\int dx dp e^{-\beta h_{\text{ph}}(x,p)} e^{-iCxt}}{\int dx dp e^{-\beta h_{\text{ph}}(x,p)}} \\ &= -ie^{i\mu_F t} \frac{\int dx e^{-\beta \frac{\omega_0^2 x^2}{2} - iCxt}}{\int dx e^{-\beta \frac{\omega_0^2 x^2}{2}}} = -ie^{i\mu_F t} e^{-\frac{\sigma^2 t^2}{2}}. \end{aligned} \quad (\text{D2})$$

In the same vein, the lesser Green's function can be expressed as [see also Eq. (A14)]

$$\begin{aligned} \mathcal{G}^<(t) &= ie^{i\mu_F t} e^{\beta\mu_F} \frac{\int dx dp e^{-\beta h_{\text{ph}}} e^{-\beta Cx} e^{-iCxt}}{\int dx dp e^{-\beta h_{\text{ph}}}} \\ &= ie^{i\mu_F t} e^{\beta\mu_F} \frac{\int dx e^{-\beta \frac{\omega_0^2 x^2}{2} - \beta Cx} e^{-iCxt}}{\int dx e^{-\beta \frac{\omega_0^2 x^2}{2}}} \\ &= ie^{i\mu_F t} e^{\beta\mu_F} e^{\frac{\sigma^2}{2}(\beta+i)^2}. \end{aligned} \quad (\text{D3})$$

The electron number is

$$\langle c^\dagger c \rangle_K = e^{\beta\mu_F} e^{\frac{\sigma^2 \beta^2}{2}}. \quad (\text{D4})$$

Let us now consider an N -site chain and start from Eq. (17) determining $C_{jj}^{\text{dbl}}(t)$. Because of the locality of single-particle correlation functions at high temperatures, we can replace $\mathcal{G}^>(k, t)$ and $\mathcal{G}^<(k, t)$ by the single-site expressions derived in Eqs. (D2) and (D3), respectively. The remaining sum in the numerator of Eq. (17) is readily evaluated using Eq. (6), $\sum_k j_k^2 = 2t_0^2 N$. The total electron number $\langle N_e \rangle_K$ is N times the electron number per site, which is derived in Eq. (D4). Collecting all pieces together, we obtain the result embodied in Eq. (26).

We continue by applying the same approximations to Eq. (10) defining $C_{jj}(t)$. Because of the assumed locality and classicality of phonons, we can approximate the Hamiltonian [Eq. (1)] as

$$H \approx \underbrace{\sum_r \left(\frac{p_r^2}{2} + \frac{\omega_0^2}{2} x_r^2 \right)}_{H_{\text{ph}}(\mathbf{x}, \mathbf{p})} + C \sum_r x_r c_r^\dagger c_r, \quad (\text{D5})$$

where \mathbf{x} and \mathbf{p} , respectively, denote (classical) coordinates and momenta of oscillators. Since the traces in Eq. (10) are to be evaluated over the single-electron subspace, we can replace $c_r^\dagger c_r \rightarrow |r\rangle\langle r|$, so that

$$e^{-\alpha H} \approx e^{-\alpha H_{\text{ph}}(\mathbf{x}, \mathbf{p})} \sum_r e^{-\alpha C x_r} |r\rangle\langle r|. \quad (\text{D6})$$

Inserting Eq. (D6) (with $\alpha = \beta, \pm it$) into Eq. (10), one obtains

$$C_{jj}(t) = \frac{\int d\mathbf{x} d\mathbf{p} e^{-\beta H_{\text{ph}}(\mathbf{x}, \mathbf{p})} \sum_{r_1 r} |\langle r_1 | j | r \rangle|^2 e^{-it C x_{r_1}} e^{-(\beta-it) C x_r}}{\int d\mathbf{x} d\mathbf{p} \sum_r e^{-\beta H_{\text{ph}}(\mathbf{x}, \mathbf{p})} e^{-\beta C x_r}}. \quad (\text{D7})$$

Because the current operator in the real-space representation is $j = -it_0 \sum_{r\gamma} |r+\gamma\rangle\langle r|$, we have $r_1 = r + \gamma$, where $\gamma = \pm 1$, and Eq. (D7) is recast as

$$C_{jj}(t) = \frac{t_0^2 \sum_r \sum_{\gamma=\pm 1} \left[\int dx_r e^{-\beta \frac{\omega_0^2 x_r^2}{2}} e^{-(\beta-it) C x_r} \right] \left[\int dx_{r+\gamma} e^{-\beta \frac{\omega_0^2 x_{r+\gamma}^2}{2}} e^{-it C x_{r+\gamma}} \right] \prod_{s \notin \{r, r+\gamma\}} \int dx_s e^{-\beta \frac{\omega_0^2 x_s^2}{2}}}{\sum_r \left[\int dx_r e^{-\beta \frac{\omega_0^2 x_r^2}{2}} e^{-\beta C x_r} \right] \prod_{s \neq r} \int dx_s e^{-\beta \frac{\omega_0^2 x_s^2}{2}}}. \quad (\text{D8})$$

The integrals in the numerator have been evaluated in the single-site limit; see Eqs. (D2) and (D3). Upon inserting the corresponding results in Eq. (D8), and performing the remaining sums (which produce the factor of $2N$ in the numerator and N in the denominator), one immediately obtains Eq. (26).

- [1] F. Rossi, *Theory of Semiconductor Quantum Devices: Microscopic Modeling and Simulation Strategies* (Springer-Verlag, Berlin, 2011).
- [2] C. Jacoboni, *Theory of Electron Transport in Semiconductors: A Pathway from Elementary Physics to Nonequilibrium Green Functions* (Springer-Verlag, Berlin, 2010).
- [3] C. Franchini, M. Reticcioli, M. Setvin, and U. Diebold, Polarons in materials, *Nat. Rev. Mater.* **6**, 560 (2021).
- [4] L. R. V. Buizza and L. M. Herz, Polarons and charge localization in metal-halide semiconductors for photovoltaic and light-emitting devices, *Adv. Mater.* **33**, 2007057 (2021).
- [5] R. Ulbricht, E. Hendry, J. Shan, T. F. Heinz, and M. Bonn, Carrier dynamics in semiconductors studied with time-

- resolved terahertz spectroscopy, *Rev. Mod. Phys.* **83**, 543 (2011).
- [6] N. Vukmirović, C. S. Ponseca, Jr., H. Němec, A. Yartsev, and V. Sundström, Insights into the charge carrier terahertz mobility in polyfluorenes from large-scale atomistic simulations and time-resolved terahertz spectroscopy, *J. Phys. Chem. C* **116**, 19665 (2012).
- [7] P. Kužel and H. Němec, Terahertz spectroscopy of nanomaterials: A close look at charge-carrier transport, *Adv. Opt. Mater.* **8**, 1900623 (2020).
- [8] R. Kubo, M. Toda, and N. Hashitsume, *Statistical Physics II: Nonequilibrium Statistical Mechanics* (Springer-Verlag, Berlin, 1985).

- [9] S. Poncé, W. Li, S. Reichardt, and F. Giustino, First-principles calculations of charge carrier mobility and conductivity in bulk semiconductors and two-dimensional materials, *Rep. Prog. Phys.* **83**, 036501 (2020).
- [10] G. Mahan, *Many-Particle Physics* (Kluwer Academic, New York, 2000).
- [11] J.-J. Zhou and M. Bernardi, Predicting charge transport in the presence of polarons: The beyond-quasiparticle regime in SrTiO₃, *Phys. Rev. Res.* **1**, 033138 (2019).
- [12] B. K. Chang, J.-J. Zhou, N.-E. Lee, and M. Bernardi, Intermediate polaronic charge transport in organic crystals from a many-body first-principles approach, *npj Comput. Mater.* **8**, 63 (2022).
- [13] S. Fratini, F. de Pasquale, and S. Ciuchi, Optical absorption from a nondegenerate polaron gas, *Phys. Rev. B* **63**, 153101 (2001).
- [14] S. Fratini and S. Ciuchi, Dynamical mean-field theory of transport of small polarons, *Phys. Rev. Lett.* **91**, 256403 (2003).
- [15] S. Fratini and S. Ciuchi, Optical properties of small polarons from dynamical mean-field theory, *Phys. Rev. B* **74**, 075101 (2006).
- [16] S. Fratini and S. Ciuchi, Bandlike motion and mobility saturation in organic molecular semiconductors, *Phys. Rev. Lett.* **103**, 266601 (2009).
- [17] P. Mitrić, V. Janković, N. Vukmirović, and D. Tanasković, Cumulant expansion in the Holstein model: Spectral functions and mobility, *Phys. Rev. B* **107**, 125165 (2023).
- [18] H. Bruus and K. Flensberg, *Many-Body Quantum Theory in Condensed Matter Physics: An Introduction* (Oxford University Press, New York, 2004).
- [19] J. Rammer, *Quantum Transport Theory* (Perseus Books, Reading, Massachusetts, 1998).
- [20] L. P. Gor'kov, A. I. Larkin, and D. E. Khmel'nitskii, Particle conductivity in a two-dimensional random potential, *JETP Lett.* **30**, 228 (1979).
- [21] K. Baumann and J. Ranninger, Quantum theory of transport coefficients. i, *Ann. Phys.* **20**, 157 (1962).
- [22] T. Holstein, Theory of transport phenomena in an electron-phonon gas, *Ann. Phys.* **29**, 410 (1964).
- [23] G. Eliashberg, Transport equation for a degenerate system of Fermi particles, *Sov. Phys. JETP* **14**, 886 (1962).
- [24] D. C. Langreth and L. P. Kadanoff, Perturbation theoretic calculation of polaron mobility, *Phys. Rev.* **133**, A1070 (1964).
- [25] G. D. Mahan, Mobility of polarons, *Phys. Rev.* **142**, 366 (1966).
- [26] Y.-C. Cheng and R. J. Silbey, A unified theory for charge-carrier transport in organic crystals, *J. Chem. Phys.* **128**, 114713 (2008).
- [27] F. Ortman, F. Bechstedt, and K. Hannewald, Theory of charge transport in organic crystals: Beyond Holstein's small-polaron model, *Phys. Rev. B* **79**, 235206 (2009).
- [28] O. S. Barišić, Calculation of excited polaron states in the Holstein model, *Phys. Rev. B* **69**, 064302 (2004).
- [29] G. L. Goodvin, A. S. Mishchenko, and M. Berciu, Optical conductivity of the Holstein polaron, *Phys. Rev. Lett.* **107**, 076403 (2011).
- [30] N. Prodanović, N. Vukmirović, Z. Ikonjić, P. Harrison, and D. Indjin, Importance of polaronic effects for charge transport in CdSe quantum dot solids, *J. Phys. Chem. Lett.* **5**, 1335 (2014).
- [31] L. Song and Q. Shi, A new approach to calculate charge carrier transport mobility in organic molecular crystals from imaginary time path integral simulations, *J. Chem. Phys.* **142**, 174103 (2015).
- [32] M. Kornjača and N. Vukmirović, Polaron mobility obtained by a variational approach for lattice Fröhlich models, *Ann. Phys.* **391**, 183 (2018).
- [33] N. Prodanović and N. Vukmirović, Charge carrier mobility in systems with local electron-phonon interaction, *Phys. Rev. B* **99**, 104304 (2019).
- [34] J. H. Fetherolf, D. Golež, and T. C. Berkelbach, A unification of the Holstein polaron and dynamic disorder pictures of charge transport in organic crystals, *Phys. Rev. X* **10**, 021062 (2020).
- [35] S. Ciuchi, F. de Pasquale, S. Fratini, and D. Feinberg, Dynamical mean-field theory of the small polaron, *Phys. Rev. B* **56**, 4494 (1997).
- [36] M. Berciu, Green's function of a dressed particle, *Phys. Rev. Lett.* **97**, 036402 (2006).
- [37] P. J. Robinson, I. S. Dunn, and D. R. Reichman, Cumulant methods for electron-phonon problems. I. Perturbative expansions, *Phys. Rev. B* **105**, 224304 (2022).
- [38] P. J. Robinson, I. S. Dunn, and D. R. Reichman, Cumulant methods for electron-phonon problems. II. The self-consistent cumulant expansion, *Phys. Rev. B* **105**, 224305 (2022).
- [39] P. Mitrić, V. Janković, N. Vukmirović, and D. Tanasković, Spectral functions of the Holstein polaron: Exact and approximate solutions, *Phys. Rev. Lett.* **129**, 096401 (2022).
- [40] G. De Filippis, V. Cataudella, A. S. Mishchenko, N. Nagaosa, A. Fierro, and A. de Candia, Crossover from super- to sub-diffusive motion and memory effects in crystalline organic semiconductors, *Phys. Rev. Lett.* **114**, 086601 (2015).
- [41] A. S. Mishchenko, N. Nagaosa, G. De Filippis, A. de Candia, and V. Cataudella, Mobility of Holstein polaron at finite temperature: An unbiased approach, *Phys. Rev. Lett.* **114**, 146401 (2015).
- [42] A. S. Mishchenko, L. Pollet, N. V. Prokof'ev, A. Kumar, D. L. Maslov, and N. Nagaosa, Polaron mobility in the "beyond quasiparticles" regime, *Phys. Rev. Lett.* **123**, 076601 (2019).
- [43] Y.-C. Wang and Y. Zhao, Diagrammatic quantum Monte Carlo toward the calculation of transport properties in disordered semiconductors, *J. Chem. Phys.* **156**, 204116 (2022).
- [44] G. Baym and N. D. Mermin, Determination of thermodynamic green's functions, *J. Math. Phys.* **2**, 232 (1961).
- [45] H. J. Vidberg and J. W. Serene, Solving the Eliashberg equations by means of n -point Padé approximants, *J. Low Temp. Phys.* **29**, 179 (1977).
- [46] C. E. Creffield, E. G. Klepfish, E. R. Pike, and S. Sarkar, Spectral weight function for the half-filled Hubbard model: A singular value decomposition approach, *Phys. Rev. Lett.* **75**, 517 (1995).
- [47] M. Jarrell and J. Gubernatis, Bayesian inference and the analytic continuation of imaginary-time quantum Monte Carlo data, *Phys. Rep.* **269**, 133 (1996).
- [48] O. Gunnarsson, M. W. Haverkort, and G. Sangiovanni, Analytical continuation of imaginary axis data for optical conductivity, *Phys. Rev. B* **82**, 165125 (2010).
- [49] J. Vučićević, J. Kokalj, R. Žitko, N. Wentzell, D. Tanasković, and J. Mravlje, Conductivity in the square lattice Hubbard model at high temperatures: Importance of vertex corrections, *Phys. Rev. Lett.* **123**, 036601 (2019).

- [50] J. Bonča, S. A. Trugman, and M. Berciu, Spectral function of the Holstein polaron at finite temperature, *Phys. Rev. B* **100**, 094307 (2019).
- [51] J. Bonča and S. A. Trugman, Dynamic properties of a polaron coupled to dispersive optical phonons, *Phys. Rev. B* **103**, 054304 (2021).
- [52] J. Bonča and S. A. Trugman, Electron removal spectral function of a polaron coupled to dispersive optical phonons, *Phys. Rev. B* **106**, 174303 (2022).
- [53] S. Miladić and N. Vukmirović, Method for obtaining polaron mobility using real and imaginary time path-integral quantum Monte Carlo, *Phys. Rev. B* **107**, 184315 (2023).
- [54] C. Zhang, E. Jeckelmann, and S. R. White, Dynamical properties of the one-dimensional Holstein model, *Phys. Rev. B* **60**, 14092 (1999).
- [55] D. Jansen, J. Bonča, and F. Heidrich-Meisner, Finite-temperature optical conductivity with density-matrix renormalization group methods for the Holstein polaron and bipolaron with dispersive phonons, *Phys. Rev. B* **106**, 155129 (2022).
- [56] V. Janković and N. Vukmirović, Spectral and thermodynamic properties of the Holstein polaron: Hierarchical equations of motion approach, *Phys. Rev. B* **105**, 054311 (2022).
- [57] V. Janković, Holstein polaron transport from numerically “exact” real-time quantum dynamics simulations, *J. Chem. Phys.* **159**, 094113 (2023).
- [58] D. Dunn, Electron-phonon interactions in an insulator, *Can. J. Phys.* **53**, 321 (1975).
- [59] T. Xing, T. Li, Y. Yan, S. Bai, and Q. Shi, Application of the imaginary time hierarchical equations of motion method to calculate real time correlation functions, *J. Chem. Phys.* **156**, 244102 (2022).
- [60] M. Kira and S. Koch, *Semiconductor Quantum Optics* (Cambridge University Press, New York, 2012).
- [61] Y. Tanimura, Numerically “exact” approach to open quantum dynamics: The hierarchical equations of motion (HEOM), *J. Chem. Phys.* **153**, 020901 (2020).
- [62] R.-X. Xu and Y. J. Yan, Dynamics of quantum dissipation systems interacting with bosonic canonical bath: Hierarchical equations of motion approach, *Phys. Rev. E* **75**, 031107 (2007).
- [63] Z. H. Li, N. H. Tong, X. Zheng, D. Hou, J. H. Wei, J. Hu, and Y. J. Yan, Hierarchical Liouville-space approach for accurate and universal characterization of quantum impurity systems, *Phys. Rev. Lett.* **109**, 266403 (2012).
- [64] L. Song and Q. Shi, Calculation of correlated initial state in the hierarchical equations of motion method using an imaginary time path integral approach, *J. Chem. Phys.* **143**, 194106 (2015).
- [65] S. Bhattacharyya, T. Sayer, and A. Montoya-Castillo, Anomalous transport of small polarons arises from transient lattice relaxation or immovable boundaries, *J. Phys. Chem. Lett.* **15**, 1382 (2024).
- [66] R. P. Feynman and F. L. Vernon Jr., The theory of a general quantum system interacting with a linear dissipative system, *Ann. Phys.* **24**, 118 (1963).
- [67] L. Chen, Y. Zhao, and Y. Tanimura, Dynamics of a one-dimensional Holstein polaron with the hierarchical equations of motion approach, *J. Phys. Chem. Lett.* **6**, 3110 (2015).
- [68] I. S. Dunn, R. Tempelaar, and D. R. Reichman, Removing instabilities in the hierarchical equations of motion: Exact and approximate projection approaches, *J. Chem. Phys.* **150**, 184109 (2019).
- [69] Y. Yan, T. Xing, and Q. Shi, A new method to improve the numerical stability of the hierarchical equations of motion for discrete harmonic oscillator modes, *J. Chem. Phys.* **153**, 204109 (2020).
- [70] See Supplemental Material at <http://link.aps.org/supplemental/10.1103/PhysRevB.109.214312> for more details on (i) the HEOM equations, (ii) the limit of vanishing electronic bandwidth from the standpoint of formally exact expressions, (iii) the summary of the parameter regimes analyzed with different methods, (iv) differences between numerically exact and bubble-approximation results in all the parameter regimes analyzed, (v) the real-time QMC method used to approach the adiabatic limit, and (vi) a comparison of dc mobilities obtained using real-axis and imaginary-axis approaches. This includes a reference to D. M. Wilkins and N. S. Dattani, Why quantum coherence is not important in the Fenna-Matthews-Olsen complex, *J. Chem. Theory Comput.* **11**, 3411 (2015).
- [71] V. Janković, Numerical study of the one-dimensional Holstein model using the momentum-space hierarchical equations of motion method, Zenodo (2023), doi:10.5281/zenodo.8068547.
- [72] A. Georges, G. Kotliar, W. Krauth, and M. J. Rozenberg, Dynamical mean-field theory of strongly correlated fermion systems and the limit of infinite dimensions, *Rev. Mod. Phys.* **68**, 13 (1996).
- [73] J. Ma and J. Cao, Förster resonance energy transfer, absorption and emission spectra in multichromophoric systems. I. Full cumulant expansions and system-bath entanglement, *J. Chem. Phys.* **142**, 094106 (2015).
- [74] T. Holstein, Studies of polaron motion: Part II. The “small” polaron, *Ann. Phys.* **8**, 343 (1959).
- [75] D. Emin, Phonon-assisted transition rates I. Optical-phonon-assisted hopping in solids, *Adv. Phys.* **24**, 305 (1975).
- [76] G. Arnold and T. Holstein, Higher-order effects in hopping-type transport of small polarons, *Ann. Phys.* **132**, 163 (1981).
- [77] H. Reik and D. Heese, Frequency dependence of the electrical conductivity of small polarons for high and low temperatures, *J. Phys. Chem. Solids* **28**, 581 (1967).
- [78] I. Lang and Y. A. Firsov, Kinetic theory of semiconductors with low mobility, *Sov. Phys. JETP* **16**, 1301 (1962).
- [79] S. Fratini and S. Ciuchi, Dynamical localization corrections to band transport, *Phys. Rev. Res.* **2**, 013001 (2020).
- [80] G. Schubert, G. Wellein, A. Weisse, A. Alvermann, and H. Fehske, Optical absorption and activated transport in polaronic systems, *Phys. Rev. B* **72**, 104304 (2005).

Holstein polaron transport from numerically “exact” real-time quantum dynamics simulations

Cite as: J. Chem. Phys. 159, 094113 (2023); doi: 10.1063/5.0165532

Submitted: 29 June 2023 • Accepted: 14 August 2023 •

Published Online: 6 September 2023



View Online



Export Citation



CrossMark

Veljko Janković^{a)}

AFFILIATIONS

Institute of Physics Belgrade, University of Belgrade, Pregrevica 118, 11080 Belgrade, Serbia

Note: This paper is part of the 2023 JCP Emerging Investigators Special Collection.

^{a)}Author to whom correspondence should be addressed: veljko.jankovic@ipb.ac.rs

ABSTRACT

Numerically “exact” methods addressing the dynamics of coupled electron–phonon systems have been intensively developed. Nevertheless, the corresponding results for the electron mobility μ_{dc} are scarce, even for the one-dimensional (1d) Holstein model. Building on our recent progress on single-particle properties, here we develop the momentum-space hierarchical equations of motion (HEOM) method to evaluate real-time two-particle correlation functions of the 1d Holstein model at a finite temperature. We compute numerically “exact” dynamics of the current–current correlation function up to real times sufficiently long to capture the electron’s diffusive motion and provide reliable results for μ_{dc} in a wide range of model parameters. In contrast to the smooth ballistic-to-diffusive crossover in the weak-coupling regime, we observe a temporally limited slow-down of the electron on intermediate time scales already in the intermediate-coupling regime, which translates to a finite-frequency peak in the optical response. Our momentum-space formulation lowers the numerical effort with respect to existing HEOM-method implementations, while we remove the numerical instabilities inherent to the undamped-mode HEOM by devising an appropriate hierarchy closing scheme. Still, our HEOM remains unstable at too low temperatures, for too strong electron–phonon coupling, and for too fast phonons.

Published under an exclusive license by AIP Publishing. <https://doi.org/10.1063/5.0165532>

I. INTRODUCTION

The electron–phonon interaction governs the transport of charge (and energy) in systems ranging from semiconductors,^{1–6} organic molecular crystals, and polymers^{7–9} to molecular aggregates relevant for photosynthesis.^{10–14} The simplest model of such diverse systems is the Holstein model,¹⁵ in which an electron is locally and linearly coupled to phonons. Well-established transport theories are formulated as perturbative expansions from either the limit of vanishing coupling (Boltzmann-like^{4,5,16} or Redfield-like^{13,14,17} theories) or vanishing electronic bandwidth (small-polaron/Lang–Firsov,¹⁸ Marcus,^{13,14,19} or Förster^{13,14,20} theories). However, in many instances, the energy scales representative of electron motion, phonons, electron–phonon interaction, and thermal fluctuations are all comparable to one another.^{1,21–23} This circumstance calls for the development of methods beyond standard transport theories.

Such methods are typically formulated under physically motivated approximations. Examples include the cumulant expansion,^{24–28} dynamical mean-field theory,^{29–33} polaron

transformation-based approaches,^{34–43} momentum-average approximation,^{44–46} and kinetic Monte Carlo approaches.^{47,48}

The approximate methods are generally computationally efficient and can thus be combined with electronic-structure methods to provide first-principles results on systems large enough that a direct comparison with experimental results is sensible.^{49–55} While the agreement between numerical and experimental results justifies the approximations introduced, it does not fully reveal their domain of validity. This can be unveiled by comparison to results produced by numerically “exact” methods, which do not lean on any approximation beyond those in the Hamiltonian. Since they are computationally intensive, numerically “exact” methods are usually applied to model Hamiltonians only.

The numerically “exact” approaches used to study interacting electron–phonon models may be roughly divided into the following: (i) quantum Monte Carlo (QMC) methods;^{56–63} (ii) wavefunction-based methods considering the electron and phonons as a closed system, such as exact diagonalization (ED)-based techniques,^{64–69} the density-matrix renormalization group (DMRG),^{70–77} thermo-field dynamics,^{78–80} and the hierarchy of Davydov’s

Ansätze,^{81–85} (iii) methods leaning on the theory of open quantum systems, such as the hierarchical equations of motion (HEOM),^{86–89} its generalizations,^{90,91} and hybridizations^{92,93} with the stochastic Schrödinger equation.^{94,95}

Many of the above-mentioned methods deliver practically exact results on the ground-state or equilibrium finite-temperature properties of the Holstein model.^{58,65,70,76} Some of them have recently been used to examine the model's single-particle properties (the electronic spectral function or linear absorption spectra).^{67–69,71,73,76,77,92,95,96} However, much more demanding numerically “exact” evaluations of two-particle correlation functions at finite temperatures, such as the ac and dc electrical conductivity, have started only recently.^{27,61–63,74,75,77,93,97–99} Each class of the above-mentioned numerically “exact” methods encounters certain issues in computations of two-particle quantities. (i) QMC methods are usually formulated directly in the thermodynamic limit but require numerical analytical continuation to reconstruct real-frequency spectra. A combination of statistical errors and uncertainties in the analytical continuation may lead to final results whose errors are comparable to the results themselves. Real-time QMC simulations witness a progressive development of the infamous sign (or phase) problem, which limits their applicability to relatively short-time dynamics. (ii) ED-based methods are applied to small clusters and typically require artificial broadening parameters to construct real-frequency spectra. The DMRG equations can be propagated only for relatively short times,^{76,77} which may not be long enough to reliably estimate the dc mobility.⁷⁷ (iii) The HEOM method treats small clusters but can, in principle, capture the full decay of correlation functions.^{97–100} Being based on a formally exact expression for the electronic reduced density matrix (RDM), the HEOM method is undoubtedly numerically “exact.” However, when employed on a finite system and truncated at a finite depth, the HEOM with undamped phonon modes suffers from numerical instabilities,¹⁰¹ which practically limit the maximum propagation time¹⁰² and whose overcoming requires further algorithmic developments.^{101,103}

In this study, we provide numerically “exact” results for the electron mobility within the 1d Holstein model. In contrast to the best currently available results, which are obtained by performing the numerical analytical continuation of imaginary-axis QMC data⁶¹ (possibly combined with real-time QMC data on rather short time scales⁶³), our results entirely follow from real-time computations. We extend the momentum-space HEOM we developed in Ref. 96 to follow the time evolution of finite-temperature two-particle correlation functions up to very long (practically infinite) real times. In addition, our momentum-space HEOM also enables us to obtain highly accurate results for imaginary-time correlation functions, which are the central quantities in QMC simulations. Our imaginary-axis results help us establish the minimum chain length and hierarchy depth needed to obtain results representative of the thermodynamic limit. The high quality of our real-time results is ensured by checking that different sum rules (e.g., the optical sum rule—OSR) are satisfied with high accuracy. We lower the numerical effort with respect to existing HEOM implementations by exploiting the translational symmetry, which reduces the number of independent dynamical variables in the formalism, and noting that the totally symmetric phonon mode does not contribute to the time evolution of correlation functions. We avoid numerical

instabilities in a wide range of parameter spaces by devising a specific closing of the hierarchy. Still, the numerical instabilities inherent to the undamped-mode HEOM prevent us from obtaining results at low temperatures, for strong electron–phonon coupling, and when electronic dynamics is much slower than phonon dynamics (the so-called antiadiabatic regime).

The paper is organized as follows. Section II specifies the model and introduces our momentum-space HEOM method for the current–current correlation function. Technical details are presented in Appendixes A–D. In Sec. III, we provide a number of numerical examples testing critical points of our methodology and present our main results concerning temperature-dependent dc mobility. Section IV is devoted to a summary and prospects for future work.

II. THEORETICAL FRAMEWORK

A. Model and definitions

We consider the Holstein model on the 1d lattice comprising N sites with periodic boundary conditions. In the momentum space, its Hamiltonian reads as

$$H = H_e + H_{\text{ph}} + H_{e-\text{ph}} \\ = \sum_k \varepsilon_k |k\rangle \langle k| + \sum_q \omega_q b_q^\dagger b_q + \sum_q V_q B_q. \quad (1)$$

The electronic and phononic wave numbers k and q may assume any of the N allowed values in the first Brillouin zone $-\pi < k, q \leq \pi$. The Hamiltonian H_e describes an electron in a free-electron band whose dispersion $\varepsilon_k = -2J \cos(k)$ originates from the nearest-neighbor electronic hopping of amplitude J . The Hamiltonian H_{ph} describes an optical-phonon branch with dispersion ω_q such that $\omega_{q=0} \neq 0$. The interaction term $H_{e-\text{ph}}$ is characterized by its strength g and contains the purely electronic operator $V_q = \sum_k |k+q\rangle \langle k|$, which increases the electronic momentum by q , and the purely phononic operator $B_q = \frac{g}{\sqrt{N}}(b_q + b_{-q}^\dagger)$, which decreases the phononic momentum by q . In the following, we set the lattice constant a_l and the elementary charge e_0 , and the physical constants \hbar and k_B to unity.

We focus on the dynamics of the current–current correlation function

$$C_{jj}(t) = \frac{1}{Z} \text{Tr} \{ j(t) j(0) e^{-\beta H} \}, \quad (2)$$

where the current operator reads as

$$j = -2J \sum_k \sin(k) |k\rangle \langle k|, \quad (3)$$

where $j(t) = e^{iHt} j e^{-iHt}$, while $Z = \text{Tr} e^{-\beta H}$ is the partition sum at temperature $T = \beta^{-1}$. Its Fourier transform $C_{jj}(\omega) = \int_{-\infty}^{+\infty} dt e^{i\omega t} C_{jj}(t)$ [with $C_{jj}(-t) = C_{jj}(t)^*$] determines the frequency-dependent (or dynamical) mobility,

$$\text{Re} \mu_{\text{ac}}(\omega) = \frac{1 - e^{-\beta\omega}}{2\omega} C_{jj}(\omega) \\ = \frac{C_{jj}(\omega) - C_{jj}(-\omega)}{2\omega}, \quad (4)$$

where the second equality follows from the fluctuation–dissipation theorem for equilibrium correlation functions, $C_{ij}(-\omega) = e^{-\beta\omega} C_{ij}(\omega)$. The dc mobility is $\mu_{dc} = \lim_{\omega \rightarrow 0} \text{Re } \mu_{ac}(\omega)$ and may be computed using only the real or only the imaginary part of $C_{ij}(t)$,¹⁰⁴

$$\begin{aligned} \mu_{dc} &= \frac{1}{T} \int_0^{+\infty} dt \text{Re } C_{ij}(t) \\ &= -2 \int_0^{+\infty} dt t \text{Im } C_{ij}(t). \end{aligned} \quad (5)$$

$C_{ij}(t)$ (for $t > 0$) carries information on the carrier's dynamics resulting from a sudden (δ -like) perturbation of the electron–phonon equilibrium. Its real part is proportional to the velocity–velocity anticommutator correlation function, which is the quantum counterpart of the velocity–velocity correlation function used, e.g., to study Brownian motion. The mean-square displacement (MSD) of the carrier's position, $\Delta x^2(t) = \langle [x(t) - x(0)]^2 \rangle$, where $\langle \dots \rangle$ denotes averaging with respect to $e^{-\beta H}/Z$, grows at a rate determined by the time-dependent diffusion constant,¹⁰⁵

$$D(t) = \frac{1}{2} \frac{d}{dt} \Delta x^2(t) = \int_0^t ds \text{Re } C_{ij}(s). \quad (6)$$

Within the model considered here, $\text{Re } C_{ij}(t)$ decays to zero in the long-time limit, so that $D(t)$ varies from 0 at short times to $D_\infty = \int_0^{+\infty} ds \text{Re } C_{ij}(s)$ at long times, where D_∞ is the diffusion constant related to the dc mobility by the Einstein relation (in the units we use, $\mu_{dc} = D_\infty/T$). The electron's dynamics then exhibits a crossover from short-time ballistic dynamics, when $\Delta x^2(t) = C_{ij}(0)t^2$ and $D(t) = C_{ij}(0)t$, to long-time diffusive dynamics, when $\Delta x^2(t) = 2D_\infty t$ and $D(t) = D_\infty$. In addition to $D(t)$, another quantity useful to describe this crossover is the diffusion exponent $\alpha(t) \geq 0$ defined by assuming that the power-law scaling $\Delta x^2(t) \propto t^{\alpha(t)}$ holds locally around instant t ,¹⁰⁶ so that

$$\alpha(t) = \frac{2tD(t)}{\Delta x^2(t)}. \quad (7)$$

At short times, $\alpha(t)$ is close to 2, while it reaches the value of unity in the long-time diffusive limit.

B. HEOM for the real-time current-current correlation function

We formulate the HEOM method for the purely electronic operator

$$i(t) = \frac{1}{Z} \text{Tr}_{\text{ph}} \left\{ e^{-iHt} j e^{-\beta H} e^{iHt} \right\}, \quad (8)$$

while $C_{ij}(t) = \text{Tr}_e \{ j_i(t) \}$. Since the totally symmetric phonon mode ($q = 0$ mode) couples to the unit operator in the electronic subspace, it does not affect the dynamics of $i(t)$, while its contributions to Z and $e^{-\beta H}$ cancel out after performing the partial trace over phonons. This decoupling of the $q = 0$ phonon mode from the rest of the phonon modes and the electronic states¹⁰⁷ somewhat lowers the number of auxiliary density operators (ADOs) $l_{\mathbf{n}}^{(n)}(t)$, which are characterized by the vector $\mathbf{n} = \{n_{qm} | q \neq 0, m = 0, 1\}$ containing $2(N-1)$ non-negative integers n_{qm} counting individual phonon

absorption and emission events whose total number is $n = \sum'_{qm} n_{qm}$. The prime on the sum indicates the omission of the $q = 0$ term. The momentum conservation implies that the ADO $l_{\mathbf{n}}^{(n)}(t)$ changes the electronic momentum by $k_{\mathbf{n}} = \sum'_{qm} q n_{qm}$, so that only N^2 matrix elements are nonzero. The only nonzero matrix elements of $l_{\mathbf{n}}^{(n)}(t)$ are the ones connecting the states whose momenta differ by $k_{\mathbf{n}}$. This requirement leads to a drastic reduction in the number of equations with respect to existing real-space HEOM formulations.^{97,99,102} A more detailed discussion in this direction is deferred to the last paragraph of Sec. III B.

The dynamics of $i(t)$ follows from the real-time HEOM

$$\begin{aligned} \partial_t \langle k | l_{\mathbf{n}}^{(n)}(t) | k + k_{\mathbf{n}} \rangle &= -i(\varepsilon_k - \varepsilon_{k+k_{\mathbf{n}}} + \mu_{\mathbf{n}}) \langle k | l_{\mathbf{n}}^{(n)}(t) | k + k_{\mathbf{n}} \rangle \\ &+ i \sum'_{qm} \sqrt{(1+n_{qm})c_{qm}} \langle k - q | l_{\mathbf{n}_{qm}^+}^{(n+1)}(t) | k + k_{\mathbf{n}} \rangle \\ &- i \sum'_{qm} \sqrt{(1+n_{qm})c_{qm}} \langle k | l_{\mathbf{n}_{qm}^-}^{(n+1)}(t) | k + k_{\mathbf{n}} + q \rangle \\ &+ i \sum'_{qm} \sqrt{n_{qm}c_{qm}} \langle k + q | l_{\mathbf{n}_{qm}^-}^{(n-1)}(t) | k + k_{\mathbf{n}} \rangle \\ &- i \sum'_{qm} \sqrt{n_{qm}} \frac{c_{q\bar{m}}}{\sqrt{c_{qm}}} \langle k | l_{\mathbf{n}_{qm}^-}^{(n-1)}(t) | k + k_{\mathbf{n}} - q \rangle, \end{aligned} \quad (9)$$

where $\mu_{\mathbf{n}} = \sum'_q \omega_q (n_{q0} - n_{q1})$. The ADO $l_{\mathbf{n}}^{(n)}(t)$ couples to ADOs at depths $n \pm 1$, which are characterized by vectors \mathbf{n}_{qm}^\pm whose components are $[\mathbf{n}_{qm}^\pm]_{q'm'}$ $= n_{q'm'} \pm \delta_{q'q} \delta_{m'm}$. The coefficients c_{qm} and $c_{q\bar{m}}$ are defined in Eqs. (A2) and (A3) of Appendix A, where we provide a detailed derivation of Eq. (9).

The initial condition for Eq. (9) is set by the equilibrium state of the interacting electron–phonon system [see also Eq. (8)]. In our previous publication,⁹⁶ we derived that the hierarchical representation of that equilibrium state can be obtained from the following imaginary-time HEOM:

$$\begin{aligned} \partial_\tau \langle k | \sigma_{\mathbf{n}}^{(n)}(\tau) | k + k_{\mathbf{n}} \rangle &= -(\varepsilon_k + \mu_{\mathbf{n}}) \langle k | \sigma_{\mathbf{n}}^{(n)}(\tau) | k + k_{\mathbf{n}} \rangle \\ &+ \sum'_{qm} \sqrt{(1+n_{qm})c_{qm}} \langle k - q | \sigma_{\mathbf{n}_{qm}^+}^{(n+1)}(\tau) | k + k_{\mathbf{n}} \rangle \\ &+ \sum'_{qm} \sqrt{n_{qm}c_{qm}} \langle k + q | \sigma_{\mathbf{n}_{qm}^-}^{(n-1)}(\tau) | k + k_{\mathbf{n}} \rangle. \end{aligned} \quad (10)$$

Equation (10) is propagated in imaginary time τ from 0 to β with the infinite-temperature initial condition $\langle k | \sigma_{\mathbf{n}}^{(n)}(0) | k + k_{\mathbf{n}} \rangle = \delta_{n,0}$. The initial condition for Eq. (9) is finally

$$\langle k | l_{\mathbf{n}}^{(n)}(0) | k + k_{\mathbf{n}} \rangle = Z_e^{-1} (-2J) \sin(k) \langle k | \sigma_{\mathbf{n}}^{(n)}(\beta) | k + k_{\mathbf{n}} \rangle, \quad (11)$$

where the so-called electronic partition sum reads as

$$Z_e = \sum_p \langle p | \sigma_0^{(0)}(\beta) | p \rangle. \quad (12)$$

A more detailed derivation is provided in Appendix A. Here, let us emphasize that the structure of the imaginary-time HEOM in Eq. (10) is fully compatible with the structure of the real-time HEOM in Eq. (9). This is different from existing approaches, in which the

structures of the imaginary-time and real-time HEOMs are not manifestly identical^{99,108} and may require appropriate rearrangement steps to obtain the initial condition for the real-time HEOM.¹⁰⁸

C. Closing the HEOM for the real-time current-current correlation function

When truncated at a finite maximum depth D , the real-time HEOM in Eq. (9) suffers from numerical instabilities appearing at sufficiently long times, which are commonly ascribed to the discrete and undamped nature of phonons.¹⁰¹ Such instabilities have been observed even for not-too-strong couplings and at not-too-low temperatures. The instabilities are particularly detrimental to evaluations of μ_{dc} , for which we need $C_{jj}(t)$ up to times so long that it has decayed almost to zero [Eq. (5)]. They may be eliminated by projecting out the unstable eigenmodes of the truncated HEOM,¹⁰¹ which requires numerically complicated filtration algorithms, or by deriving a new hierarchy of equations,¹⁰³ whose generally nontrivial relation to the original hierarchy may complicate evaluations of physically relevant quantities. The numerical instabilities reported in Ref. 101 were observed under the so-called time-nonlocal (TNL) truncation scheme, which sets all ADOs at depths $n > D$ to zero. One may thus hope that an appropriate closing of the HEOM at the maximum depth could eliminate numerical instabilities. While a number of closing schemes have been proposed recently,^{91,109,110} we find that none of them stabilizes Eq. (9). A possible reason behind our observation is that these schemes were tried and tested for the electron coupled to a phonon bath, i.e., when the spectral density of the electron-phonon interaction is a continuous function of the energy exchanged. On the other hand, here we deal with a discrete spectral density consisting of a finite number δ peaks at $\pm\omega_q$. In Appendix B, we build on previous density-matrix studies^{111–113} and derive in detail a specific closing of Eq. (9) that permits us to overcome the instabilities in many (but not all) parameter regimes. Here, let us only mention that we eliminate the ADOs at depth $D + 1$ from the equations at the maximum depth D by (i) setting the ADOs with $n \geq D + 2$ to zero and (ii) solving the resulting equations at depth $D + 1$, which then contain only the ADOs at depth D in the Markov and adiabatic approximations. The structure of the resulting equations at depth D is, however, more involved than the structure of Eq. (9) because the ADOs at depth D become mutually coupled. We eliminate these equal-depth couplings by resorting to the random phase approximation, which neglects momentum-averaged matrix elements of the ADOs at depth D due to random phases at different momenta. The above-described procedure for closing the HEOM results in equations for maximum-depth ADOs ($n = D$) that feature exponential damping terms

$$\left[\partial_t \langle k | I_n^{(n)}(t) | k + k_n \rangle \right]_{\text{close}} = -\delta_{n,D} \frac{1}{2} (\tau_k^{-1} + \tau_{k+k_n}^{-1}) \times \langle k | I_n^{(n)}(t) | k + k_n \rangle, \quad (13)$$

where τ_k is the carrier scattering time in the second-order perturbation theory and the long-chain limit [see Eq. (B7) and Ref. 42].

In our numerical computations, we assume that phonons are dispersionless, $\omega_q \equiv \omega_0$. For $\omega_0/J \geq 2$, the closing scheme in Eq. (13) cannot fully remove the numerical instabilities inherent to the undamped-mode HEOM because the carrier scattering times then

become infinite for k states in the vicinity of $\pm\pi/2$.^{26,42} We thus obtain HEOM results for $\omega_0/J \geq 2$ only at sufficiently high temperatures and for sufficiently (but not excessively) strong interactions. For $\omega_0/J < 2$, our results summarized in Secs. III A and III E show that the closing scheme in Eq. (13) removes the instabilities of Eq. (9) for not too strong g or at not too low T . The instabilities remain for strong g and at low T , while their relatively early appearance prevents us from reliably computing μ_{dc} in such parameter regimes (see Sec. III F).

D. HEOM for the imaginary-time current-current correlation function

In order for $C_{jj}(t)$ to be representative of the long-chain limit and take all relevant phonon-assisted processes into account, both N and D should be sufficiently large. The first proxy for how large N and D should be follows from analyzing the current-current correlation function $C_{jj}(\tau)$ in imaginary time.

While $C_{jj}(\tau)$ is directly accessible in QMC simulations,^{61,63,100} its evaluation using the HEOM method has not been considered so far, to the best of our knowledge. The appropriate imaginary-time HEOM is obtained from Eq. (9) by performing Wick's rotation $t \rightarrow -i\tau$. We employ the TNL truncation of the HEOM thus obtained, i.e., we simply set all the ADOs with $n > D$ to zero. $C_{jj}(\tau)$ is to be determined on the interval $[0, \beta]$, on which it is symmetric with respect to $\beta/2$. To enable as accurate an evaluation of $C_{jj}(\tau)$ as possible, we find it useful to consider the symmetrized correlation function

$$C_{jj}^{\text{sym}}(\tau) = \frac{1}{Z} \text{Tr} \left\{ e^{-\beta H/2} e^{H\tau} j e^{-H\tau} e^{-\beta H/2} j \right\}, \quad (14)$$

on the interval $[-\beta/2, \beta/2]$, which is related to $C_{jj}(\tau)$ via $C_{jj}(\tau) = C_{jj}^{\text{sym}}(\tau - \beta/2)$ for $0 \leq \tau \leq \beta$. We note that the use of the symmetrized correlation function instead of the standard one is advantageous in real-time QMC simulations¹¹⁴ and is also reported to be useful in real-time HEOM computations.^{98,99} Nevertheless, we find that the numerical instabilities of the real-time HEOM [Eqs. (9) and (13)] are reflected on both $C_{jj}(t)$ and $C_{jj}^{\text{sym}}(t)$ in the same manner, which is the reason why we consider the non-symmetrized correlation function [Eq. (2)] in all our real-time computations.

We determine $C_{jj}^{\text{sym}}(\tau)$ by two independent imaginary-time propagations: one forward from 0 to $\beta/2$ and the other backward from 0 to $-\beta/2$. The initial condition (at $\tau = 0$) for both propagations is obtained from the imaginary-time HEOM for the equilibrium state of the coupled electron-phonon system [Eq. (10)], which we (i) propagate from 0 to $\beta/2$, (ii) multiply by j from the left, and (iii) propagate once again from 0 to $\beta/2$. Since $C_{jj}^{\text{sym}}(\tau)$ is symmetric around 0, the results of the forward and backward propagations in imaginary time should coincide. We use this fact to gain insight into the maximum hierarchy depth D that is needed to obtain converged results. In more detail, we find that the relative deviation ($-\beta/2 \leq \tau \leq \beta/2$)

$$\delta_{jj}^{\text{sym}}(\tau) = 2 \frac{|C_{jj}^{\text{sym}}(\tau) - C_{jj}^{\text{sym}}(-\tau)|}{C_{jj}^{\text{sym}}(\tau) + C_{jj}^{\text{sym}}(-\tau)}, \quad (15)$$

decreases with increasing D . Furthermore, following how $C_{jj}(\tau) = [C_{jj}^{\text{sym}}(\tau - \beta/2) + C_{jj}^{\text{sym}}(\beta/2 - \tau)]/2$ ($0 \leq \tau \leq \beta$) changes with the chain length N provides information about the minimum chain length N needed to obtain results representative of the thermodynamic limit. We, however, emphasize that the estimates for D and N that stem from imaginary-axis data may differ from the corresponding estimates originating from real-time data. Whenever possible, we also perform real-time simulations for multiple N and D to ensure that our real-time results are also representative of the thermodynamic limit.

E. Sum rules

To gain additional confidence in our HEOM results, we check that certain sum rules for frequency-resolved quantities are satisfied with sufficient accuracy.^{7,115} We compare the moments of frequency-dependent quantities evaluated by (i) numerical integration over frequency and (ii) averaging an appropriate operator in the equilibrium state of the coupled electron and phonon. We consider the OSR

$$\int_0^{+\infty} d\omega \operatorname{Re} \mu_{\text{ac}}(\omega) = -\frac{\pi}{2} \langle H_e \rangle, \quad (16)$$

and the sum rules

$$\int_{-\infty}^{+\infty} \frac{d\omega}{2\pi} \omega^n C_{jj}(\omega) = M_n, \quad (17)$$

for the first three moments ($n = 0, 1, 2$) of the real-frequency current–current correlation function. In Eq. (16), we use the dynamical mobility computed using the first equalities in Eqs. (4) (for $\omega \neq 0$) and (5) (for $\omega = 0$). The electron’s kinetic energy entering Eq. (16) is evaluated using the quantities defined in Eqs. (10) and (12),⁹⁶

$$\langle H_e \rangle = \frac{1}{Z_e} \sum_k \varepsilon_k \langle k | \sigma_0^{(0)}(\beta) | k \rangle. \quad (18)$$

We note that the initial conditions $i_n^{(n)}(t=0)$ [Eq. (11)] for the real-time HEOM [Eq. (9)] do not enter Eq. (18). On the other hand, the quantities M_n entering Eq. (17) are expressed in terms of the initial conditions $i_n^{(n)}(t=0)$ for the real-time HEOM, and we derive the corresponding relations in Appendix C. Strictly speaking, Eq. (16) holds only in the long-chain limit, and in Appendix D, we demonstrate that the corresponding finite-size corrections decrease with increasing N . On the contrary, for any given N and D , Eq. (17) (with the expressions obtained in Appendix C) is exact. Having all these things considered, we conclude that checking the sum rules in Eq. (17) provides an important self-consistency check that all the numerical procedures (e.g., the numerical Fourier transformation) are properly implemented while providing limited information on the adequacy of N and D employed. In addition to a test for numerical implementation procedures, checking the OSR constitutes a nontrivial test for the adequacy of both D and N employed,

which is in line with previous studies.¹¹⁵ It is for this reason that we focus our discussion in Sec. III on the OSR. As a general trend, we observe that the sum rules in Eq. (17) are satisfied with better relative accuracy than the OSR.

III. NUMERICAL RESULTS

We limit ourselves to dispersionless optical phonons, $\omega_q \equiv \omega_0$, and perform HEOM computations for three different values of ω_0/J spanning the range from the adiabatic regime of slow phonons ($\omega_0/J = 1/3$) to the extreme quantum regime ($\omega_0/J = 1$) and the antiadiabatic regime of fast phonons ($\omega_0/J = 3$). Since most of our results are obtained for $\omega_0/J \leq 1$, we use the dimensionless interaction parameter,

$$\lambda = \frac{g^2}{2J\omega_0}, \quad (19)$$

that is appropriate to describe the zero-temperature transition from free electrons ($\lambda < 1$) to polarons ($\lambda > 1$) at such phonon frequencies.

We devote Secs. III A–III C to discussing the performance of the closing strategy embodied in Eq. (13) (Sec. III A) and the effects of finite N and D on the HEOM results in imaginary and real time (Sec. III B), as well as the accuracy with which the OSR is satisfied (Sec. III C). Section III D summarizes the most representative HEOM results for the time evolution of C_{jj} and the dynamical-mobility profile. Our most significant results, which concern the temperature dependence of μ_{dc} for different values of ω_0/J , are presented in Sec. III E. To further illustrate the capabilities and limitations of our approach, we present HEOM results for $C_{jj}(t)$ for strong electron–phonon couplings and at different temperatures in Sec. III F.

We provide HEOM data on $C_{jj}(t)$, its Fourier transformation $C_{jj}(\omega)$ computed using the FFTW3 software package,¹¹⁶ as well as $\operatorname{Re} \mu_{\text{ac}}(\omega)$, in different parameter regimes, as a freely available dataset. For more details, see Ref. 117, which contains all our numerical data, and the supplementary material of this manuscript, which contains their detailed description. Here, let us only mention that the HEOM in Eq. (9) supplemented with the closing in Eq. (13) is propagated using the algorithm proposed in Ref. 118 with the time step $\omega_0 \Delta t = (1 - 2) \times 10^{-2}$. While the maximum propagation time t_{max} generally shortens with increasing g and/or T , it is a highly nontrivial task to give its *a priori* estimate based only on the values of model parameters. Fortunately, in contrast to some other numerically “exact” methods, such as the DMRG⁷⁷ or real-time QMC,⁶³ the computational demands of the HEOM method do not increase with time t and are completely determined by $N, D, \Delta t$, and the propagation algorithm. We thus propagate the HEOM up to real times that are sufficiently long so that the integral $\int_0^t ds \operatorname{Re} C_{jj}(s)/T$ [see Eq. (5)] as a function of t enters saturation [see, e.g., Figs. 3(b) and 3(c)]. The frequency resolution in the optical response is increased by continuing $C_{jj}(t)$ symmetrically for negative times $-t_{\text{max}} \leq t \leq 0$ using $C_{jj}(-t) = C_{jj}(t)^*$, which results in the frequency step $\Delta\omega/\omega_0 = \pi/(\omega_0 t_{\text{max}})$. Therefore, if one wants both a reliable result for μ_{dc} and a finely resolved optical response, the maximum propagation time should be sufficiently long. In practice, we used $\omega_0 t_{\text{max}} \gtrsim 500$

for small g and at relatively low T , $\omega_0 t_{\max} \approx 300$ at intermediate values of g and T , and $\omega_0 t_{\max} \lesssim 100$ for large g or at high T .

A. Effectiveness and reliability of our closing strategy

We offer numerical examples demonstrating that the closing in Eq. (13) actually stabilizes the real-time HEOM [Eq. (9)] without compromising the results for μ_{dc} .

Figure 1(a) (its inset) shows the evolution of $\text{Re } C_{jj}$ ($\text{Im } C_{jj}$) with the closing in Eq. (13) and the TNL truncation in the weak-coupling regime and at a relatively low temperature. The beneficial effects of our closing strategy on HEOM stability are apparent. Moreover, the HEOM [with closing in Eq. (13)] estimate for $\mu_{\text{dc}}^{\text{HEOM}} = 68.0$ using $Jt_{\max} = 800$ agrees well with the estimate $\mu_{\text{dc}}^{\text{wcl}} = 72.5$ emerging from the weak-coupling limit [see Eq. (49) in Ref. 42]. The relative difference between the two results is under 10%, which eventually emerges as the relative error that is to be associated with $\mu_{\text{dc}}^{\text{HEOM}}$ (see Sec. III B). With TNL truncation, it is much more difficult to obtain a reliable estimate of μ_{dc} . This is evident when μ_{dc} is computed using only $\text{Re } C_{jj}(t)$ [the first equality in Eq. (5)], which under TNL truncation develops a pronounced hump for $Jt \gtrsim 100$. The same applies to the computation using only $\text{Im } C_{jj}(t)$ [the

second equality in Eq. (5)], when the small-amplitude long-time oscillations of $\text{Im } C_{jj}$ around zero are amplified by multiplication with time.

One may still argue that at higher temperatures, when carrier scattering rates entering Eq. (13) become large, our hierarchy closing may underestimate μ_{dc} . Such an effect may be particularly pronounced for not too strong coupling when the maximum depth D is not very large so that the exponentially damping terms in Eq. (13) may appreciably affect the quantity at the hierarchy root, i.e., $C_{jj}(t)$. The inset of Fig. 1(b) shows that the estimate for μ_{dc} using the closing in Eq. (13) and propagating the HEOM to sufficiently long times (we took $Jt_{\max} = 100$) is approximately the same as the one using the TNL truncation and propagating the HEOM to times before the instabilities arise (up to $Jt \approx 20$). Both of these estimates ($\mu_{\text{dc}}^{\text{HEOM}} = 0.53$) agree reasonably well with the estimate $\mu_{\text{dc}}^{\text{wcl}} = 0.61$ emerging from the weak-coupling limit.

B. Effects of finite N and D on the current-current correlation function and dc mobility

We first analyze $C_{jj}(\tau)$. We fix $g/J = \omega_0/J = T/J = 1$ and discuss the importance of finite-size effects for maximum hierarchy depth $D = 6$. Figure 2(a) shows that $C_{jj}(\tau)$ steadily approaches its long-chain limit with increasing N . The approach to that limit is quite fast because the relative deviation with respect to the results for the longest chain studied ($N = 13$) decreases by almost three orders of magnitude upon increasing N from 7 to 10 [see the inset of Fig. 2(a)]. Therefore, already, $N = 10$ should be sufficiently large to obtain results representative of the long-chain limit. Figure 2(b) shows that the quality of our imaginary-time data, quantified by the relative difference $\delta_{jj}^{\text{sym}}(\tau)$ [Eq. (15)], steadily increases with increasing D .

While Figs. 2(a) and 2(b) demonstrate a steady convergence of the imaginary-time data toward the large- N and large- D limit as N and D are increased, the situation on the real axis is somewhat more complicated, which is summarized in Figs. 3(a)–3(c). Fixing D to 6, Fig. 3(a) [Fig. 3(b)] shows that $\text{Re } C_{jj}(t)$ [$\text{Im } C_{jj}(t)$] is virtually the same for $N = 10, 13$, and 15. For $N = 7, 10$, and 13, we propagated HEOM up to $Jt_{\max} = 400$, while we used $Jt_{\max} = 300$ for $N = 15$. At longer times (not shown here), both $\text{Re } C_{jj}(t)$ and $\text{Im } C_{jj}(t)$ exhibit small-amplitude oscillations around zero. The agreement between the results for different N in the real-time domain translates to the overall profile of $\text{Re } \mu_{\text{ac}}(\omega)$ [see the inset of Fig. 3(a)]. However, the dc mobility somewhat decreases upon increasing N from 7 to 10 and 13, while its values for $N = 13$ and 15 are virtually the same [see the full dots in the inset of Fig. 3(a) and Table I]. The relative differences between μ_{dc} for different values of N considered are of the order of percent, which is also evident from the inset of Fig. 3(b) displaying the convergence to the dc limit when only $\text{Im } C_{jj}(t)$ is used to evaluate μ_{dc} [the second equality in Eq. (5)]. The integral $-2 \int_0^t ds \text{Im } C_{jj}(s)$ is expected to display long-time oscillations originating from the corresponding oscillations of $\text{Im } C_{jj}(s)$ around zero. The inset of Fig. 3(b) thus shows the smoothed data obtained using the moving-average procedure, which is employed at sufficiently long times to reliably compute μ_{dc} . In more detail, the moving average of the quantity $-2 \int_0^t ds \text{Im } C_{jj}(s)$ at instant t is computed as the arithmetic average of its N_{move} values right after t and its N_{move}

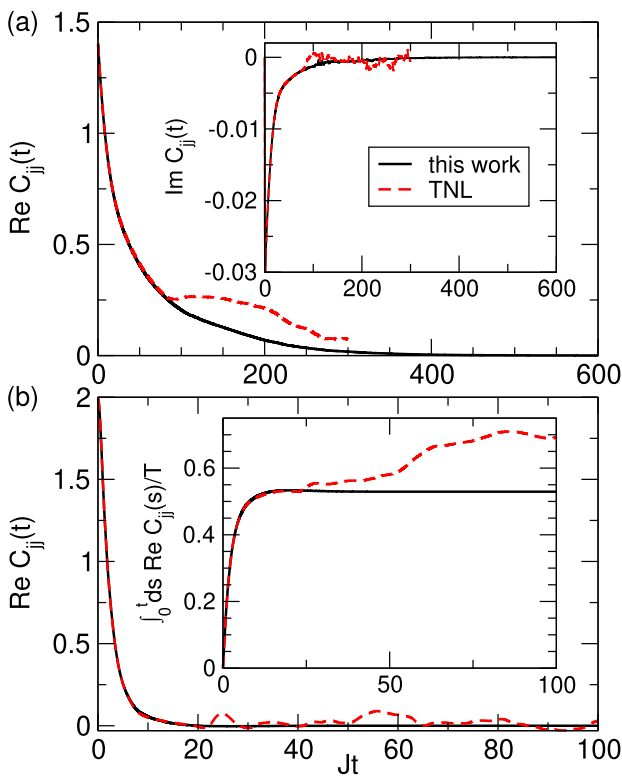


FIG. 1. Time dependence of $\text{Re } C_{jj}$ (in units of J^2) employing the closing in Eq. (13) (full black line, label “this work”) or the time-nonlocal truncation (dashed red line, label “TNL”). The values of model parameters are $\omega_0/J = 1$, $\lambda = 0.01$, and (a) $T/J = 1$, $N = 160$, $D = 2$ (in units of J^2), (b) $T/J = 10$, $N = 40$, $D = 3$. The insets show the time dependence of (a) $\text{Im } C_{jj}$, (in units of J^2) (b) the quantity $\int_0^t ds \text{Re } C_{jj}(s)/T$, which tends to μ_{dc} as $t \rightarrow +\infty$.

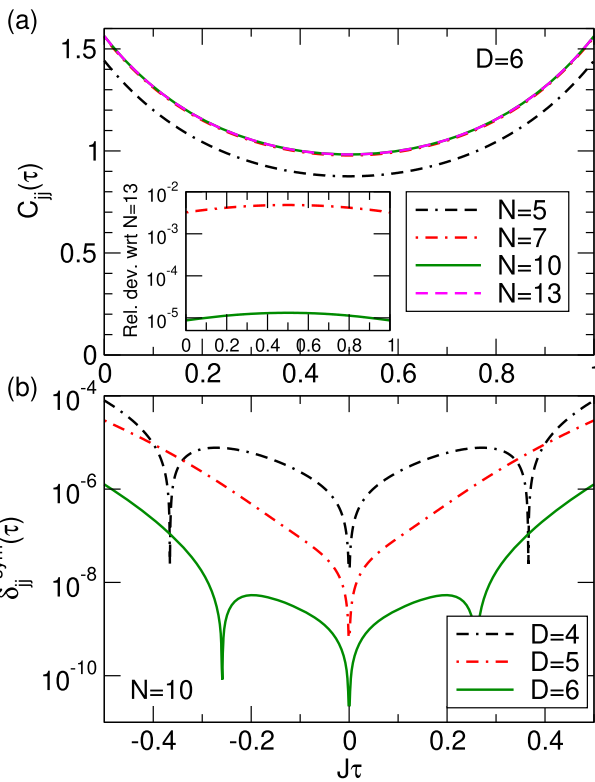


FIG. 2. (a) Current–current correlation function (in units of J^2) in imaginary time $J\tau \in [0, \beta J]$ for $D = 6$ and different chain lengths N . The inset shows the quantity $|C_{ij}^N(\tau) - C_{ij}^{N=13}(\tau)|/C_{ij}^{N=13}(\tau)$ for $N = 7$ and 10 . (b) The quantity $\delta_{ij}^{\text{sym}}(\tau)$ [Eq. (15)] as a function of imaginary time $J\tau \in [-\beta J/2, \beta J/2]$ for a 10-site chain and different maximum hierarchy depths D . Note the logarithmic scale on the vertical axis in the insets of (a) and (b). The model parameters are $g/J = \omega_0/J = T/J = 1$.

values right before t . We take N_{move} to be 10% of the total number of points for which we have HEOM data. Figure 4(a) shows that the moving-average procedure indeed smooths out the long-time oscillations of the quantity $-2\int_0^t ds \text{Im} C_{ij}(s)$, while the dependence of the final result for μ_{dc} on the averaging window is much less pronounced than, e.g., its dependence on the parity of D , *vide infra*. The μ_{dc} estimates using the two equalities in Eq. (5) agree up to a couple of percent (see Table I). The relative difference of the same order of magnitude is obtained when D is increased from 6 to 8 when $N = 10$, while decreasing D from 6 to 5 leads to a decrease in μ_{dc} of around 10% [see Fig. 3(c) and Table I]. For $N = 10$ and $D = 7$, $\text{Re} C_{ij}(t)$ becomes negative at long times, which may prevent us from reliably estimating μ_{dc} . Nevertheless, we see that following the time evolution up to $Jt_{\text{max}} = 70$ provides an estimate of μ_{dc} that differs from the estimate for $N = 10, D = 5$, by a couple of percent. We thus conclude that μ_{dc} estimates may depend on the parity of the maximum hierarchy depth D . For sufficiently large D , the estimates for D and $D + 2$ differ by a couple of percent, and those for D and $D + 1$ differ by around 10%. While we find that such a behavior of μ_{dc} as a function of D (for fixed N) is generic, the

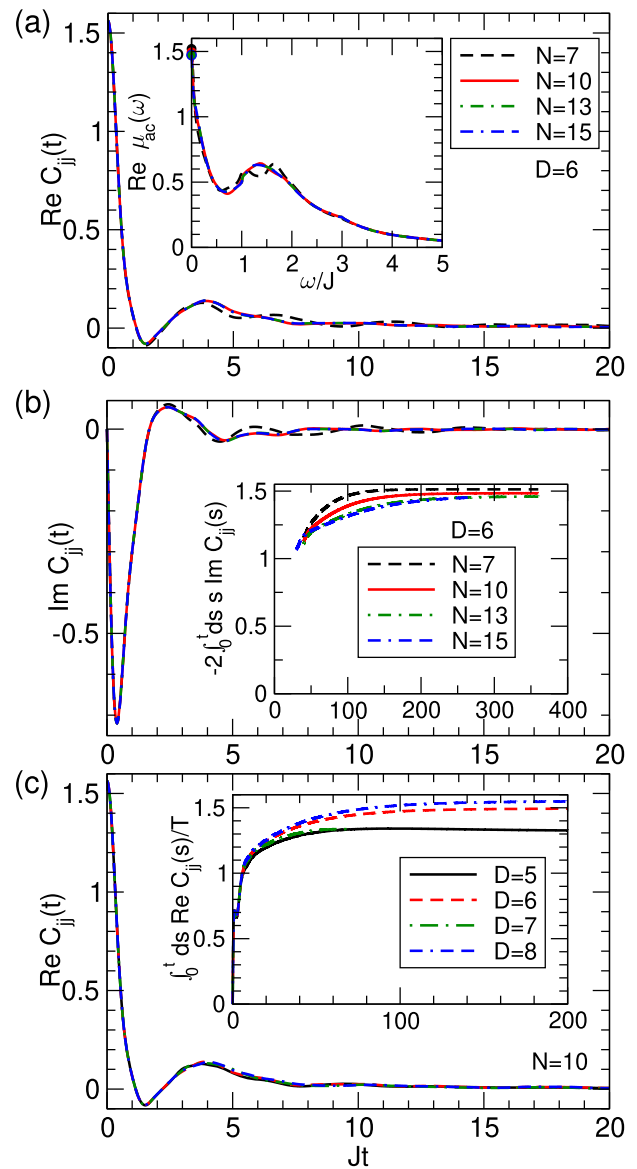


FIG. 3. Time dependence of (a) $\text{Re} C_{ij}$ and (b) $\text{Im} C_{ij}$ (both in units of J^2) for $D = 6$ and different chain lengths N . (c) Time dependence of $\text{Re} C_{ij}$ (in units of J^2) for $N = 10$ and different maximum hierarchy depths D . The inset in (a) shows the frequency profile of the dynamic mobility for $D = 6$ and different N . Full dots at $\omega = 0$ represent the results for μ_{dc} using the first equality in Eq. (5) (see also Table I). The inset in (b) shows how the result of the integration in Eq. (5) converges toward μ_{dc} as we increase the upper integration limit. To obtain smooth curves, we perform the moving average procedure described in the text. The inset in (c) shows how the result of the integration in Eq. (5) converges toward μ_{dc} as we increase the upper integration limit. The model parameters are $g/J = \omega_0/J = T/J = 1$.

magnitudes of the above-mentioned relative differences generally decrease with temperature. The preceding discussion implies that HEOM estimates for μ_{dc} should be taken with relative uncertainties not surpassing 10%.

TABLE I. Effects of finite N and D on HEOM results for the dc mobility. The HEOM is propagated up to time Jt_{\max} . Model parameters are $g/J = \omega_0/J = T/J = 1$.

(N, D)	μ_{dc} from Re $C_{jj}(t)$	μ_{dc} from Im $C_{jj}(t)$	Jt_{\max}
(10,5)	1.327	1.308	400
(10,6)	1.493	1.484	400
(10,7)	1.336	1.325	70
(10,8)	1.548	1.537	200
(7,6)	1.520	1.513	400
(13,6)	1.472	1.459	400
(15,6)	1.473	1.452	300

Without the specific HEOM closing [Eq. (13)], it would be nearly impossible to obtain meaningful results for the dc or ac mobility, which is apparent from Fig. 4(b) showing HEOM data for Re $C_{jj}(t)$ that use the TNL truncation. Model parameters are the same as in Fig. 3(c), to which the results in Fig. 4(b) are to be compared. Our closing smooths the local maximum in Re $C_{jj}(t)$ around $Jt \simeq 4$ and stabilizes the subsequent time evolution, whose oscillatory features under TNL truncation become more pronounced with increasing D . In addition to Re $C_{jj}(t)$, in Fig. 4(c), we show the quantity $\int_0^t ds \text{Re } C_{jj}(s)/T$ [see Eq. (5)] under TNL truncation (dashed lines) and our closing scheme (solid lines). While the agreement between the dashed and solid lines in Fig. 4(c) is good for $Jt \lesssim 10$, the results obtained under TNL truncation do not show any sign of reaching a long-time limit with increasing t . One could use the HEOM data with TNL truncation up to $Jt_{\max} \simeq 20$ (before the instabilities become more pronounced) to extract the dc mobility of around 1.25, and virtually the same estimate would be obtained using the HEOM data with our closing scheme up to $Jt_{\max} \simeq 20$ [see Fig. 4(c)]. Nevertheless, if one is to obtain the optical response with a decent frequency resolution using the HEOM data in Fig. 4(b) up to $Jt_{\max} \simeq 20$, one should probably perform additional numerical procedures, such as the zero-padding (to effectively increase t_{\max}), possibly combined with signal windowing.^{77,96} Such procedures,

however, may affect the intensities (and to some extent the positions) of the optical-response features, mainly in the low-frequency part that corresponds to the most challenging long-time dynamics. On the other hand, when we propagate our stabilized HEOM up to long real times, no additional numerical procedures on the HEOM data for $C_{jj}(t)$ are required to compute the optical response. While the observed dependence of our HEOM results on the parity of D could be attributed to our closing scheme, we believe that we handle this effect in an appropriate manner because we use it to estimate the relative error of our results for μ_{dc} . While a detailed explanation of our observations is beyond the scope of this investigation, we speculate about their possible origin as follows. In Eq. (9), $\mu_{\mathbf{n}}$ is the change in energy of the phononic subsystem due to the sequence of electron-phonon interaction events described by \mathbf{n} . At depth n , $\mu_{\mathbf{n}}/\omega_0$ can assume values $\pm n, \pm(n-2), \dots$, while at odd depths n , all $\mu_{\mathbf{n}}\mathbf{s}$ are nonzero, even depths feature some vectors \mathbf{n} for which $\mu_{\mathbf{n}} = 0$. At even depths, there are thus ADOs having both $\mu_{\mathbf{n}} = 0$ and $k_{\mathbf{n}} = 0$, meaning that the resonance condition $\varepsilon_k - \varepsilon_{k+k_{\mathbf{n}}} + \mu_{\mathbf{n}} = 0$ emerging from the free-rotation term in Eq. (9) is perfectly satisfied. On the other hand, at odd depths, the resonance condition is almost never perfectly met: even if $k_{\mathbf{n}} = 0$ for a particular \mathbf{n} , $\mu_{\mathbf{n}}$ is certainly nonzero. When the closing scheme in Eq. (13) is applied, the behavior of all ADOs at an odd maximum depth can be described by damped oscillations (in the lowest approximation that neglects links to other ADOs). In the same approximation, at an even maximum depth, there are ADOs that are exponentially suppressed with time without displaying any oscillatory behavior. The influence of such ADOs on the overall HEOM dynamics might be less pronounced than the influence of ADOs exhibiting damped oscillations.

We finish this section by briefly discussing the decrease in the number of active variables in our momentum-space HEOM with respect to existing real-space formulations. Namely, for an N -site chain, the number of ADOs upon hierarchy truncation at depth D is $n_{\text{ADO}}^{\text{rs}} = \binom{2N+D}{D}$ when working in real space ($q = 0$ phonon mode is considered) and $n_{\text{ADO}}^{\text{ms}} = \binom{2(N-1)+D}{D}$ when working in momentum space ($q = 0$ phonon mode is not considered). As the number of entries in each ADO is at the same time reduced by a

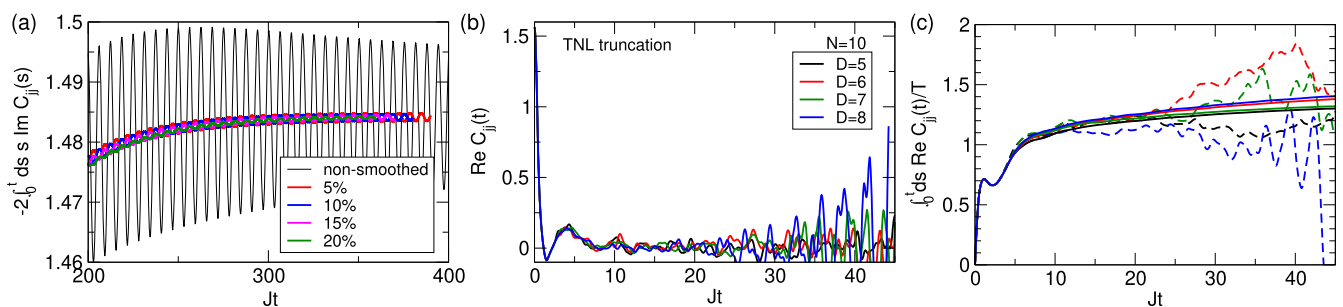


FIG. 4. (a) Long-time evolution of the quantity $-2 \int_0^t ds \text{Im } C_{jj}(s)$ [black solid line, label “non-smoothed,” see Eq. (5)] and its moving averages computed for different sizes (determined by N_{move} defined in the text) of the averaging window. Percentages are to be taken from the total number of points for which HEOM data are available. (b) Time dependence of Re C_{jj} (in units of J^2) under the TNL truncation for different values of D . (c) Time dependence of the quantity $\int_0^t ds \text{Re } C_{jj}(s)/T$ [see Eq. (5)] under the TNL truncation (dashed lines) and our closing in Eq. (13) (solid lines). The values of the model parameters and the color code are the same as in (b). The model parameters are $g/J = \omega_0/J = T/J = 1$, $N = 10$ in all three panels, and $D = 6$ in panel (a).

factor of N , the relative decrease in the number of variables that have to be propagated upon transferring from real to momentum space is

$$\frac{N^2 n_{\text{ADO}}^{\text{rs}} - N n_{\text{ADO}}^{\text{ms}}}{N^2 n_{\text{ADO}}^{\text{rs}}} = 1 - \frac{2(2N - 1)}{(2N + D)(2N + D - 1)}. \quad (20)$$

For a fixed N , the savings in computer memory increase with D . While the savings in computer memory for fixed D decrease with N , they can be substantial on relatively short chains that are still sufficiently long so that the corresponding results are representative of the long-chain limit. For example, for $N = 10$ and $D = 6$ (as in Fig. 3), the relative decrease in the number of active variables with respect to HEOM formulations in real space is around 40%.

C. Numerical examples concerning sum rules

Figure 5(a) summarizes how the relative accuracy

$$\delta_{\text{OSR}} = \frac{\left| \int_0^{+\infty} d\omega \text{Re} \mu_{\text{ac}}(\omega) - \frac{\pi}{2} |\langle H_e \rangle| \right|}{\frac{\pi}{2} |\langle H_e \rangle|}, \quad (21)$$

with which the OSR is satisfied depends on N and D for the same values of model parameters as in Figs. 2–4. We observe that, in the ranges of N and D considered, δ_{OSR} generally decreases with both N [assuming fixed D ; see black circles, right vertical and top horizontal axes in Fig. 5(a)] and D [assuming fixed N ; see red squares, left vertical and bottom horizontal axes in Fig. 5(a)].

Fixing D to 6 and varying N from 7 to 15, we observe the steepest decrease in δ_{OSR} upon increasing N from 7 to 10, while further increases in N from 10 to 13 and 15 result in a much milder decrease in δ_{OSR} . This observation is consistent with both the imaginary-axis data shown in Fig. 2(a) and the real-time data presented in Figs. 3(a) and 3(b) and Table I. Namely, the largest (and smallest) variation in $C_{ij}(\tau)$, $C_{ij}(t)$, and μ_{dc} upon increasing $N \in \{7, 10, 13, 15\}$ to the subsequent value from the sequence $[7, 10, 13, 15]$ is observed for $N = 7$ ($N = 13$). The decrease in δ_{OSR} with increasing N is, however, ultimately limited by the fact that δ_{OSR} depends on quantities that are themselves calculated numerically and thus bring their own numerical errors into the final expression. The integral over frequencies is computed using the trapezoidal rule, while $\langle H_e \rangle$ is computed for finite values of N and D (we do not use its “exact” value in the limit $N, D \rightarrow \infty$ that could be obtained using our⁹⁶ or some other⁷⁶ method). The error incurred when the integral $\int_0^{+\infty} d\omega \text{Re} \mu_{\text{ac}}(\omega)$ is evaluated using the trapezoidal rule is of the order of $(\Delta\omega/J)^3$,¹¹⁹ where the frequency step $\Delta\omega$ is related to the maximum propagation time t_{max} by $\Delta\omega/J = \pi/(Jt_{\text{max}})$. Fixing D and varying N , we use $Jt_{\text{max}} = 300$, meaning that the numerical error of the integral $\int_0^{+\infty} d\omega \text{Re} \mu_{\text{ac}}(\omega)$ is of the order of $(\pi/300)^3 \sim 10^{-6}$. In other words, $N = 15$ is sufficiently large that δ_{OSR} is most probably not dominated by finite-size effects in N but rather by the error of numerical integration. This is further corroborated by the fact that the kinetic energies for $N = 13$ and $N = 15$ differ on the seventh decimal place (see Table II), meaning that the error of the kinetic energy for $N = 15$ is at least an order of magnitude below the numerical integration error. On the other hand, for $N = 7$, δ_{OSR} is most probably limited by the finite-size effects in $\langle H_e \rangle$. The data in Table II suggest that the error of $|\langle H_e \rangle|_{N=7, D=6}$, which can be inferred from its deviation

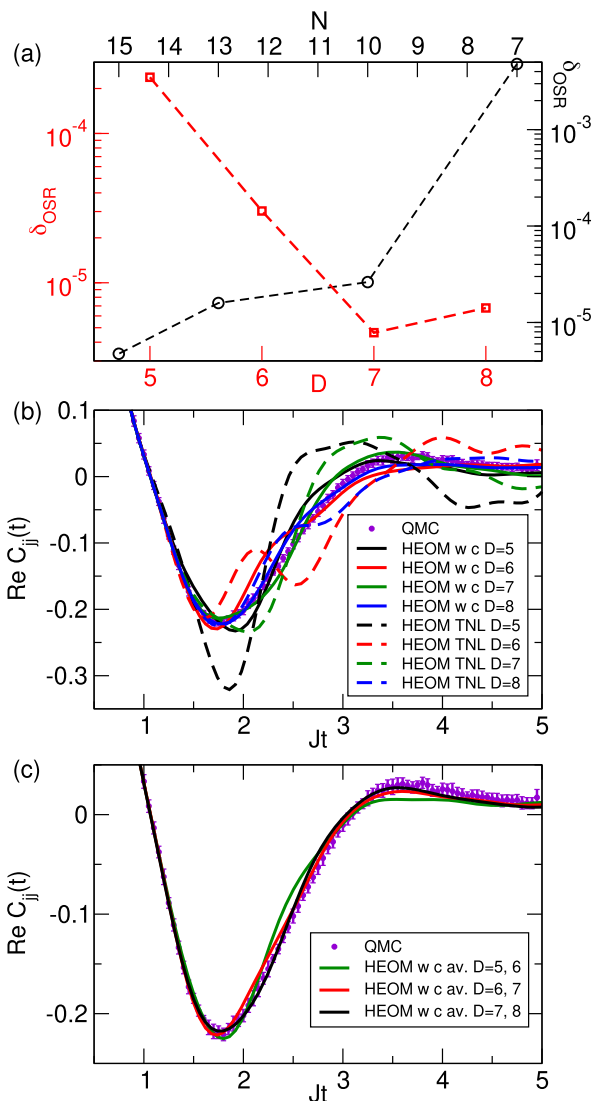


FIG. 5. (a) Relative accuracy δ_{OSR} [Eq. (21)] as a function of D for $N = 10$ (red squares, left vertical and bottom horizontal axes) and as a function of N for $D = 6$ (black circles, right vertical and top horizontal axes). The dashed lines connecting the symbols serve as guides for the eye. The model parameters are $g/J = \omega_0/J = T/J = 1$ ($\lambda = 0.5$). For $N = 10$, we use $C_{ij}(t)$ up to $Jt_{\text{max}} = 200$ for $D = 5, 6$, and 8, while for $D = 7$, we take $Jt_{\text{max}} = 70$ (see also Table I). For $D = 6$, we use $C_{ij}(t)$ up to $Jt_{\text{max}} = 300$ for $N = 7, 10, 13$, and 15. (b) Comparison of HEOM (lines) and QMC (symbols with error bars) results for $\text{Re } C_{ij}(t)$ (in units of J^2) for $N = 10$, $g/J = 1/\sqrt{3}$, $\omega_0/J = 1/3$, $T/J = 1$ ($\lambda = 0.5$), and different values of D . Solid lines (label “w c”) employ our closing [Eq. (13)], while dashed lines (label “TNL”) use the TNL truncation. (c) Comparison of HEOM results averaged over depths $D - 1$ and D (solid lines) with QMC results (symbols with error bars) for $D = 6, 7$, and 8, while other parameters assume the same values as in (b). QMC data are the courtesy of N. Vukmirović.

from $|\langle H_e \rangle|_{N=10, D=6}$, is of the order of 10^{-3} . This is consistent with the value of δ_{OSR} reported in Fig. 5(a).

A similar analysis can be repeated by fixing N and varying D . In practice, our criterion for choosing N and D is that $\delta_{\text{OSR}} \lesssim 10^{-4}$. As

TABLE II. Kinetic energy of the electron as a function of N and D for $g/J = \omega_0/J = T/J = 1$.

(N, D)	$ \langle H_e \rangle / J$
(7,6)	1.155 308 279 5
(10,6)	1.154 623 995 5
(13,6)	1.154 622 914 9
(15,6)	1.154 623 007 8

mentioned in Sec. II E and as can be seen from the supplementary material, the relative accuracy with which the sum rules in Eq. (17) are satisfied is generally better than δ_{OSR} .

At higher temperatures ($T/\omega_0 \gtrsim 3$), we find that HEOM data for fixed N and two sufficiently large consecutive depths $D - 1$ and D generally have almost the same δ_{OSR} [as in Fig. 5(a)], while there are some differences between them already at relatively short times. For example, for $g/J = 1/\sqrt{3}$, $\omega_0/J = 1/3$, and $T/J = 1$ ($\lambda = 0.5$), we find that the differences between HEOM results for different values of D (we fix $N = 10$) appear already for $Jt \simeq 2$ or $\omega_0 t \simeq 2/3$ [see Fig. 5(b)], in contrast to the situation in Figs. 3(c) and 4(c), where the differences appear at somewhat longer times. We perform HEOM computations with TNL truncation and our specific closing and find that the short-time differences observed in Fig. 5(b) cannot be exclusively attributed to our closing scheme as they are also present under the TNL truncation. Actually, our closing stabilizes the evolution of $\text{Re } C_{jj}(t)$ and lowers the differences between HEOM results for different values of D (with respect to the TNL truncation). To reveal whether our HEOM results are reliable, we compare them with QMC data obtained using the methodology developed in Ref. 63. QMC results are numerically “exact,” as their convergence with respect to all control parameters of the simulation has been carefully checked. In Figs. 5(b) and 5(c), we show QMC results with their statistical error bars. Figure 5(b) suggests that the difference between HEOM (with our closing) and QMC results decreases relatively slowly with increasing D , while HEOM dynamics for D s of the same parity ($D = 5, 7$ and $D = 6, 8$) deviate from the QMC results in a similar manner (both deviations are positive/negative). It is known that the convergence of a slowly converging sequence can be improved by performing an appropriate sequence transformation, such as the Shanks or Richardson transformation.¹²⁰ Here, inspired by the reasoning behind the Shanks transformation, we want to improve the convergence of the sequence $C_{jj}(D; t)$ in D (for fixed N and at each instant t) by handling the term whose decay (as a function of D) toward zero is the slowest. Based on Fig. 5(b), one may imagine that the dependence of $C_{jj}(D; t)$ on D can be represented as

$$C_{jj}(D; t) = C_{jj}^{D \rightarrow \infty}(t) + \alpha(t) \frac{(-1)^D}{D^a}, \quad (22)$$

where $a > 0$, $\alpha(t)$ is a complex number, $C_{jj}^{D \rightarrow \infty}(t)$ is the sought large- D limit, while the alternating term $(-1)^D$ mimics the observed alternation of HEOM results with respect to QMC results with the parity of D . We use Eq. (22) to arrive at

$$\frac{C_{jj}(D-1; t) - C_{jj}^{D \rightarrow \infty}(t)}{C_{jj}(D; t) - C_{jj}^{D \rightarrow \infty}(t)} = -\left(\frac{D-1}{D}\right)^a \approx -1, \quad (23)$$

where the last approximate equality holds for sufficiently large D (the smaller a , the smaller the minimum value of D for which the approximation is good). Equation (23) implies that

$$C_{jj}^{D \rightarrow \infty}(t) \approx \frac{C_{jj}(D; t) + C_{jj}(D-1; t)}{2}, \quad (24)$$

which suggests that the large- D limit of $C_{jj}(D; t)$ can be approached more rapidly by considering the transformed sequence $[C_{jj}(D; t) + C_{jj}(D-1; t)]/2$ instead of the original sequence $C_{jj}(D; t)$. While our arguments are not fully mathematically rigorous, they produce plausible results, as revealed in Fig. 5(c), showing how the HEOM data averaged over two consecutive depths (5 and 6, 6 and 7, 7 and 8) compare to the QMC data. We observe that the agreement with the QMC data improves with increasing the depths over which the averaging is performed. As a result, when averaging over depths 7 and 8, HEOM results are within the QMC error bars in the largest portion of the time window displayed. It then seems reasonable that our final HEOM result in this parameter regime be the average of the results for $D = 7$ and 8. Finally, whenever our dataset¹¹⁷ provides raw data for $C_{jj}(t)$ for two consecutive depths, we use the average $C_{jj}(t)$ when computing physical quantities.

D. Signatures of the electron-phonon interaction in time and frequency domains

Figures 6(a1)–6(c3) present selected results concerning the dynamics of the $j-j$ correlation function, diffusion constant, and diffusion exponent, together with the frequency profile of the dynamical mobility. Our analysis of the parameter regimes in which HEOM computations are free of numerical instabilities [see Figs. 7(a)–7(c)] identifies three typical behaviors of the aforementioned quantities.

In the weak-coupling regime ($\lambda = 0.01$) for $\omega_0/J = 1/3$ and 1, we find a smooth crossover from the ballistic electronic motion at short times toward the diffusive motion at long times. The representative results for $\omega_0/J = 1$ are shown in Figs. 1(a) and 1(b), while Figs. 6(a1)–6(a3) show representative results for $\omega_0/J = 1/3$. $\text{Re } C_{jj}(t)$, $\mathcal{D}(t)$, and $\alpha(t)$ are all monotonic functions of time, while the dynamical-mobility profile has only the Drude peak at $\omega = 0$ and bears an overall resemblance to the Drude model.

Already in the intermediate-coupling regime ($\lambda = 0.5$) for $\omega_0/J = 1/3$ and 1, the ballistic-to-diffusive crossover is not smooth. The representative results for $\omega_0/J = 1$ are presented in Figs. 3(a)–3(c), whereas Figs. 6(b1)–6(b3) show representative results for $\omega_0/J = 1/3$. $\text{Re } C_{jj}(t)$, $\mathcal{D}(t)$, and $\alpha(t)$ are non-monotonic functions of time. We observe that $\text{Re } C_{jj}(t) < 0$ on intermediate time scales, on which the diffusion constant decreases with time. This is clear from Eq. (6), which establishes a connection between the sign of $\text{Re } C_{jj}(t)$ and the intervals of monotonicity of $\mathcal{D}(t)$. $\alpha(t)$ reaches a pronounced local minimum on the very same time scale. In other words, intermediate time scales in the intermediate-interaction regime witness a temporally limited slow-down of the electronic motion. Depending on the parameter regime (typically for strong g and at high T), that slow-down may be so pronounced that the electronic motion changes its character from superdiffusive ($\alpha > 1$) to subdiffusive ($\alpha < 1$) over a limited time frame. While such a change occurs for model parameters studied in Figs. 6(b1)–6(b3),

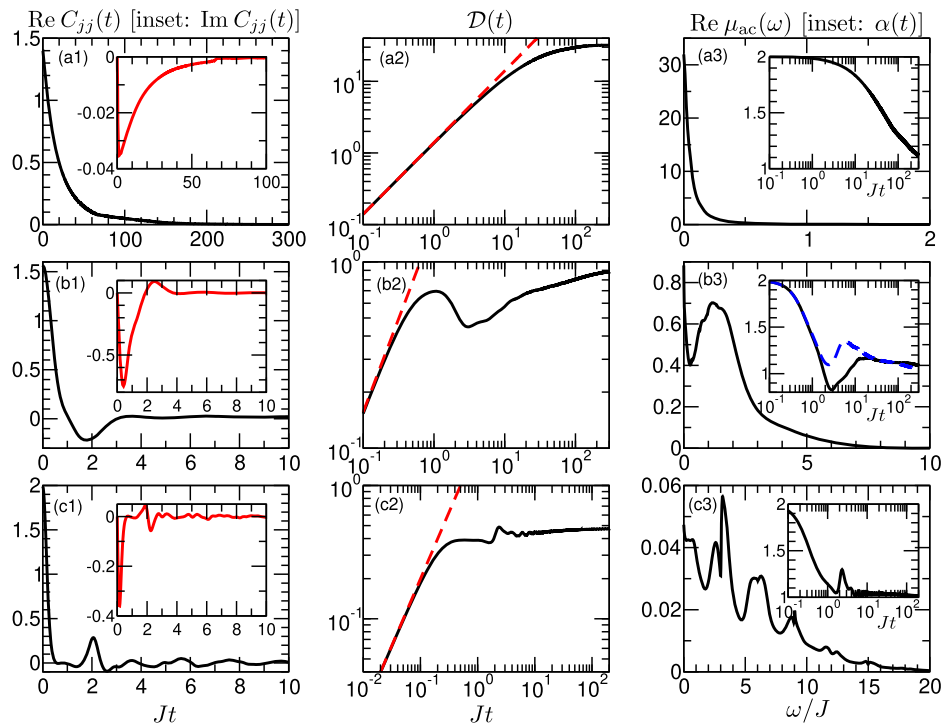


FIG. 6. Time dependence of $\text{Re } C_{jj}$ [in units of J^2 , (a1)–(c1)], \mathcal{D} [in units of J , (a2)–(c2)], and the frequency dependence of $\text{Re } \mu_{ac}(\omega)$ [(a3)–(c3)] for (a) $\omega_0/J = 1/3$, $\lambda = 0.01$, $T/J = 1$, (b) $\omega_0/J = 1/3$, $\lambda = 0.5$, $T/J = 1$, and (c) $\omega_0/J = 3$, $\lambda = 0.5$, $T/J = 10$. The insets of panels (a1)–(c1) [(a3)–(c3)] display the time dependence of $\text{Im } C_{jj}$ in units of J^2 (α). The dashed lines in (a2)–(c2) represent the short-time (ballistic) limit of the diffusion constant, $\mathcal{D}_{\text{bal}}(t) = C_{jj}(0)t$. The dashed line in the inset of (c2) represents $\alpha(t)$ for the parameter regime examined in Fig. 3. The results in (a1)–(a3) emerge from HEOM computations using $N = 128$, $D = 2$, while the remaining results are the arithmetic average of HEOM computations using: (b1)–(b3) $N = 10$, $D = 7$ and $N = 10$, $D = 8$; (c1)–(c3) $N = 5$, $D = 18$ and $N = 5$, $D = 19$.

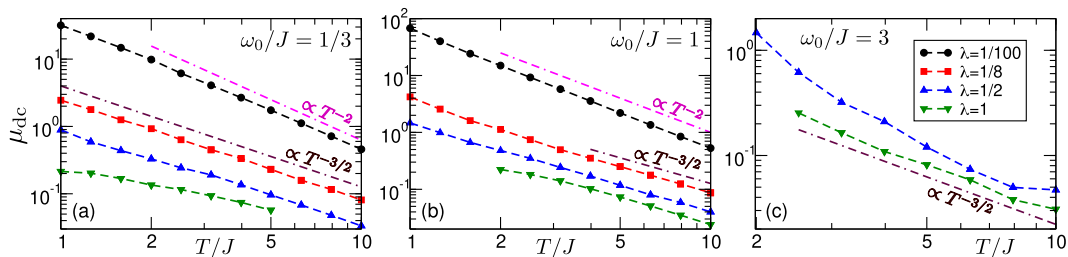


FIG. 7. HEOM-method results for the temperature-dependent dc mobility for different interaction strengths (different values of parameter λ) and (a) $\omega_0/J = 1/3$, (b) $\omega_0/J = 1$, and (c) $\omega_0/J = 3$. Full symbols are HEOM-method results, while dashed lines connecting them serve as guides to the eye. Double dashed-dotted lines show the theoretically predicted²⁶ power-law scaling $\mu_{dc} \propto T^{-2}$ or $\mu_{dc} \propto T^{-3/2}$ in appropriate limiting cases (no fitting procedures have been performed on the HEOM data).

it is absent for model parameters studied in Figs. 3(a)–3(c) [see the dashed line in the inset of Fig. 6(b3)]. Apart from the Drude peak at $\omega = 0$, the dynamical mobility features a prominent finite-frequency peak.

The available results for $\omega_0/J = 3$, which are obtained for sufficiently strong interactions and at sufficiently high temperatures, also display a non-monotonic behavior of $\text{Re } C_{jj}(t)$, $\mathcal{D}(t)$, and $\alpha(t)$. In contrast to the results for $\omega_0/J = 1/3$ and 1, $\mathcal{D}(t)$ increases in almost regular steps centered around integer multiples of $2\pi/\omega_0$. The first peak of $\text{Re } C_{jj}(t)$ is indeed centered at $2\pi/\omega_0$,

while subsequent peaks are somewhat displaced toward earlier times [see Fig. 6(c1)]. The dynamic-mobility profile is characterized by relatively broad peaks centered around integer multiples of ω_0 . These features suggest that we are close to the genuine small-polaron limit.^{18,32}

E. Temperature dependence of the dc mobility

Figures 7(a)–7(c) present the central result of our study, the HEOM-method results for the temperature dependence of μ_{dc} for three different values of ω_0/J . As discussed in Sec. III B, our results

for μ_{dc} should be assigned relative errors not surpassing 10%. The values reported in Figs. 7(a)–7(c) are obtained by averaging μ_{dc} computed using only $\text{Re } C_{jj}(t)$ or only $\text{Im } C_{jj}(t)$ [Eq. (5)]. The smoothing procedure described in Sec. III B is applied when considering only $\text{Im } C_{jj}(t)$. At elevated temperatures ($T/\omega_0 \gtrsim 3$), we additionally average HEOM results for two consecutive depths, as discussed in Sec. III C.

Section III F gives an example of numerical instabilities appearing for sufficiently strong g or at sufficiently low T , which prevent us from obtaining reliable HEOM results, e.g., when $\lambda > 1$ or when $T/J < 2$ and $\lambda = 1$ in Fig. 7(b). Our data for $\lambda = 1$ in Figs. 7(a) and 7(b) suggest that μ_{dc} enters saturation on the low-temperature side. If we could lower the temperature further, we would enter the regime of thermally activated transport, in which μ_{dc} grows with T , while we obtain HEOM results only in regimes where μ_{dc} decreases with T . Concerning the temperature dependence of μ_{dc} , we find that the HEOM mobilities at low g and for $\omega_0/J = 1/3$ and 1 are consistent with the recently found scaling $\mu_{dc} \propto T^{-2}$,²⁶ which is shown as a double dashed–dotted line. For stronger coupling and at sufficiently high temperatures, the HEOM mobilities are consistent with the scaling $\mu_{dc} \propto T^{-3/2}$, which is again shown as a double dashed–dotted line.

F. Numerical instabilities for strong electron-phonon interactions and at low temperatures

For stronger interactions, at lower temperatures, and for larger ω_0/J , the numerical instabilities appearing already at relatively short real times (despite employing our specific closing strategy) prevent us from computing the long-time dynamics of $C_{jj}(t)$ and thus μ_{dc} . As an example, in Figs. 8(a) and 8(b), we present our HEOM results in the strong-coupling regime ($\lambda = 2$) for $\omega_0/J = 1$ at a relatively low temperature $T/J = 1$ [Fig. 8(a)] and at an elevated temperature $T/J = 5$ [Fig. 8(b)].

For $T/J = 1$, numerical instabilities appear already for $Jt \gtrsim 3$ and become more pronounced at longer times. The maximum time up to which reliable HEOM results for $C_{jj}(t)$ can be obtained is thus of the same order of magnitude as the maximum time that can be reached in real-time QMC simulations, whose results are shown as full symbols (QMC error bars are omitted here for visual clarity). The inset of Fig. 8(a) shows how the integrals $\int_0^t ds \text{Re } C_{jj}(s)/T$ and $-2 \int_0^t ds \text{Im } C_{jj}(s)$, whose $t \rightarrow +\infty$ limit determines μ_{dc} , evolve as functions of their upper limit t . While the numerical instabilities become amplified when μ_{dc} is computed using only $\text{Im } C_{jj}(t)$, the data using only $\text{Re } C_{jj}(t)$ may suggest that the maximum time $Jt_{\text{max}} = 3$ is sufficiently long to capture the electron's diffusive motion [$\int_0^t ds \text{Re } C_{jj}(s)/T$ reaches a plateau for $2 \leq Jt \leq 3$]. Nevertheless, the corresponding mobility estimate may be unreliable. Namely, as discussed in Ref. 42, for strong interactions and at not too high temperatures, $\text{Re } C_{jj}(t)$ exhibits a series of peaks whose envelope decays over many phonon periods. Our HEOM computations do capture the most prominent peak centered at $t = 0$. Still, the numerical instabilities arise well before the completion of the first phonon period $2\pi/\omega_0$, meaning that the HEOM results fully miss the contributions to μ_{dc} from the peaks at later times. Such contributions may be appreciable because of the slowly decaying envelope, and one may thus expect that the HEOM result underestimates the dc mobility.

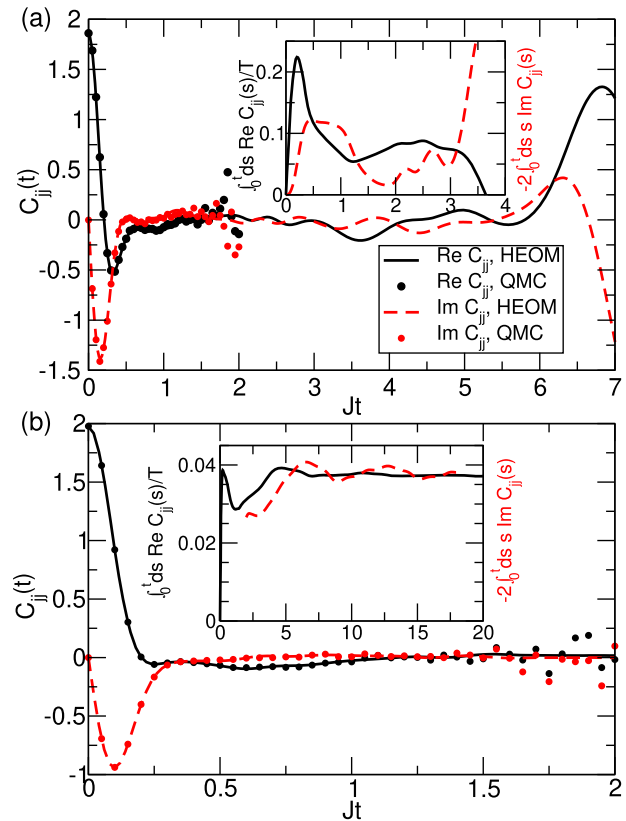


FIG. 8. Time dependence of C_{jj} (in units of J_2) computed using the HEOM method (lines) and the real-time QMC method developed in Ref. 63 (symbols) for $\omega_0/J = 1$, $\lambda = 2$, and (a) $T/J = 1$, (b) $T/J = 5$. Solid (dashed) lines display $\text{Re } C_{jj}(t)$ [$\text{Im } C_{jj}(t)$]. The insets display time evolution of $\int_0^t ds \text{Re } C_{jj}(s)/T$ (solid lines) and $-2 \int_0^t ds \text{Im } C_{jj}(s)$ (dashed lines). The HEOM computations in (a) use $N = 10$ and $D = 8$, while (b) shows the arithmetic average of HEOM results obtained for $N = 7, D = 10$ and $N = 7, D = 11$. QMC simulations in both (a) and (b) use $N = 10$, and the respective data are the courtesy of N. Vukmirović.

For strong interactions and at higher temperatures, we do not observe numerical instabilities [see Fig. 8(b)], and our HEOM method can again reach much longer times than real-time QMC methods. Higher temperatures, in combination with our closing strategy, generally stabilize the HEOM. Since the amplitude of the aforementioned later-time peaks is strongly suppressed at higher temperatures,⁴² the HEOM method may provide reliable results for μ_{dc} . The inset of Fig. 8(b) shows that mobility computations using either $\text{Re } C_{jj}(t)$ or $\text{Im } C_{jj}(t)$ [the latter in conjunction with the moving-average procedure, see the discussion of Fig. 3(b)] lead to virtually the same HEOM result, $\mu_{dc}^{\text{HEOM}} = 0.0375$.

Finally, the very good agreement between the HEOM and QMC results in Figs. 8(a) and 8(b) strongly suggests that the values of D employed in the corresponding HEOM computations are sufficiently large. One may ask themselves whether a larger value of D could mitigate the instabilities observed in Fig. 8(a). Unfortunately, the results of Ref. 101 show that the undamped-mode HEOM cannot be stabilized by further increasing D .

IV. CONCLUSION AND OUTLOOK

We develop the momentum-space HEOM method to compute the real-time current–current correlation function at finite temperature for the 1d Holstein model, which provides us with direct access to its transport properties. By exploiting the decoupling of the $q = 0$ phonon mode and formulating the HEOM in the momentum representation, we greatly reduce the number of variables with respect to existing real-space HEOM implementations. This circumstance has enabled us to obtain results that take into account all important phonon-assisted processes (i.e., D is sufficiently large) on chains that are sufficiently long (i.e., N is sufficiently large) so that the finite-size effects are minimized. Another distinctive feature of our formalism is its specific hierarchy closing strategy [Eq. (13)], which has enabled us to overcome the numerical instabilities inherent to the undamped-mode HEOM formulated on a finite chain and truncated at a finite maximum hierarchy depth. We are thus in a position to provide reliable results for the dc mobility by computing $C_{jj}(t)$ up to quite long real times by which it has almost decayed to zero, i.e., the electronic motion has become diffusive. A detailed analysis of how $C_{jj}(t)$ and, therefore, μ_{dc} depend on N and D suggests that our results for temperature-dependent mobility should be considered with uncertainties typically below 10%. Still, the instabilities remain for strong couplings, at low temperatures, and for large phonon frequencies. In such parameter regimes, we can obtain $C_{jj}(t)$ only up to relatively short real times.

Our momentum-space HEOM method, which has already achieved substantial memory savings with respect to existing real-space HEOM implementations (see Sec. III B), may be combined with advanced propagation techniques based on the tensor formalism^{80,103,121–123} or with on-the-fly filtering techniques¹²⁴ to treat longer chains or larger maximum depths. This could pave the way toward HEOM computations at lower temperatures or stronger interactions. In such parameter regimes, accurate results for electronic dynamics can be obtained using the hierarchy of Davydov's *Ansätze*.^{81,82} However, its current implementations assume that the initial state of the electron–phonon system is factorized and that phonons are in thermal equilibrium with the system with no electrons. While following the electron's dynamics from such a state can provide information on the dc mobility,^{40,83,97} it provides no information on the frequency-dependent mobility, which follows from the current–current correlation function (see Sec. II A). Its computation, in turn, necessitates an appropriate representation of the thermal equilibrium state of the interacting electrons and phonons (see Sec. II B), which has still not been addressed using the hierarchy of Davydov's *Ansätze*, to the best of our knowledge. Our study may motivate an extension of Davydov's *Ansätze* approach to compute equilibrium correlation functions in parameter regimes that are the most challenging for the HEOM method.

We also note that, at least in the limiting case of slow phonons, an interesting physical picture for the finite-frequency peak we observe in the optical response may be constructed based on the transient localization scenario.¹²⁵ While this approach was originally devised to study transport limited by intermolecular vibrations modulating the hopping amplitude, its more recent refinements¹²⁶ and applications¹²⁷ have considered the Holstein model in the limit of vanishing carrier density. A more detailed study in this direction might be the subject of future work. We finally note that the method

proposed in this manuscript cannot be directly applied to study carrier transport limited by the nonlocal electron–phonon interaction (e.g., the Peierls model).¹²⁸ The developments reported here crucially lean on the fact that the current operator j is a purely electronic operator [see Eq. (3)]. In other words, the current–current correlation function $C_{jj}(t)$ can be computed using only the electronic RDM (see Sec. II B). On the other hand, when the electron interacts linearly with intermolecular phonons modulating the hopping integral, the current operator is a mixed electron–phonon operator.^{37,100} This means that $C_{jj}(t)$ cannot be computed using only the electronic RDM. One should thus devise a procedure to retrieve correlation functions involving phonon operators from the HEOM formalism. While this complex issue is well beyond the scope of this study, the herein developed momentum-space representation of the HEOM will remain beneficial to the overall computational performance of such a procedure.

SUPPLEMENTARY MATERIAL

See the supplementary material for the details of HEOM computations [values of N and D employed, reference HEOM results for the electron's kinetic energy and moments of $C_{jj}(\omega)$, as well as the relative accuracy with which different sum rules are satisfied]. The supplementary material contains all the information needed to use our numerical data that are deposited on the Zenodo platform (see Ref. 117).

ACKNOWLEDGMENTS

The author acknowledges Nenad Vukmirović, Darko Tanasković, and Petar Mitrić for numerous insightful and stimulating discussions. The author acknowledges funding provided by the Institute of Physics Belgrade through a grant from the Ministry of Science, Technological Development, and Innovations of the Republic of Serbia. Computational time on the ARIS supercomputing facility (GRNET, Athens, Greece) was granted by the NI4OS-Europe network under the CoNTraSt project (Open Call 2022, Project No. ni4os002). Computations were also partially performed on the PARADOX-IV supercomputing facility at the Scientific Computing Laboratory, National Center of Excellence for the Study of Complex Systems, Institute of Physics Belgrade.

AUTHOR DECLARATIONS

Conflict of Interest

The author has no conflicts to disclose.

Author Contributions

Veljko Janković: Conceptualization (lead); Data curation (lead); Formal analysis (lead); Investigation (lead); Methodology (lead); Validation (lead); Visualization (lead); Writing – original draft (lead).

DATA AVAILABILITY

The data that support the findings of this study are openly available on the Zenodo platform at <http://doi.org/10.5281/zenodo.8068547>.¹¹⁷

APPENDIX A: DERIVATION OF THE HEOM FOR THE REAL-TIME CURRENT-CURRENT CORRELATION FUNCTION

The decoupling of the $q = 0$ phonon mode from the rest of the system permits us to consider Hamiltonians $H'_{\text{ph}} = \sum'_q \omega_q b_q^\dagger b_q$ and $H'_{\text{e-ph}} = \sum'_q V_q B_q$ without the $q = 0$ term, which is signaled by primes. The Feynman–Vernon influence functional theory¹²⁹ implies that the only phonon quantity that determines the dynamics of $\iota(t)$ is the equilibrium free-phonon correlation function (we assume $t > 0$ and $q_2, q_1 \neq 0$),

$$C_{q_2 q_1}(t) = \text{Tr}'_{\text{ph}} \left\{ B_{q_2}^{(I)}(t) B_{q_1} \frac{e^{-\beta H'_{\text{ph}}}}{Z'_{\text{ph}}} \right\} \\ = \delta_{q_1, -q_2} \sum_{m=0}^1 c_{q_2 m} e^{-\mu_{q_2 m} t}. \quad (\text{A1})$$

The time dependence in Eq. (A1) is in the interaction picture [signaled by the superscript (I)], $B_q^{(I)}(t) = e^{iH'_{\text{ph}} t} B_q e^{-iH'_{\text{ph}} t}$, $Z'_{\text{ph}} = \text{Tr}'_{\text{ph}} e^{-\beta H'_{\text{ph}}}$ is the free-phonon partition sum, while

$$c_{q0} = \left(\frac{g}{\sqrt{N}} \right)^2 \frac{1}{1 - e^{-\beta \omega_q}}, \quad \mu_{q0} = +i\omega_q, \quad (\text{A2})$$

$$c_{q1} = \left(\frac{g}{\sqrt{N}} \right)^2 \frac{1}{e^{\beta \omega_q} - 1}, \quad \mu_{q1} = -i\omega_q. \quad (\text{A3})$$

The partial trace over phonons in Eq. (8) is performed in the same manner as in Refs. 96, 98, 99, and 108, and the final result for ι in the interaction picture reads as

$$\iota^{(I)}(t) = \mathcal{T} e^{-[\Phi_1(t) + \Phi_2(\beta) + \Phi_3(t, \beta)]} j \frac{e^{-\beta H_e}}{Z_e}. \quad (\text{A4})$$

Here, $Z_e = Z/Z'_{\text{ph}}$ is the electronic partition sum [Eq. (12)], while the influence phases are given as

$$\Phi_1(t) = \sum'_{qm} \int_0^t ds_2 \int_0^{s_2} ds_1 V_q^{(I)}(s_2)^\times e^{-i\mu_{qm}(s_2 - s_1)} \\ \times \left[\frac{c_{qm} + c_{q\bar{m}}}{2} V_{-q}^{(I)}(s_1)^\times + \frac{c_{qm} - c_{q\bar{m}}}{2} V_{-q}^{(I)}(s_1)^\circ \right], \quad (\text{A5})$$

$$\Phi_2(\beta) = -\sum'_{qm} \int_0^\beta d\tau_2 \int_0^{\tau_2} d\tau_1 {}^C \bar{V}_{-q}(\tau_1) \\ \times e^{i\mu_{qm}(\tau_2 - \tau_1)} c_{qm} {}^C \bar{V}_{-q}(\tau_2), \quad (\text{A6})$$

$$\Phi_3(t, \beta) = -i \sum'_{qm} \int_0^t ds \int_0^\beta d\tau V_q^{(I)}(s)^\times \\ \times e^{-i\mu_{qm}s} e^{i\mu_{qm}(\beta - \tau)} c_{qm} {}^C \bar{V}_{-q}(\tau). \quad (\text{A7})$$

The influence phase $\Phi_1(t)$ describes the pure real-time evolution, and the hyperoperators V^\times and V° entering Eq. (A5) act on an arbitrary operator O as $V^\times O = [V, O]$ (commutator) and $V^\circ O = \{V, O\}$ (anticommutator), respectively. We define $\bar{m} = 1$ for $m = 0$ and vice versa. The influence phase $\Phi_2(\beta)$ represents the pure imaginary-time evolution, while $\Phi_3(t, \beta)$ takes into account the contributions

mixing the real-time and imaginary-time evolutions. The imaginary time-dependent operator in the interaction picture is defined as $\bar{V}(\tau) = e^{H_e \tau} V e^{-H_e \tau}$, while the hyperoperator ${}^C V$ appearing in Eqs. (A6) and (A7) acts on an arbitrary operator O as ${}^C V O = O V$. The time ordering symbol \mathcal{T} imposes the following hyperoperator ordering: the hyperoperators depending on real time act after the imaginary time-dependent hyperoperators; the arguments of real time-dependent hyperoperators are chronologically ordered, while the arguments of imaginary time-dependent hyperoperators are anti-chronologically ordered. This ensures that the general term in the expansion of Eq. (A4) is of the form

$$V_{q_n}^{(I)}(s_n)^{\pi_n} \dots V_{q_1}^{(I)}(s_1)^{\pi_1} j \frac{e^{-\beta H_e}}{Z_e} \bar{V}_{p_m}(\tau_m) \dots \bar{V}_{p_1}(\tau_1),$$

where $n + m$ is even, $\pi_1, \dots, \pi_n \in \{\times, \circ\}$, $t \geq s_n \geq \dots \geq s_1 \geq 0$, $\beta \geq \tau_m \geq \dots \geq \tau_1 \geq 0$, and $q_n + \dots + q_1 + p_m + \dots + p_1 = 0$.

Starting from Eq. (A4), the HEOM [Eq. (9)] is formulated in the standard manner.^{88,96} The ADO $\iota_n^{(n)}$ is defined (in the interaction picture) as

$$\iota_n^{(I, n)}(t) = f(\mathbf{n}) \mathcal{T} \prod'_{qm} \left\{ i \int_0^t ds e^{-i\mu_{qm}(t-s)} \left[\frac{c_{qm} + c_{q\bar{m}}}{2} V_{-q}^{(I)}(s)^\times \right. \right. \\ \left. \left. + \frac{c_{qm} - c_{q\bar{m}}}{2} V_{-q}^{(I)}(s)^\circ \right] + e^{-i\mu_{qm}t} \int_0^\beta d\tau e^{i\mu_{qm}(\beta - \tau)} \right. \\ \left. \times c_{qm} {}^C \bar{V}_{-q}(\tau) \right\}^{n_{qm}} e^{-[\Phi_1(t) + \Phi_2(\beta) + \Phi_3(t, \beta)]} j \frac{e^{-\beta H_e}}{Z_e}. \quad (\text{A8})$$

The rescaling factor $f(\mathbf{n})$ reads as¹²⁴

$$f(\mathbf{n}) = \prod'_{qm} [c_{qm}^{n_{qm}} n_{qm}!]^{-1/2}. \quad (\text{A9})$$

Equation (A8) explicitly shows that $\iota_n^{(n)}$ decreases the momentum of the electronic subsystem by $k_n = \sum'_{qm} q n_{qm}$, meaning that only N matrix elements $\langle k | \iota_n^{(n)} | k + k_n \rangle$ connecting the free-electron states whose momenta differ by k_n assume nonzero values.

Setting $t = 0$ in Eq. (A8) gives the following initial condition for the real-time HEOM:

$$\iota_n^{(n)}(0) = j f(\mathbf{n}) \mathcal{T} \prod'_{qm} \left\{ \int_0^\beta d\tau e^{i\mu_{qm}(\beta - \tau)} c_{qm} {}^C \bar{V}_{-q}(\tau) \right\}^{n_{qm}} \\ \times e^{-\Phi_2(\beta)} \frac{e^{-\beta H_e}}{Z_e}. \quad (\text{A10})$$

In Eq. (A10), we may move the current operator to the left-most position because all the hyperoperators act on the operator $j e^{-\beta H_e} / Z_e$ from the right. Similarly to Ref. 96, one may now recognize that $\iota_n^{(n)}(0)$ is the product of operator j and the ADO $\sigma_n^{(n)}(\beta)$, which is one of the components in the hierarchical representation of the (unnormalized) reduced density operator,

$$\sigma_0^{(0)}(\beta) = \mathcal{T} e^{-\Phi_2(\beta)} e^{-\beta H_e}. \quad (\text{A11})$$

To actually evaluate $\sigma_n^{(n)}(\beta)$ and the normalization constant $Z_e = \text{Tr} e^{\sigma_0^{(0)}(\beta)}$, we consider the imaginary time-dependent analog of Eq. (A11),

$$\sigma_0^{(0)}(\tau) = \mathcal{T} e^{-\Phi_2(\tau)} e^{-\tau H_e}, \quad (\text{A12})$$

where $0 \leq \tau \leq \beta$. As discussed in detail in Ref. 96, Eq. (A12) can be transformed into the imaginary-time HEOM given in Eq. (10).

APPENDIX B: DERIVATION OF THE CLOSING SCHEME IN EQ. (13)

Here, we provide a detailed derivation of our strategy for hierarchy closing that is embodied in Eq. (13).

Let us consider the equation for $\langle k | l_{\mathbf{D}}^{(D)}(t) | k + k_{\mathbf{D}} \rangle$ at the maximum depth D , which contains the ADOs $l_{\mathbf{D}+}^{(D+1)}$ at depth $D + 1$. The equation of motion for $l_{\mathbf{D}+}^{(D+1)}$ contains ADOs at depth $D + 2$, which will be set to zero. Moreover, its coupling with the ADOs at depth D will be restricted by assuming it couples back only to the original ADO $l_{\mathbf{D}}^{(D)}$ we are considering. With these assumptions, the equation at depth $D + 1$ reads as

$$\begin{aligned} \partial_t \langle k | l_{\mathbf{D}+}^{(D+1)}(t) | k + k_{\mathbf{D}} + q \rangle &= -i(\varepsilon_k - \varepsilon_{k+k_{\mathbf{D}}+q} + \mu_{\mathbf{D}+}) \langle k | l_{\mathbf{D}+}^{(D+1)}(t) | k + k_{\mathbf{D}} + q \rangle \\ &+ i\sqrt{(1 + D_{qm})c_{qm}} \langle k + q | l_{\mathbf{D}}^{(D)}(t) | k + k_{\mathbf{D}} + q \rangle \\ &- i\sqrt{1 + D_{qm}} \frac{c_{qm}}{\sqrt{c_{qm}}} \langle k | l_{\mathbf{D}}^{(D)}(t) | k + k_{\mathbf{D}} \rangle. \end{aligned} \quad (\text{B1})$$

Using the initial condition $\langle k | l_{\mathbf{D}+}^{(D+1)}(0) | k + k_{\mathbf{D}} + q \rangle = 0$, which is appropriate because the imaginary-time HEOM in Eq. (10) is truncated at the maximum depth D , Eq. (B1) can be formally integrated to yield

$$\begin{aligned} \langle k | l_{\mathbf{D}+}^{(D+1)}(t) | k + k_{\mathbf{D}} + q \rangle &= i\sqrt{1 + D_{qm}} \int_0^t dt_1 e^{-i(\varepsilon_k - \varepsilon_{k+k_{\mathbf{D}}+q} + \mu_{\mathbf{D}+})(t-t_1)} \\ &\times \left[\sqrt{c_{qm}} e^{-i(\varepsilon_{k+q} - \varepsilon_{k+k_{\mathbf{D}}+q} + \mu_{\mathbf{D}})t_1} f_1(t_1) \right. \\ &\left. - \frac{c_{qm}}{\sqrt{c_{qm}}} e^{-i(\varepsilon_k - \varepsilon_{k+k_{\mathbf{D}}+q} + \mu_{\mathbf{D}})t_1} f_2(t_1) \right]. \end{aligned} \quad (\text{B2})$$

We have introduced the auxiliary function $f_1(t)$ representing the slowly changing part of the ADO at depth D by factoring out the oscillating (rapidly changing) part as follows:

$$\langle k + q | l_{\mathbf{D}}^{(D)}(t) | k + k_{\mathbf{D}} + q \rangle = e^{-i(\varepsilon_{k+q} - \varepsilon_{k+k_{\mathbf{D}}+q} + \mu_{\mathbf{D}})t} f_1(t), \quad (\text{B3})$$

and similarly for $f_2(t)$. Under the integral entering Eq. (B2), we introduce the variable change $s = t - t_1$ and subsequently apply the Markovian approximation $f_{1/2}(t-s) \approx f_{1/2}(t)$ to the slowly changing part. As a result, we obtain

$$\begin{aligned} \langle k | l_{\mathbf{D}+}^{(D+1)}(t) | k + k_{\mathbf{D}} + q \rangle &= i\sqrt{(1 + D_{qm})c_{qm}} \left\{ \sqrt{c_{qm}} \int_0^t ds e^{-i[\varepsilon_k - \varepsilon_{k+q} + (\delta_{m0} - \delta_{m1})\omega_q]s} \right. \\ &\times \langle k + q | l_{\mathbf{D}}^{(D)}(t) | k + k_{\mathbf{D}} + q \rangle - \frac{c_{qm}}{\sqrt{c_{qm}}} \\ &\times \int_0^t ds e^{-i[\varepsilon_{k+k_{\mathbf{D}}} - \varepsilon_{k+k_{\mathbf{D}}+q} + (\delta_{m0} - \delta_{m1})\omega_q]s} \\ &\left. \times \langle k | l_{\mathbf{D}}^{(D)}(t) | k + k_{\mathbf{D}} \rangle \right\}. \end{aligned} \quad (\text{B4})$$

Using the last result, we write one of the terms that couple the equations at depths D and $D + 1$ [the third term on the RHS of Eq. (9)] as follows:

$$\begin{aligned} -i \sum'_{qm} \sqrt{(1 + D_{qm})c_{qm}} \langle k | l_{\mathbf{D}+}^{(D+1)}(t) | k + k_{\mathbf{D}} + q \rangle &= \sum'_{qm} (1 + D_{qm})c_{qm} \int_0^t ds e^{-i[\varepsilon_k - \varepsilon_{k+q} + (\delta_{m0} - \delta_{m1})\omega_q]s} \\ &\times \langle k + q | l_{\mathbf{D}}^{(D)}(t) | k + k_{\mathbf{D}} + q \rangle \\ - \sum'_{qm} (1 + D_{qm})c_{qm} \int_0^t ds e^{-i[\varepsilon_{k+k_{\mathbf{D}}} - \varepsilon_{k+k_{\mathbf{D}}+q} + (\delta_{m0} - \delta_{m1})\omega_q]s} &\times \langle k | l_{\mathbf{D}}^{(D)}(t) | k + k_{\mathbf{D}} \rangle. \end{aligned} \quad (\text{B5})$$

The second term on the RHS of Eq. (9) can be written and analyzed in an analogous manner.

To evaluate Eq. (B5), we have to know the detailed structure of the vector \mathbf{D} that characterizes the ADOs at the maximum depth D . We also observe that the second term on the RHS of Eq. (B5) depends only on the quantity $\langle k | l_{\mathbf{D}}^{(D)}(t) | k + k_{\mathbf{D}} \rangle$ whose differential equation we are considering. On the other hand, the matrix elements of $l_{\mathbf{D}}^{(D)}$ entering the first term on the RHS of Eq. (B5) depend on q . This term may be neglected by invoking a sort of random phase approximation: the matrix elements $\langle k + q | l_{\mathbf{D}}^{(D)}(t) | k + k_{\mathbf{D}} + q \rangle$ are typically oscillatory functions of q , and one may then argue that their average over all momenta q is close to zero. A similar approximation is also at the heart of the momentum-average approximation.^{44,45} In the remaining terms, we (i) exploit that for dispersionless optical phonons ($\omega_q \equiv \omega_0$), c_{qm} does not depend on q , (ii) neglect the contributions containing D_{qm} , and (iii) evaluate the remaining integral in Eq. (B5) by invoking the so-called adiabatic approximation, in which the upper limit t of the integral is replaced by $+\infty$. We furthermore keep only the real part of the integral evaluated so that

$$\int_0^t ds e^{-i\Omega s} \approx \int_0^{+\infty} ds e^{-i\Omega s} \approx \pi\delta(\Omega). \quad (\text{B6})$$

This way, we introduce physically motivated damping of the ADOs at the terminal level of the hierarchy. The damping effectively replaces higher-order phonon-assisted processes that are not explicitly taken into account, while phonon-assisted processes involving

at most D phonons are completely taken into account through the HEOM. In the resulting expressions, we recognize the second-order approximation for carrier scattering time out of the free-electron state $|k\rangle$,

$$\frac{1}{\tau_k} = 2\pi \frac{g^2}{N} \sum_q' \left[(1 - e^{-\beta\omega_0})^{-1} \delta(\varepsilon_k - \varepsilon_{k-q} - \omega_0) + (e^{\beta\omega_0} - 1)^{-1} \delta(\varepsilon_k - \varepsilon_{k+q} + \omega_0) \right], \quad (\text{B7})$$

for which an analytical expression in the limit of infinite N has been derived in Refs. 42 and 26. Even though we perform HEOM computations on finite chains, in Eq. (13) we use the value of τ_k obtained in the infinite-chain limit. We believe that such a procedure is appropriate because we invested great effort to perform computations with a sufficiently large N .

Instead of neglecting the term containing D_{qm} in Eq. (B5), we may have replaced D_{qm} by its average value $D/[2(N-1)]$ at depth D [the sum $\sum_{qm}' D_{qm}$, which is equal to D , contains $2(N-1)$ terms]. Such a replacement would lead to larger damping factors at depth D , which may have already been overestimated by using the value of τ_k in the infinite-chain limit. Since the substitution $D_{qm} \rightarrow D/[2(N-1)]$ does not improve the stability of the hierarchy at low temperatures, for strong interactions, and for fast phonons, we decided not to use it in our computations.

APPENDIX C: SUM RULES

The zeroth-moment sum rule states that

$$M_0 = \int_{-\infty}^{+\infty} \frac{d\omega}{2\pi} C_{jj}(\omega) = \langle j^2 \rangle. \quad (\text{C1})$$

Since j is a purely electronic operator, the evaluation of M_0 necessitates only the operator $t_0^{(0)}(t=0)$,

$$M_0 = -2J \sum_k \sin(k) \langle k | t_0^{(0)}(t=0) | k \rangle \equiv C_{jj}(t=0). \quad (\text{C2})$$

On the other hand, to evaluate M_n for $n \geq 1$, we need all ADOs $t_n^{(n)}(t=0)$ at depths starting from 0 and concluding with n . The first-moment sum rule is

$$M_1 = \int_{-\infty}^{+\infty} \frac{d\omega}{2\pi} \omega C_{jj}(\omega) = \langle [j, H] j \rangle. \quad (\text{C3})$$

It can be shown that

$$[j, H] = [j, H_{e-\text{ph}}] = -2J \sum_{q \neq 0, p} [\sin(p+q) - \sin(p)] |p+q\rangle \langle p| B_q. \quad (\text{C4})$$

Therefore,

$$M_1 = -2J \sum_{q \neq 0, p} [\sin(p+q) - \sin(p)] \times \left\langle p \left| \text{Tr}_{\text{ph}} \left\{ B_q j \frac{e^{-\beta H}}{Z} \right\} \right| p+q \right\rangle. \quad (\text{C5})$$

The second-moment sum rule is somewhat more cumbersome to evaluate

$$M_2 = \int_{-\infty}^{+\infty} \frac{d\omega}{2\pi} \omega^2 C_{jj}(\omega) = \langle [[j, H], H] j \rangle. \quad (\text{C6})$$

We separately evaluate the three contributions to the double commutator

$$[[j, H], H] = \underbrace{[[j, H], H_e]}_{K_1} + \underbrace{[[j, H], H_{\text{ph}}]}_{K_2} + \underbrace{[[j, H], H_{e-\text{ph}}]}_{K_3}, \quad (\text{C7})$$

starting from the result for $[j, H]$ embodied in Eq. (C4). We obtain

$$K_1 = -2J \sum_{q \neq 0, p} [\sin(p+q) - \sin(p)] (\varepsilon_p - \varepsilon_{p+q}) |p+q\rangle \langle p| B_q, \quad (\text{C8})$$

$$K_2 = -2J \sum_{q \neq 0, p} [\sin(p+q) - \sin(p)] \omega_q \frac{g}{\sqrt{N}} \times (|p+q\rangle \langle p| b_q - |p+q\rangle \langle p| b_q^\dagger), \quad (\text{C9})$$

$$K_3 = -2J \sum_{\substack{q_1 \neq 0 \\ q_2 \neq 0}} \sum_p |p+q_1+q_2\rangle \langle p| B_{q_2} B_{q_1} \times [\sin(p+q_1+q_2) - \sin(p+q_1) - \sin(p+q_2) + \sin(p)]. \quad (\text{C10})$$

In addition to the single-phonon-assisted ADO $\text{Tr}_{\text{ph}} \{ B_q j \frac{e^{-\beta H}}{Z} \}$, the evaluation of $\langle K_1 j \rangle$, $\langle K_2 j \rangle$, and $\langle K_3 j \rangle$ necessitates their contributions describing phonon absorption and emission, which stem from the definition $B_q = \frac{g}{\sqrt{N}} (b_q + b_{-q}^\dagger)$, as well as the two-phonon-assisted ADO $\text{Tr}_{\text{ph}} \{ B_{q_2} B_{q_1} j \frac{e^{-\beta H}}{Z} \}$. In the following, we compute these (electronic) operators using the ideas developed in Refs. 130 and 131.

Denoting $\frac{e^{-\beta H}}{Z} = \rho_T^{\text{eq}}$, we can write

$$j \rho_T^{\text{eq}} = \mathcal{T} \exp \left[- \int_0^\beta d\tau \sum_q' C \bar{V}_q(\tau) C \bar{B}_q(\tau) \right] \times j \frac{e^{-\beta H_e}}{Z_e} \frac{e^{-\beta H_{\text{ph}}'}}{Z_{\text{ph}}'}. \quad (\text{C11})$$

To evaluate phonon-assisted contributions, we introduce auxiliary fields $f_q(\tau)$ and consider their functional

$$j \rho_{T,f}^{\text{eq}} = \mathcal{T} \exp \left[- \int_0^\beta d\tau \sum_q' C [\bar{V}_q(\tau) + f_q(\tau)] C \bar{B}_q(\tau) \right] \times j \frac{e^{-\beta H_e}}{Z_e} \frac{e^{-\beta H_{\text{ph}}'}}{Z_{\text{ph}}'}. \quad (\text{C12})$$

Defining

$$j \rho_f^{\text{eq}} = j \text{Tr}_{\text{ph}} \rho_{T,f}^{\text{eq}}, \quad (\text{C13})$$

one can show that

$$\left[j \frac{\delta \rho_f^{\text{eq}}}{\delta f_q(\beta)} \right]_{f=0} = -\text{Tr}_{\text{ph}} \{ B_q j \rho_T^{\text{eq}} \}, \quad (\text{C14})$$

$$\left[j \frac{\delta^2 \rho_f^{\text{eq}}}{\delta f_{q_2}(\beta) \delta f_{q_1}(\beta)} \right]_{f=0} = \text{Tr}_{\text{ph}} \{ B_{q_2} B_{q_1} j \rho_T^{\text{eq}} \}. \quad (\text{C15})$$

On the other hand,

$$\rho_f^{\text{eq}} = \mathcal{T} e^{-\Phi_{2,f}(\beta)} \frac{e^{-\beta H_c}}{Z_e}, \quad (\text{C16})$$

where the influence phase $\Phi_{2,f}(\beta)$ is a functional of auxiliary fields $f_q(\tau)$ [cf. Eq. (A6)],

$$\begin{aligned} \Phi_{2,f}(\beta) = & - \int_0^\beta d\tau_2 \int_0^{\tau_2} d\tau_1 \sum_{qm}^C [\bar{V}_{-q}(\tau_1) + f_{-q}(\tau_1)] \\ & \times e^{i\mu_{qm}(\tau_2-\tau_1)} c_{qm}^C [\bar{V}_q(\tau_2) + f_q(\tau_2)]. \end{aligned} \quad (\text{C17})$$

It then follows that

$$\frac{\delta \rho_f^{\text{eq}}}{\delta f_{q_1}(\beta)} = \mathcal{T} \left\{ - \frac{\delta \Phi_{2,f}(\beta)}{\delta f_{q_1}(\beta)} e^{-\Phi_{2,f}(\beta)} \right\} \frac{e^{-\beta H_c}}{Z_e}, \quad (\text{C18})$$

$$\begin{aligned} & \frac{\delta^2 \rho_f^{\text{eq}}}{\delta f_{q_2}(\beta) \delta f_{q_1}(\beta)} \\ & = \mathcal{T} \left\{ \left[- \frac{\delta^2 \Phi_{2,f}(\beta)}{\delta f_{q_2}(\beta) \delta f_{q_1}(\beta)} + \frac{\delta \Phi_{2,f}(\beta)}{\delta f_{q_2}(\beta)} \frac{\delta \Phi_{2,f}(\beta)}{\delta f_{q_1}(\beta)} \right] e^{-\Phi_{2,f}(\beta)} \right\} \\ & \quad \times \frac{e^{-\beta H_c}}{Z_e}, \end{aligned} \quad (\text{C19})$$

The explicit evaluation of the functional derivatives produces

$$\frac{\delta \Phi_{2,f}(\beta)}{\delta f_{q_1}(\beta)} = - \int_0^\beta d\tau \sum_m c_{q_1 m} e^{i\mu_{q_1 m}(\beta-\tau)} [\bar{V}_{-q_1}(\tau) + f_{-q_1}(\tau)], \quad (\text{C20})$$

$$\frac{\delta^2 \Phi_f(\beta)}{\delta f_{q_2}(\beta) \delta f_{q_1}(\beta)} = -\delta_{q_2, -q_1} \sum_m c_{q_1 m}. \quad (\text{C21})$$

Using the definition of ADOs $l_n^{(n)}$ at $t=0$ [Eq. (A8)] and rescaling factors $f(\mathbf{n})$ [Eq. (A9)], we finally obtain

$$\text{Tr}_{\text{ph}} \{ B_q j \rho_T^{\text{eq}} \} = - \sum_m \frac{1}{f(\mathbf{0}_{qm}^+)} l_{\mathbf{0}_{qm}^+}^{(1)}(t=0), \quad (\text{C22})$$

$$\begin{aligned} \text{Tr}_{\text{ph}} \{ B_{q_2} B_{q_1} \rho_T^{\text{eq}} \} = & \delta_{q_2, -q_1} \left(\sum_m c_{q_1 m} \right) l_{\mathbf{0}}^{(0)}(t=0) + \sum_{m_2 m_1} \\ & \times \frac{1}{f(\mathbf{0}_{(q_1 m_1), (q_2 m_2)}^{++})} l_{\mathbf{0}_{(q_1 m_1), (q_2 m_2)}^{++}}^{(2)}(t=0). \end{aligned} \quad (\text{C23})$$

The contributions that differentiate between absorption and emission of a single phonon are most straightforwardly obtained by explicitly setting up an equation of motion for such processes and comparing the kinetic term in the equation thus obtained with the kinetic term in Eq. (9). This procedure yields

$$\frac{g}{\sqrt{N}} \text{Tr}_{\text{ph}} \{ b_q j \rho_T^{\text{eq}} \} = - \frac{1}{f(\mathbf{0}_{q0}^+)} l_{\mathbf{0}_{q0}^+}^{(1)}(t=0), \quad (\text{C24})$$

$$\frac{g}{\sqrt{N}} \text{Tr}_{\text{ph}} \{ b_{-q}^\dagger j \rho_T^{\text{eq}} \} = - \frac{1}{f(\mathbf{0}_{q1}^+)} l_{\mathbf{0}_{q1}^+}^{(1)}(t=0). \quad (\text{C25})$$

The final result for the first-moment sum rule reads as

$$\begin{aligned} M_1 = & 2J \sum_{q \neq 0, p} \sum_m \frac{\sin(p+q) - \sin(p)}{f(\mathbf{0}_{qm}^+)} \\ & \times \langle p | l_{\mathbf{0}_{qm}^+}^{(1)}(t=0) | p+q \rangle. \end{aligned} \quad (\text{C26})$$

The final result for the second-moment sum rule reads as

$$M_2 = \langle K_{1j} \rangle + \langle K_{2j} \rangle + \langle K_{3j} \rangle, \quad (\text{C27})$$

where

$$\begin{aligned} \langle K_{1j} \rangle = & 2J \sum_{q \neq 0, p} \sum_m \frac{\sin(p+q) - \sin(p)}{f(\mathbf{0}_{qm}^+)} (\epsilon_p - \epsilon_{p+q}) \\ & \times \langle p | l_{\mathbf{0}_{qm}^+}^{(1)}(t=0) | p+q \rangle, \end{aligned} \quad (\text{C28})$$

$$\begin{aligned} \langle K_{2j} \rangle = & 2J \sum_{q \neq 0, p} \sum_m (-1)^m \frac{\sin(p+q) - \sin(p)}{f(\mathbf{0}_{qm}^+)} \omega_q \\ & \times \langle p | l_{\mathbf{0}_{qm}^+}^{(1)}(t=0) | p+q \rangle, \end{aligned} \quad (\text{C29})$$

and

$$\begin{aligned} \langle K_{3j} \rangle = & -2J \sum_{q \neq 0, p} \sum_m 4 \sin(p) \sin^2(q/2) c_{qm} \langle p | l_{\mathbf{0}}^{(0)}(t=0) | p \rangle \\ & - 2J \sum_{\substack{q_2, q_1 \neq 0 \\ p}} \sum_{m_2, m_1} \frac{\langle p | l_{\mathbf{0}_{(q_1 m_1), (q_2 m_2)}^{++}}^{(2)}(t=0) | p+q_1+q_2 \rangle}{f(\mathbf{0}_{(q_1 m_1), (q_2 m_2)}^{++})} \\ & \times [\sin(p+q_1+q_2) - \sin(p+q_1) - \sin(p+q_2) + \sin(p)]. \end{aligned} \quad (\text{C30})$$

APPENDIX D: OPTICAL SUM RULE AND FINITE-SIZE EFFECTS

We find that the relative accuracy with which the OSR is satisfied increases with increasing N , see Sec. III C. This observation suggests that the OSR formulated in Eq. (16) is strictly valid only in the long-chain limit, while on finite chains there are finite-size corrections that vanish as $N \rightarrow +\infty$. In the following, we provide a derivation of the OSR for finite N , identify the finite-size corrections, and demonstrate that they vanish in the long-chain limit.

Let us start by noting that the current operator on an N -site chain, defined in Eq. (3), may be expressed in the site basis as

$$j = iJ \sum_{m=0}^{N-1} (|m\rangle \langle m \oplus 1| - |m \oplus 1\rangle \langle m|). \quad (\text{D1})$$

The cyclic addition $\oplus [a \oplus b = (a+b) \bmod N]$ takes into account that sites 0 and $N-1$ are first neighbors because of the periodic boundary conditions. Our derivation of the OSR makes use of the continuity equation

$$\tilde{j} = \frac{dP}{dt} = -i[P, H], \quad (\text{D2})$$

where the polarization operator (in the site basis) is given as

$$P = -\sum_{m=0}^{N-1} m|m\rangle\langle m|. \quad (\text{D3})$$

While the current operators \tilde{j} and j are identical in the infinite-chain limit, their difference on a finite chain reads as

$$\tilde{j} - j = -i\widehat{P}_{N-1,0}, \quad (\text{D4})$$

where

$$\widehat{P}_{N-1,0} = N(|N-1\rangle\langle 0| - |0\rangle\langle N-1|). \quad (\text{D5})$$

Our derivation starts from the integral $I = \int_{-\infty}^{+\infty} d\omega \text{Re}\mu_{ac}(\omega)$, whose integrand is expressed using the first equality in Eq. (4). Substituting $C_{jj}(\omega)$ in terms of $C_{jj}(t)$, writing the resulting expression in the eigenbasis $\{|\alpha\rangle\}$ of the full Hamiltonian H ($H|\alpha\rangle = E_{\alpha}|\alpha\rangle$), and performing the integrations over time and frequency, we obtain

$$I = \pi \sum_{\alpha'\alpha} \frac{\langle \alpha' | j | \alpha \rangle \langle \alpha | j | \alpha' \rangle}{E_{\alpha} - E_{\alpha'}} \frac{e^{-\beta E_{\alpha'}} - e^{-\beta E_{\alpha}}}{Z}. \quad (\text{D6})$$

We can eliminate the energy difference $E_{\alpha} - E_{\alpha'}$ in the denominator of each term by expressing one of the current operators using the continuity equation [Eq. (D2)]. We should, however, take into account the finite-size correction entering Eq. (D4). We then obtain

$$\begin{aligned} I &= -i\pi \sum_{\alpha'\alpha} \langle \alpha' | P | \alpha \rangle \langle \alpha | j | \alpha' \rangle \frac{e^{-\beta E_{\alpha'}} - e^{-\beta E_{\alpha}}}{Z} \\ &\quad + i\pi j \sum_{\alpha'\alpha} \frac{\langle \alpha' | \widehat{P}_{N-1,0} | \alpha \rangle \langle \alpha | j | \alpha' \rangle}{E_{\alpha} - E_{\alpha'}} \frac{e^{-\beta E_{\alpha'}} - e^{-\beta E_{\alpha}}}{Z} \\ &= I_1 + I_2. \end{aligned} \quad (\text{D7})$$

The term I_1 can then be written as

$$I_1 = -i\pi \text{Tr} \left\{ [P, j] \frac{e^{-\beta H}}{Z} \right\}. \quad (\text{D8})$$

The commutator $[P, j]$, where both operators are defined on a finite chain, is equal to

$$[P, j] = -iH_e - i\widehat{P}_{N-1,0}, \quad (\text{D9})$$

so that

$$\begin{aligned} I_1 &= -\pi \text{Tr}_e \left\{ H_e \frac{\sigma_0^{(0)}(\beta)}{Z_e} \right\} - \pi j \text{Tr}_e \left\{ \widehat{P}_{N-1,0} \frac{\sigma_0^{(0)}(\beta)}{Z_e} \right\} \\ &= I_{1,1} + I_{1,2}. \end{aligned} \quad (\text{D10})$$

While the term $I_{1,1}$ alone gives the desired result for the OSR ($I = -\pi \langle H_e \rangle$), the terms $I_{1,2}$ and I_2 are finite-size corrections. The

term I_2 can be transformed by applying the steps that led to Eq. (D6) in the reverse order, which gives

$$\begin{aligned} I_2 &= \int_{-\infty}^{+\infty} d\omega \frac{1 - e^{-\beta\omega}}{2\omega} \int_{-\infty}^{+\infty} dt e^{i\omega t} \\ &\quad \times \text{Tr} \left\{ e^{iHt} \widehat{P}_{N-1,0} e^{-iHt} j \frac{e^{-\beta H}}{Z} \right\} \\ &= \int_{-\infty}^{+\infty} d\omega \frac{1 - e^{-\beta\omega}}{2\omega} \int_{-\infty}^{+\infty} dt e^{i\omega t} \text{Tr}_e \{ \dot{P}_{N-1,0} \iota(t) \}. \end{aligned} \quad (\text{D11})$$

Both $I_{1,2}$ and I_2 reduce to expectation values of the purely electronic operator $\widehat{P}_{N-1,0}$ with respect to the reduced (purely electronic) density matrix $\sigma_0^{(0)}(\beta)/Z_e$ (for $I_{1,2}$) or $\iota(t)$ (for I_2) that is diagonal in the momentum representation. For example,

$$\text{Tr}_e \{ \dot{P}_{N-1,0} \iota(t) \} = -2i \sum_k \langle k | \iota(t) | k \rangle \sin \left(2\pi n_k \frac{N-1}{N} \right), \quad (\text{D12})$$

where the sum is over N allowed values of the wave number $k = 2\pi n_k/N$, with n_k being N consecutive integers. As $N \rightarrow +\infty$, $(N-1)/N \rightarrow 1$, and each term entering Eq. (D12) tends to zero. In other words, the finite-size correction I_2 vanishes in the infinite-chain limit. The same reasoning may be applied to show that $I_{1,2}$ vanishes in the infinite-chain limit.

REFERENCES

- C. Franchini, M. Reticcioli, M. Setvin, and U. Diebold, "Polarons in materials," *Nat. Rev. Mater.* **6**, 560–586 (2021).
- L. R. V. Buizza and L. M. Herz, "Polarons and charge localization in metal-halide semiconductors for photovoltaic and light-emitting devices," *Adv. Mater.* **33**, 2007057 (2021).
- C. Jacoboni, *Theory of Electron Transport in Semiconductors: A Pathway from Elementary Physics to Nonequilibrium Green Functions* (Springer-Verlag Berlin Heidelberg, 2010).
- F. Rossi, *Theory of Semiconductor Quantum Devices: Microscopic Modeling and Simulation Strategies* (Springer-Verlag Berlin Heidelberg, 2011).
- G. Mahan, *Many-Particle Physics* (Kluwer Academic, New York, 2000).
- A. S. Alexandrov and J. T. Devreese, *Advances in Polaron Physics* (Springer-Verlag Berlin Heidelberg, 2010).
- V. Coropceanu, J. Cornil, D. A. da Silva Filho, Y. Olivier, R. Silbey, and J.-L. Brédas, "Charge transport in organic semiconductors," *Chem. Rev.* **107**, 926–952 (2007).
- M. Mladenović and N. Vukmirović, "Charge carrier localization and transport in organic semiconductors: Insights from atomistic multiscale simulations," *Adv. Funct. Mater.* **25**, 1915–1932 (2015).
- A. Köhler and H. Bässler, *Electronic Processes in Organic Semiconductors* (Wiley-VCH Verlag GmbH & Co. KGaA, 2015).
- M. Schröter, S. Ivanov, J. Schulze, S. Polyutov, Y. Yan, T. Pullerits, and O. Kühn, "Exciton-vibrational coupling in the dynamics and spectroscopy of Frenkel excitons in molecular aggregates," *Phys. Rep.* **567**, 1–78 (2015).
- S. J. Jang and B. Mennucci, "Delocalized excitons in natural light-harvesting complexes," *Rev. Mod. Phys.* **90**, 035003 (2018).
- V. van Amerongen, L. Valkunas, and R. van Grondelle, *Photosynthetic Excitons* (World Scientific Publishing Co. Pte., Ltd., 2000).
- V. May and O. Kühn, *Charge and Energy Transfer Dynamics in Molecular Systems*, 3rd ed. (WILEY-VCH Verlag GmbH & Co. KGaA, Weinheim, 2011).
- L. Valkunas, D. Abramavicius, and T. Mančal, *Molecular Excitation Dynamics and Relaxation* (WILEY-VCH Verlag GmbH & Co. KGaA, 2013).
- T. Holstein, "Studies of polaron motion: Part I. The molecular-crystal model," *Ann. Phys.* **8**, 325–342 (1959).

- ¹⁶S. Poncé, W. Li, S. Reichardt, and F. Giustino, “First-principles calculations of charge carrier mobility and conductivity in bulk semiconductors and two-dimensional materials,” *Rep. Prog. Phys.* **83**, 036501 (2020).
- ¹⁷A. G. Redfield, “The theory of relaxation processes,” in *Advances in Magnetic Resonance, Advances in Magnetic and Optical Resonance Vol. 1*, edited by J. S. Waugh (Academic Press, 1965), pp. 1–32.
- ¹⁸I. Lang and Y. A. Firsov, “Kinetic theory of semiconductors with low mobility,” *Sov. Phys. JETP* **16**, 1301–1312 (1963).
- ¹⁹R. A. Marcus, “Electron transfer reactions in chemistry. Theory and experiment,” *Rev. Mod. Phys.* **65**, 599–610 (1993).
- ²⁰T. Förster, “Delocalized excitation and excitation transfer. Bulletin no. 18,” Technical Report FSU-2690-18, Florida State University; Department of Chemistry, Tallahassee, 1964).
- ²¹A. Zhugayevych and S. Tretiak, “Theoretical description of structural and electronic properties of organic photovoltaic materials,” *Annu. Rev. Phys. Chem.* **66**, 305–330 (2015).
- ²²A. Ishizaki and G. R. Fleming, “Quantum coherence in photosynthetic light harvesting,” *Annu. Rev. Condens. Matter Phys.* **3**, 333–361 (2012).
- ²³A. Chenu and G. D. Scholes, “Coherence in energy transfer and photosynthesis,” *Annu. Rev. Phys. Chem.* **66**, 69–96 (2015).
- ²⁴P. J. Robinson, I. S. Dunn, and D. R. Reichman, “Cumulant methods for electron-phonon problems. I. Perturbative expansions,” *Phys. Rev. B* **105**, 224304 (2022).
- ²⁵P. J. Robinson, I. S. Dunn, and D. R. Reichman, “Cumulant methods for electron-phonon problems. II. The self-consistent cumulant expansion,” *Phys. Rev. B* **105**, 224305 (2022).
- ²⁶P. Mitrić, V. Janković, N. Vukmirović, and D. Tanasković, “Cumulant expansion in the Holstein model: Spectral functions and mobility,” *Phys. Rev. B* **107**, 125165 (2023).
- ²⁷J. Ma and J. Cao, “Förster resonance energy transfer, absorption and emission spectra in multichromophoric systems. I. Full cumulant expansions and system-bath entanglement,” *J. Chem. Phys.* **142**, 094106 (2015).
- ²⁸J. A. Nöthling, T. Mančal, and T. P. J. Krüger, “Accuracy of approximate methods for the calculation of absorption-type linear spectra with a complex system–bath coupling,” *J. Chem. Phys.* **157**, 095103 (2022).
- ²⁹S. Ciuchi, F. de Pasquale, S. Fratini, and D. Feinberg, “Dynamical mean-field theory of the small polaron,” *Phys. Rev. B* **56**, 4494–4512 (1997).
- ³⁰S. Fratini, F. de Pasquale, and S. Ciuchi, “Optical absorption from a nondegenerate polaron gas,” *Phys. Rev. B* **63**, 153101 (2001).
- ³¹S. Fratini and S. Ciuchi, “Dynamical mean-field theory of transport of small polarons,” *Phys. Rev. Lett.* **91**, 256403 (2003).
- ³²S. Fratini and S. Ciuchi, “Optical properties of small polarons from dynamical mean-field theory,” *Phys. Rev. B* **74**, 075101 (2006).
- ³³P. Mitrić, V. Janković, N. Vukmirović, and D. Tanasković, “Spectral functions of the Holstein polaron: Exact and approximate solutions,” *Phys. Rev. Lett.* **129**, 096401 (2022).
- ³⁴M. Grover and R. Silbey, “Exciton migration in molecular crystals,” *J. Chem. Phys.* **54**, 4843–4851 (1971).
- ³⁵D. R. Yarkony and R. Silbey, “Variational approach to exciton transport in molecular crystals,” *J. Chem. Phys.* **67**, 5818–5827 (1977).
- ³⁶R. Silbey and R. W. Munn, “General theory of electronic transport in molecular crystals. I. Local linear electron–phonon coupling,” *J. Chem. Phys.* **72**, 2763–2773 (1980).
- ³⁷K. Hannewald and P. A. Bobbert, “Anisotropy effects in phonon-assisted charge-carrier transport in organic molecular crystals,” *Phys. Rev. B* **69**, 075212 (2004).
- ³⁸Y.-C. Cheng and R. J. Silbey, “A unified theory for charge-carrier transport in organic crystals,” *J. Chem. Phys.* **128**, 114713 (2008).
- ³⁹F. Ortmann, F. Bechstedt, and K. Hannewald, “Theory of charge transport in organic crystals: Beyond Holstein’s small-polaron model,” *Phys. Rev. B* **79**, 235206 (2009).
- ⁴⁰D. Chen, J. Ye, H. Zhang, and Y. Zhao, “On the Munn–Silbey approach to polaron transport with off-diagonal coupling and temperature-dependent canonical transformations,” *J. Phys. Chem. B* **115**, 5312–5321 (2011).
- ⁴¹M. Kornjača and N. Vukmirović, “Polaron mobility obtained by a variational approach for lattice Fröhlich models,” *Ann. Phys.* **391**, 183–202 (2018).
- ⁴²N. Prodanović and N. Vukmirović, “Charge carrier mobility in systems with local electron-phonon interaction,” *Phys. Rev. B* **99**, 104304 (2019).
- ⁴³J. H. Fetherolf, D. Golež, and T. C. Berkelbach, “A unification of the Holstein polaron and dynamic disorder pictures of charge transport in organic crystals,” *Phys. Rev. X* **10**, 021062 (2020).
- ⁴⁴M. Berciu, “Green’s function of a dressed particle,” *Phys. Rev. Lett.* **97**, 036402 (2006).
- ⁴⁵G. L. Goodvin, M. Berciu, and G. A. Sawatzky, “Green’s function of the Holstein polaron,” *Phys. Rev. B* **74**, 245104 (2006).
- ⁴⁶G. L. Goodvin, A. S. Mishchenko, and M. Berciu, “Optical conductivity of the Holstein polaron,” *Phys. Rev. Lett.* **107**, 076403 (2011).
- ⁴⁷D. Balzer, T. J. Smolders, D. Blyth, S. N. Hood, and I. Kassal, “Delocalised kinetic Monte Carlo for simulating delocalisation-enhanced charge and exciton transport in disordered materials,” *Chem. Sci.* **12**, 2276 (2021).
- ⁴⁸J. T. Willson, W. Liu, D. Balzer, and I. Kassal, “Jumping kinetic Monte Carlo: Fast and accurate simulations of partially delocalized charge transport in organic semiconductors,” *J. Phys. Chem. Lett.* **14**, 3757–3764 (2023).
- ⁴⁹K. Hannewald and P. A. Bobbert, “*Ab initio* theory of charge-carrier conduction in ultrapure organic crystals,” *Appl. Phys. Lett.* **85**, 1535–1537 (2004).
- ⁵⁰F. Ortmann, F. Bechstedt, and K. Hannewald, “Charge transport in organic crystals: Interplay of band transport, hopping and electron–phonon scattering,” *New J. Phys.* **12**, 023011 (2010).
- ⁵¹J.-J. Zhou and M. Bernardi, “Predicting charge transport in the presence of polarons: The beyond-quasiparticle regime in SrTiO₃,” *Phys. Rev. Res.* **1**, 033138 (2019).
- ⁵²L. Cupellini, F. Lipparini, and J. Cao, “Absorption and circular dichroism spectra of molecular aggregates with the full cumulant expansion,” *J. Phys. Chem. B* **124**, 8610–8617 (2020).
- ⁵³N. Vukmirović, “Calculations of electron mobility in II–VI semiconductors,” *Phys. Rev. B* **104**, 085203 (2021).
- ⁵⁴B. K. Chang, J.-J. Zhou, N.-E. Lee, and M. Bernardi, “Intermediate polaronic charge transport in organic crystals from a many-body first-principles approach,” *npj Comput. Mater.* **8**, 63 (2022).
- ⁵⁵S. Hutsch, M. Panhans, and F. Ortmann, “Charge carrier mobilities of organic semiconductors: *Ab initio* simulations with mode-specific treatment of molecular vibrations,” *npj Comput. Mater.* **8**, 228 (2022).
- ⁵⁶H. De Raedt and A. Lagendijk, “Numerical calculation of path integrals: The small-polaron model,” *Phys. Rev. B* **27**, 6097–6109 (1983).
- ⁵⁷H. De Raedt and A. Lagendijk, “Numerical study of Holstein’s molecular-crystal model: Adiabatic limit and influence of phonon dispersion,” *Phys. Rev. B* **30**, 1671–1678 (1984).
- ⁵⁸N. V. Prokofev and B. V. Svistunov, “Polaron problem by diagrammatic quantum Monte Carlo,” *Phys. Rev. Lett.* **81**, 2514–2517 (1998).
- ⁵⁹A. S. Mishchenko, N. V. Prokofev, A. Sakamoto, and B. V. Svistunov, “Diagrammatic quantum Monte Carlo study of the Fröhlich polaron,” *Phys. Rev. B* **62**, 6317–6336 (2000).
- ⁶⁰A. S. Mishchenko, “Diagrammatic Monte Carlo method as applied to the polaron problems,” *Phys.-Usp.* **48**, 887 (2005).
- ⁶¹A. S. Mishchenko, N. Nagaosa, G. De Filippis, A. de Candia, and V. Cataudella, “Mobility of Holstein polaron at finite temperature: An unbiased approach,” *Phys. Rev. Lett.* **114**, 146401 (2015).
- ⁶²Y.-C. Wang and Y. Zhao, “Diagrammatic quantum Monte Carlo toward the calculation of transport properties in disordered semiconductors,” *J. Chem. Phys.* **156**, 204116 (2022).
- ⁶³S. Miladić and N. Vukmirović, “Method for obtaining polaron mobility using real and imaginary time path-integral quantum Monte Carlo,” *Phys. Rev. B* **107**, 184315 (2023).
- ⁶⁴P. Prelovšek and J. Bonča, “Ground state and finite temperature Lanczos methods,” in *Strongly Correlated Systems: Numerical Methods*, edited by A. Avella and F. Mancini (Springer Berlin Heidelberg, Berlin, Heidelberg, 2013), pp. 1–30.
- ⁶⁵J. Bonča, S. A. Trugman, and I. Batistić, “Holstein polaron,” *Phys. Rev. B* **60**, 1633–1642 (1999).

- ⁶⁶O. S. Barišić, "Calculation of excited polaron states in the Holstein model," *Phys. Rev. B* **69**, 064302 (2004).
- ⁶⁷J. Bonča, S. A. Trugman, and M. Berciu, "Spectral function of the Holstein polaron at finite temperature," *Phys. Rev. B* **100**, 094307 (2019).
- ⁶⁸J. Bonča and S. A. Trugman, "Dynamic properties of a polaron coupled to dispersive optical phonons," *Phys. Rev. B* **103**, 054304 (2021).
- ⁶⁹J. Bonča and S. A. Trugman, "Electron removal spectral function of a polaron coupled to dispersive optical phonons," *Phys. Rev. B* **106**, 174303 (2022).
- ⁷⁰E. Jeckelmann and S. R. White, "Density-matrix renormalization-group study of the polaron problem in the Holstein model," *Phys. Rev. B* **57**, 6376–6385 (1998).
- ⁷¹C. Zhang, E. Jeckelmann, and S. R. White, "Dynamical properties of the one-dimensional Holstein model," *Phys. Rev. B* **60**, 14092–14104 (1999).
- ⁷²J. Ren, W. Li, T. Jiang, Y. Wang, and Z. Shuai, "Time-dependent density matrix renormalization group method for quantum dynamics in complex systems," *Wiley Interdiscip. Rev.: Comput. Mol. Sci.* **12**, e1614 (2022).
- ⁷³J. Ren, Z. Shuai, and G. Kin-Lic Chan, "Time-dependent density matrix renormalization group algorithms for nearly exact absorption and fluorescence spectra of molecular aggregates at both zero and finite temperature," *J. Chem. Theory Comput.* **14**, 5027–5039 (2018).
- ⁷⁴W. Li, J. Ren, and Z. Shuai, "Finite-temperature TD-DMRG for the carrier mobility of organic semiconductors," *J. Phys. Chem. Lett.* **11**, 4930–4936 (2020).
- ⁷⁵Y. Ge, W. Li, J. Ren, and Z. Shuai, "Computational method for evaluating the thermoelectric power factor for organic materials modeled by the Holstein model: A time-dependent density matrix renormalization group formalism," *J. Chem. Theory Comput.* **18**, 6437–6446 (2022).
- ⁷⁶D. Jansen, J. Bonča, and F. Heidrich-Meisner, "Finite-temperature density-matrix renormalization group method for electron-phonon systems: Thermodynamics and Holstein-polaron spectral functions," *Phys. Rev. B* **102**, 165155 (2020).
- ⁷⁷D. Jansen, J. Bonča, and F. Heidrich-Meisner, "Finite-temperature optical conductivity with density-matrix renormalization group methods for the Holstein polaron and bipolaron with dispersive phonons," *Phys. Rev. B* **106**, 155129 (2022).
- ⁷⁸R. Borrelli and M. F. Gelin, "Quantum electron-vibrational dynamics at finite temperature: Thermo field dynamics approach," *J. Chem. Phys.* **145**, 224101 (2016).
- ⁷⁹R. Borrelli and M. F. Gelin, "Simulation of quantum dynamics of excitonic systems at finite temperature: An efficient method based on thermo field dynamics," *Sci. Rep.* **7**, 9127 (2017).
- ⁸⁰R. Borrelli and M. F. Gelin, "Finite temperature quantum dynamics of complex systems: Integrating thermo-field theories and tensor-train methods," *Wiley Interdiscip. Rev.: Comput. Mol. Sci.* **11**, e1539 (2021).
- ⁸¹Y. Zhao, "The hierarchy of Davydov's Ansatz: From guesswork to numerically 'exact' many-body wave functions," *J. Chem. Phys.* **158**, 080901 (2023).
- ⁸²Y. Zhao, K. Sun, L. Chen, and M. Gelin, "The hierarchy of Davydov's Ansatz and its applications," *Wiley Interdiscip. Rev.: Comput. Mol. Sci.* **12**, e1589 (2022).
- ⁸³L. Chen and Y. Zhao, "Finite temperature dynamics of a Holstein polaron: The thermo-field dynamics approach," *J. Chem. Phys.* **147**, 214102 (2017).
- ⁸⁴Z. Huang, L. Chen, N. Zhou, and Y. Zhao, "Transient dynamics of a one-dimensional Holstein polaron under the influence of an external electric field," *Ann. Phys.* **529**, 1600367 (2017).
- ⁸⁵A. D. Somoza, K.-W. Sun, R. A. Molina, and Y. Zhao, "Dynamics of coherence, localization and excitation transfer in disordered nanorings," *Phys. Chem. Chem. Phys.* **19**, 25996–26013 (2017).
- ⁸⁶Y. Tanimura, "Stochastic Liouville, Langevin, Fokker-Planck, and master equation approaches to quantum dissipative systems," *J. Phys. Soc. Jpn.* **75**, 082001 (2006).
- ⁸⁷R.-X. Xu and Y. J. Yan, "Dynamics of quantum dissipation systems interacting with bosonic canonical bath: Hierarchical equations of motion approach," *Phys. Rev. E* **75**, 031107 (2007).
- ⁸⁸A. Ishizaki and G. R. Fleming, "Unified treatment of quantum coherent and incoherent hopping dynamics in electronic energy transfer: Reduced hierarchy equation approach," *J. Chem. Phys.* **130**, 234111 (2009).
- ⁸⁹Y. Tanimura, "Numerically 'exact' approach to open quantum dynamics: The hierarchical equations of motion (HEOM)," *J. Chem. Phys.* **153**, 020901 (2020).
- ⁹⁰C.-Y. Hsieh and J. Cao, "A unified stochastic formulation of dissipative quantum dynamics. I. Generalized hierarchical equations," *J. Chem. Phys.* **148**, 014103 (2018).
- ⁹¹H.-D. Zhang, R.-X. Xu, X. Zheng, and Y. Yan, "Statistical quasi-particle theory for open quantum systems," *Mol. Phys.* **116**, 780–812 (2018).
- ⁹²Y. Ke and Y. Zhao, "Hierarchy of stochastic Schrödinger equation towards the calculation of absorption and circular dichroism spectra," *J. Chem. Phys.* **146**, 174105 (2017).
- ⁹³Y. Ke and Y. Zhao, "An extension of stochastic hierarchy equations of motion for the equilibrium correlation functions," *J. Chem. Phys.* **146**, 214105 (2017).
- ⁹⁴L. Diósi and W. T. Strunz, "The non-Markovian stochastic Schrödinger equation for open systems," *Phys. Lett. A* **235**, 569–573 (1997).
- ⁹⁵J. Roden, W. T. Strunz, and A. Eisfeld, "Non-Markovian quantum state diffusion for absorption spectra of molecular aggregates," *J. Chem. Phys.* **134**, 034902 (2011).
- ⁹⁶V. Janković and N. Vukmirović, "Spectral and thermodynamic properties of the Holstein polaron: Hierarchical equations of motion approach," *Phys. Rev. B* **105**, 054311 (2022).
- ⁹⁷D. Wang, L. Chen, R. Zheng, L. Wang, and Q. Shi, "Communications: A non-perturbative quantum master equation approach to charge carrier transport in organic molecular crystals," *J. Chem. Phys.* **132**, 081101 (2010).
- ⁹⁸L. Song and Q. Shi, "Calculation of correlated initial state in the hierarchical equations of motion method using an imaginary time path integral approach," *J. Chem. Phys.* **143**, 194106 (2015).
- ⁹⁹T. Xing, T. Li, Y. Yan, S. Bai, and Q. Shi, "Application of the imaginary time hierarchical equations of motion method to calculate real time correlation functions," *J. Chem. Phys.* **156**, 244102 (2022).
- ¹⁰⁰L. Song and Q. Shi, "A new approach to calculate charge carrier transport mobility in organic molecular crystals from imaginary time path integral simulations," *J. Chem. Phys.* **142**, 174103 (2015).
- ¹⁰¹I. S. Dunn, R. Tempelaar, and D. R. Reichman, "Removing instabilities in the hierarchical equations of motion: Exact and approximate projection approaches," *J. Chem. Phys.* **150**, 184109 (2019).
- ¹⁰²L. Chen, Y. Zhao, and Y. Tanimura, "Dynamics of a one-dimensional Holstein polaron with the hierarchical equations of motion approach," *J. Phys. Chem. Lett.* **6**, 3110–3115 (2015).
- ¹⁰³Y. Yan, T. Xing, and Q. Shi, "A new method to improve the numerical stability of the hierarchical equations of motion for discrete harmonic oscillator modes," *J. Chem. Phys.* **153**, 204109 (2020).
- ¹⁰⁴C. Karrasch, D. M. Kennes, and J. E. Moore, "Transport properties of the one-dimensional Hubbard model at finite temperature," *Phys. Rev. B* **90**, 155104 (2014).
- ¹⁰⁵B. Bertini, F. Heidrich-Meisner, C. Karrasch, T. Prosen, R. Steinigeweg, and M. Žnidarič, "Finite-temperature transport in one-dimensional quantum lattice models," *Rev. Mod. Phys.* **93**, 025003 (2021).
- ¹⁰⁶G. De Filippis, V. Cataudella, A. S. Mishchenko, N. Nagaosa, A. Fierro, and A. de Candia, "Crossover from super- to subdiffusive motion and memory effects in crystalline organic semiconductors," *Phys. Rev. Lett.* **114**, 086601 (2015).
- ¹⁰⁷N. Lu and S. Mukamel, "Polaron and size effects in optical line shapes of molecular aggregates," *J. Chem. Phys.* **95**, 1588–1607 (1991).
- ¹⁰⁸Y. Tanimura, "Reduced hierarchical equations of motion in real and imaginary time: Correlated initial states and thermodynamic quantities," *J. Chem. Phys.* **141**, 044114 (2014).
- ¹⁰⁹D. Hou, S. Wang, R. Wang, L. Z. Ye, R. X. Xu, X. Zheng, and Y. J. Yan, "Improving the efficiency of hierarchical equations of motion approach and application to coherent dynamics in Aharonov-Bohm interferometers," *J. Chem. Phys.* **142**, 104112 (2015).
- ¹¹⁰T. P. Fay, "A simple improved low temperature correction for the hierarchical equations of motion," *J. Chem. Phys.* **157**, 054108 (2022).
- ¹¹¹V. M. Axt and S. Mukamel, "Nonlinear optics of semiconductor and molecular nanostructures; a common perspective," *Rev. Mod. Phys.* **70**, 145–174 (1998).
- ¹¹²F. Rossi and T. Kuhn, "Theory of ultrafast phenomena in photoexcited semiconductors," *Rev. Mod. Phys.* **74**, 895–950 (2002).
- ¹¹³V. Janković and N. Vukmirović, "Dynamics of exciton formation and relaxation in photoexcited semiconductors," *Phys. Rev. B* **92**, 235208 (2015).

- ¹¹⁴D. Thirumalai and B. Berne, "Methods for simulating time correlation functions in quantum systems," *Comput. Phys. Commun.* **63**, 415–426 (1991).
- ¹¹⁵G. Schubert, G. Wellein, A. Weisse, A. Alvermann, and H. Fehske, "Optical absorption and activated transport in polaronic systems," *Phys. Rev. B* **72**, 104304 (2005).
- ¹¹⁶M. Frigo and S. G. Johnson, "The design and implementation of FFTW3," *Proc. IEEE* **93**, 216–231 (2005).
- ¹¹⁷V. Janković (2023), "Numerical study of the one-dimensional Holstein model using the momentum-space hierarchical equations of motion method," Zenodo.
- ¹¹⁸D. M. Wilkins and N. S. Dattani, "Why quantum coherence is not important in the Fenna-Matthews-Olsen complex," *J. Chem. Theory Comput.* **11**, 3411–3419 (2015).
- ¹¹⁹W. H. Press, S. A. Teukolsky, W. T. Vetterling, and B. P. Flannery, *Numerical Recipes in C*, 2nd ed. (Cambridge University Press, Cambridge, 1992).
- ¹²⁰C. M. Bender and S. A. Orszag, *Advanced Mathematical Methods for Scientists and Engineers* (McGraw-Hill Book Company, 1978).
- ¹²¹Q. Shi, Y. Xu, Y. Yan, and M. Xu, "Efficient propagation of the hierarchical equations of motion using the matrix product state method," *J. Chem. Phys.* **148**, 174102 (2018).
- ¹²²Y. Yan, M. Xu, T. Li, and Q. Shi, "Efficient propagation of the hierarchical equations of motion using the Tucker and hierarchical Tucker tensors," *J. Chem. Phys.* **154**, 194104 (2021).
- ¹²³E. Mangaud, A. Jaouadi, A. Chin, and M. Desouter-Lecomte, "Survey of the hierarchical equations of motion in tensor-train format for non-Markovian quantum dynamics," *Eur. Phys. J.: Spec. Top.* (published online 2023). <https://doi.org/10.1140/epjs/s11734-023-00919-0>
- ¹²⁴Q. Shi, L. Chen, G. Nan, R.-X. Xu, and Y. Yan, "Efficient hierarchical Liouville space propagator to quantum dissipative dynamics," *J. Chem. Phys.* **130**, 084105 (2009).
- ¹²⁵S. Fratini, D. Mayou, and S. Ciuchi, "The transient localization scenario for charge transport in crystalline organic materials," *Adv. Funct. Mater.* **26**, 2292–2315 (2016).
- ¹²⁶S. Fratini and S. Ciuchi, "Dynamical localization corrections to band transport," *Phys. Rev. Res.* **2**, 013001 (2020).
- ¹²⁷S. Fratini and S. Ciuchi, "Displaced Drude peak and bad metal from the interaction with slow fluctuations," *SciPost Phys.* **11**, 039 (2021).
- ¹²⁸Y. Zhao, D. W. Brown, and K. Lindenberg, "On the Munn–Silbey approach to nonlocal exciton–phonon coupling," *J. Chem. Phys.* **100**, 2335–2345 (1994).
- ¹²⁹R. Feynman and F. Vernon, "The theory of a general quantum system interacting with a linear dissipative system," *Ann. Phys.* **24**, 118–173 (1963).
- ¹³⁰L. Zhu, H. Liu, W. Xie, and Q. Shi, "Explicit system-bath correlation calculated using the hierarchical equations of motion method," *J. Chem. Phys.* **137**, 194106 (2012).
- ¹³¹A. Kato and Y. Tanimura, "Quantum heat current under non-perturbative and non-Markovian conditions: Applications to heat machines," *J. Chem. Phys.* **145**, 224105 (2016).

Fermionic-propagator and alternating-basis quantum Monte Carlo methods for correlated electrons on a lattice

Cite as: J. Chem. Phys. 158, 044108 (2023); doi: 10.1063/5.0133597

Submitted: 4 November 2022 • Accepted: 2 January 2023 •

Published Online: 24 January 2023



View Online



Export Citation



CrossMark

Veljko Janković^{a)}  and Jakša Vučičević^{b)} 

AFFILIATIONS

Institute of Physics Belgrade, University of Belgrade, Pregrevica 118, 11080 Belgrade, Serbia

^{a)} Author to whom correspondence should be addressed: veljko.jankovic@ipb.ac.rs

^{b)} jaksa.vucicevic@ipb.ac.rs

ABSTRACT

Ultracold-atom simulations of the Hubbard model provide insights into the character of charge and spin correlations in and out of equilibrium. The corresponding numerical simulations, on the other hand, remain a significant challenge. We build on recent progress in the quantum Monte Carlo (QMC) simulation of electrons in continuous space and apply similar ideas to the square-lattice Hubbard model. We devise and benchmark two discrete-time QMC methods, namely the fermionic-propagator QMC (FPQMC) and the alternating-basis QMC (ABQMC). In FPQMC, the time evolution is represented by snapshots in real space, whereas the snapshots in ABQMC alternate between real and reciprocal space. The methods may be applied to study equilibrium properties within the grand-canonical or canonical ensemble, external field quenches, and even the evolution of pure states. Various real-space/reciprocal-space correlation functions are also within their reach. Both methods deal with matrices of size equal to the number of particles (thus independent of the number of orbitals or time slices), which allows for cheap updates. We benchmark the methods in relevant setups. In equilibrium, the FPQMC method is found to have an excellent average sign and, in some cases, yields correct results even with poor imaginary-time discretization. ABQMC has a significantly worse average sign, but also produces good results. Out of equilibrium, FPQMC suffers from a strong dynamical sign problem. On the contrary, in ABQMC, the sign problem is not time-dependent. Using ABQMC, we compute survival probabilities for several experimentally relevant pure states.

Published under an exclusive license by AIP Publishing. <https://doi.org/10.1063/5.0133597>

I. INTRODUCTION

The last two decades have witnessed remarkable developments in laser and ultracold-atom technologies that have enabled experimental studies of strongly correlated electrons in and out of equilibrium.^{1,2} Ultracold atoms in optical lattices^{2,3} and optical tweezers arrays^{4–6} have been used as quantum simulators for paradigmatic models of condensed-matter physics, such as the Hubbard model.^{7,8} Recent experiments with fermionic ultracold atoms have probed the equation of state,⁹ charge, and spin correlation functions,^{10–13} as well as transport properties (by monitoring charge and spin diffusion^{14–17}).

These experimental achievements pose a significant challenge for the theory. The level of difficulty, however, greatly depends on whether one computes instantaneous (equal-time) correlations

or the full time/frequency dependence of dynamical correlators. The other factor is whether one considers thermal equilibrium or out-of-equilibrium setups.

Instantaneous correlators in equilibrium are the best-case scenario. The average density, double occupancy, and correlations between particle or spin densities on adjacent sites are still very important. They serve as a thermometer: the temperature in cold-atom experiments cannot be measured directly and is often gauged in comparison with numerical simulations.^{11,14} For this kind of application, current state-of-the-art methods^{18–43} are often sufficient. Equal-time multipoint density correlations are also of interest, as they hold information, e.g., about the emergence of string patterns^{13,44,45} or the effect of holes on antiferromagnetic correlations.^{46–48} However, measuring density at a larger number of points simultaneously is more difficult in many algorithms. For

example, in the Hirsch–Fye (HF) algorithm,^{24,49} one cannot do this straight-forwardly, as the auxiliary Ising spins only distinguish between singly occupied and doubly occupied/empty sites.

Of even greater interest and much greater difficulty are the time-dependent correlations in equilibrium. These pertain to studies of transport and hydrodynamics at the level of linear response theory.^{50–52} The limitations of current state-of-the-art methods here become starkly apparent. If one is interested in long-wavelength behavior (as is precisely the case in the study of hydrodynamic properties⁵²), the lattices treated in the simulation need to be sufficiently large. The finite-temperature Lanczos method^{53,54} can only treat up to 20 lattice sites^{50,55} and is unsuitable for such applications. Quantum Monte Carlo (QMC) methods can treat up to 300 sites,^{29,30} but only under certain conditions: doping away from half-filling leads to a significant sign problem, which becomes more severe as the lattice size, inverse temperature, and coupling constant are increased. Moreover, QMC methods are formulated in imaginary time and require ill-defined analytical continuation to reconstruct optical conductivity or any other real-frequency spectrum.⁵¹

Direct real-time calculations, regardless of proximity to the equilibrium, are the most difficult.^{31,56–69} These present an alternative to analytical continuation in equilibrium calculations but are necessary to describe non-equilibrium regimes, e.g., in external field quenches.¹⁶ In the corresponding Kadanoff–Baym–Keldysh three- or two-piece contour formalism, QMC computations are plagued by the dynamical sign problem, which has so far been overcome in only the smallest systems.⁶¹ The time-dependent density matrix renormalization group^{70–72} produces practically exact results, however, only in one-dimensional^{63,64} or ladder systems.⁷³ Simulations based on the nonequilibrium Green's functions formalism⁷⁴ are also possible but not numerically exact. They can, however, treat much larger systems over much longer time scales than other real-time approaches.^{64,75–77}

The main goal of this work is to construct a numerically exact way to compute spatially resolved densities in setups relevant for optical lattice experiments. This includes general multipoint correlators in real space and momentum space, and we focus on densities of charge and spin. We are interested in both the equilibrium expectation values and their time dependence in transient regimes. (The latter can formally be used to access temporal correlations in equilibrium as well.)

We take a largely unexplored QMC route^{78–80} toward the computation of correlation functions in the square-lattice Hubbard model. Current state-of-the-art methods, such as the continuous-time interaction-expansion (CT-INT),^{31–33} the continuous-time auxiliary field (CT-AUX),^{31,34} and HF,^{24,49} rely on the computation of large matrix determinants, which, in many cases, presents the bottleneck of the algorithm. In CT-INT and CT-AUX, the size of the matrices generally grows with coupling, inverse temperature, and lattice size. In the HF, which is based on the Suzuki–Trotter decomposition (STD), the matrix size is fixed, yet presents a measure of the systematic error: the size of the matrix scales with both the number of time slices and the number of lattice sites. A rather separate approach is possible, where the size of the matrices scales only with the total number of electrons. This approach builds on the path-integral MC (PIMC).^{81,82} In PIMC, the trajectories of individual electrons are tracked. In continuous-space models,

PIMC was used successfully even in the calculation of dynamical response functions.^{83,84} The downside is that the antisymmetry of electrons feeds into the overall sign of a given configuration, thus contributing to the sign problem. A more sophisticated idea was put forward in Refs. 85–87. Namely, the propagation between two time slices can be described by a single many-fermion propagator, which groups (blocks) all possible ways the electrons can go from one set of positions to another—including all possible exchanges. The many-fermion propagator is evaluated as a determinant of a matrix of size equal to the total number of electrons. This scheme automatically eliminates one important source of the sign problem and improves the average sign drastically. Such *permutation blocking* algorithms have been utilized with great success to compute thermodynamic quantities in continuous-space fermionic models.^{88–96} Here, we investigate and test analogous formulations in the *lattice models* of interest and try generalizing the approach to real-time dynamics.

We develop and test two slightly different QMC methods. The Fermionic-propagator QMC (FPQMC) is a real-space method similar to the permutation-blocking and fermionic-propagator PIMC, respectively, developed by Dornheim *et al.*⁹⁰ and Filinov *et al.*⁹⁶ for continuous models. On the other hand, the alternating-basis QMC (ABQMC) method is formulated simultaneously in both real and reciprocal space, which makes measuring distance- and momentum-resolved quantities equally simple. The motion of electrons and their interactions are treated on an equal footing. Both methods are based on the STD and are straight-forwardly formulated along any part of or the entire Kadanoff–Baym–Keldysh three-piece contour. This allows access to both real- and imaginary-time correlation functions in and out of equilibrium. Unlike CT-INT, CT-AUX, and HF, our methods can also be used to treat canonical ensembles as well as the time evolution of pure states. Our formulation ensures that the measurement of an arbitrary multipoint charge or spin correlation function is algorithmically trivial and cheap.

We perform benchmarks on several examples where numerically exact results are available.

In calculations of instantaneous correlators for the 2D Hubbard model in equilibrium, our main finding is that the FPQMC method has a rather manageable sign problem. The average sign is anti-correlated with coupling strength, which is in sharp contrast with some of the standard QMC methods. More importantly, we find that the average sign drops off relatively slowly with the lattice size and the number of time slices—we have been able to converge results with as many as eight time slices, or as many as 80 lattice sites. At strong coupling and at half-filling, we find the average sign to be very close to 1. In the temperature range relevant for optical-lattice experiments, we find that the average occupancy can be computed to a high accuracy with as few as two time slices; the double occupancy and the instantaneous spin–spin correlations require somewhat finer time discretization, but often not more than six time-slices in total. We also document that FPQMC appears to be sign-problem-free for Hubbard chains.

However, in calculations of the time-evolving and spatially resolved density, we find that the FPQMC sign problem is mostly prohibitive of obtaining results. Nevertheless, employing the ABQMC algorithm, we are able to compute survival probabilities of various pure states on 4×4 clusters—in the ABQMC formulation, the sign-problem is manifestly independent of time and interaction

strength, and one can scan the entire time evolution for multiple strengths of interaction in a single run. The numerical results reveal several interesting trends. Similarly to observations made in Ref. 97, we find in general that the survival probability decays over longer times when interactions are stronger. At shorter times, we observe that the behavior depends strongly on the type of the initial state, likely related to the average density.

The paper is organized as follows: The FPQMC and ABQMC methods are developed in Sec. II and applied to equilibrium and out-of-equilibrium setups in Sec. III. Section IV discusses the FPQMC and ABQMC methods in light of other widely used QMC algorithms. Section V summarizes our main findings and their implications, and discusses prospects for further work.

II. MODEL AND METHOD

A. Hubbard Hamiltonian

We study the Hubbard model on a square-lattice cluster containing $N_c = N_x N_y$ sites under periodic boundary conditions (PBC). The Hamiltonian reads as

$$H = H_0 + H_{\text{int}}. \quad (1)$$

The noninteracting (single-particle) part H_0 of the Hamiltonian describes a band of itinerant electrons

$$H_0 = -J \sum_{\langle \mathbf{r}, \mathbf{r}' \rangle \sigma} c_{\mathbf{r}\sigma}^\dagger c_{\mathbf{r}'\sigma} = \sum_{\mathbf{k}\sigma} \varepsilon_{\mathbf{k}} n_{\mathbf{k}\sigma}, \quad (2)$$

where J is the hopping amplitude between the nearest-neighbor lattice sites \mathbf{r} and \mathbf{r}' , while the operators $c_{\mathbf{r}\sigma}^\dagger$ ($c_{\mathbf{r}\sigma}$) create (destroy) an electron of spin σ on lattice site \mathbf{r} . Under PBC, H_0 is diagonal in the momentum representation; the wave vector \mathbf{k} may assume any of the N_c allowed values in the first Brillouin zone of the lattice. The free-electron dispersion is given by $\varepsilon_{\mathbf{k}} = -2J(\cos k_x + \cos k_y)$. The density operator is $n_{\mathbf{k}\sigma} = c_{\mathbf{k}\sigma}^\dagger c_{\mathbf{k}\sigma}$ with $c_{\mathbf{k}\sigma} = \sum_{\mathbf{r}} \langle \mathbf{k} | \mathbf{r} \rangle c_{\mathbf{r}\sigma}$. The Hamiltonian of the on-site Hubbard interaction (two-particle part) reads as

$$H_{\text{int}} = U \sum_{\mathbf{r}} n_{\mathbf{r}\uparrow} n_{\mathbf{r}\downarrow}, \quad (3)$$

where U is the interaction strength, while $n_{\mathbf{r}\sigma} = c_{\mathbf{r}\sigma}^\dagger c_{\mathbf{r}\sigma}$.

If the number of particles is not fixed, Eq. (1) additionally features the chemical-potential term $-\mu \sum_{\mathbf{r}\sigma} n_{\mathbf{r}\sigma} = -\mu \sum_{\mathbf{k}\sigma} n_{\mathbf{k}\sigma}$ that can be added to either H_0 or H_{int} . Here, since we develop a coordinate-space QMC method, we add it to H_{int} .

B. FPQMC method

Finding viable approximations to the exponential of the form $e^{-\alpha H}$ is crucial to many QMC methods. With $\alpha = 1/T$ (T denotes temperature), this is the Boltzmann operator, which will play a role whenever the system is in thermal equilibrium. In the formulation of dynamical responses, the time-evolution operator will also have this form, with $\alpha = it$, where t is the (real) time. One possible way to deal with these is the lowest-order STD⁹⁸

$$e^{-\alpha H} \approx \left(e^{-\Delta\alpha H_0} e^{-\Delta\alpha H_{\text{int}}} \right)^{N_\alpha}, \quad (4)$$

where the interval of length $|\alpha|$ is divided into N_α subintervals of length $|\Delta\alpha|$ each, where $\Delta\alpha = \alpha/N_\alpha$. The error of the approximation is of the order of $|\Delta\alpha|^2 \| [H_0, H_{\text{int}}] \|$, where the norm $\| [H_0, H_{\text{int}}] \|$ may be defined as the largest (in modulus) eigenvalue of the commutator $[H_0, H_{\text{int}}]$.⁸⁰ The error can in principle be made arbitrarily small by choosing N_α large enough. However, the situation is complicated by the fact that the RHS of Eq. (4) contains both single-particle and two-particle contributions. The latter are diagonal in the coordinate representation, so that the spectral decomposition of $e^{-\Delta\alpha H_{\text{int}}}$ is performed in terms of totally antisymmetric states in the coordinate representation, aka the Fock states,

$$|\Psi_i\rangle = \prod_{\sigma} \prod_{j=1}^{N_\sigma} c_{\mathbf{r}_j^\sigma}^\dagger |\emptyset\rangle \quad (5)$$

that contain N_σ electrons of spin σ whose positions $\mathbf{r}_1^\sigma, \dots, \mathbf{r}_{N_\sigma}^\sigma$ are ordered according to a certain rule. We define $\varepsilon_{\text{int}}(\Psi_i) \equiv \langle \Psi_i | H_{\text{int}} | \Psi_i \rangle$. On the other hand, the matrix element of $e^{-\Delta\alpha H_0}$ between many-body states $|\Psi_i'\rangle$ and $|\Psi_i\rangle$ can be expressed in terms of determinants of single-electron propagators

$$\langle \Psi_i' | e^{-\Delta\alpha H_0} | \Psi_i \rangle = \prod_{\sigma} \det S(\Psi_i', \Psi_i, \Delta\alpha, \sigma), \quad (6)$$

$$[S(\Psi_i', \Psi_i, \Delta\alpha, \sigma)]_{j_1 j_2} = \langle \mathbf{r}_{j_1}^{\sigma'} | e^{-\Delta\alpha H_0} | \mathbf{r}_{j_2}^\sigma \rangle. \quad (7)$$

We provide a formal proof of Eqs. (6) and (7) in Appendix A. The same equations lie at the crux of conceptually similar permutation-blocking⁹⁰ and fermionic-propagator⁹⁶ PIMC methods, which are formulated for continuous-space models. When $\Delta\alpha$ is purely real (purely imaginary), the quantity on the right-hand side of Eq. (7) is the imaginary-time (real-time) lattice propagator of a free particle in the coordinate representation.⁸⁰ Its explicit expressions are given in Appendix B.

Further developments of the method somewhat depend on the physical situation of interest. We formulate the method first in equilibrium and then in out-of-equilibrium situations. To facilitate discussion, in Figs. 1(a)–1(d), we summarize the contours appropriate for the different situations we consider.

1. FPQMC method for thermodynamic quantities

The equilibrium properties at temperature $T = \beta^{-1}$ follow from the partition function $Z \equiv \text{Tr} e^{-\beta H}$, which may be computed by dividing the imaginary-time interval $[0, \beta]$ into N_τ slices of length $\Delta\tau \equiv \beta/N_\tau$, employing Eq. (4), and inserting the spectral decompositions of $e^{-\Delta\tau H_{\text{int}}}$. The corresponding approximant for Z reads as

$$Z \approx \sum_{\mathcal{C}} \mathcal{D}_{\beta}(\mathcal{C}, \Delta\tau) e^{-\Delta\tau \varepsilon_{\text{int}}(\mathcal{C})}. \quad (8)$$

The configuration

$$\mathcal{C} = \{ |\Psi_{i,1}\rangle, \dots, |\Psi_{i,N_\tau}\rangle \} \quad (9)$$

resides on the contour depicted in Fig. 1(a) and consists of N_τ Fock states $|\Psi_{i,l}\rangle$ in the coordinate representation. $\mathcal{D}_{\beta}(\mathcal{C}, \Delta\tau)$ depends

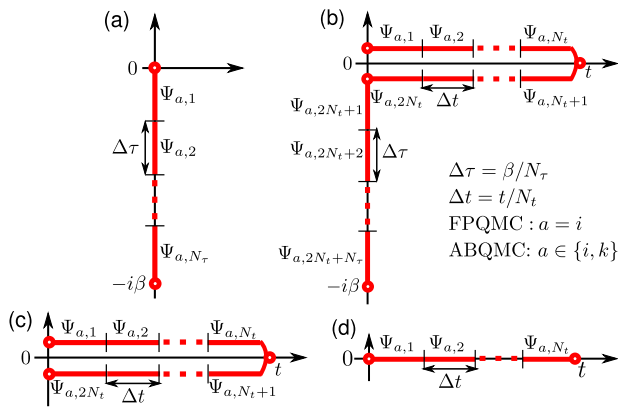


FIG. 1. Contours appropriate for computing (a) thermodynamic quantities at temperature $T = 1/\beta$, (b) time-dependent quantities after quantum quench in which the Hamiltonian is suddenly changed from $H(0)$ at $t < 0$ to H at $t > 0$, (c) time-dependent quantities during evolution from a pure state $|\psi(0)\rangle \equiv |\Psi_{i,1}\rangle$, (d) the survival probability of the initial pure state $|\psi(0)\rangle \equiv |\Psi_{i,1}\rangle$. In (a) and (b), the vertical part is divided into N_τ identical slices of length $\Delta\tau$. In (b)–(d), each horizontal line is divided into N_t identical slices of length Δt . Within the FPQMC method, a many-body state in the coordinate representation $|\Psi_{i,l}\rangle$ [Eq. (5)] is associated with each slice l . Within the ABQMC method, in addition to $|\Psi_{i,l}\rangle$, each slice l features a many-body state in the momentum representation $|\Psi_{k,l}\rangle$ [Eq. (29)].

on the temperature and imaginary-time discretization through the imaginary-time step $\Delta\tau$

$$\begin{aligned} \mathcal{D}_\beta(\mathcal{C}, \Delta\tau) &\equiv \prod_{l=1}^{N_\tau} \langle \Psi_{i,l|\oplus 1} | e^{-\Delta\tau H_0} | \Psi_{i,l} \rangle \\ &= \prod_{l=1}^{N_\tau} \prod_{\sigma} \det S(\Psi_{i,l|\oplus 1}, \Psi_{i,l}, \Delta\tau, \sigma) \end{aligned} \quad (10)$$

and is a product of $2N_\tau$ determinants of imaginary-time single-particle propagators on a lattice (this is emphasized by adding the subscript β). The cyclic addition in Eq. (10) is the standard addition for $l = 1, \dots, N_\tau - 1$, while $N_\tau \oplus 1 = 1$. The symbol $\varepsilon_{\text{int}}(\mathcal{C})$ stands for

$$\varepsilon_{\text{int}}(\mathcal{C}) \equiv \sum_{l=1}^{N_\tau} \varepsilon_{\text{int}}(\Psi_{i,l}). \quad (11)$$

By virtue of the cyclic invariance under trace, the thermodynamic expectation value of an observable A can be expressed as

$$\langle A \rangle = \frac{1}{N_\tau} \sum_{l=0}^{N_\tau-1} \frac{1}{Z} \text{Tr} \left\{ (e^{-\Delta\tau H})^l A (e^{-\Delta\tau H})^{N_\tau-l} \right\}. \quad (12)$$

The FPQMC method is particularly suitable for observables diagonal in the coordinate representation (e.g., the interaction energy H_{int} or the real-space charge density $n_{r\sigma}$). Such observables will be distinguished by adding the subscript i . Equation (12), combined with the lowest-order STD [Eq. (4)], produces the following approximant for $\langle A_i \rangle$:

$$\langle A_i \rangle \approx \frac{\sum_{\mathcal{C}} \mathcal{D}_\beta(\mathcal{C}, \Delta\tau) e^{-\Delta\tau \varepsilon_{\text{int}}(\mathcal{C})} \frac{1}{N_\tau} \sum_{l=1}^{N_\tau} \mathcal{A}_i(\Psi_{i,l})}{\sum_{\mathcal{C}} \mathcal{D}_\beta(\mathcal{C}, \Delta\tau) e^{-\Delta\tau \varepsilon_{\text{int}}(\mathcal{C})}}, \quad (13)$$

where

$$\mathcal{A}_i(\Psi_{i,l}) \equiv \langle \Psi_{i,l} | A_i | \Psi_{i,l} \rangle. \quad (14)$$

Defining the weight $w(\mathcal{C}, \Delta\tau)$ of configuration \mathcal{C} as

$$w(\mathcal{C}, \Delta\tau) \equiv |\mathcal{D}_\beta(\mathcal{C}, \Delta\tau)| e^{-\Delta\tau \varepsilon_{\text{int}}(\mathcal{C})}, \quad (15)$$

Eq. (13) is rewritten as

$$\langle A_i \rangle \approx \frac{\langle \text{sgn}(\mathcal{C}) \frac{1}{N_\tau} \sum_{l=1}^{N_\tau} \mathcal{A}_i(\Psi_{i,l}) \rangle_w}{\langle \text{sgn}(\mathcal{C}) \rangle_w}, \quad (16)$$

where $\langle \dots \rangle_w$ denotes the weighted average over all \mathcal{C} with respect to the weight $w(\mathcal{C})$; $\text{sgn}(\mathcal{C}) \equiv \mathcal{D}_\beta(\mathcal{C}, \Delta\tau) / |\mathcal{D}_\beta(\mathcal{C}, \Delta\tau)|$ is the sign of configuration \mathcal{C} , while $|\langle \text{sgn} \rangle| \equiv |\langle \text{sgn}(\mathcal{C}) \rangle_w|$ is the average sign of the QMC simulation.

By construction, our FPQMC approach yields exact results for the noninteracting electrons (ideal gas, $U = 0$) and in the atomic limit ($J = 0$). In both limits, due to $[H_0, H_{\text{int}}] = 0$, the FPQMC method with arbitrary N_τ should recover the exact results. However, the performance of the method, quantified through the average sign of the simulation, deteriorates with increasing N_τ . For $N_\tau = 1$, the FPQMC algorithm is sign-problem-free because it sums only diagonal elements $\langle \Psi_{i,1} | e^{-\beta H_0} | \Psi_{i,1} \rangle$ of the positive operator $e^{-\beta H_0}$. The sign problem is absent also for $N_\tau = 2$ because $\mathcal{D}_\beta(\mathcal{C}, \beta/2)$ is a square of a real number.

An important feature of the above-presented methodology is its direct applicability in both the grand-canonical and canonical ensemble. The grand-canonical formulation is essential to current state-of-the-art approaches³¹ (e.g., CT-INT or CT-AUX) relying on the thermal Wick's theorem, which is not valid in the canonical ensemble.⁹⁹ In the auxiliary-field QMC,^{22,23,25,27,28} the Hubbard–Stratonovich transformation¹⁰⁰ decouples many-body propagators into sums (or integrals) over one-body operators whether the particle number is fixed or not. Working in the grand-canonical ensemble is then analytically and computationally more convenient because the traces over *all possible* fermion occupations result in determinants.^{23,101} In the canonical ensemble, the computation of traces over constrained fermion occupations is facilitated by observing that the Hubbard–Stratonovich decoupling produces an ensemble of noninteracting systems¹⁰¹ to which theories developed for noninteracting systems in the canonical ensemble, such as particle projection^{102,103} or recursive methods,^{104,105} can be applied. While such procedures may be numerically costly and/or unstable,¹⁰¹ a very recent combination of the auxiliary-field QMC with the recursive auxiliary partition function formalism¹⁰⁵ is reported to be stable and scale favorably with the numbers of particles and available orbitals.¹⁰⁶ In contrast to all these approaches, the formulation of the FPQMC method does not depend on whether the electron number is fixed or not. However, the selection of MC updates does depend on the ensemble we work with. In the canonical ensemble, the updates should conserve the number of electrons; in the grand-canonical ensemble, we also need to include the updates that insert/remove electrons. Our MC updates, together with the

procedure used to extract MC results and estimate their statistical error, are presented in great detail in Sec. SI of the [supplementary material](#).

2. FPQMC method for time-dependent quantities

Ideally, numerical simulations of quench experiments such as those from Refs. 14, 16, and 17 should provide the time-dependent expectation value $\langle A(t) \rangle$ of an observable A at times $t > 0$ after the Hamiltonian undergoes a sudden change from $H(0)$ for $t < 0$ to H for $t > 0$. Again, in many instances,^{14,17} the experimentally measurable observable A is diagonal in the coordinate representation, which will be emphasized by the subscript i . The computation proceeds along the three-piece Kadanoff–Baym–Keldysh contour¹

$$\langle A_i(t) \rangle = \frac{\text{Tr}(e^{-\beta H(0)} e^{iHt} A_i e^{-iHt})}{\text{Tr}(e^{-\beta H(0)} e^{iHt} e^{-iHt})}, \quad (17)$$

where one may employ the above-outlined fermionic-propagator approach after dividing the whole contour into a number of slices, see Fig. 1(b). While H is the Hubbard Hamiltonian given in Eqs. (1)–(3), $H(0)$ describes correlated electrons whose charge (or spin) density is spatially modulated by external fields.

The immediate complication (compared to the equilibrium case) is that there are now three operators (instead of one) that need to be decomposed via the STD. A preset accuracy determined by the size of both $\Delta\tau$ and Δt will, therefore, require a larger number of time-slices. In turn, this will enlarge the configuration space to be sampled and potentially worsen the sign problem in the MC summation. Even worse, the individual terms in the denominator depend on time, so that the sign problem becomes time-dependent (dynamical). The problem is expected to become worse at long times t , yet vanishes in the $t \rightarrow 0$ limit.

To simplify the task and yet keep it relevant, we consider the evolution from a pure state $|\psi(0)\rangle$ that is an eigenstate of real-space density operators $n_{r\sigma}$, so that its most general form is given by Eq. (5). Such a setup has been experimentally realized.^{5,6,14,17} Replacing $e^{-\beta H(0)} \rightarrow |\psi(0)\rangle\langle\psi(0)|$ in Eq. (17) leads to the expression for the time-dependent expectation value of the observable A_i

$$\langle A_i(t) \rangle = \frac{\langle \psi(0) | e^{iHt} A_i e^{-iHt} | \psi(0) \rangle}{\langle \psi(0) | e^{iHt} e^{-iHt} | \psi(0) \rangle}. \quad (18)$$

Here, the STD should be applied to both the forward and backward evolution operators, see Fig. 1(c), which requires a larger number of time-slices to reach the desired accuracy (in terms of the systematic error). Nevertheless, Eq. (18) is the simplest example in which the applicability of the real-time FPQMC method to follow the evolution of real-space observables may be examined.

Generally speaking, the symmetries of the model should be exploited to enable as efficient as possible MC evaluation of Eq. (18). Recent experimental¹⁵ and theoretical¹⁰⁷ studies have discussed the dynamical symmetry of the Hubbard model, according to which the temporal evolution of certain observables is identical for repulsive and attractive interactions of the same magnitude. The symmetry relies on specific transformation laws of the Hamiltonian H , the

initial state $|\psi(0)\rangle$, and the observable of interest A_i under the combined action of two symmetry operations. The first is the bipartite lattice symmetry, or the π -boost¹⁵ operation, which exploits the symmetry $\epsilon_{\mathbf{k}} = -\epsilon_{\mathbf{k}+(\pi,\pi)}$ of the free-electron dispersion and is represented by the unitary operator B . The second is the time reversal symmetry represented by the antiunitary operator T ($TiT = -i$) that reverses electron spin and momentum according to $Tc_{r\sigma}^{(\dagger)}T = (-1)^{\delta_{r,i}}c_{r\bar{\sigma}}^{(\dagger)}$ and $Tc_{k\sigma}^{(\dagger)}T = (-1)^{\delta_{k,i}}c_{-k,\bar{\sigma}}^{(\dagger)}$. In Appendix C, we formulate our FPQMC method to evaluate Eq. (18) in a way that manifestly respects the dynamical symmetry of the model (each contribution to the MC sums respects the symmetry). Here, we only cite the final expression for the time-dependent expectation value of an observable A_i that satisfies $TBA_iBT = A_i$ when the evolution starts from a state $|\psi(0)\rangle$ satisfying $TB|\psi(0)\rangle = e^{i\chi}|\psi(0)\rangle$

$$\langle A_i(t) \rangle \approx \frac{\sum_{\mathcal{C}} \mathcal{A}_i(\Psi_{i,N_t+1}) \text{Re}\{\mathcal{D}_{2t}(\mathcal{C}, \Delta t)\} \cos[\Delta\epsilon_{\text{int}}(\mathcal{C})\Delta t]}{\sum_{\mathcal{C}} \text{Re}\{\mathcal{D}_{2t}(\mathcal{C}, \Delta t)\} \cos[\Delta\epsilon_{\text{int}}(\mathcal{C})\Delta t]}. \quad (19)$$

Here, the configuration resides on the contour depicted in Fig. 1(c), which is divided into $2N_t$ slices in total, and contains $2N_t - 1$ independent states. We assume that states $|\Psi_{i,l}\rangle$ for $l = 1, \dots, N_t$ ($l = N_t + 1, \dots, 2N_t$) lie on the forward (backward) branch of the contour, while $|\Psi_{i,1}\rangle \equiv |\psi(0)\rangle$. $\mathcal{A}_i(\Psi_{i,N_t+1})$ is defined as in Eq. (14), while

$$\Delta\epsilon_{\text{int}}(\mathcal{C}) \equiv \sum_{l=1}^{N_t} [\epsilon_{\text{int}}(\Psi_{i,l+N_t}) - \epsilon_{\text{int}}(\Psi_{i,l})]. \quad (20)$$

The symbol $\mathcal{D}_{2t}(\mathcal{C}, \Delta t)$ stands for the following combination of forward and backward fermionic propagators (which is also emphasized by the subscript $2t$):

$$\mathcal{D}_{2t}(\mathcal{C}, \Delta t) = \prod_{l=N_t+1}^{2N_t} \langle \Psi_{i,l\oplus 1} | e^{iH_0\Delta t} | \Psi_{i,l} \rangle \prod_{l=1}^{N_t} \langle \Psi_{i,l\oplus 1} | e^{-iH_0\Delta t} | \Psi_{i,l} \rangle. \quad (21)$$

The bipartite lattice symmetry guarantees that $\mathcal{D}_{2t}(\mathcal{C}, \Delta t) = \mathcal{D}_{2t}(\mathcal{C}, -\Delta t)$, see Eq. (C9). The numerator and denominator of the RHS of Eq. (19) are term-by-term invariant under the transformations $\Delta t \rightarrow -\Delta t$ and $\Delta\epsilon_{\text{int}}(\mathcal{C}) \rightarrow -\Delta\epsilon_{\text{int}}(\mathcal{C})$ that respectively reflect the transformation properties under the time reversal symmetry and the fact that the dynamics of $\langle A_i(t) \rangle$ are identical in the repulsive and the attractive model. Defining $w(\mathcal{C}) \equiv |\text{Re}\{\mathcal{D}_{2t}(\mathcal{C}, \Delta t)\}|$ and $\text{sgn}(\mathcal{C}) \equiv \text{Re}\{\mathcal{D}_{2t}(\mathcal{C}, \Delta t)\} / |\text{Re}\{\mathcal{D}_{2t}(\mathcal{C}, \Delta t)\}|$, Eq. (19) is recast as

$$\langle A_i(t) \rangle \approx \frac{\langle \mathcal{A}_i(\Psi_{i,N_t+1}) \text{sgn}(\mathcal{C}) \cos[\Delta\epsilon_{\text{int}}(\mathcal{C})\Delta t] \rangle_w}{\langle \text{sgn}(\mathcal{C}) \cos[\Delta\epsilon_{\text{int}}(\mathcal{C})\Delta t] \rangle_w}. \quad (22)$$

The sign problem in the MC evaluation of Eq. (22) is dynamical. It generally becomes more serious with increasing time t and interaction strength $|U|$. Moreover, $w(\mathcal{C})$ also depends on both t and U , meaning that MC evaluations for different t s and U s should be performed separately, using different Markov chains. It is thus highly desirable to employ further symmetries in order to improve the performance of the method. Particularly relevant initial states

$|\psi(0)\rangle$, from both an experimental^{14,17} and theoretical¹⁰⁸ viewpoint, are pure density-wave-like states. Such states correspond to extreme spin-density wave (SDW) and charge-density wave (CDW) patterns, which one obtains by applying strong external density-modulating fields. The SDW-like state can be written as

$$|\psi_{\text{SDW}}(\mathcal{G})\rangle = \prod_{\mathbf{r}_1 \in \mathcal{G}} c_{\mathbf{r}_1 \uparrow}^\dagger \prod_{\mathbf{r}_2 \in \mathcal{U} \setminus \mathcal{G}} c_{\mathbf{r}_2 \downarrow}^\dagger |\emptyset\rangle, \quad (23)$$

where \mathcal{G} denotes the multitude of sites on which the electron spins are polarized up, while set \mathcal{U} contains all sites of the cluster studied. The electron spins on sites belonging to $\mathcal{U} \setminus \mathcal{G}$ are thus polarized down. Such states have been experimentally realized in Ref. 17. The CDW-like states have also been realized in experiment,¹⁴ and they read as

$$|\psi_{\text{CDW}}(\mathcal{G})\rangle = \prod_{\mathbf{r} \in \mathcal{G}} c_{\mathbf{r} \uparrow}^\dagger c_{\mathbf{r} \downarrow}^\dagger |\emptyset\rangle. \quad (24)$$

The sites belonging to \mathcal{G} are doubly occupied, while the remaining sites are empty. The state $|\psi_{\text{CDW}}(\mathcal{G})\rangle$ can be obtained from the corresponding $|\psi_{\text{SDW}}(\mathcal{G})\rangle$ state by applying the partial particle-hole transformation that acts on spin-down electrons only

$$|\psi_{\text{SDW}}(\mathcal{G})\rangle = \prod_{\mathbf{r} \in \mathcal{U}} \left(c_{\mathbf{r} \downarrow}^\dagger (1 - n_{\mathbf{r} \downarrow}) + c_{\mathbf{r} \downarrow} n_{\mathbf{r} \downarrow} \right) |\psi_{\text{CDW}}(\mathcal{G})\rangle, \quad (25)$$

see also Refs. 109 and 110. By combining the partial particle-hole, time-reversal, and bipartite lattice symmetries, the authors of Ref. 108 have shown that the time evolution of spatially resolved charge and spin densities starting from states $|\psi_{\text{CDW}}(\mathcal{G})\rangle$ and $|\psi_{\text{SDW}}(\mathcal{G})\rangle$, respectively, obey

$$\begin{aligned} \langle \psi_{\text{CDW}}(\mathcal{G}) | e^{iHt} (n_{\mathbf{r} \uparrow} + n_{\mathbf{r} \downarrow} - 1) e^{-iHt} | \psi_{\text{CDW}}(\mathcal{G}) \rangle \\ = \langle \psi_{\text{SDW}}(\mathcal{G}) | e^{iHt} (n_{\mathbf{r} \uparrow} - n_{\mathbf{r} \downarrow}) e^{-iHt} | \psi_{\text{SDW}}(\mathcal{G}) \rangle. \end{aligned} \quad (26)$$

Equation (26) may be used to acquire additional statistics by combining the Markov chains for the two symmetry-related evolutions. The procedure is briefly described in Appendix C and applied to all corresponding computations presented in Sec. III B.

3. ABQMC method for time-dependent quantities

In this section, we develop the so-called alternating-basis QMC method, which is aimed at removing the dynamical character of the sign problem in real-time FPQMC simulations. Moreover, using the ABQMC method, the results for different real times t and different interactions U may be obtained using just a single Markov chain, in contrast to the FPQMC method, which employs separate chains for each t and U .

Possible advantages of the ABQMC over the FPQMC method are most easily appreciated on the example of the survival probability of the initial state $|\psi(0)\rangle$

$$P(t) = |\langle \psi(0) | e^{-iHt} | \psi(0) \rangle|^2, \quad (27)$$

which is the probability of finding the system in its initial state after a time t has passed. Evaluating Eq. (27) by any discrete-time QMC

method necessitates only one STD, see Fig. 1(d). The survival probability is thus the simplest example on which the applicability of any QMC method to out-of-equilibrium setups can be systematically studied.

The FPQMC computation of $P(t)$ may proceed via the ratio

$$\mathcal{R}(t) = \frac{\langle \psi(0) | e^{-iHt} | \psi(0) \rangle}{\langle \psi(0) | e^{-iH_0 t} | \psi(0) \rangle} \quad (28)$$

of the survival-probability amplitudes in the presence and absence of electron-electron interactions. However, the average sign of the MC simulation of Eq. (28) is proportional to the survival-probability amplitude of the noninteracting system, which generally decays very quickly to zero, especially for large clusters.⁶² This means that the dynamical sign problem in the FPQMC evaluation of Eq. (28) may become very severe already at relatively short times t .

Instead of expressing the many-body free propagator $\langle \Psi_i' | e^{-iH_0 \Delta t} | \Psi_i \rangle$ as a determinant of single-particle free propagators [Eqs. (6) and (7)], we could have introduced the spectral decomposition of $e^{-iH_0 \Delta t}$ in terms of Fock states $|\Psi_k\rangle$ in the momentum representation. In analogy with Eq. (5), such states are defined as

$$|\Psi_k\rangle = \prod_{\sigma} \prod_{j=1}^{N_{\sigma}} c_{\mathbf{k}_j^{\sigma}}^\dagger |\emptyset\rangle. \quad (29)$$

The state $|\Psi_k\rangle$ contains N_{σ} electrons of spin σ whose momenta $\mathbf{k}_1^{\sigma}, \dots, \mathbf{k}_{N_{\sigma}}^{\sigma}$ are ordered according to a certain rule and we define $\varepsilon_0(\Psi_k) \equiv \langle \Psi_k | H_0 | \Psi_k \rangle$. In this case, the final expression for the survival probability of state $|\psi(0)\rangle$ that satisfies $TB|\psi(0)\rangle = e^{iX}|\psi(0)\rangle$ reads as

$$P(t) \approx \left| \frac{\sum_{\mathcal{C}} \text{Re}\{\mathcal{D}(\mathcal{C})\} \cos[\varepsilon_0(\mathcal{C})\Delta t] \cos[\varepsilon_{\text{int}}(\mathcal{C})\Delta t]}{\sum_{\mathcal{C}} \text{Re}\{\mathcal{D}(\mathcal{C})\}} \right|^2. \quad (30)$$

A derivation of Eq. (30) is provided in Appendix D. The MC evaluation of Eq. (30) should sample a much larger configuration space than the MC evaluation of Eq. (28). The configuration \mathcal{C} in Eq. (30) also resides on the contour depicted in Fig. 1(d), but comprises $2N_t - 1$ states in total: N_t Fock states $|\Psi_{k,l}\rangle$ ($l = 1, \dots, N_t$) and $N_t - 1$ Fock states $|\Psi_{i,l}\rangle$ ($l = 2, \dots, N_t$) (again, $|\Psi_{i,1}\rangle \equiv |\psi(0)\rangle$). $\mathcal{D}(\mathcal{C})$ is the product of $2N_t$ Slater determinants

$$\mathcal{D}(\mathcal{C}) = \prod_{l=1}^{N_t} \langle \Psi_{i,l} | \Psi_{k,l} \rangle \langle \Psi_{k,l} | \Psi_{i,l} \rangle \quad (31)$$

that stem from the sequence of basis alternations between the momentum and coordinate eigenbasis. Using the notation of Eqs. (5) and (29), the most general Slater determinant $\langle \Psi_i | \Psi_k \rangle$ entering Eq. (10) is given as

$$\langle \Psi_i | \Psi_k \rangle = \prod_{\sigma} \det \tilde{\mathcal{S}}(\Psi_i, \Psi_k, \sigma), \quad (32)$$

$$[\tilde{\mathcal{S}}(\Psi_i, \Psi_k, \sigma)]_{j_1 j_2} = \langle \mathbf{r}_{j_1}^{\sigma} | \mathbf{k}_{j_2}^{\sigma} \rangle = \frac{\exp(i\mathbf{k}_{j_2}^{\sigma} \cdot \mathbf{r}_{j_1}^{\sigma})}{\sqrt{N_c}}, \quad (33)$$

where $1 \leq j_1, j_2 \leq N_{\sigma}$. The symbol $\varepsilon_0(\mathcal{C})$ stands for [cf. Eq. (11)]

$$\varepsilon_0(\mathcal{C}) \equiv \sum_{l=1}^{N_\tau} \varepsilon_0(\Psi_{k,l}). \quad (34)$$

We note that each term in Eq. (30) is invariant under transformations $\varepsilon_0(\mathcal{C}) \rightarrow -\varepsilon_0(\mathcal{C})$ and $\Delta t \rightarrow -\Delta t$, which reflect the action of the bipartite lattice symmetry and the time reversal symmetry, respectively. Being term-by-term invariant under the transformation $\varepsilon_{\text{int}}(\mathcal{C}) \rightarrow -\varepsilon_{\text{int}}(\mathcal{C})$, Eq. (30) explicitly satisfies the requirement that the dynamics of $P(t)$ for repulsive and attractive interactions of the same magnitude are identical. Defining $w(\mathcal{C}) \equiv |\text{Re}\{\mathcal{D}(\mathcal{C})\}|$ and $\text{sgn}(\mathcal{C}) \equiv \text{Re}\{\mathcal{D}(\mathcal{C})\}/|\text{Re}\{\mathcal{D}(\mathcal{C})\}|$, Eq. (30) is recast as

$$P(t) \approx \left| \frac{\langle \text{sgn}(\mathcal{C}) \cos[\varepsilon_0(\mathcal{C})\Delta t] \cos[\varepsilon_{\text{int}}(\mathcal{C})\Delta t] \rangle_w}{\langle \text{sgn}(\mathcal{C}) \rangle_w} \right|^2. \quad (35)$$

This choice for w is optimal in the sense that it minimizes the variance of $\langle \text{sgn}(\mathcal{C}) \rangle_w$,¹¹¹ whose modulus is the average sign of the ABQMC simulation. The sign problem encountered in the MC evaluation of Eq. (35) does not depend on either time t or interaction strength U , i.e., it is not dynamical. The weight $w(\mathcal{C})$ in Eq. (35) does not depend on either Δt or any other property of configuration \mathcal{C} ($\varepsilon_0, \varepsilon_{\text{int}}$). Therefore, the MC evaluation of Eq. (35) may be performed simultaneously (using a single Markov chain) for any U and any t . This presents a technical advantage over the FPQMC method, which may be outweighed by the huge increase in configuration space when going from FPQMC to ABQMC. To somewhat reduce the dimension of the ABQMC configuration space and improve the sampling efficiency, we design the MC updates so as to respect the momentum conservation law throughout the real-time evolution. The momentum conservation poses the restriction that all the momentum-space states $|\Psi_{k,l}\rangle$ have the same total electron momentum $\mathbf{K} \equiv \sum_{k\sigma} \mathbf{k} \langle \Psi_{k,l} | n_{k\sigma} | \Psi_{k,l} \rangle$ [modulo $(2\pi, 2\pi)$]. The MC updates in the ABQMC method for the evaluation of the survival probability are presented in great detail in Sec. III of the [supplementary material](#).

By relying on the partial particle-hole and bipartite lattice symmetries, in [Appendix D](#) we demonstrate that the dynamics of the survival probabilities of states $|\psi_{\text{SDW}}(\mathcal{G})\rangle$ and $|\psi_{\text{CDW}}(\mathcal{G})\rangle$ are identical, i.e.,

$$|\langle \psi_{\text{SDW}}(\mathcal{G}) | e^{-iHt} | \psi_{\text{SDW}}(\mathcal{G}) \rangle|^2 = |\langle \psi_{\text{CDW}}(\mathcal{G}) | e^{-iHt} | \psi_{\text{CDW}}(\mathcal{G}) \rangle|^2. \quad (36)$$

Evaluating Eq. (35), additional statistics can be acquired by combining the Markov chains for the $P(t)$ calculations starting from the two symmetry-related states $|\psi_{\text{CDW}}(\mathcal{G})\rangle$ and $|\psi_{\text{SDW}}(\mathcal{G})\rangle$. The procedure is similar to that described in [Appendix C](#), and we apply it to all corresponding computations presented in Sec. III C.

III. NUMERICAL RESULTS

We first apply the FPQMC method to equilibrium situations (the particle number is not fixed), see Sec. III A, and then to time-dependent local densities during the evolution of pure states, see Sec. III B. Section III C presents our ABQMC results for the survival probability of pure states. Our implementation of the ABQMC method on the full Kadanoff-Baym-Keldysh contour [Eq. (17)] is benchmarked in Sec. SVII of the [supplementary material](#).

A. Equilibrium results: Equation of state

We start by considering the Hubbard dimer, the minimal model capturing the subtle interplay between electron delocalization and electron-electron interaction.¹¹² We opt for moderate temperature $T/J = 1$ and interaction $U/J = 4$, so that the expected number of imaginary-time slices needed to obtain convergent FPQMC results is not very large. [Figure 2](#) presents the equation of state (i.e., the dependence of the electron density $\rho_e = \langle \widehat{N}_\uparrow + \widehat{N}_\downarrow \rangle / N_c$ on the chemical potential μ) for a range of μ below the half-filling. Here, \widehat{N}_\uparrow and \widehat{N}_\downarrow are the operators of the total number of spin-up and spin-down electrons, respectively. [Figure 2](#) suggests that already $N_\tau = 2$ imaginary-time slices suffice to obtain very good results in the considered range of μ , while increasing N_τ from 2 to 4 somewhat improves the accuracy of the FPQMC results. It is interesting that, irrespective of the value of N_τ , FPQMC simulations on the dimer are manifestly sign-problem-free. First, the one-dimensional imaginary-time propagator defined in Eq. (B2) is positive, $\mathcal{I}(J\Delta\tau, l) = [e^{J\Delta\tau} + (-1)^l e^{-J\Delta\tau}] / 2$ for both $l = 0$ and 1. Second, the configuration containing two electrons of the same spin is of weight $\cosh^2(J\Delta\tau) - \sinh^2(J\Delta\tau) \equiv 1$, implying that the weights of all configurations are positive. Furthermore, our results on longer chains suggest that FPQMC simulations of one-dimensional lattice fermions do not display a sign problem. While similar statements have been repeated for continuum one-dimensional models of both noninteracting^{85,86} and interacting fermions,⁸⁷ there is, to the best of our knowledge, no rigorous proof that the sign problem is absent from coordinate-space QMC simulations of one-dimensional fermionic systems. While we do not provide such a proof either, [Fig. 3](#) is an illustrative example showing how the FPQMC results for the double occupancy $\sum_\tau \langle n_{\uparrow\tau} n_{\downarrow\tau} \rangle / N_c$ of the Hubbard chain at half-filling approach the reference result (taken from Ref. 113) as the imaginary-time discretization becomes finer. For all N_τ s considered, the average sign of FPQMC simulations is $|\langle \text{sgn} \rangle| = 1$.

We now apply the FPQMC method to evaluate the equation of state on larger clusters. We focus on a 4×4 cluster, which may already be representative of the thermodynamic limit at $T/J \gtrsim 1$.⁵⁰ We compare our $\rho_e(\mu)$ results with the results of the numerical linked-cluster expansion (NLCE) method.⁴⁰⁻⁴² The NLCE results are numerically exact and converged with respect to the control parameter, i.e., the maximal cluster-size used. NLCE is commonly

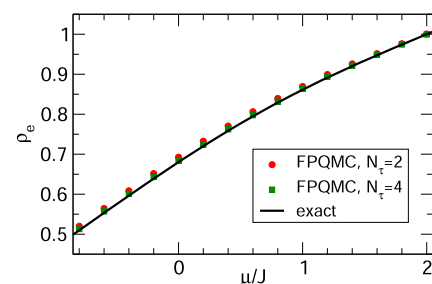


FIG. 2. Equation of state $\rho_e(\mu)$ for the Hubbard dimer with $T/J = 1$, $U/J = 4$. Full red circles (green squares) are the results of FPQMC simulations employing $N_\tau = 2$ ($N_\tau = 4$) imaginary-time slices, while the solid black line is computed using the exact diagonalization. The estimated statistical error of the FPQMC data is in all cases smaller than the symbol size.

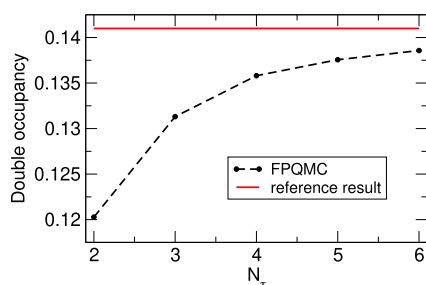


FIG. 3. Double occupancy of the $N_c = 20$ -site Hubbard chain at half-filling ($\mu = U/2$, $\rho_e = 1$) as a function of the number N_τ of imaginary-time slices. The remaining parameters are $U/J = 3$ and $T/J = 1$. The dotted line connecting full symbols (FPQMC results) serves as a guide to the eye. The reference result is taken from Ref. 113. The relative deviation of the FPQMC result with $N_\tau = 6$ from the reference result is around 2%. The statistical error bars of the FPQMC results are smaller than the symbol size.

used to benchmark methods and understand experimental data.^{9,10} Again, we keep $U/J = 4$, but we take $T/J = 1.0408$ to be able to compare results to the data of Ref. 41. Figure 4(a) reveals that the FPQMC results with only $N_\tau = 2$ imaginary-time slices agree very well (within a couple of percent) with the NLCE results over a wide range of chemical potentials. This is a highly striking observation, especially keeping in mind that the FPQMC method with $N_\tau = 2$ is sign-problem-free, see Fig. 4(b). It is unclear whether other STD-based methods would reach here the same level of accuracy with only two imaginary-time slices (and without the sign problem). This may be a specific property of the FPQMC method. Finer imaginary-time discretization introduces the sign problem, see Fig. 4(b), which becomes more pronounced as the density is increased and reaches a plateau for $\rho_e \gtrsim 0.8$. Still, the sign problem remains manageable. Increasing N_τ for 2 to 6 somewhat improves the agreement of the density ρ_e [the inset of Fig. 4(a)] and considerably improves the agreement of the double occupancy [Fig. 4(c)] with the referent NLCE results. Still, comparing the insets of Figs. 4(a) and 4(c), we observe that the agreement between FPQMC ($N_\tau = 6$) and NLCE results for ρ_e is significantly better than for the double occupancy. The systematic error in FPQMC comes from the time-discretization and the finite size of the system. At $N_\tau = 6$, it is not *a priori* clear which error contributes more, but it appears most likely that the time-discretization error is dominant. In any case, the reason why systematic error is greater for the double occupancy than for the average density could be that the double occupancy contains more detailed information about the correlations in the system. This might be an indication that measurement of multipoint density correlations will generally be more difficult—it may require a finer time resolution and/or greater lattice size.

The average sign above the half-filling, $\rho_e = 1$, mirrors that below the half-filling. The particle-hole symmetry ensures that $\rho_e(\mu) = 2 - \rho_e(U - \mu)$, but that it also governs the average sign is not immediately obvious from the construction of the method. A formal demonstration of the electron-doping-hole-doping symmetry of the average sign is, however, possible (see Appendix E). Note that we restrict our density calculations to $\rho_e < 1$ because, in this case, the numerical effort to manipulate the determinants [Eqs. (7) and (10)]

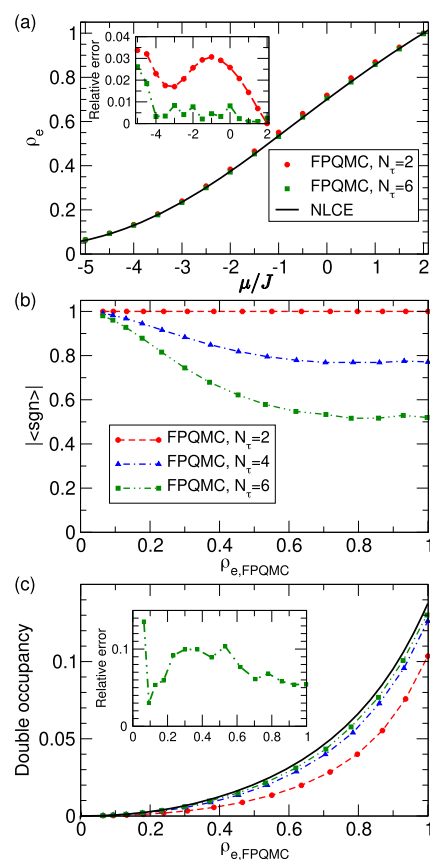


FIG. 4. (a) Equation of state $\rho_e(\mu)$ for the Hubbard model on a 4×4 cluster with the following values of model parameters: $U/J = 4$, $T/J = 1.0408$. (b) The average sign as a function of the FPQMC estimate $\rho_{e,\text{FPQMC}}$ of the electron density for different values of N_τ . The dashed lines are guides for the eye. (c) The double occupancy $\sum_\tau \langle n_{\uparrow\tau} n_{\downarrow\tau} \rangle / N_c$ as a function of the FPQMC estimate $\rho_{e,\text{FPQMC}}$ of the electron density for different values of N_τ . In (a) and (c), full symbols represent FPQMC results, the solid line shows the NLCE data taken from Ref. 41, while the insets show the relative deviation of FPQMC results from the reference NLCE results. The estimated statistical error of the FPQMC data is in all cases smaller than the symbol size.

is lower (size of the corresponding matrices is given by the number of particles of a given spin). The performance of the FPQMC algorithm to compute $\rho_e(\mu)$ (average time needed to propose/accept an MC update and acceptance rates of individual MC updates) is discussed in Sec. SIII of the [supplementary material](#).

We further benchmark our method in the case of very strong coupling, $U/J = 24$ and, again, $T/J = 1.0408$. Figure 5(a) compares the FPQMC results on a 4×4 cluster using $N_\tau = 2, 4$, and 6 imaginary-time slices with the NLCE results. At extremely low fillings $\rho_e \lesssim 0.1$, the relative importance of the interaction term with respect to the kinetic term is quite small, and taking only $N_\tau = 2$ suffices to reach a very good agreement between the FPQMC and NLCE results, see the inset of Fig. 5(a). As the filling is increased, the interaction effects become increasingly important, and it is necessary to increase N_τ in order to accurately describe the competition between

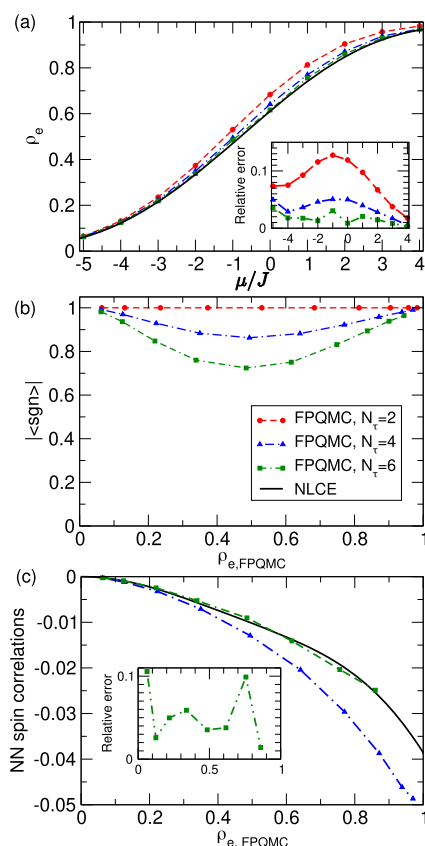


FIG. 5. (a) Equation of state $\rho_e(\mu)$ for the Hubbard model on a 4×4 cluster with the following values of model parameters: $U/J = 24$, $T/J = 1.0408$. (b) The average sign as a function of the FPQMC estimate $\rho_{e, \text{FPQMC}}$ of the electron density for different values of N_τ . (c) Nearest-neighbor spin correlations $\sum_{r\delta} \langle S_r^z S_{r+\delta}^z \rangle / N_c$ as a function of the FPQMC estimate $\rho_{e, \text{FPQMC}}$ of the electron density for $N_\tau = 4$ and 6. In (a) and (c), full symbols represent FPQMC results, the solid line shows the NLCE data taken from Ref. 41, while the insets show the relative deviation of FPQMC results from the reference NLCE results. The dashed or dashed-dotted lines connecting the symbols serve as guides to the eye. The estimated statistical error of the FPQMC data are in all cases smaller than the symbol size.

the kinetic and interaction terms. In the inset of Fig. 5(a), we see that $N_\tau = 6$ is sufficient to reach an excellent (within a couple of percent) agreement between FPQMC and NLCE results over a broad range of fillings. At very high fillings $\rho_e \gtrsim 0.9$ and for $N_\tau = 6$, our MC updates that insert/remove particles have very low acceptance rates, which may lead to a slow sampling of the configuration space. It is for this reason that FPQMC results with $N_\tau = 6$ do not significantly improve over $N_\tau = 4$ in this parameter regime. For $N_\tau = 6$, an inefficient sampling near the half-filling also renders the corresponding results for the nearest-neighbor spin correlations $\sum_{r\delta} \langle S_r^z S_{r+\delta}^z \rangle / N_c$ inaccurate, so that they are not displayed in Fig. 5(c). Here, vector δ connects nearest-neighboring sites, while $S_r^z = (n_{r\uparrow} - n_{r\downarrow})/2$ is the operator of z projection of the local spin. At lower fillings, $\rho_e \lesssim 0.8$, the agreement between our FPQMC results with $N_\tau = 6$ and the NLCE results is good, while decreasing N_τ from 6 to 4 severely deteriorates the quality of the FPQMC results.

At this strong coupling, the dependence of the average sign on the density is somewhat modified, see Fig. 5(b). The minimal sign is no longer reached around half-filling but at quarter-filling, $\rho_e \sim 0.5$, around which $|\langle \text{sgn} \rangle|$ appears to be symmetric. Comparing Fig. 5(b) to Fig. 4(b), we see that the average sign does not become smaller with increasing interaction, in sharp contrast with interaction-expansion-based methods, such as CT-INT^{32,33} or configuration PIMC.⁸⁹

To better understand the relation between the average sign and the interaction, in Fig. 6(a) we plot $|\langle \text{sgn} \rangle|$ as a function of the ratio $U/(4J)$ of the typical interaction and kinetic energy. We take $N_\tau = 6$ and adjust the chemical potential using the data from Ref. 41 so that $\rho_e \approx 0.5$. We see that $|\langle \text{sgn} \rangle|$ monotonically increases with the interaction and reaches a plateau at very strong interactions. This is different from interaction-expansion-based QMC methods, whose sign problem becomes more pronounced as the interaction is

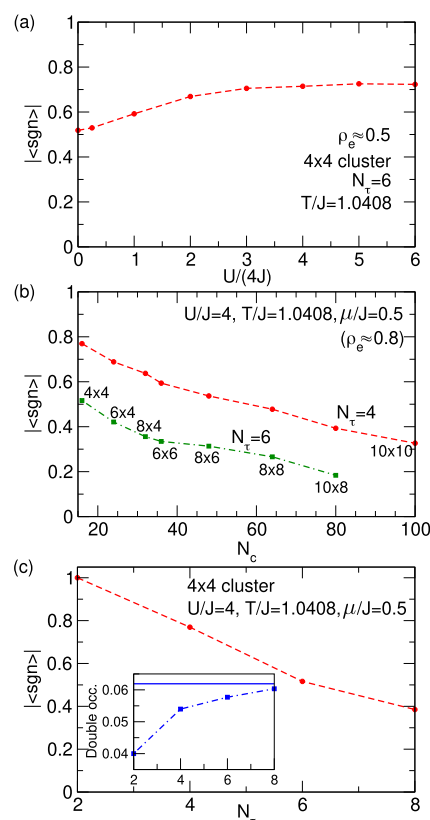


FIG. 6. (a) The average sign as a function of the ratio between the typical interaction and kinetic energies. Full symbols are results of FPQMC computations on a 4×4 cluster with $N_\tau = 6$, the temperature is fixed to $T/J = 1.0408$, and the chemical potential at each U is chosen such that $\rho_e \approx 0.5$. (b) The average sign as a function of the cluster size N_c for the values of model parameters summarized in the figure. The FPQMC results (full symbols) are obtained using $N_\tau = 4$ and 6. (c) Average sign as a function of N_τ . The FPQMC results (full symbols) are obtained on a 4×4 cluster for the values of model parameters summarized in the main part of the figure. The inset shows how the FPQMC result for double occupancy approaches the referent NLCE result as the imaginary-time discretization becomes finer.

increased. Moreover, for weak interactions, the performance of the FPQMC method deteriorates at high densities, see Fig. 4(b), while methods such as CT-INT become problematic at low densities. The FPQMC method could thus become a method of choice to study the regimes of moderate coupling and temperature, which are highly relevant for optical lattice experiments. Figure 6(b) shows the decrease of the average sign with the cluster size N_c in the weak-coupling and moderate-temperature regime at filling $\rho_e \approx 0.8$. We observe that for both $N_\tau = 4$ and $N_\tau = 6$, the average sign decreases linearly with N_c . For $N_\tau = 6$, we observe that the decrease for $N_c \lesssim 40$ is somewhat faster than the decrease for $N_c \gtrsim 40$. We, however, note that the acceptance rates of our MC updates strongly decrease with N_c and that this decrease is more pronounced for finer imaginary-time discretizations. That is why we were not able to obtain any meaningful result for the 10×10 cluster with $N_\tau = 6$. At fixed cluster size and filling, the average sign decreases linearly with N_τ , see the main part of Fig. 6(c), while the double occupancy tends to the referent NLCE value, see the inset of Fig. 6(c).

In Sec. SIV of the supplementary material, we provide an implementation of the ABQMC method in the equilibrium setup. Figures 7(a) and 7(b), which deal with the same parameter regimes as Figs. 4 and 5, respectively, clearly illustrate the advantages of the fermionic-propagator approach with respect to the alternating-basis approach in equilibrium. The average sign of ABQMC simulations with only two imaginary-time slices is orders of magnitude smaller than the sign of FPQMC simulations with three times finer imaginary-time discretization. Since the FPQMC and ABQMC methods are related by an exact transformation, they should produce

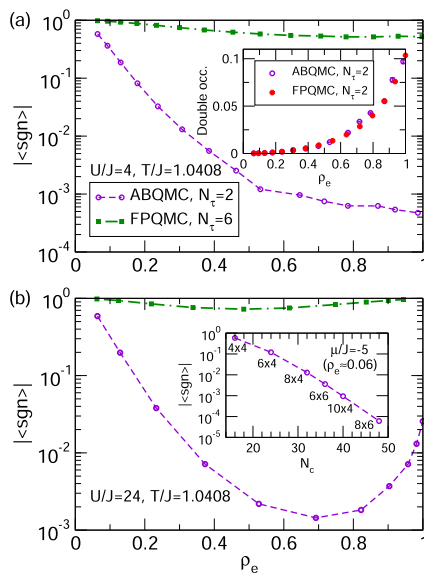


FIG. 7. Average sign as a function of the electron density in ABQMC simulations with $N_\tau = 2$ (open circles) and FPQMC simulations with $N_\tau = 6$ (full squares) for $T/J = 1.0408$ and (a) $U/J = 4$ and (b) $U/J = 24$. The inset in panel (a) compares ABQMC (open circles) and FPQMC (full circles) results for the double occupancy as a function of ρ_e (both methods employ $N_\tau = 2$). The inset in panel (b) shows the average sign of ABQMC simulations with $N_\tau = 2$ as a function of cluster size N_c at low density ($\rho_e \approx 0.06$, $\mu/J = -5$).

the same results for thermodynamic quantities (assuming that N_τ is the same in both methods). This is shown in the inset of Fig. 7(a) on the example of the double occupancy. The inset of Fig. 7(b) suggests that the average sign decreases exponentially with the cluster size N_c . Overall, our current implementation of the ABQMC method in equilibrium cannot be used to simulate larger clusters with a finer imaginary-time discretization.

B. Time-dependent results using FPQMC method: Local charge and spin densities

1. Benchmarks on small clusters

In Figs. 8(a) and 8(b), we benchmark our FPQMC method for time-dependent local densities on the example of the CDW state of the Hubbard tetramer, see the inset of Fig. 8(b). We follow the evolution of local charge densities on initially occupied sites for different ratios U/D , where D is the half-bandwidth of the free-electron band ($D = 2J$ for the tetramer). For all the interaction strengths considered, taking $N_t = 2$ real-time slices on each branch (four slices in total) is sufficient to accurately describe the evolution of local densities up to times $Dt \sim 2$, see full symbols in Fig. 8(a). At longer times, $2 < Dt \leq 4$, taking $N_t = 3$ improves results obtained using $N_t = 2$, compare empty to full symbols in Fig. 8(a). Nevertheless, for the strongest interaction considered ($U/D = 1$), 6 real-time slices are not sufficient to bring the FPQMC result closer to the exact result at times $3 \leq Dt \leq 4$. The average sign strongly depends on time, and it drops by an order of magnitude upon increasing N_t from 2 to 3, see Fig. 8(b). Despite this, the discrepancy between the $N_t = 3$ result

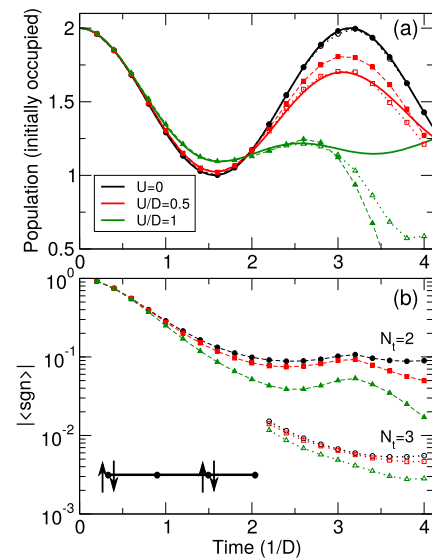


FIG. 8. (a) Time-dependent population of sites occupied in the initial CDW state of a tetramer for different interaction strengths. Solid lines represent exact results, full symbols connected by dashed lines are FPQMC results using $N_t = 2$ real-time slices, while empty symbols connected by dotted lines are FPQMC results using $N_t = 3$ real-time slices. The initial CDW state is schematically depicted in panel (b). (b) Time-dependent average sign of the FPQMC simulation using $N_t = 2$ (full symbols connected by dashed lines) and $N_t = 3$ (empty symbols connected by dotted lines) for different interaction strengths. In (a) and (b), FPQMC simulations using $N_t = 3$ real-time slices are carried out only for $2 < Dt \leq 4$.

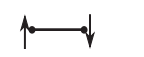
and the exact result for $U/D = 1$ cannot be ascribed to statistical errors but rather to the systematic error of the FPQMC method (the minimum N_t needed to obtain results with certain systematic error increases with both time and interaction strength).

2. Results on larger clusters

Figure 9(a) summarizes the evolution of local charge densities on initially occupied sites of a half-filled 4×4 cluster, on which the electrons are initially arranged as depicted in the inset of Fig. 9(b). This state is representative of a CDW pattern formed by applying strong external density-modulating fields with wave vector $\mathbf{q} = (\pi, 0)$. The FPQMC method employs four real-time slices in total, i.e., the forward and backward branches are divided into $N_t = 2$ identical slices each. On the basis of the $N_t = 2$ results in Fig. 8(a), we present the FPQMC dynamics up to the maximum time $Dt_{\max} = 2$. The extent of the dynamical sign problem is shown in Fig. 9(b).

At the shortest times, $Dt \lesssim 1$, the results for all the interactions considered do not significantly differ from the noninteracting result. The same also holds for the average sign. As expected, the decrease of $|\langle \text{sgn} \rangle|$ with time becomes more rapid as the interaction U and time discretization $\Delta t = t/N_t$ are increased. The oscillatory nature of $\langle \text{sgn} \rangle$ as a function of time [see Eq. (22)] is correlated with the discontinuities in time-dependent populations observed in Fig. 9(a) for $U/D \geq 0.5$. Namely, at the shortest times and for all the interactions considered, $\langle \text{sgn} \rangle$ is positive, while for sufficiently strong interactions, it becomes negative at longer times. This change is indicated in Fig. 9(b) by placing the symbols “+” and “−” next to each relevant point. We now see that the discontinuities in populations occur precisely around instants at which $\langle \text{sgn} \rangle$ turns from positive to negative values. Focusing on $U/D = 1$, in Figs. 9(c1)–9(c3) we show the MC series for the population of initially occupied sites at instants before

TABLE I. Schematic representations of the initial states of small systems on which the ABQMC method for $P(t)$ is benchmarked.

system	$ \psi_{\text{CDW}}\rangle$	$ \psi_{\text{SDW}}\rangle$
Dimer		
Tetramer		

[(c1)] and after [(c2), (c3)] $\langle \text{sgn} \rangle$ passes through zero. The corresponding series for $\langle \text{sgn} \rangle$ are presented in Figs. 9(d1)–9(d3). Well before [Figs. 9(c1) and 9(d1)] and after [Figs. 9(c3) and 9(d3)] $\langle \text{sgn} \rangle$ changes sign, the convergence with the number of MC steps is excellent, while it is somewhat slower close to the positive-to-negative transition point, see Figs. 9(c2) and 9(d2). Still, the convergence at $Dt = 1.4$ cannot be denied, albeit the statistical error of the population is larger than at $Dt = 1.2$ and 1.6. At longer times $Dt \geq 1.5$, when $\langle \text{sgn} \rangle$ is negative and of appreciable magnitude, the population again falls in the physical range $[0, 2]$. Nevertheless, at such long times, the systematic error may be large due to the coarse real-time discretization.

In Sec. SV of the [supplementary material](#), we discuss FPQMC results for the dynamics of local charge densities starting from some other initial states.

C. Time-dependent results using ABQMC method: Survival probability

1. Benchmarks on small clusters

We first benchmark our ABQMC method for the survival probability on Hubbard dimers and tetramers. The initial states

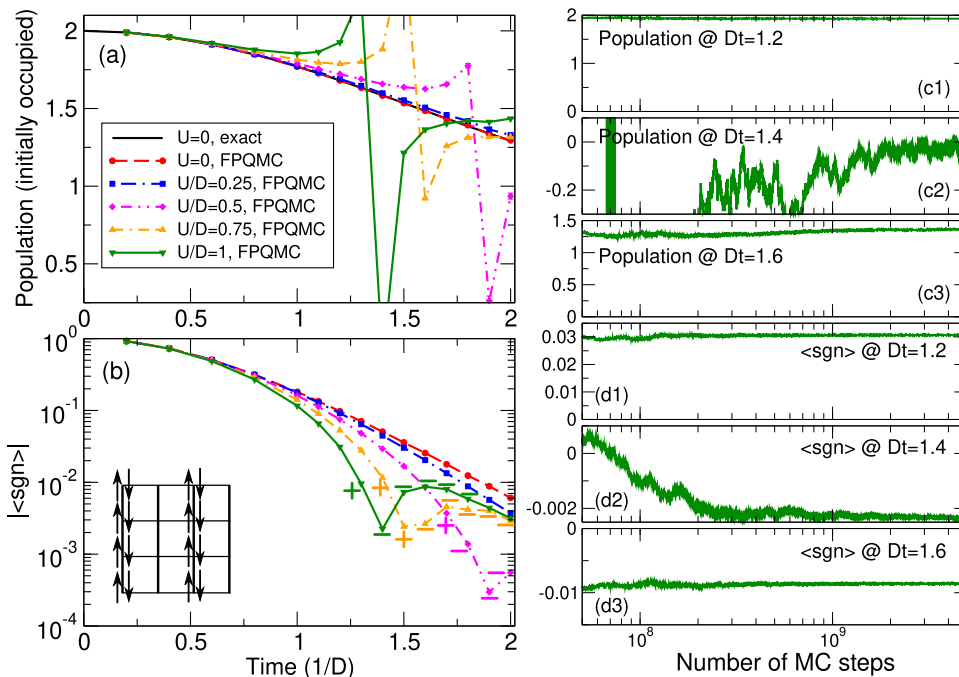


FIG. 9. (a) Time-dependent population of sites occupied in the initial CDW state of a 4×4 cluster, which is schematically depicted in the inset of panel (b). FPQMC results using $N_t = 2$ real-time slices (four slices in total) are shown for five different interaction strengths (symbols) and compared with the noninteracting result (solid line). (b) Magnitude of the average sign as a function of time for different interaction strengths. The color code is the same as in panel (a). For $U/D = 0.5, 0.75$, and 1 and $Dt \geq 1.2$, symbols “+” and “−” next to each point specify whether $\langle \text{sgn} \rangle$ is positive or negative. (c) MC series for the population of initially occupied sites for $U/D = 1$ and (c1) $Dt = 1.2$, (c2) $Dt = 1.4$, and (c3) $Dt = 1.6$. (d) MC series for $\langle \text{sgn} \rangle$ for $U/D = 1$ and (d1) $Dt = 1.2$, (d2) $Dt = 1.4$, and (d3) $Dt = 1.6$. Note the logarithmic scale on the abscissa in (c) and (d).

are schematically summarized in Table I. In both cases, we are at half-filling.

Figures 10(a1)–10(e2) present the time evolution of the survival probability of the initial CDW-like and SDW-like states depicted in Table I for the dimer (left panels, $D = J$) and tetramer (right panels, $D = 2J$) for different values of U/D starting from the limit of a weakly nonideal gas ($U/D = 0.05$) and approaching the atomic limit ($U/D = 20$). The results are obtained using $N_t = 2$ (full red circles) and $N_t = 4$ (blue stars) real-time slices and contrasted with the exact result (solid black lines). The ABQMC results with $N_t = 2$ agree both qualitatively (oscillatory behavior) and quantitatively with the exact result up to $t_{\max} \sim 1/U$. Increasing N_t from 2 to 4 may help decrease the deviation of the ABQMC data from the exact result at later times. Even when finer real-time discretization does not lead to better quantitative agreement, it may still help the ABQMC method qualitatively reproduce the gross features of the exact result. The converged values of $|\langle \text{sgn} \rangle|$ for the dimer and tetramer

TABLE II. Modulus of the average sign for ABQMC simulations of $P(t)$ on dimer and tetramer with $N_t = 2, 3$, and 4.

System	$N_t = 2$	$N_t = 3$	$N_t = 4$
Dimer	1/2	1/4	1/8
Tetramer	1/8	2.4×10^{-2}	3×10^{-3}

for $N_t = 2, 3$, and 4 are summarized in Table II. For the dimer, increasing N_t by one reduces $|\langle \text{sgn} \rangle|$ by a factor of 2. In contrast, in the case of the tetramer, increasing N_t by one reduces $|\langle \text{sgn} \rangle|$ by almost an order of magnitude.

2. Results on larger clusters

We move on to discuss the survival probability dynamics of different 16-electron and eight-electron states on a 4×4

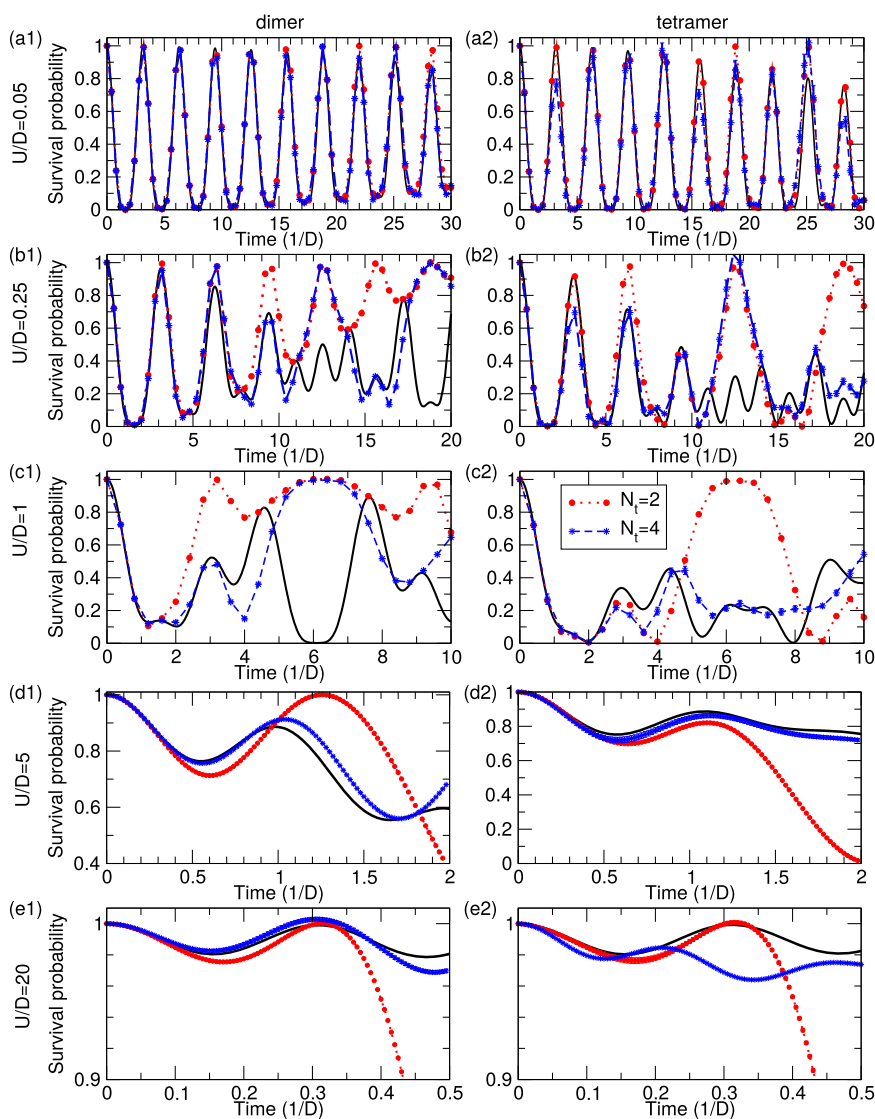


FIG. 10. Time dependence of the survival probability of the initial state $|\psi_{\text{CDW}}\rangle$ or $|\psi_{\text{SDW}}\rangle$ (see Table I) for the dimer [(a1)–(e1)] and tetramer [(a2)–(e2)] for five different interaction strengths starting from the noninteracting limit and approaching the atomic limit: $U/D = 0.05$ [(a1) and (a2)], $U/D = 0.25$ [(b1) and (b2)], $U/D = 1$ [(c1) and (c2)], $U/D = 5$ [(d1) and (d2)], and $U/D = 20$ [(e1) and (e2)]. The ABQMC results with $N_t = 2$ (red full circles) and $N_t = 4$ (blue stars) are compared with the exact result (black solid lines). The dotted/dashed lines connecting subsequent circles/stars are guides to the eye. In most cases, the MC error bars are smaller than the linear size of the symbols.

cluster. Figures 11(a) and 11(b) present $P(t)$ for 16-electron states schematically depicted in their respective insets. These states are representative of CDW patterns formed by applying strong external density-modulating fields with wave vectors $\mathbf{q} = (\pi, 0)$ in Figs. 11(a) and $\mathbf{q} = (\pi, \pi)$ in Fig. 11(b). Figures 11(c) and 11(d) present $P(t)$ for eight-electron states schematically depicted in their respective insets. The ABQMC method employs $N_t = 2$ real-time slices. The results are shown up to the maximum time $Dt_{\max} = 2.5$, which we chose on the basis of the results presented in Fig. 10(c2).

As a sensibility check of our ABQMC results, we first compare the exact result in the noninteracting limit, see solid lines in Figs. 11(a)–11(d), with the corresponding ABQMC prediction, see full circles in Figs. 11(a)–11(d). While the exact and ABQMC results agree quite well in Figs. 11(b) and 11(c), the agreement in Figs. 11(a) and 11(d) is not perfect. Since no systematic errors are expected in ABQMC at $U = 0$, the discrepancy must be due to statistical error. We confirm this expectation in Fig. 12 where we see that the obtained curve tends to the exact one with the increasing number of MC steps. The average sign cited in Fig. 11(d) suggests that more MC steps are needed to obtain fully converged results. Even though the converged average sign in Figs. 11(a)–11(c) is of the same order of magnitude, we find that the rate of convergence depends on both the number and the initial configuration of electrons.

In Figs. 11(a)–11(d), we observe that weak interactions ($U/D \lesssim 0.5$) do not cause any significant departure of $P(t)$ from the corresponding noninteracting result. On the other hand, the effect of somewhat stronger interactions on $P(t)$ depends crucially on the filling. In the 16-electron case, the increasing interactions speed up the initial decay of P , see Figs. 11(a) and 11(b), while in the eight-electron case interactions have little effect at $Dt < 1$, see Figs. 11(c) and 11(d). This we attribute to the essential difference in the overall electron density and the relative role of the interaction term in the Hamiltonian. In the 16-electron case, starting from the moderate coupling $U/D \sim 1$, there is a clear revival of the initial

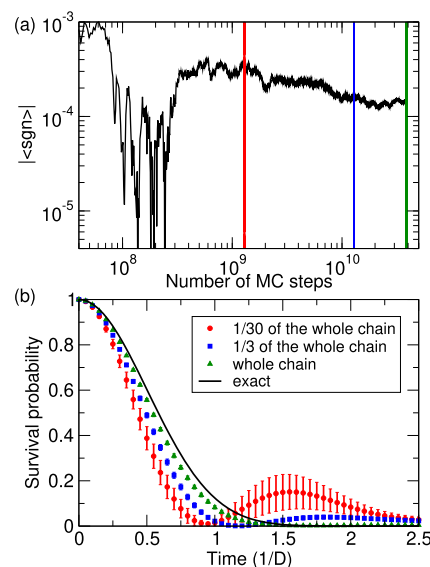


FIG. 12. (a) Average sign as a function of the number of MC steps in the ABQMC simulation of $P(t)$ for the 16-electron initial state schematically depicted in Fig. 11(a). (b) Time dependence of the survival probability for $U = 0$ extracted using the first 1/30 of the total number of MC steps completed (1.29×10^9 steps, full red circles), the first 1/3 of the total number of MC steps completed (1.29×10^{10} steps, full blue squares), and all the MC steps completed (3.87×10^{10} steps, full green up-triangles). These results are compared to the exact result in the noninteracting limit, which is represented by the solid line. The vertical lines in (a), whose colors match the colors of the symbols in (b), denote the ending points of the simulations.

state in Fig. 11(a), while no such a revival is observed in Fig. 11(b). Furthermore, the memory loss of the initial density-wave pattern is more rapid in Fig. 11(a) than in Fig. 11(b), even at $U = 0$. The revival of the initial state is observed in the eight-electron case as well: at

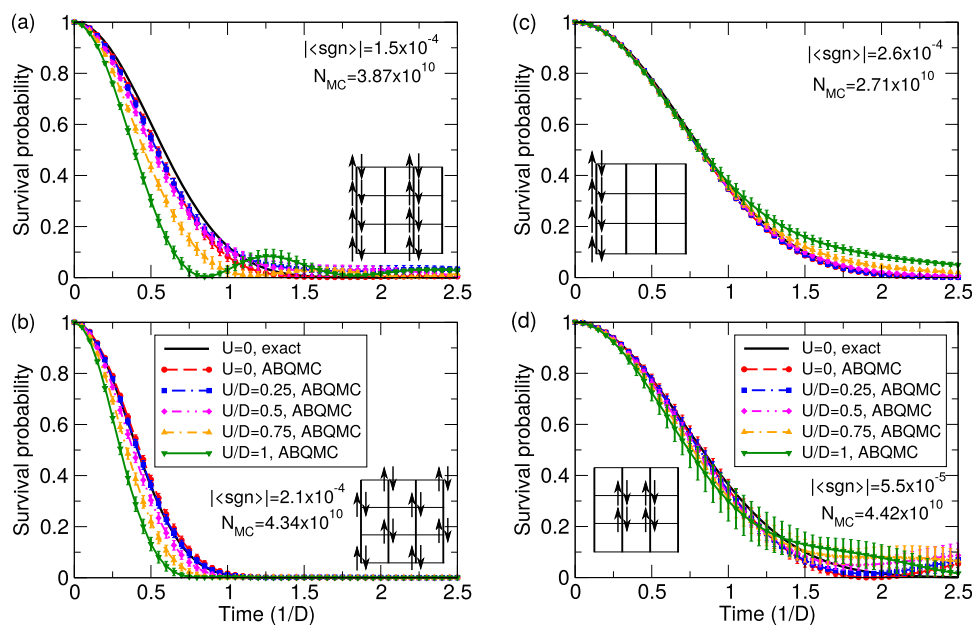


FIG. 11. Survival-probability dynamics of the 16-electron states [in (a) and (b)] and 8-electron states [in (c) and (d)] that are schematically depicted in the respective insets. The ABQMC results are shown for five different interaction strengths (symbols) and compared with the noninteracting result (solid line). We cite the converged value of the average sign $|\langle \text{sgn} \rangle|$, as well as the total number N_{MC} of MC steps completed.

$t < 1/D$ there is barely any effect of the interaction, yet at longer times it boosts P . However, in contrast to the 16-electron case, the results in Figs. 11(c) and 11(d) exhibit a weaker dependence of the survival-probability dynamics on the initial density-wave pattern. Indeed, the exact results in the noninteracting case are identical for both patterns in Figs. 11(c) and 11(d). Except in the case of the (π, π) wave, the interactions lead to a persistence of the initial pattern at longer times, $t > 1/D$. The precise form of temporal correlations that develop due to interactions apparently depends on the initial spatial arrangement of the electrons.

Section SVI of the [supplementary material](#) presents additional ABQMC results for the time-dependent survival probability.

IV. RELATION TO OTHER ALGORITHMS

As mentioned in the introduction, a variant of the FPQMC method was first proposed by De Raedt and Lagendijk in the 1980s.^{78–80} They, however, explicitly retain permutation operators appearing in Eq. (A5) in their final expression for Z , see, e.g., Eq. (3) in Ref. 78 or Eqs. (4.13) and (4.14) in Ref. 80. On the other hand, we analytically perform summation over permutation operators, thus grouping individual contributions into determinants. This is much more efficient [as the factorial number of terms is captured in only $O(N^3)$ steps, or even faster] and greatly improves the average sign (cancellations between different permutations are already contained in the determinant, see Fig. 7). The approach followed by De Raedt and Lagendijk later became known as permutation-sampling QMC, and the route followed by us is known as antisymmetric-propagator QMC,^{85,86} permutation-blocking QMC,⁹⁰ or fermionic-propagator QMC.⁹⁶ The analytical summation over permutation operators entering Eq. (A5) was first performed by Takahashi and Imada.⁸⁵

Our FPQMC method employs the lowest-order STD [Eq. (4)], which was also used in the permutation-sampling QMC method of De Raedt and Lagendijk.^{78–80} The maximum number of imaginary-time slices N_τ they could use was limited by the acceptance rates of MC updates, which decrease quickly with increasing N_τ and the cluster size N_c . In our present implementation of FPQMC, we encounter the same issue, and our sampling becomes prohibitively inefficient when the total number of time slices is greater than 6–8, depending on the cluster size. To circumvent this issue, the fermionic-propagator idea was combined with higher-order STDs^{98,114–116} and more advanced sampling techniques^{117,118} to simulate the equilibrium properties of continuum models of interacting fermions in the canonical^{90,92} and grand-canonical⁹⁶ ensembles. More recent algorithmic developments enabled simulations with as much as 2000 imaginary-time slices,¹¹⁹ which is a great improvement. Whether similar ideas can be applied to lattice systems to improve the efficiency of sampling is currently unclear. Generally, more sophisticated STD schemes have been regarded as not useful in lattice-model applications.¹²⁰ It is important to note that the success of the antisymmetric-propagator algorithms in continuous systems relies on weak degeneracy. This corresponds to an extremely low occupancy regime in lattice models, and it is precisely in this regime that our FPQMC method has an average sign close to 1 [see Figs. 4(b) and 5(b)], and the sampling is most efficient [see Sec. SIII of the [supplementary material](#)]. Near half-filling, lattice models present a fundamentally different physics,

which may ultimately require a substantially different algorithmic approach.

We further emphasize that the low acceptance rates and the resulting inefficiency of sampling that we encounter are directly related to the discrete nature of space in our model. Some strategies for treating the analogous problem in continuous-space models may not be applicable here. For example, in continuous-space models, acceptance rates of individual updates can be adjusted by moving electrons over shorter distances, so that the new configuration weight is less likely to be substantially different from the old one. In contrast, in lattice models, electronic coordinates are discrete, and the minimum distance the electrons may cover is set by the lattice constant; in most cases, moving a single electron by a single lattice spacing in a single time slice is sufficient to drastically reduce the configuration weight. There is no general rule on how electrons should be moved to ensure that the new configuration weight is close to the original one. This is particularly true for the updates that insert/remove a particle, and the problem becomes more pronounced with increasing N_τ . When each of the N_τ states $|\Psi_{i,l}\rangle$ [see Eq. (9)] is changed to $|\Psi'_{i,l}\rangle$, the chances that at least one of $\langle \Psi'_{i,l} | e^{-\Delta\tau H_0} | \Psi_{i,l} \rangle$ is much smaller than $\langle \Psi_{i,l} | e^{-\Delta\tau H_0} | \Psi_{i,l} \rangle$ [see Eq. (10)] increase with N_τ . Our configuration weight is appreciable only in small, mutually disconnected regions of the configuration space, the movement between which is difficult. In Sec. V, we touch upon possible strategies to improve sampling of such a structured configuration space.

It is also important to compare our methods to the HF QMC method,^{24,49} which is a well-established STD-based method for the treatment of the Hubbard model. The HF method is manifestly sign-problem-free but only at particle-hole symmetry. The sign problem can become severe away from half-filling, or on lattices other than the simple square lattice with no longer-range hoppings. On the other hand, our FPQMC method is nearly sign-problem-free at low occupancy, but also near half-filling, albeit only at strong coupling [see Figs. 4(b) and 5(b)]. The other important difference is that matrices manipulated in HF are of the size $N_c N_\tau$, while in FPQMC, the matrices are of the size $< 2N_c$, i.e., given by the number of particles. Algorithmic complexity of the individual MC step in FPQMC scales only linearly with N_τ , while in HF, the MC step may go as $O(N_\tau^2)$ [determinant is $O(N^3)$, but fast updates $O(N^2)$ are possible when the determinant is not calculated from scratch⁴⁹]. Low cost of individual steps in FPQMC has allowed us to perform as many as $\sim 10^{10}$ MC steps in some calculations. This advantage, however, weighs against an increased configuration space to be sampled. In HF the number of possible configurations is $2^{N_c N_\tau}$ (space is spanned by $N_c N_\tau$ auxiliary Ising spins), while in FPQMC it is $4^{N_c N_\tau}$ (although, symmetries can be used to significantly reduce the number of possible configurations). The ABQMC method manipulates matrices of the same size as does FPQMC, but with twice the number, and the configuration space is *a priori* even bigger ($16^{N_c N_\tau}$). Our methods also have the technical advantage that the measurements of multipoint charge and spin correlation functions are algorithmically trivial and cheap. Especially in ABQMC, the densities in both coordinate and momentum space can be simply read off the configuration. This is not possible in HF, where the auxiliary Ising spin only distinguishes between singly occupied and doubly-occupied/empty sites. Most importantly, the ABQMC/FPQMC methods can be readily applied to canonical ensembles and pure states, which may

not be possible with the HF method. However, the HF is commonly used with tens of time slices for lattice sizes of order $N_c = 100\text{--}200$; in FPQMC, algorithmic developments related to configuration updates are necessary before it can become a viable alternative to the HF in a wide range of applications.

Finally, we are unaware of any numerically exact method for large lattice systems, which can treat the full Kadanoff–Baym–Keldysh contour, and yield real-time correlation functions. Our ABQMC method represents an interesting example of a real-time QMC method with manifestly no dynamical sign problem. However, the average sign is generally poor. To push ABQMC to larger number of time slices (as needed for calculation of the time-dependence of observables) and lattices larger than 4×4 will require further work, and most likely, conceptually new ideas.

V. SUMMARY AND OUTLOOK

We revisit one of the earliest proposals for a QMC treatment of the Hubbard model, namely the permutation-sampling QMC method developed in Refs. 78–80. Motivated by recent progress in the analogous approach to continuous space models, we group all permutations into a determinant, which is known as the antisymmetric-propagator,⁸⁵ permutation-blocking,⁹⁰ or fermionic-propagator⁹⁶ idea. We devise and implement two slightly different QMC methods. Depending on the details of the STD scheme, we distinguish between (1) the FPQMC method, where snapshots are given by real-space Fock states and determinants represent antisymmetric propagators between those states, and (2) the ABQMC method, where slices alternate between real and reciprocal space representation and determinants are simple Slater determinants. We thoroughly benchmark both methods against the available numerically exact data and then use ABQMC to obtain some new results in the real-time domain.

The FPQMC method exhibits several promising properties. The average sign can be close to 1 and does not drop off rapidly with either the size of the system or the number of time slices. In 1D, the method appears to be sign-problem-free. At present, the limiting factor is not the average sign but rather the ability to sample the large configuration space. At discretizations finer than $N_\tau = 6\text{--}8$, further algorithmic developments are necessary. Nevertheless, our calculations show that excellent results for instantaneous correlators can be obtained with very few time slices and efficiently. Average density, double occupancy, and antiferromagnetic correlations can already be computed with high accuracy at temperatures and coupling strengths relevant for optical-lattice experiments. The FPQMC method is promising for further applications in equilibrium setups. In real-time applications, however, the sign problem in FPQMC is severe.

On the other hand, the ABQMC method has a significant sign problem in equilibrium applications but has some advantages in real-time applications. In ABQMC, the sign problem is manifestly time-independent, and calculations can be performed for multiple times and coupling strengths with a single Markov chain. We use this method to compute time-dependent survival probabilities of different density-modulated states and identify several trends. The relevant transient regime is short, and based on benchmarks, we estimate the systematic error due to the time discretization here to be small. Our results reveal that interactions speed up the initial decay

of the survival probability but facilitate the persistence of the initial charge pattern at longer times. Additionally, we observe a characteristic value of the coupling constant, $U \sim 0.5D$, below which the interaction has no visible effect on time evolution. These findings bare qualitative predictions for future ultracold-atom experiments, but are limited to dynamics at the shortest wave-lengths, as dictated by the maximal size of the lattice that we can treat. We finally note that, within the ABQMC method, uniform currents, which are diagonal in the momentum representation, may be straightforwardly treated.

There is room for improvement in both the ABQMC and FPQMC methods. We already utilize several symmetries of the Hubbard model to improve efficiency and enforce some physical properties of solutions, but more symmetries can certainly be uncovered in the configuration spaces. Further grouping of configurations connected by symmetries can be used to alleviate some of the sign problem or improve efficiency. Also, sampling schemes may be improved along the lines of the recently proposed many-configuration Markov chain MC, which visits an arbitrary number of configurations at every MC step.¹²¹ Moreover, a better insight into the symmetries of the configuration space may make deterministic, structured sampling (along the lines of quasi-MC methods^{122–124}) superior to the standard pseudo-random sampling.

SUPPLEMENTARY MATERIAL

See the [supplementary material](#) for (i) a detailed description of MC updates within the FPQMC method, (ii) a detailed description of MC updates within the ABQMC method for time-dependent survival probability, (iii) details on the performance of the FPQMC method in equilibrium calculations, (iv) discussion on the applicability of the ABQMC method in equilibrium calculations, (v) additional FPQMC calculations of time-dependent local densities, (vi) additional ABQMC calculations of time-dependent survival probability, and (vii) formulation and benchmarks of ABQMC method in quench setups (on the full three-piece Kadanoff–Baym–Keldysh contour).

ACKNOWLEDGMENTS

We acknowledge funding provided by the Institute of Physics Belgrade through a grant from the Ministry of Education, Science, and Technological Development of the Republic of Serbia as well as by the Science Fund of the Republic of Serbia under the Key2SM project (PROMIS program, Grant No. 6066160). Numerical simulations were performed on the PARADOX-IV supercomputing facility at the Scientific Computing Laboratory, National Center of Excellence for the Study of Complex Systems, Institute of Physics Belgrade.

AUTHOR DECLARATIONS

Conflict of Interest

The authors have no conflicts to disclose.

Author Contributions

J.V. conceived the research. V.J. developed the formalism and computational codes under the guidance of J.V., conducted all numerical

simulations, analyzed their results, and prepared the initial version of the manuscript. Both authors contributed to the submitted version of the manuscript.

Veljko Janković: Conceptualization (supporting); Data curation (lead); Formal analysis (lead); Investigation (lead); Methodology (lead); Software (lead); Validation (lead); Visualization (lead); Writing – original draft (lead); Writing – review & editing (equal).
Jakša Vučićević: Conceptualization (lead); Funding acquisition (lead); Project administration (lead); Resources (lead); Software (supporting); Supervision (lead); Writing – review & editing (equal).

DATA AVAILABILITY

The data that support the findings of this study are available from the corresponding author upon reasonable request.

APPENDIX A: MANY-BODY PROPAGATOR AS A DETERMINANT OF SINGLE-PARTICLE PROPAGATORS

The demonstration of Eqs. (6) and (7) can be conducted for each spin component separately. We thus fix the spin index σ and further omit it from the definition of the many-fermion state $|\Psi_i\rangle$ [Eq. (5)]. Since H_0 is diagonal in the momentum representation, we express the state $|\Psi_i\rangle$ in the momentum representation

$$|\Psi_i\rangle = \sum_{\{\mathbf{k}_j\}} \left(\prod_{l=1}^N \langle \mathbf{k}_l | \mathbf{r}_l \rangle c_{\mathbf{k}_l}^\dagger \right) |\emptyset\rangle \quad (\text{A1})$$

and similarly for $|\Psi'_i\rangle$. While the positions $\mathbf{r}_1, \dots, \mathbf{r}_N$ are ordered according to a certain rule, the wave vectors $\mathbf{k}_1, \dots, \mathbf{k}_N$ entering Eq. (A1) are not ordered, and there is no restriction on the sum over them. We have

$$\begin{aligned} \langle \Psi'_i | e^{-\Delta\alpha H_0} | \Psi_i \rangle &= \sum_{\{\mathbf{k}'_j\}} \sum_{\{\mathbf{k}_j\}} e^{-\Delta\alpha \epsilon_{\mathbf{k}'_1}} \dots e^{-\Delta\alpha \epsilon_{\mathbf{k}'_N}} \\ &\times \langle \mathbf{r}'_N | \mathbf{k}'_N \rangle \dots \langle \mathbf{r}'_1 | \mathbf{k}'_1 \rangle \langle \mathbf{k}_1 | \mathbf{r}_1 \rangle \langle \mathbf{k}_N | \mathbf{r}_N \rangle \\ &\times \langle \emptyset | c_{\mathbf{k}'_N} \dots c_{\mathbf{k}'_1} c_{\mathbf{k}_1}^\dagger \dots c_{\mathbf{k}_N}^\dagger | \emptyset \rangle. \end{aligned} \quad (\text{A2})$$

The sums over $\{\mathbf{k}'_j\}$ are eliminated by employing the identity⁸⁰

$$\begin{aligned} \langle \emptyset | c_{\mathbf{k}'_N} \dots c_{\mathbf{k}'_1} c_{\mathbf{k}_1}^\dagger \dots c_{\mathbf{k}_N}^\dagger | \emptyset \rangle \\ = \sum_{\mathcal{P}} \text{sgn}(\mathcal{P}) \delta(\mathbf{k}'_1, \mathbf{k}_{\mathcal{P}(1)}) \dots \delta(\mathbf{k}'_N, \mathbf{k}_{\mathcal{P}(N)}), \end{aligned} \quad (\text{A3})$$

where the permutation operator \mathcal{P} acts on the set of indices $\{1, \dots, N\}$, while $\text{sgn}(\mathcal{P}) = \pm 1$ is the permutation parity. We then observe that

$$\prod_{l=1}^N \langle \mathbf{r}'_l | \mathbf{k}_{\mathcal{P}(l)} \rangle = \prod_{l=1}^N \langle \mathbf{r}'_{\mathcal{P}^{-1}(l)} | \mathbf{k}_l \rangle, \quad (\text{A4})$$

which permits us to perform the sums over individual \mathbf{k}_j s independently. Combining Eqs. (A2)–(A4) and changing the permutation variable $\mathcal{P}' = \mathcal{P}^{-1}$ we eventually obtain

$$\begin{aligned} \langle \Psi'_i | e^{-\Delta\alpha H_0} | \Psi_i \rangle &= \sum_{\mathcal{P}'} \text{sgn}(\mathcal{P}') \prod_{l=1}^N \langle \mathbf{r}'_{\mathcal{P}'(l)} | e^{-\Delta\alpha H_0} | \mathbf{r}_l \rangle \\ &= \det S(\Psi'_i, \Psi_i, \Delta\alpha), \end{aligned} \quad (\text{A5})$$

where matrix $S(\Psi'_i, \Psi_i, \Delta\alpha)$ (here without the spin index) is defined in Eq. (7).

APPENDIX B: PROPAGATOR OF A FREE PARTICLE ON THE SQUARE LATTICE

Here, we provide the expressions for the propagator of a free particle on the square lattice in imaginary [$\Delta\alpha = \Delta\tau$ in Eq. (7)] and real [$\Delta\alpha = i\Delta t$ in Eq. (7)] time. In imaginary time,

$$\langle \mathbf{r}' | e^{-\Delta\tau H_0} | \mathbf{r} \rangle = \mathcal{I}(2J\Delta\tau, r'_x - r_x) \mathcal{I}(2J\Delta\tau, r'_y - r_y), \quad (\text{B1})$$

where the one-dimensional imaginary-time propagator (l is an integer)

$$\mathcal{I}(z, l) = \frac{1}{N} \sum_{j=0}^{N-1} \cos\left(\frac{2\pi j l}{N}\right) \exp\left(z \cos\left(\frac{2\pi j}{N}\right)\right) \quad (\text{B2})$$

is related to the modified Bessel function of the first kind $I_l(z)$ via

$$\lim_{N \rightarrow \infty} \mathcal{I}(z, l) = \frac{1}{\pi} \int_0^\pi d\theta \cos(l\theta) e^{z \cos \theta} = I_l(z). \quad (\text{B3})$$

In real time,

$$\langle \mathbf{r}' | e^{-i\Delta t H_0} | \mathbf{r} \rangle = \mathcal{J}(2J\Delta t, r'_x - r_x) \mathcal{J}(2J\Delta t, r'_y - r_y), \quad (\text{B4})$$

where the one-dimensional real-time propagator (l is an integer)

$$\mathcal{J}(z, l) = \frac{1}{N} \sum_{j=0}^{N-1} \cos\left(\frac{2\pi j l}{N}\right) \exp\left(iz \cos\left(\frac{2\pi j}{N}\right)\right) \quad (\text{B5})$$

is related to the Bessel function of the first kind $J_l(z)$ via

$$\lim_{N \rightarrow \infty} \mathcal{J}(z, l) = \frac{1}{\pi} \int_0^\pi d\theta \cos(l\theta) e^{iz \cos \theta} = i^l J_l(z). \quad (\text{B6})$$

For finite N , $\mathcal{J}(z, 2l)$ is purely real, while $\mathcal{J}(z, 2l+1)$ is purely imaginary.

APPENDIX C: DERIVATION OF THE FPQMC FORMULAE THAT MANIFESTLY RESPECT THE DYNAMICAL SYMMETRY OF THE HUBBARD MODEL

Here, we derive the FPQMC expression for the time-dependent expectation value of a local observable [Eq. (18)] that manifestly respects the dynamical symmetry of the Hubbard model.

We start by defining the operation of the bipartite lattice symmetry, which is represented by a unitary, hermitean, and involutive operator B ($B^\dagger = B = B^{-1}$) whose action on electron creation and annihilation operators in the real space is given as

$$Bc_{r\sigma}^{(\dagger)}B = (-1)^{r_x+r_y}c_{r\sigma}^{(\dagger)}. \quad (\text{C1})$$

In the momentum space, B is actually the so-called π -boost¹⁵

$$Bc_{\mathbf{k}\sigma}^{(\dagger)}B = c_{\mathbf{k}+\mathbf{Q}\sigma}^{(\dagger)} \quad (\text{C2})$$

that increases the electronic momentum by $\mathbf{Q} = (\pi, \pi)$. The time reversal operator T is an antiunitary (unitary and antilinear), involutive, and hermitean operator whose action on electron creation and annihilation operators in the real space is given as

$$Tc_{\mathbf{r}\uparrow}^{(\dagger)}T = c_{\mathbf{r}\downarrow}^{(\dagger)}, \quad Tc_{\mathbf{r}\downarrow}^{(\dagger)}T = -c_{\mathbf{r}\uparrow}^{(\dagger)}, \quad (\text{C3})$$

while the corresponding relations in the momentum space read as

$$Tc_{\mathbf{k}\uparrow}^{(\dagger)}T = c_{-\mathbf{k}\downarrow}^{(\dagger)}, \quad Tc_{\mathbf{k}\downarrow}^{(\dagger)}T = -c_{-\mathbf{k}\uparrow}^{(\dagger)}. \quad (\text{C4})$$

Using Eqs. (C1)–(C4), consequently

$$BH_0B = -H_0, \quad BH_{\text{int}}B = H_{\text{int}}, \quad TH_0T = H_0, \quad (\text{C5})$$

$$TH_{\text{int}}T = H_{\text{int}}.$$

In Sec. II B 2, we assumed that the initial state $|\psi(0)\rangle$ is an eigenstate of local density operators $n_{r\sigma}$, which means that $B|\psi(0)\rangle = e^{i\chi_B}|\psi(0)\rangle$, see Eq. (C1).

The denominator of Eq. (18)

$$A_{\text{den}}(t) = \langle \psi(0) | e^{iHt} e^{-iHt} | \psi(0) \rangle \quad (\text{C6})$$

is purely real, $A_{\text{den}}(t) = A_{\text{den}}(t)^*$, so that

$$A_{\text{den}}(t) \approx \frac{1}{2} \left\langle \psi(0) \left| \left(e^{iH_0\Delta t} e^{iH_{\text{int}}\Delta t} \right)^{N_t} \left(e^{-iH_0\Delta t} e^{-iH_{\text{int}}\Delta t} \right)^{N_t} \right| \psi(0) \right\rangle$$

$$+ \frac{1}{2} \left\langle \psi(0) \left| \left(e^{iH_{\text{int}}\Delta t} e^{iH_0\Delta t} \right)^{N_t} \left(e^{-iH_{\text{int}}\Delta t} e^{-iH_0\Delta t} \right)^{N_t} \right| \psi(0) \right\rangle. \quad (\text{C7})$$

We thus obtain

$$A_{\text{den}}(t) \approx \sum_{\mathcal{C}} \{ \text{Re}\{\mathcal{D}_{2t}(\mathcal{C}, \Delta t)\} \cos[\Delta\varepsilon_{\text{int}}(\mathcal{C})\Delta t] - \text{Im}\{\mathcal{D}_{2t}(\mathcal{C}, \Delta t)\} \sin[\Delta\varepsilon_{\text{int}}(\mathcal{C})\Delta t] \}, \quad (\text{C8})$$

where configuration \mathcal{C} consists of $2N_t - 1$ independent states $|\Psi_{i,2}\rangle, \dots, |\Psi_{i,2N_t}\rangle, |\Psi_{i,1}\rangle \equiv |\psi(0)\rangle$, while $\mathcal{D}_{2t}(\mathcal{C}, \Delta t)$ and $\Delta\varepsilon_{\text{int}}(\mathcal{C})$ are defined in Eqs. (21) and (20), respectively. The denominator is also invariant under time reversal, $A_{\text{den}}(t) = A_{\text{den}}(-t)$, which is not a consequence of a specific behavior of the initial state under time reversal but rather follows from $A_{\text{den}}(t) \equiv \langle \psi(0) | \psi(0) \rangle$. In other words, Eq. (C8) should contain only contributions invariant under the transformation $\Delta t \rightarrow -\Delta t$. Using the bipartite lattice symmetry, under which $B|\Psi_{i,l}\rangle = e^{i\chi_l}|\Psi_{i,l}\rangle$, we obtain

$$\mathcal{D}_{2t}(\mathcal{C}, -\Delta t) = \prod_{l=N_t+1}^{2N_t} \langle \Psi_{i,l\oplus 1} | BB e^{-iH_0\Delta t} BB | \Psi_{i,l} \rangle$$

$$\times \prod_{l=1}^{N_t} \langle \Psi_{i,l\oplus 1} | BB e^{iH_0\Delta t} BB | \Psi_{i,l} \rangle$$

$$= \prod_{l=N_t+1}^{2N_t} \langle \Psi_{i,l\oplus 1} | e^{iH_0\Delta t} | \Psi_{i,l} \rangle \prod_{l=1}^{N_t} \langle \Psi_{i,l\oplus 1} | e^{-iH_0\Delta t} | \Psi_{i,l} \rangle$$

$$= \mathcal{D}_{2t}(\mathcal{C}, \Delta t). \quad (\text{C9})$$

Equation (C8) then reduces to

$$A_{\text{den}}(t) = \sum_{\mathcal{C}} \text{Re}\{\mathcal{D}_{2t}(\mathcal{C}, \Delta t)\} \cos[\Delta\varepsilon_{\text{int}}(\mathcal{C})\Delta t]. \quad (\text{C10})$$

We now turn to the numerator of Eq. (18)

$$A_{\text{num}}(t) = \langle \psi(0) | e^{iHt} A_i e^{-iHt} | \psi(0) \rangle, \quad (\text{C11})$$

which is also purely real, $A_{\text{num}}(t) = A_{\text{num}}(t)^*$, so that

$$A_{\text{num}}(t) \approx \sum_{\mathcal{C}} \mathcal{A}_i(\Psi_{i,N_t+1}) \{ \text{Re}\{\mathcal{D}_{2t}(\mathcal{C}, \Delta t)\} \cos[\Delta\varepsilon_{\text{int}}(\mathcal{C})\Delta t] - \text{Im}\{\mathcal{D}_{2t}(\mathcal{C}, \Delta t)\} \sin[\Delta\varepsilon_{\text{int}}(\mathcal{C})\Delta t] \}. \quad (\text{C12})$$

In the following discussion, we assume that the time reversal operation changes $|\psi(0)\rangle$ by a phase factor, $T|\psi(0)\rangle = e^{i\chi_T}|\psi(0)\rangle$. This, combined with $B|\psi(0)\rangle = e^{i\chi_B}|\psi(0)\rangle$, gives the assumption on $|\psi(0)\rangle$ that is mentioned before Eq. (19). We further assume that $TBA_iBT = A_i$. Under these assumptions, the numerator is invariant under time reversal, $A_{\text{num}}(-t) = A_{\text{num}}(t)$, meaning that Eq. (C12) should contain only contributions invariant under the transformation $\Delta t \rightarrow -\Delta t$. Using Eq. (C9), Eq. (C12) reduces to

$$A_{\text{num}}(t) \approx \sum_{\mathcal{C}} \mathcal{A}_i(\Psi_{i,N_t+1}) \text{Re}\{\mathcal{D}_{2t}(\mathcal{C}, \Delta t)\} \cos[\Delta\varepsilon_{\text{int}}(\mathcal{C})\Delta t], \quad (\text{C13})$$

and Eq. (22) follows immediately.

An example of the initial state $|\psi(0)\rangle$ and the observable A_i that satisfy $TB|\psi(0)\rangle = e^{i\chi}|\psi(0)\rangle$ and $TBA_iBT = A_i$ are the CDW state $|\psi_{\text{CDW}}\rangle$ [Eq. (24)] and the local charge density $A_i = \sum_{\sigma} n_{r\sigma}$. While the time-reversal operation may change a general SDW state [Eq. (23)] by more than a phase factor, Eq. (C13) is still applicable when the observable of interest is the local spin density $A_i = n_{r\uparrow} - n_{r\downarrow}$. This follows from the transformation law $T(n_{r\uparrow} - n_{r\downarrow})T = n_{r\downarrow} - n_{r\uparrow}$ and the fact that the roles of spin-up and spin-down electrons in the state $T|\psi_{\text{SDW}}\rangle$ are exchanged with respect to the state $|\psi_{\text{SDW}}\rangle$.

We now explain how we use Eq. (26) to enlarge statistics in computations of time-dependent local spin (charge) densities when the evolution starts from state $|\psi_{\text{SDW}}\rangle$ in Eq. (23) [$|\psi_{\text{CDW}}\rangle$ in Eq. (24)]. Let us limit the discussion to the spin (charge) density at fixed position \mathbf{r} . Suppose that we obtained Markov chains (of length N_{CDW}) $\{\mathcal{N}_1^{\text{CDW}}(t), \dots, \mathcal{N}_{N_{\text{CDW}}}^{\text{CDW}}(t)\}$ and $\{\mathcal{D}_1^{\text{CDW}}, \dots, \mathcal{D}_{N_{\text{CDW}}}^{\text{CDW}}\}$ for the numerator and denominator. Suppose also that we obtained Markov chains (of length N_{SDW}) $\{\mathcal{N}_1^{\text{SDW}}(t), \dots, \mathcal{N}_{N_{\text{SDW}}}^{\text{SDW}}(t)\}$ and $\{\mathcal{D}_1^{\text{SDW}}, \dots, \mathcal{D}_{N_{\text{SDW}}}^{\text{SDW}}\}$ for the numerator and denominator. Using these Markov chains, we found that the best result for the time-dependent local spin (charge) density is obtained by joining them into one Markov chain $\{\mathcal{N}_1^{\text{SDW}}(t), \dots, \mathcal{N}_{N_{\text{SDW}}}^{\text{SDW}}(t), \mathcal{N}_1^{\text{CDW}}(t), \dots, \mathcal{N}_{N_{\text{CDW}}}^{\text{CDW}}(t)\}$ of length $N_{\text{SDW}} + N_{\text{CDW}}$ for the numerator, and another Markov chain

$\{\mathcal{D}_1^{\text{SDW}}, \dots, \mathcal{D}_{N_{\text{SDW}}}^{\text{SDW}}, \mathcal{D}_1^{\text{CDW}}, \dots, \mathcal{D}_{N_{\text{CDW}}}^{\text{CDW}}\}$ of length $N_{\text{SDW}} + N_{\text{CDW}}$ for the denominator. If individual chain lengths N_{CDW} and N_{SDW} are sufficiently large, the manner in which the chains are joined is immaterial; here, we append the CDW chain to the SDW chain, and we note that other joining possibilities lead to the same final result (within the statistical error bars). To further reduce statistical error bars, we also combine SDW + CDW chains at all positions \mathbf{r} that have the same spin (charge) density by the symmetry of the initial state.

APPENDIX D: DERIVATION OF THE ABQMC FORMULA FOR THE SURVIVAL PROBABILITY

We start from the survival-probability amplitude

$$A_P(t) = \frac{\langle \psi(0) | e^{-iHt} | \psi(0) \rangle}{\langle \psi(0) | \psi(0) \rangle}, \quad (\text{D1})$$

whose numerator can be expressed as

$$\begin{aligned} \langle \psi(0) | e^{-iHt} | \psi(0) \rangle &\approx \frac{1}{2} \langle \psi(0) | \left(e^{-iH_0 \Delta t} e^{-iH_{\text{int}} \Delta t} \right)^{N_t} | \psi(0) \rangle + \frac{1}{2} \langle \psi(0) | \left(e^{-iH_{\text{int}} \Delta t} e^{-iH_0 \Delta t} \right)^{N_t} | \psi(0) \rangle \\ &= \sum_{\Psi_{i,2} \dots \Psi_{i,N_t}} \text{Re} \left\{ \prod_{l=1}^{N_t} \langle \Psi_{i,l} | e^{-iH_0 \Delta t} | \Psi_{i,l} \rangle \right\} e^{-i\varepsilon_{\text{int}}(\mathcal{C}) \Delta t} \\ &= \sum_{\Psi_{i,2} \dots \Psi_{i,N_t}} \sum_{\Psi_{k,1} \dots \Psi_{k,N_t}} \text{Re} \left\{ \prod_{l=1}^{N_t} \langle \Psi_{i,l} | \Psi_{k,l} \rangle \langle \Psi_{k,l} | \Psi_{i,l} \rangle e^{-i\varepsilon_0(\mathcal{C}) \Delta t} \right\} e^{-i\varepsilon_{\text{int}}(\mathcal{C}) \Delta t} \\ &= \sum_{\mathcal{C}} \{ \text{Re}\{\mathcal{D}(\mathcal{C})\} \cos[\varepsilon_0(\mathcal{C}) \Delta t] + \text{Im}\{\mathcal{D}(\mathcal{C})\} \sin[\varepsilon_0(\mathcal{C}) \Delta t] \} e^{-i\varepsilon_{\text{int}}(\mathcal{C}) \Delta t}. \end{aligned} \quad (\text{D2})$$

In going from the second to the third line of Eq. (D2), we introduced spectral decompositions of N_t factors $e^{-iH_0 \Delta t}$. The configuration \mathcal{C} entering the last line of Eq. (D2) consists of $N_t - 1$ independent states $|\Psi_{i,2}\rangle, \dots, |\Psi_{i,N_t}\rangle$ in the coordinate representation and N_t independent states $|\Psi_{k,1}\rangle, \dots, |\Psi_{k,N_t}\rangle$ in the momentum representation, while $|\Psi_{i,1}\rangle \equiv |\psi(0)\rangle$. $\mathcal{D}(\mathcal{C})$ and $\varepsilon_0(\mathcal{C})$ are defined in Eqs. (31) and (34), respectively. By virtue of the bipartite lattice symmetry, under which $\mathcal{D}(\mathcal{C})$ remains invariant, while $\varepsilon_0(\mathcal{C})$ changes sign, the summand containing $\sin[\varepsilon_0(\mathcal{C}) \Delta t]$ in Eq. (D2) vanishes, so that

$$\langle \psi(0) | e^{-iHt} | \psi(0) \rangle \approx \sum_{\mathcal{C}} \text{Re}\{\mathcal{D}(\mathcal{C})\} \cos[\varepsilon_0(\mathcal{C}) \Delta t] e^{-i\varepsilon_{\text{int}}(\mathcal{C}) \Delta t}. \quad (\text{D3})$$

This form should be used, e.g., when $|\psi(0)\rangle$ is the SDW state defined in Eq. (23). When the initial state is the CDW state defined in Eq. (24), $T|\psi(0)\rangle = e^{ix} |\psi(0)\rangle$, $\langle \psi(0) | e^{-iHt} | \psi(0) \rangle$ is purely real, so that

$$\langle \psi(0) | e^{-iHt} | \psi(0) \rangle \approx \sum_{\mathcal{C}} \text{Re}\{\mathcal{D}(\mathcal{C})\} \cos[\varepsilon_0(\mathcal{C}) \Delta t] \cos[\varepsilon_{\text{int}}(\mathcal{C}) \Delta t]. \quad (\text{D4})$$

Equation (30) then follows by combining Eq. (D4) with $\langle \psi(0) | \psi(0) \rangle = \sum_{\mathcal{C}} \text{Re}\{\mathcal{D}(\mathcal{C})\}$.

We now provide a formal demonstration of Eq. (36). The partial particle-hole transformation is represented by a unitary, hermitean, and involutive operator P ($P^\dagger = P = P^{-1}$), whose action on electron creation and annihilation operators in real space is given as^{109,110}

$$P c_{\mathbf{r}\uparrow} P = c_{\mathbf{r}\uparrow}, \quad P c_{\mathbf{r}\uparrow}^\dagger P = c_{\mathbf{r}\uparrow}^\dagger, \quad (\text{D5})$$

$$P c_{\mathbf{r}\downarrow} P = (-1)^{r_x+r_y} c_{\mathbf{r}\downarrow}^\dagger, \quad P c_{\mathbf{r}\downarrow}^\dagger P = (-1)^{r_x+r_y} c_{\mathbf{r}\downarrow}. \quad (\text{D6})$$

The interaction Hamiltonian H_{int} thus transforms under the partial particle-hole transformation as $PH_{\text{int}}P = U\widehat{N}_\uparrow - H_{\text{int}}$. The action of the partial particle-hole transformation in the momentum space reads as $[\mathbf{Q} = (\pi, \pi)]$

$$P c_{\mathbf{k}\uparrow} P = c_{\mathbf{k}\uparrow}, \quad P c_{\mathbf{k}\uparrow}^\dagger P = c_{\mathbf{k}\uparrow}^\dagger, \quad (\text{D7})$$

$$P c_{\mathbf{k}\downarrow} P = c_{\mathbf{Q}-\mathbf{k},\downarrow}^\dagger, \quad P c_{\mathbf{k}\downarrow}^\dagger P = c_{\mathbf{Q}-\mathbf{k},\downarrow}. \quad (\text{D8})$$

The kinetic energy, therefore, remains invariant under the partial particle-hole transformation, i.e., $PH_0P = H_0$. Equations (D5) and (D6) imply that $P|\emptyset\rangle = \prod_{\mathbf{r} \in \mathcal{U}} c_{\mathbf{r}\downarrow}^\dagger |\emptyset\rangle$. We then find that $P|\psi_{\text{CDW}}\rangle = |\psi_{\text{SDW}}\rangle$, i.e., the partial particle-hole transformation transforms the CDW state defined in Eq. (24) into the SDW state defined in Eq. (23) and vice versa.¹⁰⁸ The states $|\psi_{\text{CDW}}\rangle$ and $|\psi_{\text{SDW}}\rangle$ have the same number of spin-up electrons, while their numbers of spin-down electrons add to N_c . Using the combination of the partial particle-hole transformation P and the bipartite lattice transformation B defined in Appendix C, one obtains

$$\langle \psi_{\text{CDW}} | e^{-iHt} | \psi_{\text{CDW}} \rangle = e^{-iN_t(\psi)Ut} \langle \psi_{\text{SDW}} | e^{-iHt} | \psi_{\text{SDW}} \rangle^*, \quad (\text{D9})$$

where $N_t(\psi) = \langle \psi_{\text{CDW}} | \widehat{N}_\uparrow | \psi_{\text{CDW}} \rangle = \langle \psi_{\text{SDW}} | \widehat{N}_\uparrow | \psi_{\text{SDW}} \rangle$ is the total number of spin-up electrons in CDW and SDW states. Equation (36) then follows immediately from Eq. (D9).

A similar procedure to that described in Appendix C is used to combine Markov chains for the survival probabilities of the CDW and SDW states related by the dynamical symmetry in Eq. (D9).

APPENDIX E: USING THE PARTICLE-HOLE SYMMETRY TO DISCUSS THE AVERAGE SIGN OF THE FPQMC METHOD FOR CHEMICAL POTENTIALS μ AND $U - \mu$

The (full) particle-hole transformation is represented by a unitary, hermitean, and involutive operator P_f ($P_f^\dagger = P_f = P_f^{-1}$) whose action on electron creation and annihilation operators in real space is defined as^{109,110}

$$P_f c_{r\sigma} P_f = (-1)^{r_x+r_y} c_{r\sigma}^\dagger. \quad (\text{E1})$$

The corresponding formula in the momentum space reads as

$$P_f c_{\mathbf{k}\sigma} P_f = c_{\mathbf{Q}-\mathbf{k},\sigma}^\dagger. \quad (\text{E2})$$

Let us fix J, U, T , and N_τ and compute the equation of state $\rho_e(\mu)$ using Eq. (13) in which $\mathcal{A}_i(\Psi_{i,l}) = [N_\uparrow(C) + N_\downarrow(C)]/N_C$. It is convenient to make the μ -dependence in $\varepsilon_{\text{int}}(C, \mu)$ explicit. In the sums entering Eq. (13) we make the substitution

$$C \rightarrow C' = \{|\Phi_{i,l}\rangle = P_f |\Psi_{i,l}\rangle | l = 1, \dots, N_\tau\} \quad (\text{E3})$$

under which

$$\mathcal{D}_\beta(C, \Delta\tau) = \mathcal{D}_\beta(C', \Delta\tau), \quad (\text{E4})$$

$$\varepsilon_{\text{int}}(C, \mu) = \varepsilon_{\text{int}}(C', U - \mu) + (U - 2\mu)N_\tau N_C, \quad (\text{E5})$$

$$N_\sigma(C') = N_C - N_\sigma(C). \quad (\text{E6})$$

It then follows that

$$\begin{aligned} & \frac{\sum_C \mathcal{D}_\beta(C, \Delta\tau) e^{-\Delta\tau\varepsilon_{\text{int}}(C, \mu)} [N_\uparrow(C) + N_\downarrow(C)]/N_C}{\sum_C \mathcal{D}_\beta(C, \Delta\tau) e^{-\Delta\tau\varepsilon_{\text{int}}(C, \mu)}} \\ &= 2 - \frac{\sum_{C'} \mathcal{D}_\beta(C', \Delta\tau) e^{-\Delta\tau\varepsilon_{\text{int}}(C', U - \mu)} [N_\uparrow(C') + N_\downarrow(C')]/N_C}{\sum_{C'} \mathcal{D}_\beta(C', \Delta\tau) e^{-\Delta\tau\varepsilon_{\text{int}}(C', U - \mu)}}. \end{aligned} \quad (\text{E7})$$

The FPQMC simulations of the ratios in the last equation are performed for chemical potentials μ and $U - \mu$, which are symmetric with respect to the chemical potential $U/2$ at the half-filling. Since $\varepsilon_{\text{int}}(C, \mu)$ and $\varepsilon_{\text{int}}(C', U - \mu)$ differ by a constant additive factor, the corresponding configuration weights differ by a constant multiplicative factor, and the average signs of the two FPQMC simulations are thus mutually equal.

REFERENCES

- ¹H. Aoki, N. Tsuji, M. Eckstein, M. Kollar, T. Oka, and P. Werner, "Nonequilibrium dynamical mean-field theory and its applications," *Rev. Mod. Phys.* **86**, 779–837 (2014).
- ²L. Tarruell and L. Sanchez-Palencia, "Quantum simulation of the Hubbard model with ultracold fermions in optical lattices," *C. R. Phys.* **19**, 365–393 (2018).
- ³I. Bloch, J. Dalibard, and W. Zwerger, "Many-body physics with ultracold gases," *Rev. Mod. Phys.* **80**, 885–964 (2008).
- ⁴S. Murmann, A. Bergschneider, V. M. Klinkhamer, G. Zürn, T. Lompe, and S. Jochim, "Two fermions in a double well: Exploring a fundamental building block of the Hubbard model," *Phys. Rev. Lett.* **114**, 080402 (2015).

- ⁵B. M. Spar, E. Guardado-Sanchez, S. Chi, Z. Z. Yan, and W. S. Bakr, "Realization of a Fermi-Hubbard optical tweezer array," *Phys. Rev. Lett.* **128**, 223202 (2022).
- ⁶Z. Z. Yan, B. M. Spar, M. L. Prichard, S. Chi, H.-T. Wei, E. Ibarra-García-Padilla, K. R. A. Hazzard, and W. S. Bakr, "Two-dimensional programmable tweezer arrays of fermions," *Phys. Rev. Lett.* **129**, 123201 (2022).
- ⁷J. Hubbard, "Electron correlations in narrow energy bands," *Proc. R. Soc. London, Ser. A* **276**, 238–257 (1963).
- ⁸"The Hubbard model at half a century," *Nat. Phys.* **9**, 523 (2013).
- ⁹E. Cocchi, L. A. Miller, J. H. Drewes, M. Koschorreck, D. Pertot, F. Brennecke, and M. Köhl, "Equation of state of the two-dimensional Hubbard model," *Phys. Rev. Lett.* **116**, 175301 (2016).
- ¹⁰E. Cocchi, L. A. Miller, J. H. Drewes, C. F. Chan, D. Pertot, F. Brennecke, and M. Köhl, "Measuring entropy and short-range correlations in the two-dimensional Hubbard model," *Phys. Rev. X* **7**, 031025 (2017).
- ¹¹M. F. Parsons, A. Mazurenko, C. S. Chiu, G. Ji, D. Greif, and M. Greiner, "Site-resolved measurement of the spin-correlation function in the Fermi-Hubbard model," *Science* **353**, 1253–1256 (2016).
- ¹²L. W. Cheuk, M. A. Nichols, K. R. Lawrence, M. Okan, H. Zhang, E. Khatami, N. Trivedi, T. Paiva, M. Rigol, and M. W. Zwierlein, "Observation of spatial charge and spin correlations in the 2D Fermi-Hubbard model," *Science* **353**, 1260–1264 (2016).
- ¹³C. S. Chiu, G. Ji, A. Bohrdt, M. Xu, M. Knap, E. Demler, F. Grusdt, M. Greiner, and D. Greif, "String patterns in the doped Hubbard model," *Science* **365**, 251–256 (2019).
- ¹⁴P. T. Brown, D. Mitra, E. Guardado-Sanchez, R. Nourafkan, A. Reymbaut, C.-D. Hébert, S. Bergeron, A.-M. S. Tremblay, J. Kokalj, D. A. Huse, P. Schauss, and W. S. Bakr, "Bad metallic transport in a cold atom Fermi-Hubbard system," *Science* **363**, 379–382 (2019).
- ¹⁵U. Schneider, L. Hackermüller, J. P. Ronzheimer, S. Will, S. Braun, T. Best, I. Bloch, E. Demler, S. Mandt, D. Rasch, and A. Rosch, "Fermionic transport and out-of-equilibrium dynamics in a homogeneous Hubbard model with ultracold atoms," *Nat. Phys.* **8**, 213–218 (2012).
- ¹⁶W. Xu, W. R. McGehee, W. N. Morong, and B. DeMarco, "Bad-metal relaxation dynamics in a Fermi lattice gas," *Nat. Commun.* **10**, 1588 (2019).
- ¹⁷M. A. Nichols, L. W. Cheuk, M. Okan, T. R. Hartke, E. Mendez, T. Senthil, E. Khatami, H. Zhang, and M. W. Zwierlein, "Spin transport in a Mott insulator of ultracold fermions," *Science* **363**, 383–387 (2019).
- ¹⁸J. E. Hirsch, D. J. Scalapino, R. L. Sugar, and R. Blankenbecler, "Efficient Monte Carlo procedure for systems with fermions," *Phys. Rev. Lett.* **47**, 1628–1631 (1981).
- ¹⁹J. E. Hirsch, R. L. Sugar, D. J. Scalapino, and R. Blankenbecler, "Monte Carlo simulations of one-dimensional fermion systems," *Phys. Rev. B* **26**, 5033–5055 (1982).
- ²⁰R. Blankenbecler, D. J. Scalapino, and R. L. Sugar, "Monte Carlo calculations of coupled boson-fermion systems. I," *Phys. Rev. D* **24**, 2278–2286 (1981).
- ²¹D. J. Scalapino and R. L. Sugar, "Monte Carlo calculations of coupled Boson-Fermion systems. II," *Phys. Rev. B* **24**, 4295–4308 (1981).
- ²²J. E. Hirsch, "Monte Carlo study of the two-dimensional Hubbard model," *Phys. Rev. Lett.* **51**, 1900–1903 (1983).
- ²³J. E. Hirsch, "Two-dimensional Hubbard model: Numerical simulation study," *Phys. Rev. B* **31**, 4403–4419 (1985).
- ²⁴J. E. Hirsch and R. M. Fye, "Monte Carlo method for magnetic impurities in metals," *Phys. Rev. Lett.* **56**, 2521–2524 (1986).
- ²⁵S. R. White, D. J. Scalapino, R. L. Sugar, E. Y. Loh, J. E. Gubernatis, and R. T. Scalettar, "Numerical study of the two-dimensional Hubbard model," *Phys. Rev. B* **40**, 506–516 (1989).
- ²⁶S. Zhang, J. Carlson, and J. E. Gubernatis, "Constrained path quantum Monte Carlo method for fermion ground states," *Phys. Rev. Lett.* **74**, 3652–3655 (1995).
- ²⁷S. Zhang, "Finite-temperature Monte Carlo calculations for systems with fermions," *Phys. Rev. Lett.* **83**, 2777–2780 (1999).
- ²⁸S. Zhang and H. Krakauer, "Quantum Monte Carlo method using phase-free random walks with Slater determinants," *Phys. Rev. Lett.* **90**, 136401 (2003).
- ²⁹C. N. Varney, C.-R. Lee, Z. J. Bai, S. Chiesa, M. Jarrell, and R. T. Scalettar, "Quantum Monte Carlo study of the two-dimensional fermion Hubbard model," *Phys. Rev. B* **80**, 075116 (2009).

- ³⁰J. P. F. LeBlanc, A. E. Antipov, F. Becca, I. W. Bulik, G. K.-L. Chan, C.-M. Chung, Y. Deng, M. Ferrero, T. M. Henderson, C. A. Jiménez-Hoyos, E. Kozik, X.-W. Liu, A. J. Millis, N. V. Prokofev, M. Qin, G. E. Scuseria, H. Shi, B. V. Svistunov, L. F. Tocchio, I. S. Tupitsyn, S. R. White, S. Zhang, B.-X. Zheng, Z. Zhu, E. Gull Simons Collaboration on the Many-Electron Problem, “Solutions of the two-dimensional Hubbard model: Benchmarks and results from a wide range of numerical algorithms,” *Phys. Rev. X* **5**, 041041 (2015).
- ³¹E. Gull, A. J. Millis, A. I. Lichtenstein, A. N. Rubtsov, M. Troyer, and P. Werner, “Continuous-time Monte Carlo methods for quantum impurity models,” *Rev. Mod. Phys.* **83**, 349–404 (2011).
- ³²A. N. Rubtsov and A. I. Lichtenstein, “Continuous-time quantum Monte Carlo method for fermions: Beyond auxiliary field framework,” *JETP Lett.* **80**, 61–65 (2004).
- ³³A. N. Rubtsov, V. V. Savkin, and A. I. Lichtenstein, “Continuous-time quantum Monte Carlo method for fermions,” *Phys. Rev. B* **72**, 035122 (2005).
- ³⁴E. Gull, P. Werner, O. Parcollet, and M. Troyer, “Continuous-time auxiliary-field Monte Carlo for quantum impurity models,” *Europhys. Lett.* **82**, 57003 (2008).
- ³⁵N. V. Prokofev and B. V. Svistunov, “Polaron problem by diagrammatic quantum Monte Carlo,” *Phys. Rev. Lett.* **81**, 2514–2517 (1998).
- ³⁶N. Prokofev and B. Svistunov, “Bold diagrammatic Monte Carlo technique: When the sign problem is welcome,” *Phys. Rev. Lett.* **99**, 250201 (2007).
- ³⁷E. Kozik, K. Van Houcke, E. Gull, L. Pollet, N. Prokofev, B. Svistunov, and M. Troyer, “Diagrammatic Monte Carlo for correlated fermions,” *Europhys. Lett.* **90**, 10004 (2010).
- ³⁸K. Van Houcke, E. Kozik, N. Prokofev, and B. Svistunov, “Diagrammatic Monte Carlo,” *Phys. Procedia* **6**, 95–105 (2010).
- ³⁹W. Wu, M. Ferrero, A. Georges, and E. Kozik, “Controlling Feynman diagrammatic expansions: Physical nature of the pseudogap in the two-dimensional Hubbard model,” *Phys. Rev. B* **96**, 041105 (2017).
- ⁴⁰M. Rigol, T. Bryant, and R. R. P. Singh, “Numerical linked-cluster approach to quantum lattice models,” *Phys. Rev. Lett.* **97**, 187202 (2006).
- ⁴¹E. Khatami and M. Rigol, “Thermodynamics of strongly interacting fermions in two-dimensional optical lattices,” *Phys. Rev. A* **84**, 053611 (2011).
- ⁴²B. Tang, E. Khatami, and M. Rigol, “A short introduction to numerical linked-cluster expansions,” *Comput. Phys. Commun.* **184**, 557–564 (2013).
- ⁴³F. Šimkovic IV, R. Rossi, and M. Ferrero, “Two-dimensional Hubbard model at finite temperature: Weak, strong, and long correlation regimes,” *Phys. Rev. Res.* **4**, 043201 (2022).
- ⁴⁴J. Yang, L. Liu, J. Mongkolkiattichai, and P. Schauss, “Site-resolved imaging of ultracold fermions in a triangular-lattice quantum gas microscope,” *PRX Quantum* **2**, 020344 (2021).
- ⁴⁵S. Humeniuk and Y. Wan, “Numerically exact mimicking of quantum gas microscopy for interacting lattice fermions,” *Phys. Rev. B* **104**, 075155 (2021).
- ⁴⁶J. Koepsell, D. Bourgund, P. Sompet, S. Hirthe, A. Bohrdt, Y. Wang, F. Grusdt, E. Demler, G. Salomon, C. Gross, and I. Bloch, “Microscopic evolution of doped Mott insulators from polaronic metal to Fermi liquid,” *Science* **374**, 82–86 (2021).
- ⁴⁷Y. Wang, A. Bohrdt, S. Ding, J. Koepsell, E. Demler, and F. Grusdt, “Higher-order spin-hole correlations around a localized charge impurity,” *Phys. Rev. Res.* **3**, 033204 (2021).
- ⁴⁸D. Garwood, J. Mongkolkiattichai, L. Liu, J. Yang, and P. Schauss, “Site-resolved observables in the doped spin-imbalanced triangular Hubbard model,” *Phys. Rev. A* **106**, 013310 (2022).
- ⁴⁹K. Mikelsons, “Extensions of numerical methods for strongly correlated electron systems,” Ph.D. thesis, University of Cincinnati, 2009.
- ⁵⁰J. Vučićević, J. Kokalj, R. Žitko, N. Wentzell, D. Tanasković, and J. Mravlje, “Conductivity in the square lattice Hubbard model at high temperatures: Importance of vertex corrections,” *Phys. Rev. Lett.* **123**, 036601 (2019).
- ⁵¹E. W. Huang, R. Sheppard, B. Moritz, and T. P. Devereaux, “Strange metallicity in the doped Hubbard model,” *Science* **366**, 987–990 (2019).
- ⁵²J. Vučićević, S. Preditin, and M. Ferrero, “Charge fluctuations, hydrodynamics and transport in the square-lattice Hubbard model,” *arXiv:2208.04047* (2022).
- ⁵³J. Jaklič and P. Prelovšek, “Finite-temperature properties of doped antiferromagnets,” *Adv. Phys.* **49**, 1–92 (2000).
- ⁵⁴P. Prelovšek and J. Bonča, “Ground state and finite temperature Lanczos methods,” in *Strongly Correlated Systems: Numerical Methods*, edited by A. Avella and F. Mancini (Springer, Berlin, Heidelberg, 2013), pp. 1–30.
- ⁵⁵A. Vranić, J. Vučićević, J. Kokalj, J. Skolimowski, R. Žitko, J. Mravlje, and D. Tanasković, “Charge transport in the Hubbard model at high temperatures: Triangular versus square lattice,” *Phys. Rev. B* **102**, 115142 (2020).
- ⁵⁶P. Werner, T. Oka, and A. J. Millis, “Diagrammatic Monte Carlo simulation of nonequilibrium systems,” *Phys. Rev. B* **79**, 035320 (2009).
- ⁵⁷M. Schiró and M. Fabrizio, “Real-time diagrammatic Monte Carlo for nonequilibrium quantum transport,” *Phys. Rev. B* **79**, 153302 (2009).
- ⁵⁸M. Schiró, “Real-time dynamics in quantum impurity models with diagrammatic Monte Carlo,” *Phys. Rev. B* **81**, 085126 (2010).
- ⁵⁹E. Gull, D. R. Reichman, and A. J. Millis, “Numerically exact long-time behavior of nonequilibrium quantum impurity models,” *Phys. Rev. B* **84**, 085134 (2011).
- ⁶⁰G. Cohen, D. R. Reichman, A. J. Millis, and E. Gull, “Green’s functions from real-time bold-line Monte Carlo,” *Phys. Rev. B* **89**, 115139 (2014).
- ⁶¹G. Cohen, E. Gull, D. R. Reichman, and A. J. Millis, “Taming the dynamical sign problem in real-time evolution of quantum many-body problems,” *Phys. Rev. Lett.* **115**, 266802 (2015).
- ⁶²M. S. Church and B. M. Rubenstein, “Real-time dynamics of strongly correlated fermions using auxiliary field quantum Monte Carlo,” *J. Chem. Phys.* **154**, 184103 (2021).
- ⁶³C. Karrasch, D. M. Kennes, and J. E. Moore, “Transport properties of the one-dimensional Hubbard model at finite temperature,” *Phys. Rev. B* **90**, 155104 (2014).
- ⁶⁴N. Schlünzen, J.-P. Joost, F. Heidrich-Meisner, and M. Bonitz, “Nonequilibrium dynamics in the one-dimensional Fermi-Hubbard model: Comparison of the nonequilibrium Green-functions approach and the density matrix renormalization group method,” *Phys. Rev. B* **95**, 165139 (2017).
- ⁶⁵A. Akbari, M. J. Hashemi, A. Rubio, R. M. Nieminen, and R. van Leeuwen, “Challenges in truncating the hierarchy of time-dependent reduced density matrices equations,” *Phys. Rev. B* **85**, 235121 (2012).
- ⁶⁶D. Lacroix, S. Hermanns, C. M. Hinz, and M. Bonitz, “Ultrafast dynamics of finite Hubbard clusters: A stochastic mean-field approach,” *Phys. Rev. B* **90**, 125112 (2014).
- ⁶⁷Z. Li, N. Tong, X. Zheng, D. Hou, J. Wei, J. Hu, and Y. Yan, “Hierarchical Liouville-space approach for accurate and universal characterization of quantum impurity systems,” *Phys. Rev. Lett.* **109**, 266403 (2012).
- ⁶⁸S. Wang, X. Zheng, J. Jin, and Y. J. Yan, “Hierarchical Liouville-space approach to nonequilibrium dynamical properties of quantum impurity systems,” *Phys. Rev. B* **88**, 035129 (2013).
- ⁶⁹R. E. V. Profumo, C. Groth, L. Messio, O. Parcollet, and X. Waintal, “Quantum Monte Carlo for correlated out-of-equilibrium nanoelectronic devices,” *Phys. Rev. B* **91**, 245154 (2015).
- ⁷⁰M. A. Cazalilla and J. B. Marston, “Time-dependent density-matrix renormalization group: A systematic method for the study of quantum many-body out-of-equilibrium systems,” *Phys. Rev. Lett.* **88**, 256403 (2002).
- ⁷¹S. R. White and A. E. Feiguin, “Real-time evolution using the density matrix renormalization group,” *Phys. Rev. Lett.* **93**, 076401 (2004).
- ⁷²U. Schollwöck, “Time-dependent density-matrix renormalization-group methods,” *J. Phys. Soc. Jpn.* **74**, 246–255 (2005).
- ⁷³C. Yang and A. E. Feiguin, “Spectral function of the two-dimensional Hubbard model: A density matrix renormalization group plus cluster perturbation theory study,” *Phys. Rev. B* **93**, 081107 (2016).
- ⁷⁴G. Stefanucci and R. van Leeuwen, *Nonequilibrium Many-Body Theory of Quantum Systems: A Modern Introduction* (Cambridge University Press, New York, 2013).
- ⁷⁵N. Schlünzen, S. Hermanns, M. Scharnke, and M. Bonitz, “Ultrafast dynamics of strongly correlated fermions—Nonequilibrium Green functions and selfenergy approximations,” *J. Phys.: Condens. Matter* **32**, 103001 (2019).
- ⁷⁶N. Schlünzen, J. P. Joost, and M. Bonitz, “Achieving the scaling limit for nonequilibrium Green functions simulations,” *Phys. Rev. Lett.* **124**, 076601 (2020).

- ⁷⁷J.-P. Joost, N. Schlünzen, H. Ohldag, M. Bonitz, F. Lackner, and I. Březinová, “Dynamically screened ladder approximation: Simultaneous treatment of strong electronic correlations and dynamical screening out of equilibrium,” *Phys. Rev. B* **105**, 165155 (2022).
- ⁷⁸H. De Raedt and A. Lagendijk, “Monte Carlo calculation of the thermodynamic properties of a quantum model: A one-dimensional fermion lattice model,” *Phys. Rev. Lett.* **46**, 77–80 (1981).
- ⁷⁹H. De Raedt and A. Lagendijk, “Monte Carlo calculation of the thermodynamic properties of a one-dimensional fermion lattice model,” *J. Stat. Phys.* **27**, 731–744 (1982).
- ⁸⁰H. De Raedt and A. Lagendijk, “Monte Carlo simulation of quantum statistical lattice models,” *Phys. Rep.* **127**, 233–307 (1985).
- ⁸¹D. M. Ceperley, “Path integrals in the theory of condensed helium,” *Rev. Mod. Phys.* **67**, 279–355 (1995).
- ⁸²D. Thirumalai and B. J. Berne, “Methods for simulating time correlation functions in quantum systems,” *Comput. Phys. Commun.* **63**, 415–426 (1991).
- ⁸³T. Dornheim, S. Groth, J. Vorberger, and M. Bonitz, “*Ab initio* path integral Monte Carlo results for the dynamic structure factor of correlated electrons: From the electron liquid to warm dense matter,” *Phys. Rev. Lett.* **121**, 255001 (2018).
- ⁸⁴P. Hamann, T. Dornheim, J. Vorberger, Z. A. Moldabekov, and M. Bonitz, “Dynamic properties of the warm dense electron gas based on *ab initio* path integral Monte Carlo simulations,” *Phys. Rev. B* **102**, 125150 (2020).
- ⁸⁵M. Takahashi and M. Imada, “Monte Carlo calculation of quantum systems,” *J. Phys. Soc. Jpn.* **53**, 963–974 (1984).
- ⁸⁶A. P. Lyubartsev, “Simulation of excited states and the sign problem in the path integral Monte Carlo method,” *J. Phys. A: Math. Gen.* **38**, 6659–6674 (2005).
- ⁸⁷A. P. Lyubartsev, “Interacting electrons in one dimension: A path integral Monte Carlo study,” *J. Phys. A: Math. Theor.* **40**, 7151–7157 (2007).
- ⁸⁸V. S. Filinov, M. Bonitz, W. Ebeling, and V. E. Fortov, “Thermodynamics of hot dense H-plasmas: Path integral Monte Carlo simulations and analytical approximations,” *Plasma Phys. Control. Fusion* **43**, 743–759 (2001).
- ⁸⁹T. Schoof, M. Bonitz, A. Filinov, D. Hochstuhl, and J. W. Dufty, “Configuration path integral Monte Carlo,” *Contrib. Plasma Phys.* **51**, 687–697 (2011).
- ⁹⁰T. Dornheim, S. Groth, A. Filinov, and M. Bonitz, “Permutation blocking path integral Monte Carlo: A highly efficient approach to the simulation of strongly degenerate non-ideal fermions,” *New J. Phys.* **17**, 073017 (2015).
- ⁹¹T. Dornheim, T. Schoof, S. Groth, A. Filinov, and M. Bonitz, “Permutation blocking path integral Monte Carlo approach to the uniform electron gas at finite temperature,” *J. Chem. Phys.* **143**, 204101 (2015).
- ⁹²S. Groth, T. Schoof, T. Dornheim, and M. Bonitz, “*Ab initio* quantum Monte Carlo simulations of the uniform electron gas without fixed nodes,” *Phys. Rev. B* **93**, 085102 (2016).
- ⁹³T. Dornheim, S. Groth, and M. Bonitz, “The uniform electron gas at warm dense matter conditions,” *Phys. Rep.* **744**, 1–86 (2018).
- ⁹⁴T. Dornheim, “Fermion sign problem in path integral Monte Carlo simulations: Quantum dots, ultracold atoms, and warm dense matter,” *Phys. Rev. E* **100**, 023307 (2019).
- ⁹⁵T. Dornheim, “Fermion sign problem in path integral Monte Carlo simulations: Grand-canonical ensemble,” *J. Phys. A: Math. Theor.* **54**, 335001 (2021).
- ⁹⁶A. Filinov, P. R. Levashov, and M. Bonitz, “Thermodynamics of the uniform electron gas: Fermionic path integral Monte Carlo simulations in the restricted grand canonical ensemble,” *Contrib. Plasma Phys.* **61**, e202100112 (2021).
- ⁹⁷C. Watzenböck, M. Fellinger, K. Held, and A. Toschi, “Long-term memory magnetic correlations in the Hubbard model: A dynamical mean-field theory analysis,” *SciPost Phys.* **12**, 184 (2022).
- ⁹⁸M. Suzuki, “Generalized Trotter’s formula and systematic approximants of exponential operators and inner derivations with applications to many-body problems,” *Commun. Math. Phys.* **51**, 183–190 (1976).
- ⁹⁹A. L. Fetter and J. D. Walecka, *Quantum Theory of Many-Particle Systems* (McGraw-Hill, Boston, 1971).
- ¹⁰⁰J. E. Hirsch, “Discrete Hubbard-Stratonovich transformation for Fermion lattice models,” *Phys. Rev. B* **28**, 4059–4061 (1983).
- ¹⁰¹T. Shen, Y. Liu, Y. Yu, and B. M. Rubenstein, “Finite temperature auxiliary field quantum Monte Carlo in the canonical ensemble,” *J. Chem. Phys.* **153**, 204108 (2020).
- ¹⁰²R. D. Sedgewick, D. J. Scalapino, R. L. Sugar, and L. Capriotti, “Canonical and grand canonical ensemble expectation values from quantum Monte Carlo simulations,” *Phys. Rev. B* **68**, 045120 (2003).
- ¹⁰³C. N. Gilbreth, S. Jensen, and Y. Alhassid, “Reducing the complexity of finite-temperature auxiliary-field quantum Monte Carlo,” *Comput. Phys. Commun.* **264**, 107952 (2021).
- ¹⁰⁴P. Borrmann and G. Franke, “Recursion formulas for quantum statistical partition functions,” *J. Chem. Phys.* **98**, 2484–2485 (1993).
- ¹⁰⁵H. Barghathi, J. Yu, and A. Del Maestro, “Theory of noninteracting fermions and bosons in the canonical ensemble,” *Phys. Rev. Res.* **2**, 043206 (2020).
- ¹⁰⁶T. Shen, H. Barghathi, J. Yu, A. Del Maestro, and B. Rubenstein, “A stable, recursive auxiliary field quantum Monte Carlo algorithm in the canonical ensemble: Applications to thermometry and the Hubbard model,” *arXiv:2212.08654* (2022).
- ¹⁰⁷J. Yu, N. Sun, and H. Zhai, “Symmetry protected dynamical symmetry in the generalized Hubbard models,” *Phys. Rev. Lett.* **119**, 225302 (2017).
- ¹⁰⁸H. Zhai, N. Sun, J. Yu, and P. Zhang, “New relations between spin and charge dynamics of the Fermi Hubbard model,” *New J. Phys.* **21**, 015003 (2019).
- ¹⁰⁹C. N. Yang and S. C. Zhang, “SO₄ symmetry in a Hubbard model,” *Mod. Phys. Lett. B* **04**, 759–766 (1990).
- ¹¹⁰G.-S. Tian, “Particle-hole transformations and sum rules for the Hubbard model,” *Phys. Lett. A* **228**, 383–390 (1997).
- ¹¹¹T. D. Kieu and C. J. Griffin, “Monte Carlo simulations with indefinite and complex-valued measures,” *Phys. Rev. E* **49**, 3855–3859 (1994).
- ¹¹²A. Avella, F. Mancini, and T. Saikawa, “The 2-site Hubbard and *t*-*J* models,” *Eur. Phys. J. B* **36**, 445–473 (2003).
- ¹¹³O. I. Pătu, A. Klümper, and A. Foerster, “Quantum critical behavior and thermodynamics of the repulsive one-dimensional Hubbard model in a magnetic field,” *Phys. Rev. B* **101**, 035149 (2020).
- ¹¹⁴M. Takahashi and M. Imada, “Monte Carlo calculation of quantum systems. II. Higher order correction,” *J. Phys. Soc. Jpn.* **53**, 3765–3769 (1984).
- ¹¹⁵M. Suzuki, “Fractal decomposition of exponential operators with applications to many-body theories and Monte Carlo simulations,” *Phys. Lett. A* **146**, 319–323 (1990).
- ¹¹⁶K. Sakkos, J. Casulleras, and J. Boronat, “High order Chin actions in path integral Monte Carlo,” *J. Chem. Phys.* **130**, 204109 (2009).
- ¹¹⁷N. Prokofev, B. Svistunov, and I. Tupitsyn, “‘Worm’ algorithm in quantum Monte Carlo simulations,” *Phys. Lett. A* **238**, 253–257 (1998).
- ¹¹⁸M. Boninsegni, N. Prokofev, and B. V. Svistunov, “Worm algorithm for continuous-space path integral Monte Carlo simulations,” *Phys. Rev. Lett.* **96**, 070601 (2006).
- ¹¹⁹T. Dornheim, S. Groth, and M. Bonitz, “Permutation blocking path integral Monte Carlo simulations of degenerate electrons at finite temperature,” *Contrib. Plasma Phys.* **59**, e201800157 (2019).
- ¹²⁰W. von der Linden, “A quantum Monte Carlo approach to many-body physics,” *Phys. Rep.* **220**, 53–162 (1992).
- ¹²¹F. Šimkovic and R. Rossi, “Many-configuration Markov-chain Monte Carlo,” *arXiv:2102.05613* [physics.comp-ph] (2021).
- ¹²²H. Niederreiter, “Quasi-Monte Carlo methods and pseudo-random numbers,” *Bull. Am. Math. Soc.* **84**, 957–1041 (1978).
- ¹²³M. Maček, P. T. Dumitrescu, C. Bertrand, B. Triggs, O. Parcollet, and X. Waintal, “Quantum quasi-Monte Carlo technique for many-body perturbative expansions,” *Phys. Rev. Lett.* **125**, 047702 (2020).
- ¹²⁴C. Bertrand, D. Bauernfeind, P. T. Dumitrescu, M. Maček, X. Waintal, and O. Parcollet, “Quantum quasi Monte Carlo algorithm for out-of-equilibrium Green functions at long times,” *Phys. Rev. B* **103**, 155104 (2021).

Cumulant expansion in the Holstein model: Spectral functions and mobilityPetar Mitrić , Veljko Janković , Nenad Vukmirović , and Darko Tanasković *Institute of Physics Belgrade, University of Belgrade, Pregrevica 118, 11080 Belgrade, Serbia*

(Received 29 December 2022; revised 6 March 2023; accepted 17 March 2023; published 30 March 2023)

We examine the range of validity of the second-order cumulant expansion (CE) for the calculation of spectral functions, quasiparticle properties, and mobility of the Holstein polaron. We devise an efficient numerical implementation that allows us to make comparisons in a broad interval of temperature, electron-phonon coupling, and phonon frequency. For a benchmark, we use the dynamical mean-field theory which gives, as we have recently shown, rather accurate spectral functions in the whole parameter space, even in low dimensions. We find that in one dimension, the CE resolves well both the quasiparticle and the first satellite peak in a regime of intermediate coupling. At high temperatures, the charge mobility assumes a power law $\mu \propto T^{-2}$ in the limit of weak coupling and $\mu \propto T^{-3/2}$ for stronger coupling. We find that, for stronger coupling, the CE gives slightly better results than the self-consistent Migdal approximation (SCMA), while the one-shot Migdal approximation is appropriate only for a very weak electron-phonon interaction. We also analyze the atomic limit and the spectral sum rules. We derive an analytical expression for the moments in CE and find that they are exact up to the fourth order, as opposed to the SCMA where they are exact to the third order. Finally, we analyze the results in higher dimensions.

DOI: [10.1103/PhysRevB.107.125165](https://doi.org/10.1103/PhysRevB.107.125165)**I. INTRODUCTION**

The cumulant expansion (CE) method presents an alternative to the usual Dyson equation approach in the calculation of spectral functions of interacting quantum many-particle systems [1]. In this method, we express the Green's function in real time as an exponential function of an auxiliary quantity $C(t)$, called the cumulant, which can be calculated perturbatively [2]. In the late 1960s, it was established that the lowest order CE gives the exact solution of the problem of a core hole coupled to bosonic excitations (plasmons or phonons) [3,4]. While there were early papers that emphasized the potential role of CE as an approximate method to treat the electronic correlations in metals beyond the *GW* approximation [5–8] and the electron-phonon interaction in semiconductors and narrow band metals beyond the Migdal approximation (MA) [9–11], a surge of studies of CE has appeared only recently.

Renewed interest has emerged due to the possibility of combining CE with *ab initio* band-structure calculations. The CE for the electron-phonon interaction was used to obtain the spectral functions of several doped transition-metal oxides [12,13], showing a favorable comparison with angle-resolved photoemission spectroscopy [14]. A particularly appealing feature of the CE approach is that it describes the quasiparticle part of the spectrum as well as the satellite structure (sidebands). Combining the CE with the Kubo formula for charge transport gives an attractive route to calculate mobility in semiconductors beyond the Boltzmann approach, which is applicable only for weak electron-phonon coupling [15]. This was very recently demonstrated for SrTiO₃ [16] and naphthalene [17]. CE was also applied to elemental metals where a correction to the standard MA is discussed [18]. Similarly, the CE is successfully used to treat the electronic correlations beyond the *GW* approximation [19–25]. Further-

more, CE was used to study absorption spectra in molecular aggregates representative of photosynthetic pigment-protein complexes [26–28].

Despite the wide use of the lowest order CE, there seems to be a lack of studies establishing its range of validity, which represents the central motivation for this paper. To achieve this, we turn to simplified models of the electron-phonon interaction. CE for the Fröhlich model [29,30] gives the ground-state energy and the effective mass similar to the exact quantum Monte Carlo calculations for moderate interaction [31]. This is in contrast to the Dyson-Migdal approach, which severely underestimates mass renormalization. A comparison of the corresponding spectral functions is, however, missing, since reliable quantum Monte Carlo results are not available due to the well-known problems with analytical continuation. The Holstein polaron model gives a unique opportunity to explore the applicability of the CE since various numerically exact methods are developed and applied to this model covering different parameter regimes [32–49]. This was the approach of a very recent work by Reichman and collaborators [50,51]. Still, there are several questions that remained unresolved. Most importantly, a comparison of spectral functions was made just for a small set of parameters on a finite-size lattice, where the benchmark spectral functions were available from the finite-temperature Lanczos results, while the charge transport was not examined.

In our recent work [52], we established that the dynamical mean-field theory (DMFT) [53] gives close to exact spectral functions of the Holstein polaron for different phonon frequencies, electron-phonon couplings, and temperatures even in low dimensions, covering practically the whole parameter space. This method is computationally very fast and precise, which makes us ideally positioned to perform comprehensive comparisons with the CE method, which is the goal of

this paper. Within the CE, we calculate the spectral functions and charge mobility for a broad set of parameters and make detailed comparisons with DMFT and (self-consistent) MA. We find that the one-shot MA is appropriate only for very weak electron-phonon coupling. The validity of the CE and self-consistent Migdal approximation (SCMA) is much broader and for intermediate interaction CE even outperforms SCMA. We also derive analytical CE expressions for the ground-state energy, renormalized mass, and scattering rate as well as the spectral sum rules, and make comparisons between the methods. We establish a power-law behavior for the charge mobility at high temperatures. We also compare the performance of different methods as the bandwidth is reduced toward the atomic limit.

The remaining part of the paper is organized as follows. In Sec. II, we introduce the CE method and present details of its implementation on the Holstein model. DMFT and SCMA are here introduced as benchmark methods. Representative spectral functions are shown in Sec. III from weak toward the strong coupling. The high-temperature and atomic limits are analyzed in detail, as well as the spectral sum rules. In Sec. IV, we present the results for the effective mass and ground-state energy. The temperature dependence of the electron mobility is analyzed in Sec. V, and Sec. VI contains our conclusions. Some details concerning numerical implementations and additional figures for various parameters are shown in the Appendix and in the Supplemental Material (SM) [54].

II. MODEL AND METHODS

The Holstein model is the simplest model of the lattice electrons interacting with the phonons. It assumes a local electron-phonon interaction and dispersionless phonons. The Hamiltonian is given by

$$H = -t_0 \sum_{\langle ij \rangle} (c_i^\dagger c_j + \text{H.c.}) - g \sum_i n_i (a_i^\dagger + a_i) + \omega_0 \sum_i a_i^\dagger a_i. \quad (1)$$

Here, t_0 is the hopping parameter between the nearest neighbors and ω_0 is the phonon frequency. c_i and a_i are the electron and the phonon annihilation operators, $n_i = c_i^\dagger c_i$, and g denotes the electron-phonon coupling strength. We set \hbar, k_B , elementary charge e , and lattice constant to 1. We also often use a parameter $\alpha = g/\omega_0$. We study the model in the thermodynamic limit (number of sites $N \rightarrow \infty$). Furthermore, we consider a dynamics of a single electron in the conduction band and treat the electrons as spinless, since we are interested only in weakly doped semiconductors. This is equivalent to setting the chemical potential far below the conduction band, i.e., considering the limit $\tilde{\mu} \rightarrow -\infty$. This case is often referred to as the Holstein polaron problem. We mostly focus on the one-dimensional (1D) system, but we also consider the system in 2D and 3D.

A. Cumulant expansion

1. General theory

The central quantity of this paper is the electron spectral function $A_{\mathbf{k}}(\omega) = (-1/\pi)\text{Im}G_{\mathbf{k}}(\omega)$, where \mathbf{k} is the momen-

tum and $G_{\mathbf{k}}(\omega)$ is the retarded Green's function in frequency domain [1]. Its exact evaluation is often a formidable task, which is why approximate techniques are usually employed. One needs to be careful with such approaches not to violate some analytic properties, such as the pole structure of the Green's function, the positivity of the spectral function, or the spectral sum rules. At least some of these properties can be easily satisfied if the Green's function is not calculated directly but instead through some auxiliary quantity, such as the self-energy $\Sigma_{\mathbf{k}}(\omega)$. In the latter case, the connection with the Green's function is established via the Dyson equation

$$G_{\mathbf{k}}(\omega) = \frac{1}{G_{\mathbf{k},0}(\omega)^{-1} - \Sigma_{\mathbf{k}}(\omega)} = \frac{1}{\omega - \varepsilon_{\mathbf{k}} - \Sigma_{\mathbf{k}}(\omega)}, \quad (2)$$

where $G_{\mathbf{k},0}(\omega)$ is the noninteracting Green's function and $\varepsilon_{\mathbf{k}}$ is the noninteracting dispersion relation.

An alternative to the Dyson equation based approaches is the so-called cumulant expansion method [19], in which the exponential ansatz is chosen for the Green's function in the time domain:

$$G_{\mathbf{k}}(t) = G_{\mathbf{k},0}(t)e^{C_{\mathbf{k}}(t)} = -i\theta(t)e^{-i\varepsilon_{\mathbf{k}}t}e^{C_{\mathbf{k}}(t)}. \quad (3)$$

Here, $\theta(t)$ is the Heaviside step function and $C_{\mathbf{k}}(t)$ plays the role of an auxiliary quantity which is called the cumulant. Both Eqs. (2) and (3) would correspond to the same Green's function in frequency and time domain if the cumulant $C_{\mathbf{k}}(t)$ and the self-energy $\Sigma_{\mathbf{k}}(\omega)$ could be evaluated exactly [1]. In practice, however, one of these approaches is expected to perform better. The spectral function within the CE can be obtained as follows:

$$A_{\mathbf{k}}(\omega + \varepsilon_{\mathbf{k}}) = \frac{1}{\pi} \text{Re} \int_0^\infty dt e^{i\omega t} e^{C_{\mathbf{k}}(t)}. \quad (4)$$

Equation (4) circumvents the Fourier transform of the whole Green's function $A_{\mathbf{k}}(\omega) = -\frac{1}{\pi}\text{Im}G_{\mathbf{k}}(\omega)$, which is useful in practice, as the free electron part $e^{-i\varepsilon_{\mathbf{k}}t}$ typically oscillates much more quickly than $e^{C_{\mathbf{k}}(t)}$.

The expression for $C_{\mathbf{k}}(t)$ in the lowest order perturbation expansion can be obtained by taking the leading terms in the Taylor expansion of the Dyson equation $G_{\mathbf{k}}(\omega) = (G_{\mathbf{k},0}(\omega)^{-1} - \Sigma_{\mathbf{k}}(\omega))^{-1} \approx G_{\mathbf{k},0}(\omega) + G_{\mathbf{k},0}(\omega)\Sigma_{\mathbf{k}}(\omega)G_{\mathbf{k},0}(\omega)$, taking its inverse Fourier transform and equating it to Eq. (3), where the cumulant in the exponent is replaced with its linear approximation $e^{C_{\mathbf{k}}(t)} \approx 1 + C_{\mathbf{k}}(t)$:

$$C_{\mathbf{k}}(t) = ie^{i\varepsilon_{\mathbf{k}}t} \int_{-\infty}^{\infty} \frac{d\omega}{2\pi} \frac{e^{-i\omega t} \Sigma_{\mathbf{k}}(\omega)}{(\omega - \varepsilon_{\mathbf{k}} + i0^+)^2}. \quad (5)$$

Using the spectral representation of the self-energy

$$\Sigma_{\mathbf{k}}(\omega) = \int \frac{d\nu}{\pi} \frac{|\text{Im}\Sigma_{\mathbf{k}}(\nu)|}{\omega - \nu + i0^+}, \quad (6)$$

and the contour integration over ω , Eq. (5) simplifies to [19]

$$C_{\mathbf{k}}(t) = \frac{1}{\pi} \int_{-\infty}^{\infty} d\omega \frac{|\text{Im}\Sigma_{\mathbf{k}}(\omega + \varepsilon_{\mathbf{k}})|}{\omega^2} (e^{-i\omega t} + i\omega t - 1). \quad (7)$$

The corresponding spectral function satisfies the first two sum rules, irrespective of $\Sigma_{\mathbf{k}}(\omega)$. This is a consequence of the behavior of $C_{\mathbf{k}}(t)$ for small t ; see Sec. III C. In general, $C_{\mathbf{k}}(t=0) = 0$ is sufficient for the first spectral sum rule $\int A_{\mathbf{k}}(\omega)d\omega = 1$ to be satisfied. The second sum rule

$\int A_{\mathbf{k}}(\omega)\omega d\omega = \varepsilon_{\mathbf{k}}$ can also be satisfied if we additionally impose that the cumulant's first derivative at $t = 0$ is vanishing, $\frac{dC_{\mathbf{k}}}{dt}(0) = 0$. Both of these conditions are satisfied by the cumulant function in Eq. (7), as it is a quadratic function of time for small arguments $e^{-i\omega t} + i\omega t - 1 \approx -\omega^2 t^2/2$ for $t \rightarrow 0$.

The application of Eq. (7) is facilitated by the fact that it does not contain any iterative self-consistent calculations. However, one needs to overcome the numerical challenges caused by the removable singularity at $\omega = 0$ and by the rapidly oscillating trigonometric factor $e^{-i\omega t}$ for large t . The latter is important for the weak electron-phonon couplings, where it is necessary to propagate $C_{\mathbf{k}}(t)$ up to long times until the Green's function is sufficiently damped out. The same problem occurs in other regimes as well (e.g., close to the atomic limit), where the Green's function does not attenuate at all; see Sec. II A 4.

The numerical singularity at $\omega = 0$ can be completely avoided if we consider the cumulant's second derivative

$$\frac{d^2 C_{\mathbf{k}}(t)}{dt^2} = \int_{-\infty}^{\infty} \frac{d\omega}{\pi} \text{Im} \Sigma_{\mathbf{k}}(\omega + \varepsilon_{\mathbf{k}}) e^{-i\omega t} \equiv 2e^{i\varepsilon_{\mathbf{k}} t} \tilde{\sigma}_{\mathbf{k}}(t), \quad (8)$$

where we used $\text{Im} \Sigma_{\mathbf{k}}(\omega) < 0$ and introduced $\tilde{\sigma}_{\mathbf{k}}(t) \equiv \int_{-\infty}^{\infty} \text{Im} \Sigma_{\mathbf{k}}(\omega) e^{-i\omega t} \frac{d\omega}{2\pi}$. Then, $C_{\mathbf{k}}(t)$ is obtained as a double integral over time of Eq. (8),

$$C_{\mathbf{k}}(t) = 2 \int_0^t dt' \int_0^{t'} dt'' e^{i\varepsilon_{\mathbf{k}} t''} \tilde{\sigma}_{\mathbf{k}}(t''), \quad (9)$$

where the lower boundaries of both integrals have to be zero, as guaranteed by the initial conditions $C_{\mathbf{k}}(0) = \frac{dC_{\mathbf{k}}}{dt}(0) = 0$. Using the Cauchy formula for repeated integration, this can also be written as a single integral:

$$C_{\mathbf{k}}(t) = 2 \int_0^t (t-x) e^{i\varepsilon_{\mathbf{k}} x} \tilde{\sigma}_{\mathbf{k}}(x) dx. \quad (10)$$

This completely removed the problem of numerical singularities. Still, the problem of rapid oscillations of the subintegral function remains due to the presence of $e^{i\varepsilon_{\mathbf{k}} x}$ term. In Sec. II A 3, we provide an elegant solution for this issue, focusing on the case of the Holstein model.

2. Asymptotic expansion for cumulant when $t \rightarrow \infty$

The asymptotic expansion of $C_{\mathbf{k}}(t)$ for large times, as we now demonstrate, completely determines the quasiparticle properties within this method. This is one of the main motivations for studying the $t \rightarrow \infty$ limit. From Eq. (8), we see that

$$\begin{aligned} i \frac{dC_{\mathbf{k}}}{dt}(t \rightarrow \infty) &= i \int_0^{\infty} \frac{d^2 C_{\mathbf{k}}(t)}{dt^2} dt \\ &= -\frac{i}{\pi} \int_{-\infty}^{\infty} d\omega |\text{Im} \Sigma_{\mathbf{k}}(\omega + \varepsilon_{\mathbf{k}})| \int_0^{\infty} dt e^{-i\omega t} \\ &= \Sigma_{\mathbf{k}}(\varepsilon_{\mathbf{k}}), \end{aligned} \quad (11)$$

where we used the identity $\int_0^{\infty} dt e^{-i\omega t} = \pi \delta(\omega) - i\mathcal{P}\frac{1}{\omega}$ and the Kramers-Kronig relations for the self-energy. Hence, the cumulant function $C_{\mathbf{k}}(t)$, and also the whole exponent in Eq. (3) is a linear function of time $C_{\mathbf{k}}(t) - i\varepsilon_{\mathbf{k}} t \approx -i\tilde{E}_{\mathbf{k}} t +$

const for $t \rightarrow \infty$, where

$$\tilde{E}_{\mathbf{k}} = \varepsilon_{\mathbf{k}} + \Sigma_{\mathbf{k}}(\varepsilon_{\mathbf{k}}). \quad (12)$$

As a consequence, the Green's function in Fourier space has a simple pole situated at $\tilde{E}_{\mathbf{k}}$, as seen from the following expression:

$$G_{\mathbf{k}}(\omega) = -i \int_0^{\infty} e^{it(\omega - \varepsilon_{\mathbf{k}} - \frac{iC_{\mathbf{k}}(t)}{t})} dt. \quad (13)$$

Therefore, quasiparticle properties are encoded in $\tilde{E}_{\mathbf{k}}$: its real and imaginary parts correspond to the quasiparticle energy and scattering rate, respectively. We note that, in our present analysis, we implicitly assumed that $\frac{dC_{\mathbf{k}}}{dt}(t \rightarrow \infty)$ exists and is finite. Although this is generally true, there are a few exceptions. In the Holstein model, the first assumption is violated at the atomic limit [$t_0 = 0$; see Eq. (28)], while the second assumption is violated at the adiabatic limit ($\omega_0 = 0$) for $k = 0$ or $k = \pm\pi$; see Eqs. (18) or (19).

The knowledge that we gained about the analytic properties of the $C_{\mathbf{k}}(t)$ provides us with an intuitive understanding of how the shape of the cumulant determines the shape of the spectral function. The asymptotic limits $t \rightarrow \infty$ [where $C_{\mathbf{k}}(t)$ is linear] and $t \rightarrow 0$ [where $C_{\mathbf{k}}(t)$ is quadratic] by themselves, to a large extent, describe only the simple one-peak spectral functions, while the crossover between these limits is responsible for the emergence of satellite peaks. This can be explained as follows: If the cumulant was quadratic over the whole t domain $C_{\mathbf{k}}(t) = ct^2$, the spectral function would have a simple Gaussian shape. Similarly, the Lorentzian shape would be obtained from the linear cumulant $C_{\mathbf{k}}(t) = ct$. This suggests that the simple crossover between quadratic (at small t) and linear (at large t) behaviors would also give a simple one-peak shape of the spectral function. The information about phonon satellites is thus completely encoded in the $C_{\mathbf{k}}(t)$ for intermediate times t , which depends on the system and approximation in which the cumulant function is calculated.

3. Second-order cumulant expansion for the Holstein model

Let us now concentrate on a specific example, the Holstein model on a hypercubic lattice in n dimensions. The second-order cumulant is given by Eq. (7), where the self-energy is taken to be in the MA $\Sigma_{\mathbf{k}}(\omega) = \Sigma_{\mathbf{k}}^{\text{MA}}(\omega)$, i.e., of the second (lowest) order with respect to the electron-phonon coupling g . This is in accordance with the derivation from Sec. II A 1, since we restricted ourselves to the lowest order terms in the Taylor expansion of the Dyson equation and of $e^{C_{\mathbf{k}}(t)}$. An alternative derivation of this expression is given in Sec. I of the SM [54]. MA is briefly discussed in Sec. II B 1. For our present purpose, we only need the expression for the imaginary part of the self-energy

$$\text{Im} \Sigma_{\mathbf{k}}^{\text{MA}}(\omega) = -\pi g^2 [(n_{\text{ph}} + 1)\rho(\omega - \omega_0) + n_{\text{ph}}\rho(\omega + \omega_0)], \quad (14)$$

where $n_{\text{ph}} = 1/(e^{\omega_0/T} - 1)$ is the Bose factor, $\rho(\omega) = \frac{1}{N} \sum_{\mathbf{k}} \delta(\omega - \varepsilon_{\mathbf{k}})$ is the density of electron states for the system of size N , which we take in the thermodynamic limit $N \rightarrow \infty$, and $\varepsilon_{\mathbf{k}} = -2t_0 \sum_{j=1}^n \cos k_j$ is the noninteracting dispersion relation.

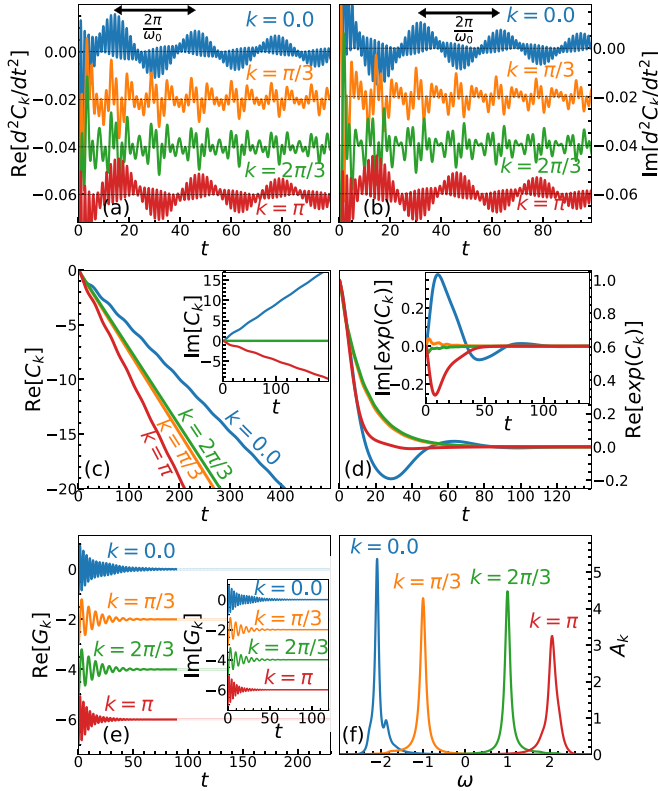


FIG. 1. (a)–(f) The cumulant, Green's, and spectral function on the example of the one-dimensional Holstein model with the following values of the model parameters: $\omega_0 = 0.2$, $g = 0.2$, $T = 0.3$, and $t_0 = 1$.

The expression for the cumulant function, as seen from Eq. (10), is related to the inverse Fourier transform of $\text{Im}\Sigma^{\text{MA}}(\omega)$, which in turn is completely determined by the inverse Fourier transform of the density of states $\tilde{\rho}(t)$. The latter admits a closed-form solution

$$\begin{aligned} \tilde{\rho}(t) &= \int_{-\infty}^{\infty} \frac{d\omega e^{-i\omega t}}{(2\pi)^{n+1}} \int_{|0, 2\pi)^n} d^n \mathbf{k} \delta\left(\omega + 2t_0 \sum_{j=1}^n \cos k_j\right) \\ &= \frac{1}{2\pi} \left(\frac{1}{2\pi} \int_0^{2\pi} dk e^{2it_0 t \cos k} \right)^n = \frac{J_0(2t_0 t)^n}{2\pi}, \end{aligned} \quad (15)$$

where J_0 is the Bessel function of the first kind of order zero. Hence, Eqs. (10), (14), and (15) imply that the cumulant function can be written as

$$C_{\mathbf{k}}(t) = -g^2 \int_0^t dx (t-x) iD(x) e^{ix\varepsilon_{\mathbf{k}}} J_0(2t_0 x)^n, \quad (16)$$

where $iD(t) = (n_{\text{ph}} + 1)e^{-i\omega_0 t} + n_{\text{ph}}e^{i\omega_0 t}$ is the phonon propagator in real time (for $t > 0$). In Fig. 1, we illustrate the cumulant function, as well as the corresponding Green's function and spectral function. Figures 1(a) and 1(b) show the second derivative of the cumulant

$$\frac{d^2 C_{\mathbf{k}}(t)}{dt^2} = -g^2 iD(t) e^{it\varepsilon_{\mathbf{k}}} J_0(2t_0 t)^n \quad (17)$$

to demonstrate the rapid oscillations that are also present in the cumulant itself. These are not easily observed by inspect-

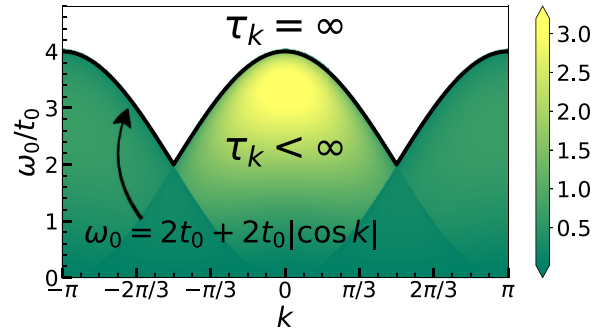


FIG. 2. Quasiparticle lifetime $\tau_{\mathbf{k}}$ in the CE method for $T/t_0 = 2$ and $g/t_0 = 1$.

ing $C_{\mathbf{k}}(t)$ directly, as the linear behavior dominates for large times. We observe that the $k = 0$ and $k = \pi$ results possess an oscillating envelope with period $2\pi/\omega_0$, while intermediate momenta have a much less regular structure. This can have direct consequences on the spectral functions, as the satellite peaks are expected to be at a distance ω_0 from each other. To be more explicit, oscillating envelopes suggest that there is a much higher chance for the occurrence of satellite peaks near the bottom ($k \approx 0$) and the top ($k \approx \pi$) of the band, than otherwise. However, that does not guarantee that the satellite peaks will in fact occur. Figure 1(c) shows that $\text{Re}C_{\mathbf{k}}(t)$ is declining faster for $k > 0$ than for $k = 0$. As a consequence, $e^{C_{\mathbf{k}}(t)}$ in Fig. 1(d) attenuates slower for $k = 0$, having enough time to complete a full period, while $k = \pi$ results are reminiscent of an overdamped oscillator. A similar, although much less evident, effect can be seen in the Green's function itself; see Fig. 1(e). This is why the $k = \pi$ spectral function in Fig. 1(f) has a simple one-peak shape, while only the $k = 0$ result captures one small satellite peak.

From a numerical point of view, Eq. (16) is treated using Levin's collocation method [55], which is reviewed in Appendix A. It provides a controlled, accurate, and numerically efficient way to integrate the product of trigonometric, Bessel, and some slowly varying function. This approach avoids using a dense t grid, which would otherwise be required, as the subintegral function in Eq. (16) has the same type of rapid oscillations present in $d^2 C_{\mathbf{k}}(t)/dt^2$.

4. Lifetime

Another question of practical importance is how long we should propagate the cumulant function in real time until the corresponding Green's function attenuates. A rough estimate of such quantity is given by the quasiparticle lifetime $\tau_{\mathbf{k}}$. The lifetime is given by $\tau_{\mathbf{k}} = 1/(2|\text{Im}\tilde{E}_{\mathbf{k}}|)$, where $\tilde{E}_{\mathbf{k}}$ is given by Eq. (12) and the self-energy is taken in the MA [see Eq. (14)]:

$$\begin{aligned} \tau_{\mathbf{k}}^{-1} &= 2|\text{Im}\tilde{E}_{\mathbf{k}}| = 2g^2 \frac{\theta(4t_0^2 - (\varepsilon_{\mathbf{k}} - \omega_0)^2)}{\sqrt{4t_0^2 - (\varepsilon_{\mathbf{k}} - \omega_0)^2}} (n_{\text{ph}} + 1) \\ &\quad + 2g^2 \frac{\theta(4t_0^2 - (\varepsilon_{\mathbf{k}} + \omega_0)^2)}{\sqrt{4t_0^2 - (\varepsilon_{\mathbf{k}} + \omega_0)^2}} n_{\text{ph}}. \end{aligned} \quad (18)$$

This is illustrated in Fig. 2. We observe that there is a considerable part of the parameter space where the lifetime is

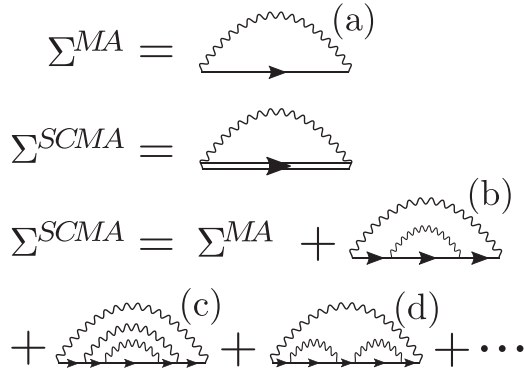


FIG. 3. Feynman diagrams in the Migdal approximation and the self-consistent Migdal approximation.

infinite, which means that the corresponding Green's function never attenuates. This occurs for $\omega_0 > 2t_0 + 2t_0|\cos k|$ in the case of finite temperatures, and for $\omega_0 > 4t_0 \sin^2 k/2$ in the $T = 0$ case. In these regimes, one could presume that this is reflected in the spectral functions through the appearance of Dirac delta peaks, which is not expected at finite temperatures. This illustrates one of the limitations of this method.

B. Benchmark methods

1. Migdal and self-consistent Migdal approximation

The Migdal approximation [56] is the simplest perturbation approach, whose self-energy is represented with a single, lowest order Feynman diagram, as shown in Fig. 3(a). The imaginary part of the self-energy is given by Eq. (14) in the case when there is just a single electron in the band, regardless of the dispersion relation or the number of dimensions of the system. The corresponding real part is obtained using the Kramers-Kronig relations, and in 1D reads as

$$\begin{aligned} \text{Re}\Sigma^{\text{MA}}(\omega) &= g^2(n_{\text{ph}} + 1) \frac{\theta((\omega - \omega_0)^2 - 4t_0^2) \text{sgn}(\omega - \omega_0)}{\sqrt{(\omega - \omega_0)^2 - 4t_0^2}} \\ &+ g^2 n_{\text{ph}} \frac{\theta((\omega + \omega_0)^2 - 4t_0^2) \text{sgn}(\omega + \omega_0)}{\sqrt{(\omega + \omega_0)^2 - 4t_0^2}}. \end{aligned} \quad (19)$$

The range of validity of the MA can be extended if we substitute the noninteracting electron propagator in Fig. 3(a) with an interacting one. At the same time, the interacting propagator itself is expressed through the self-energy via the Dyson equation. These relations constitute the SCMA. Figure 3 illustrates that the SCMA self-energy consists of a series of noncrossing diagrams, whose lowest order coincides with the MA. Figure 3(b) shows the second-order contribution, while the third-order contributions are shown in Figs. 3(c) and 3(d).

Mathematically, the self-consistency relations are straightforwardly derived and, in our case, read as

$$\Sigma^{\text{SCMA}}(\omega) = g^2(n_{\text{ph}} + 1)G(\omega - \omega_0) + g^2 n_{\text{ph}} G(\omega + \omega_0), \quad (20a)$$

$$G(\omega) = \frac{1}{(2\pi)^n} \int_{-\pi}^{\pi} d^n \mathbf{k} \frac{1}{\omega - \varepsilon_{\mathbf{k}} - \Sigma^{\text{SCMA}}(\omega)}, \quad (20b)$$

where $G(\omega)$ is the local Green's function. We see that in the case of the Holstein model, the SCMA self-energy is \mathbf{k} independent.

2. Dynamical mean-field theory

Dynamical mean-field theory is a nonperturbative approximate method, that represents a natural generalization of the traditional mean-field theory [57]. It simplifies the original lattice problem by mapping it to a single site impurity problem, embedded into an external bath that is described with a frequency-dependent (i.e., dynamical) field $G_0(\omega)$, which needs to be determined self-consistently. This simplification is reflected on the self-energy, which is assumed to be \mathbf{k} -independent $\Sigma_{\mathbf{k}}(\omega) = \Sigma(\omega)$. The DMFT becomes exact in the limit of infinite dimensions or, equivalently, infinite coordination number.

In practice, $G_0(\omega)$ and $\Sigma(\omega)$ are determined self-consistently, by imposing that the local Green's function of the lattice problem

$$G(\omega) = \int_{-\infty}^{\infty} \frac{\rho(\epsilon)d\epsilon}{\omega - \Sigma(\omega) - \epsilon}, \quad (21)$$

and the self-energy $\Sigma(\omega)$ coincide with the corresponding quantities of the impurity problem. Here, $\rho(\epsilon)$ is the noninteracting density of states. The self-consistent loop is closed using the Dyson equation $G_0(\omega) = (G^{-1}(\omega) + \Sigma(\omega))^{-1}$. In the case of the Holstein model, the (polaron) impurity problem can be solved exactly, directly on the real-frequency axis, in terms of the continued fraction expansion [53]. Furthermore, in the one-dimensional case, Eq. (21) assumes a closed-form solution and reads as

$$G(\omega) = \text{Re} \frac{1}{2t_0 B(\omega) \sqrt{1 - \frac{1}{B(\omega)^2}}} + i \text{Im} \frac{-i}{2t_0 \sqrt{1 - B(\omega)^2}}, \quad (22)$$

where $B(\omega) = (\omega - \Sigma(\omega))/(2t_0)$; see Supplemental Material of Ref. [52]. We note that Eq. (22) can also be used for the SCMA in Eq. (20).

We have very recently shown [52], by using extensive comparisons with several numerically exact methods covering various parameter regimes, that the DMFT can provide a rather accurate solution for the Holstein polaron even in low dimension. Hence, the DMFT has emerged as a unique numerical method that gives close to exact spectral functions in practically the whole space of parameters, irrespective of the number of dimensions. This makes the DMFT an ideal benchmark method for comparisons with the CE results for the Holstein model.

III. SPECTRAL FUNCTIONS

In this section, we present the CE spectral functions of the 1D Holstein model. The DMFT is used as a benchmark, while MA and SCMA represent the main competitors and alternatives to the CE method. Section III A shows the results for $k = 0$, whereas heat plots and the $k = \pi$ results are shown in Sec. III B. High-temperature spectral functions and spectral sum rules are presented in Sec. III C. The behavior near the atomic limit is discussed in Sec. III D. We present only

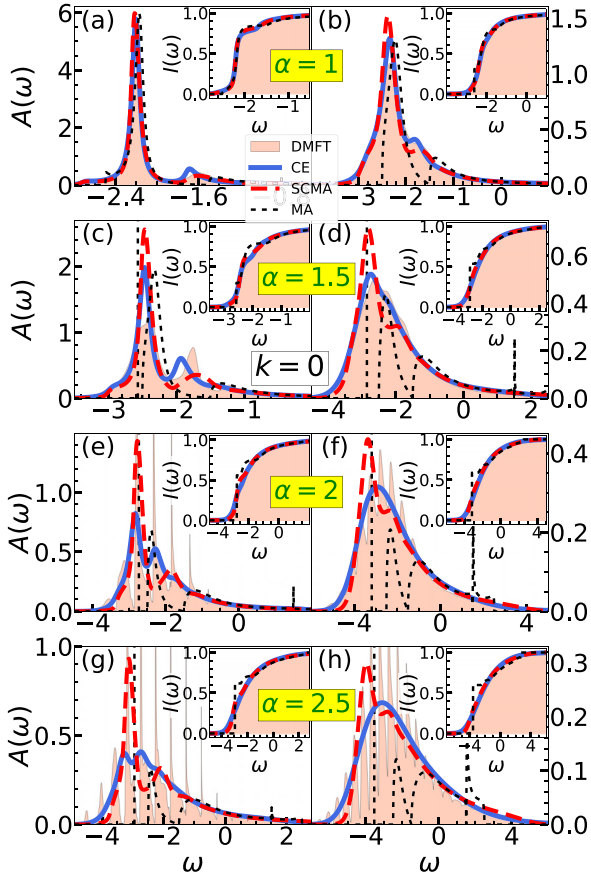


FIG. 4. (a)–(h) Spectral functions for $t_0 = 1$, $\omega_0 = 0.5$ and $k = 0$. In the left panels $T = 0.3$, while $T = 0.7$ in the right panels. Insets show the integrated spectral weights $I_k(\omega) = \int_{-\infty}^{\omega} A_k(v) dv$.

the results for $\omega_0 = 0.5$, while the results for other phonon frequencies and various momenta are shown in Sec. II of SM [54]. The 2D spectral functions are presented in Appendix B.

A. Low and intermediate temperatures for $k = 0$

In the weak-coupling limit $\alpha \rightarrow 0$, all these approximate methods (DMFT, CE, SCMA, MA) provide accurate results. In Fig. 4, we investigate how far from this strict limit each of our methods continues to give reasonably accurate spectral functions. In Fig. 4(a), we see that for $\alpha = 1$ all methods correctly capture the quasiparticle peak, which dominates in the structure of the spectrum. The MA satellite peak is slightly shifted towards higher frequencies, which becomes significantly more pronounced at higher temperatures; see Fig. 4(b). The limitations of the MA become more obvious for stronger couplings, where even the position and weight of the quasiparticle peak are inaccurate; see Figs. 4(c)–4(h).

While the quasiparticle properties of the CE and SCMA seem to be quite similar if α is not too large, some difference in satellite peaks is already visible in Figs. 4(b) and 4(c). Figure 4(c) shows that SCMA gives broader satellites than the DMFT benchmark, whereas CE slightly underestimates the position of the satellite. Neither CE nor SCMA can be characterized as distinctly better in this regime. On the other hand, Figs. 4(e) and 4(g) display a clear advantage of the CE.

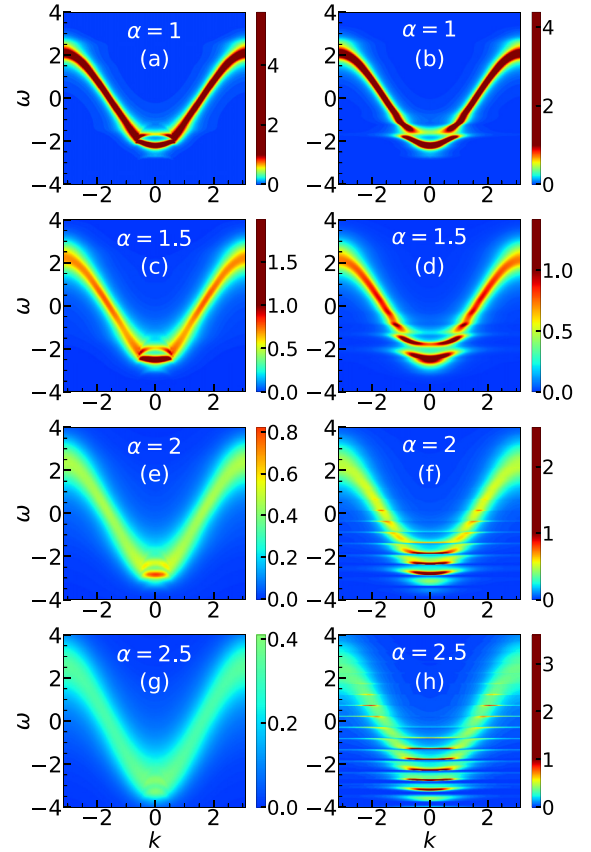


FIG. 5. (a)–(h) Heat maps of $A_k(\omega)$ for $t_0 = 1$, $\omega_0 = 0.5$, and $T = 0.3$. In the left panels, we present CE results, while the DMFT benchmark is presented in the right panel. All plots use the same color coding.

We see that it captures rather well the most distinctive features of the solutions, which are the first few satellites. This is not the case for SCMA.

Figures 4(f) and 4(h) demonstrate that the CE gives a rather quick crossover toward the high-temperature limit, as it predicts a simple broad one-peak structure for the spectral function already for $T = 0.7$. This large difference between the spectral functions for $T_1 = 0.3$ and $T_2 = 0.7$ can be understood by examining the ratio of their corresponding lifetimes $\tau(T_1)/\tau(T_2) = n_{\text{ph}}(T_2)/n_{\text{ph}}(T_1) \approx 8.5$. This implies that $\text{Re}C_k(t)$ for $T = 0.7$ has a much steeper slope as a function time, which suppresses the appearance of satellites, as explained in Sec. II A 3.

B. Low and intermediate temperatures for $k \neq 0$

To proceed with the analysis of the CE, we want to answer: (i) Whether the conclusions that we reached for $k = 0$ can be carried over to other momenta as well? (ii) Does CE continue to be better than SCMA at much higher temperatures? The first question is answered in Fig. 5, where we compare CE and DMFT heat plots. Figures 5(a) and 5(b) demonstrate that CE results are quite reminiscent of the DMFT results for $\alpha = 1$, even at nonzero momenta. The same conclusion holds for weaker couplings as well. On the other hand, there are differences between the results for somewhat stronger

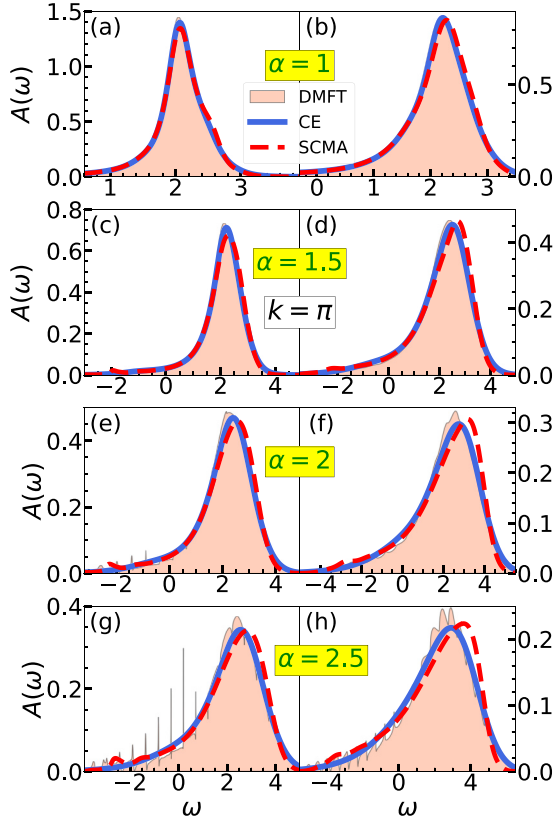


FIG. 6. (a)–(h) Spectral functions for $t_0 = 1$, $\omega_0 = 0.5$, and $k = \pi$. In the left panels $T = 0.3$, while $T = 0.7$ in the right panels.

coupling $\alpha = 1.5$, as shown in Figs. 5(c) and 5(d). While the polaron bands in both of these figures are convex, the CE predicts the first satellite to be concave, unlike the DMFT. In other words, CE predicts that the distance between the polaron peak and the satellites decreases as we increase the momentum. This is counterintuitive, as the satellites are perceived as the quasiparticle that absorbed or emitted a phonon, which should consequently be just at energy distance ω_0 apart. These limitations of the CE are much more pronounced for stronger electron-phonon couplings. While the DMFT solution in Figs. 5(f) and 5(h) exhibits a series of distinct bands, Figs. 5(e) and 5(g) demonstrate that the polaron and satellite bands of the CE merge into a single band at higher momenta. However, the most noticeable feature here is the fact that the CE is too smeared, as if the temperature is too high. This is a consequence of the fact that the lifetime in Eq. (18) scales as $\tau_{\mathbf{k}} \sim 1/g^2$. While the heat maps reveal noticeable discrepancies between the DMFT and CE for $k \neq 0$, it seems that these differences are much less pronounced around $k = \pi$. A more detailed comparison is presented in Fig. 6 that shows the results for the same regimes as in Fig. 4. The DMFT solution in Figs. 6(a)–6(d) shows that the main feature of the spectral function is a single broad peak for $\alpha \lesssim 1.5$, which is in agreement with the CE results. This is also the case for the SCMA, although we observe a slight tendency of the main peak to lean toward higher frequencies at higher temperatures. For larger interaction strengths, CE cannot fully reproduce the sharp peaks at lower frequencies of the low-temperature spectral function or the fine structure of the main peak at higher

temperatures; see Figs. 4(e)–4(h). Similarly, CE misses the quasiparticle peak as well, situated at low energy, although it is typically tiny and not (clearly) visible in Figs. 6(a)–6(h) (see Appendix C). A detailed comparison of the spectral functions for other momenta and phonon frequencies is presented in Sec. II of the SM [54].

Overall, we find that the CE gives the most accurate results for $k = 0$ and $k = \pi$ and that it is less accurate for other momenta. Although it cannot fully reproduce a tiny quasiparticle peak for $k = \pi$, it describes well a wide single-peak structure, which is the most prominent feature of the spectrum. A much larger discrepancy for $k = \pi$, between the CE and a reliable benchmark, was reported in Ref. [50] by examining the system on a finite lattice system with $N = 6$. In Appendix C, we examine the same parameter regime as in Ref. [50] and show that these discrepancies are significantly reduced in the thermodynamic limit.

C. Spectral functions at high temperatures and spectral sum rules

In Fig. 7, we show CE, SCMA, and DMFT spectral functions at high temperatures for the same electron-phonon couplings as in Figs. 4 and 6. We see that CE performs very well both for $k = 0$ and $k = \pi$. There are only small discrepancies at stronger interactions [see, e.g., Fig. 7(c)]. In contrast, the SCMA solution gets tilted relative to the DMFT and CE. In addition, it poorly reproduces the low-frequency part of the spectrum. It is not obvious whether the CE method is exact in the high-temperature limit $T \rightarrow \infty$. As we now demonstrate, this can be answered by examining the spectral sum rules:

$$\mathcal{M}_n(\mathbf{k}) = \int_{-\infty}^{\infty} A_{\mathbf{k}}(\omega) \omega^n d\omega. \quad (23)$$

These can be calculated both exactly,

$$\mathcal{M}_n^{\text{exact}}(\mathbf{k}) = \left\langle \underbrace{[\dots [c_{\mathbf{k}}, H], H] \dots, H]}_{n \text{ times}} c_{\mathbf{k}}^\dagger \right\rangle_T, \quad (24)$$

and within the CE approximation, where by combining Eqs. (4) and (23) we find

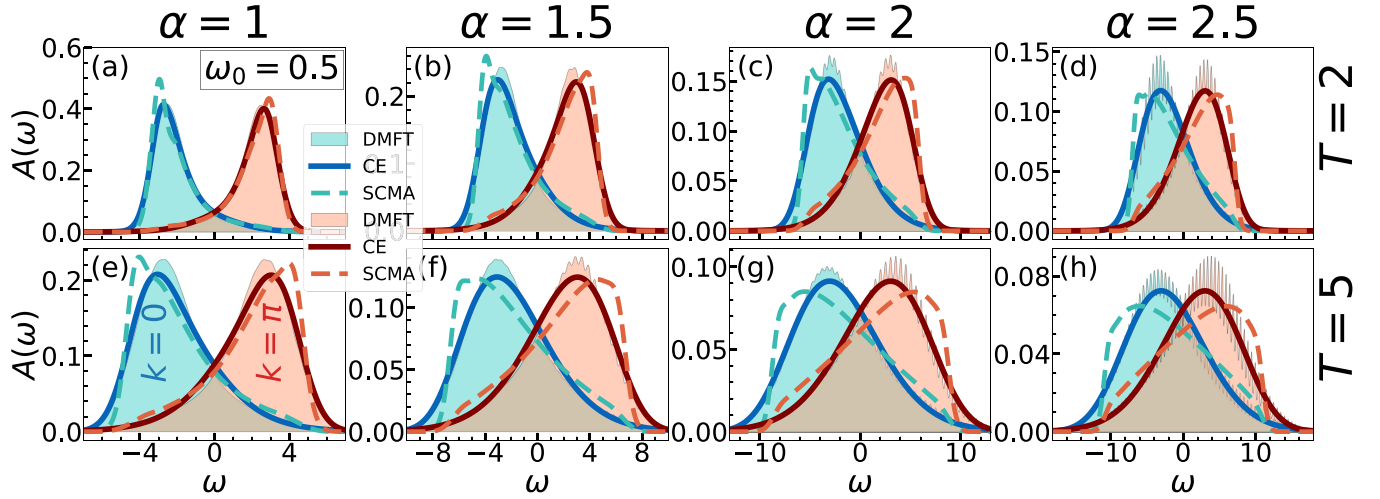
$$\begin{aligned} \mathcal{M}_n^{\text{CE}}(\mathbf{k}) &= \text{Re} \left[i^n \left(\frac{d}{dt} \right)^n e^{C_{\mathbf{k}}(t)} \right] \Big|_{t=0} \\ &\quad - \sum_{p=1}^n \binom{n}{p} (-\varepsilon_{\mathbf{k}})^p \mathcal{M}_{n-p}^{\text{CE}}(\mathbf{k}). \end{aligned} \quad (25)$$

The difference between these quantities $\mathcal{M}_n^{\text{CE}}(\mathbf{k}) - \mathcal{M}_n^{\text{exact}}(\mathbf{k})$ is zero for $n = 0$ and $n = 1$, as noted in Sec. II A 1. Higher order sum rules for the CE method are easily calculated, while the evaluation of the exact sum rules quickly becomes cumbersome for increasing n . The first five ($0 \leq n \leq 4$) sum rules were already calculated by Kornilovitch [58]

$$\mathcal{M}_2(\mathbf{k}) = \varepsilon_{\mathbf{k}}^2 + (2n_{\text{ph}} + 1)g^2, \quad (26a)$$

$$\mathcal{M}_3(\mathbf{k}) = \varepsilon_{\mathbf{k}}^3 + g^2\omega_0 + 2g^2(2n_{\text{ph}} + 1)\varepsilon_{\mathbf{k}}, \quad (26b)$$

$$\begin{aligned} \mathcal{M}_4(\mathbf{k}) &= \varepsilon_{\mathbf{k}}^4 + 2g^2\varepsilon_{\mathbf{k}}\omega_0 + g^2(2n_{\text{ph}} + 1) \\ &\quad \times (2t_0^2 + 3\varepsilon_{\mathbf{k}}^2 + \omega_0^2) + 3g^4(2n_{\text{ph}} + 1)^2. \end{aligned} \quad (26c)$$


 FIG. 7. (a)–(h) CE, DMFT, and SCMA spectral functions in 1D for $t_0 = 1$, $\omega_0 = 0.5$, and $k = 0, \pi$.

All of these are correctly predicted by the CE. However, the disagreement between $\mathcal{M}_n^{\text{exact}}$ and $\mathcal{M}_n^{\text{CE}}$ appears for $n = 5$, where we find

$$\begin{aligned} \mathcal{M}_5^{\text{exact}}(\mathbf{k}) &= \varepsilon_{\mathbf{k}}^5 + 3g^2\omega_0(2t_0^2 + \varepsilon_{\mathbf{k}}^2) + g^2\omega_0^3 \\ &\quad + 2g^2(2\varepsilon_{\mathbf{k}}^3 + 5g^2\omega_0 + \varepsilon_{\mathbf{k}}\omega_0^2 + 2t_0^2\varepsilon_{\mathbf{k}})(2n_{\text{ph}} + 1) \\ &\quad + 7g^4\varepsilon_{\mathbf{k}}(2n_{\text{ph}} + 1)^2, \end{aligned} \quad (27a)$$

$$\mathcal{M}_5^{\text{CE}}(\mathbf{k}) = \mathcal{M}_5^{\text{exact}}(\mathbf{k}) - 2g^4\varepsilon_{\mathbf{k}}(2n_{\text{ph}} + 1)^2. \quad (27b)$$

Hence, CE cannot be exact in the limit $T \rightarrow \infty$. However, we see that there are two limits where CE can potentially be exact: the weak-coupling limit $g \rightarrow 0$ and the atomic limit $\varepsilon_{\mathbf{k}} \rightarrow 0$. It turns out that CE is actually exact in both of these limits, as seen from Eqs. (3), (7), and (14) for the weak-coupling and Sec. III D for the atomic limit. We note that the SCMA gives correct sum rules only for $n \leq 3$ [42]. This is a consequence of the fact that SCMA ignores one of the fourth-order diagrams ($\sim g^4$) since it includes only the noncrossing diagrams. Also, we numerically checked that the DMFT results are in agreement with all of the sum rules that we listed above.

D. Atomic limit

In the atomic limit ($t_0 = 0$), the cumulant function can be evaluated exactly:

$$C(t) = \alpha^2(-2n_{\text{ph}} - 1 + it\omega_0 + iD(t)). \quad (28)$$

This follows from Eq. (16), using $J_0(0) = 1$. If we express the phonon propagator as $iD(t) = 2\sqrt{n_{\text{ph}}(n_{\text{ph}} + 1)} \cos[\omega_0(t + \frac{i}{2T})]$ and use the modified Jacobi-Anger identity

$$\begin{aligned} e^{2\alpha^2\sqrt{n_{\text{ph}}(n_{\text{ph}}+1)}\cos[\omega_0(t+\frac{i}{2T})]} \\ = \sum_{l=-\infty}^{\infty} I_l(2\alpha^2\sqrt{n_{\text{ph}}(n_{\text{ph}}+1)})e^{-il\omega_0 t}e^{\frac{l\omega_0}{2T}}, \end{aligned} \quad (29)$$

where I_l are the modified Bessel functions of the first kind, the spectral function [see Eqs. (3) and (4)] can be calculated

analytically and reads as

$$\begin{aligned} A(\omega) &= e^{-\alpha^2(2n_{\text{ph}}+1)} \\ &\quad \times \sum_{l=-\infty}^{\infty} I_l(2\alpha^2\sqrt{n_{\text{ph}}(n_{\text{ph}}+1)})e^{\frac{l\omega_0}{2T}}\delta(\omega + \alpha^2\omega_0 - l\omega_0). \end{aligned} \quad (30)$$

In the limit $T \rightarrow 0$, the previous expression reduces to

$$A(\omega) = e^{-\alpha^2} \sum_{l=0}^{\infty} \frac{\alpha^{2l}}{l!} \delta(\omega + \omega_0(\alpha^2 - l)). \quad (31)$$

This proves that CE gives correct results in the atomic limit, as Eqs. (30) and (31) coincide with the known exact results [1,44].

In contrast, the SCMA (let alone the MA) does not share this property, which is easy to show at zero temperature. In this case, Eq. (20a) and the Dyson equation imply that

$$G(\omega) = \frac{1}{\omega - g^2G(\omega - \omega_0)}. \quad (32)$$

The previous equation can be solved by the iterative application of itself in terms of the continued fraction

$$G(\omega) = \frac{1}{\omega - \frac{g^2}{\omega - \omega_0 - \frac{g^2}{\omega - 2\omega_0 - \frac{g^2}{\omega - 3\omega_0 - \dots}}}}. \quad (33)$$

This does not coincide with Eq. (35) from Ref. [53], which represents the exact solution. Thus, SCMA cannot reproduce the correct result in the atomic limit.

While the CE is exact in the atomic limit ($t_0 = 0$), it is not immediately obvious how far from this limit it continues to give reliable results. This is why we now examine the regimes with small hopping parameter t_0 . Since the lifetime is infinitely large in some of these regimes (see Fig. 2), we introduce artificial attenuation η for the Green's function in real time by making a replacement $G(t) \rightarrow G(t)e^{-\eta t}$. The results are presented in Fig. 8. Here, the dotted line is the analytic solution in the atomic limit ($t_0 = 0$), determined by Eq. (30), where the Dirac delta functions have been replaced by Lorentzians of half-width η . It is used as a measure to see

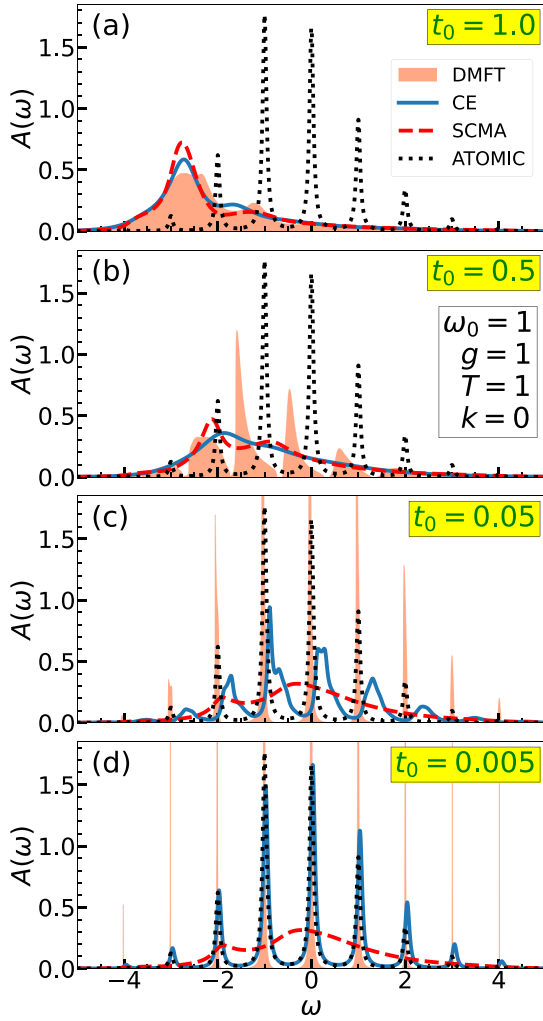


FIG. 8. (a)–(f) CE, DMFT, and SCMA spectral functions close to the atomic limit. Here, we use artificial Lorentzian broadening with half width set to $\eta = 0.05$.

how far the regime we are examining is from the exact atomic limit. In Fig. 8(a), we see that DMFT, SCMA, and CE spectral functions are in agreement. This regime is quite far from the atomic limit, as indicated by the dotted line. Figure 8(b) shows that the DMFT spectral function already consists of a series of peaks for $t_0 = 0.5$, while the CE and SCMA spectral functions are too flattened out. While the CE solution significantly improved in Fig. 8(c), it is still not giving satisfactory results, even though the DMFT suggests that we are already close to the atomic limit. Only for $t_0 \lesssim 0.005$ does the CE solution give accurate results; see Fig. 8(d). However, this is practically already at the atomic limit. It is interesting to note that while both the DMFT and the CE are exact in the weak-coupling and in the atomic limit, their behavior in other regimes can be quite different.

IV. QUASIPARTICLE PROPERTIES

We now investigate the quasiparticle properties obtained from the CE method and compare them extensively to the results obtained from the DMFT and SCMA. We note that

the lifetime within the CE was already studied in Sec. II A 4, so we supplement that study here with the results for the ground-state energy and the effective mass. Here we show the results in one, two, and three dimensions. Comparison with the MA ground-state energy, in the 1D case, is presented in Sec. III of the SM [54].

A. Ground-state energy

The polaron band dispersion $E_{p,\mathbf{k}}$ within the CE is given by the real part of Eq. (12), where the self-energy is taken in the MA:

$$E_{p,\mathbf{k}} = \varepsilon_{\mathbf{k}} + \text{Re}\Sigma^{\text{MA}}(\varepsilon_{\mathbf{k}}). \quad (34)$$

Since we deal with a single electron in the band, the ground-state energy E_p is given by $E_{p,\mathbf{k}=0}$ evaluated at zero temperature. In the 1D case, E_p is straightforwardly evaluated using Eq. (19) and reads as follows:

$$E_p^{1\text{D}} = -2t_0 - \frac{\alpha^2 \omega_0^2}{\sqrt{\omega_0^2 + 4\omega_0 t_0}}. \quad (35)$$

For the expression in higher dimensions, we need to go back to Eq. (14) that holds in any number of dimensions. At $T = 0$, it reads as

$$\text{Im}\Sigma^{\text{MA}}(\omega) = -\pi\alpha^2\omega_0^2\rho(\omega - \omega_0). \quad (36)$$

The real part of $\Sigma^{\text{MA}}(\omega)$ is obtained using the Kramers-Kronig relation

$$\text{Re}\Sigma^{\text{MA}}(\omega) = \pi\alpha^2\omega_0^2\mathcal{H}[\rho](\omega - \omega_0), \quad (37)$$

where $\mathcal{H}[\rho](\omega) = \mathcal{P} \int_{-\infty}^{\infty} \frac{d\nu}{\pi} \frac{\rho(\nu)}{\omega - \nu}$ is the Hilbert transform of the density of states $\rho(\omega)$ and \mathcal{P} is the Cauchy principle value. The evaluation of the Hilbert transform may be reduced to the evaluation of the Fourier transform \mathcal{F} , using the following identity:

$$\mathcal{F}^{-1}\mathcal{H}[\rho](t) = -i \text{sgn}(t) \mathcal{F}^{-1}[\rho](t). \quad (38)$$

The inverse Fourier transform of the density of states on the right-hand side was already calculated in Eq. (15) for the case of the hypercubic lattice with the nearest-neighbor hopping. Hence, $\mathcal{H}[\rho](\omega)$ is obtained by applying \mathcal{F} on both sides of Eq. (38),

$$\mathcal{H}[\rho](\omega) = \frac{1}{\pi} \int_0^{\infty} dx J_0(2t_0x)^n \sin(x\omega), \quad (39)$$

where n is the number of dimensions. The polaron band dispersion then reads as

$$E_{p,\mathbf{k}} = \varepsilon_{\mathbf{k}} + \alpha^2\omega_0^2 \int_0^{\infty} dx J_0(2t_0x)^n \sin(x(\varepsilon_{\mathbf{k}} - \omega_0)). \quad (40)$$

E_p is thus a linear function with respect to α^2 , whose intercept is $\varepsilon_{\mathbf{k}}$, while its slope can be calculated accurately using the numerical scheme described in Appendix A. In the 2D case, it admits an analytical solution

$$E_p^{2\text{D}} = -4t_0 - \frac{2\alpha^2\omega_0^2}{\pi(4t_0 + \omega_0)} K\left(\frac{4t_0}{4t_0 + \omega_0}\right), \quad (41)$$

where $K(k) = \int_0^{\pi/2} d\theta / \sqrt{1 - k^2 \sin^2 \theta}$ is the complete elliptic integral of the first kind. In the case $n = 3$, the integral

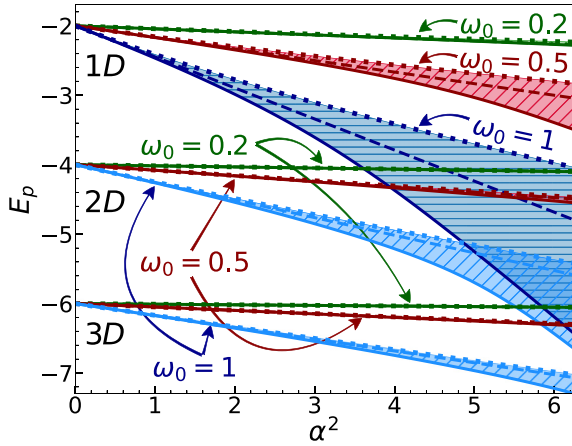


FIG. 9. Ground-state energy within the DMFT (solid line), CE (dashed line), and SCMA (dotted line). Here, $t_0 = 1$ and $T = 0$.

in Eq. (40) does not admit a closed-form solution and thus requires numerical calculation.

The polaron band dispersion $E_{p,\mathbf{k}}$ (and thus the ground state E_p) within the DMFT and SCMA is obtained numerically, as the smallest solution of the following equation:

$$E_{p,\mathbf{k}} = \varepsilon_{\mathbf{k}} + \text{Re}\Sigma(E_{p,\mathbf{k}}). \quad (42)$$

Results for the 1D, 2D, and 3D case are presented in Fig. 9. The DMFT benchmark, which is known to be very accurate [52], always gives the lowest ground-state energy predictions in comparison to the CE and SCMA. We see that CE always outperforms the SCMA, despite the fact that its predictions of the energy are always a linear function of α^2 . In the 1D case, we see that CE results for $\omega_0 = 0.5$ start to deviate more significantly from the DMFT just around $\alpha = 2.5$. Hence, the range of validity for the CE is similar as for the spectral functions in Fig. 4. The analogous conclusions can also be drawn from $\omega_0 = 1$ data as well. In contrast, all three methods seem to be in agreement for $\omega_0 = 0.2$ in the whole range of presented values of α . This is a consequence of the fact that the ground-state energy correction is small, as seen from Eqs. (35), (40), and (41) by fixing α and decreasing ω_0 . However, if we fix $g = \omega_0\alpha$ and then decrease ω_0 , the ground-state energy would change substantially [see, e.g., Eq. (35)], and the CE would certainly give poorer results.

Similar trends are observed in higher dimensions as well. Seemingly, the range of validity of the CE is increased in higher dimensions. However, one should keep in mind that the hopping parameter is always taken to be unity, which means that the bandwidth of the 2D and 3D systems are, respectively, two and three times larger than their 1D counterpart. Therefore, the correlation is weaker for a given coupling α .

B. Effective mass

Around the bottom ($|\mathbf{k}| \approx 0$) of the conduction band, the dispersion $E_{p,\mathbf{k}}$ assumes the following parabolic form:

$$E_{p,\mathbf{k}} \approx \text{const} + \frac{\mathbf{k}^2}{2m^*}, \quad (43)$$

where m^* is the effective mass, which we now calculate.

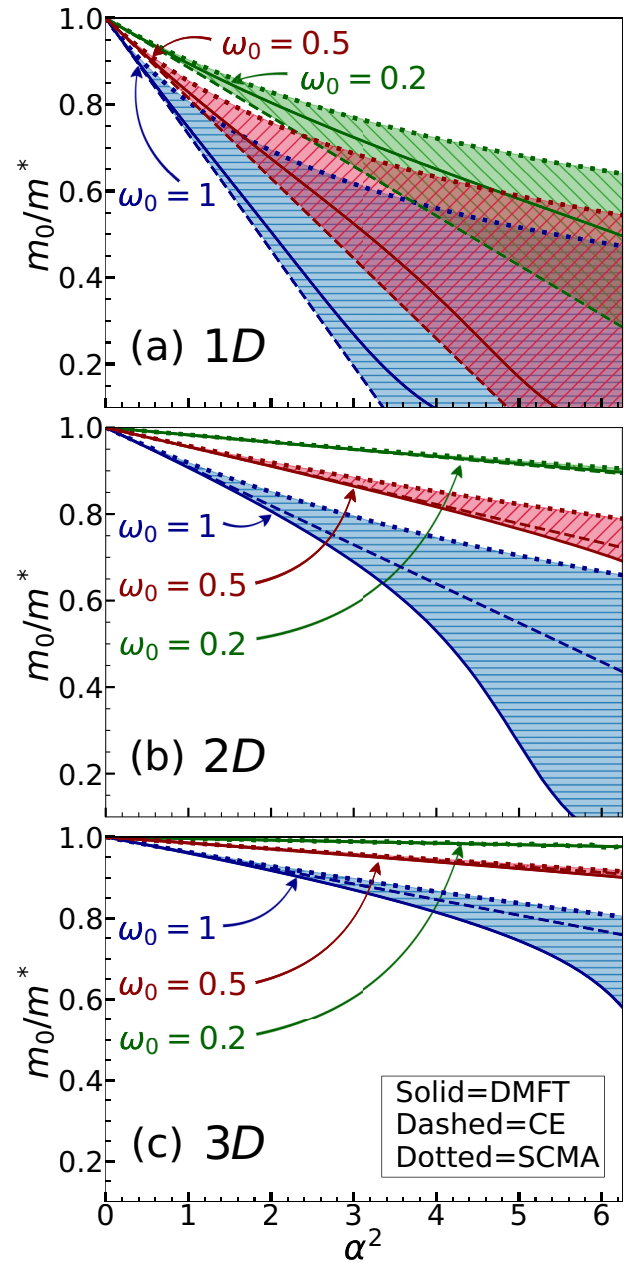


FIG. 10. Effective mass results within the DMFT, CE, and SCMA for $t_0 = 1$ and $T = 0$.

In the 1D case, one obtains the analytical result for the effective mass using Eqs. (19) and (34),

$$\left. \frac{m^*}{m_0} \right|_{1D, T=0} = \frac{1}{1 - \frac{(2t_0 + \omega_0)\alpha^2 \sqrt{\omega_0}}{(4t_0 + \omega_0)^{3/2}}}, \quad (44)$$

where $m_0 = 1/(2t_0)$ is the band mass which remains the same irrespective of the number of dimensions. Results for the higher number of dimensions are evaluated using Eq. (40). As for the ground-state energy, the 2D case admits an analytic solution

$$\left. \frac{m^*}{m_0} \right|_{2D, T=0} = \frac{1}{1 - \frac{2\alpha^2\omega_0}{\pi(8t_0 + \omega_0)} E\left(\frac{4t_0}{4t_0 + \omega_0}\right)}, \quad (45)$$

where $E(k) = \int_0^{\pi/2} d\theta \sqrt{1 - k^2 \sin^2 \theta}$ is the complete elliptic integral of the second kind. Results in the n -dimensional case are given by

$$\frac{m^*}{m_0} \Big|_{T=0} = \frac{1}{1 + \pi \alpha^2 \omega_0^2 \frac{d\mathcal{H}[\rho]}{d\omega} \Big|_{\omega=-2m_0-\omega_0}}, \quad (46)$$

and require numerical calculation in the general case. From Eq. (46) we see that m_0/m^* is a linear function of α^2 . This linear behavior has to break down at one point, as m_0/m^* cannot be negative. This happens for strong interaction, where the CE is certainly not expected to be reliable. The mass renormalization within the DMFT and SCMA is calculated numerically as

$$\frac{m^*}{m_0} \Big|_{T=0} = 1 - \frac{d\Sigma(\omega)}{d\omega} \Big|_{\omega=E_p}, \quad (47)$$

where E_p is the ground-state energy. Results for the DMFT, CE, and SCMA effective mass in different parameter regimes and for different number of dimensions are presented in Fig. 10. In the 1D case, we see that the CE always underestimates, while the SCMA overestimates the results from the DMFT benchmark. Still, CE clearly outperforms the SCMA for $\omega_0 = 1$ and $\omega_0 = 0.5$, while the results in the vicinity of the adiabatic limit ($\omega_0 = 0.2$) seem to be equally well (poor) represented by both methods.

In the higher-dimensional case, we see that the CE is always a clearly better approximation than the SCMA, while both of them overestimate the DMFT predictions. As for the ground-state energy, we emphasize again that the hopping parameter was set to 1. As a consequence, the system has a larger bandwidth in the higher-dimensional case and, therefore, the correlations are weaker.

V. MOBILITY

The mobility is defined as the DC conductivity, normalized to the concentration of charge carriers n_e (and their unit charge which we set to $e = 1$), i.e., $\mu = \sigma^{\text{DC}}/n_e$. It can be calculated using the Kubo formalism, which relates μ to the current-current correlation function [1]. The latter can be written as a sum of the so-called bubble part, which is completely determined by the spectral functions $A_{\mathbf{k}}(\omega)$ and the vertex corrections. Within the DMFT, the vertex corrections vanish [57,59], while estimating their contribution in the general case is beyond the scope of this paper. In the following, we calculate the mobility solely from the bubble part.

In the case of a 1D system with a single spinless electron in the band, the mobility in the bubble approximation can be written as [1,60]

$$\mu = \frac{4\pi t_0^2}{T} \frac{\sum_{\mathbf{k}} \int_{-\infty}^{\infty} dv A_{\mathbf{k}}(v)^2 e^{-v/T} \sin^2 k}{\sum_{\mathbf{k}} \int_{-\infty}^{\infty} dv A_{\mathbf{k}}(v) e^{-v/T}}. \quad (48)$$

The processing time required for the calculation of μ within the CE method rises linearly with the number of k points we sum over. This is not the case for the DMFT and SCMA, as their self-energies are k independent and thus need to be calculated only once for a given parameter set. In every parameter regime the CE was applied to, we checked that 64 sampling points in the Brillouin zone are enough to be representative of

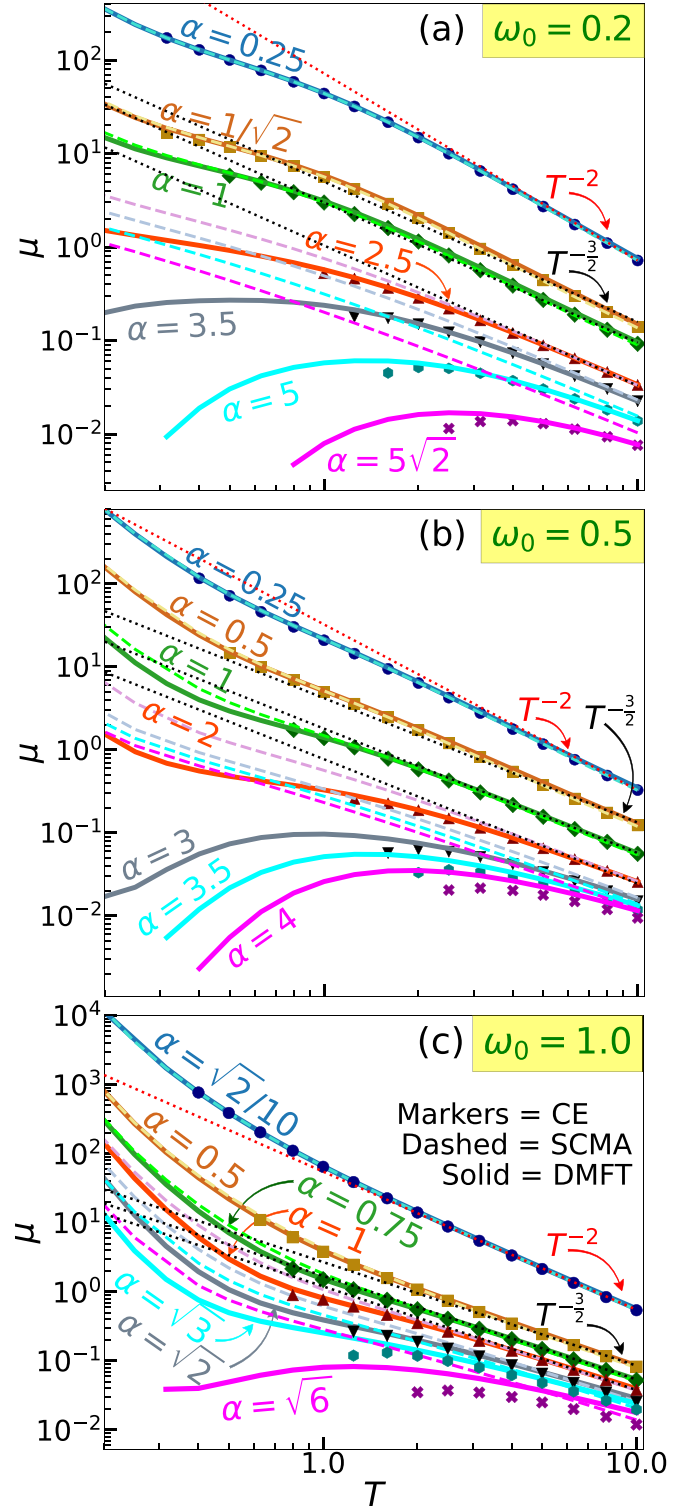


FIG. 11. Temperature dependence of the mobility for the CE, DMFT, and SCMA. The dotted red (black) lines are auxiliary lines with the power law behavior $\mu \propto T^{-2}$ ($\mu \propto T^{-3/2}$). Here $t_0 = 1$.

the thermodynamic limit. This was also crosschecked using the DMFT.

The exponential term $e^{-v/T}$ in Eq. (48) has some important implications. Despite the factor $\sin^2 k$, it implies that the largest contribution to the mobility most commonly comes

from the spectral functions around the bottom of the band ($k \approx 0$), as they are typically situated at lower frequencies with respect to their higher momentum counterparts. This is actually helpful, as we have seen that the CE is more reliable for $k \approx 0$ than for $0 < k < \pi$. However, $e^{-\nu/T}$ also introduces numerical instabilities, as even a small numerical noise of $A_k(\nu)$ at $\nu \ll -1$ will be inflated and give an enormous overall error in the mobility. This is why the integrals in Eq. (48) require introducing some kind of negative frequency cutoff $\int_{-\infty}^{\infty} \rightarrow \int_{-\Lambda}^{\infty}$. We always check that the mobility results converge with respect to Λ . This is easily done in both the DMFT and SCMA due to the high numerical accuracy of our numerical implementations. The convergence with respect to Λ is much harder to achieve within the CE, as the Green's functions are initially calculated in the time domain and require the use of numerical Fourier transform. We have implemented a well-known interpolation scheme [61] to increase the precision of the Fourier transform. Still, the numerical noise at low temperatures and strong interactions prevented us from precisely calculating the mobility in these regimes. We show only the data where an accurate calculation was possible.

In Fig. 11, we present numerical results for the temperature dependence of the electron mobility. For weak electron-phonon coupling, all methods are in agreement; see Fig. 11(a) for $\alpha \leq 1$ and Figs. 11(b) and 11(c) for $\alpha \leq 0.5$. Electron-phonon scattering is weak in these regimes, which is why the quasiparticle lifetime τ_k is long, and the linear time dependence dominates in the cumulant function. The spectral function and its square can thus be approximated as $A_k(\omega) \approx \delta(\omega - E_{p,k})$ and $A_k^2(\omega) \approx \frac{\tau_k}{\pi} \delta(\omega - E_{p,k})$, where δ is the Dirac delta function and $E_{p,k}$ is given by Eq. (34). The mobility from Eq. (48) thus simplifies to

$$\mu_{\text{weak}} \approx \frac{4t_0^2}{T} \frac{\sum_k \tau_k e^{-E_{p,k}/T} \sin^2 k}{\sum_k e^{-E_{p,k}/T}}. \quad (49)$$

At high temperatures, Eq. (49) further simplifies as $e^{-E_{p,k}/T} \approx 1$. In this case, the lifetime is inversely proportional to the temperature $\tau_k \propto 1/T$, as seen from Eq. (18), which implies the power-law behavior of the mobility $\mu_{\text{weak}} \propto 1/T^2$. This conclusion holds only for very weak electron-phonon couplings, where the assumption of weak scattering is still satisfied despite the high temperatures; see Figs. 11(a) and 11(b) for $\alpha = 0.25$ and Fig. 11(c) for $\alpha = \sqrt{2}/10$. This assumption is also violated at extremely high temperatures $T \rightarrow \infty$.

For stronger couplings, in the limit of high-temperatures $T \gg t_0, \omega_0$, the Green's function in the time domain is quickly damped, which is why $C_k(t)$ can be approximated with just the lowest order (quadratic) Taylor expansion around $t = 0$. Hence, Eqs. (3) and (17) imply that the Green's function can be written as

$$G_k(t) = -i\theta(t) e^{-i\varepsilon_k t} e^{-\frac{g^2}{2}(2n_{\text{ph}}+1)t^2}, \quad (50)$$

while the corresponding spectral function is given by the Gaussian:

$$A_k(\omega) = \frac{e^{-\frac{(\omega-\varepsilon_k)^2}{2g^2(2n_{\text{ph}}+1)}}}{\sqrt{2\pi g^2(2n_{\text{ph}}+1)}}. \quad (51)$$

Plugging this back into Eq. (48) and changing the sum over momenta to integral, we obtain

$$\mu_{\text{high-}T} = \frac{t_0}{g} \sqrt{\frac{\pi}{2n_{\text{ph}}+1}} \exp\left(-\frac{g^2(2n_{\text{ph}}+1)}{4T^2}\right) \frac{I_1\left(\frac{2t_0}{T}\right)}{I_0\left(\frac{2t_0}{T}\right)}, \quad (52)$$

where I_0 and I_1 are modified Bessel functions of the first kind, of zeroth and first orders, respectively. Equation (52) can be simplified by using the following approximations: $2n_{\text{ph}}+1 \approx 2T/\omega_0$ and $I_1(2t_0/T)/I_0(2t_0/T) \approx t_0/T$, that are valid for large T . Such a simplified formula coincides with the mobility obtained by combining the Einstein relation, between the mobility and diffusion coefficient, with the Marcus formula [45,62]. Furthermore, Eq. (52) implies the power-law behavior for the mobility $\mu_{\text{high-}T} \propto T^{-3/2}$, in the limit $T \gg t_0, \omega_0$. This is confirmed by our numerical results for a wide range of the electron-phonon coupling strengths, where all three methods are in agreement; see Fig. 11(a) for $1/\sqrt{2} \leq \alpha \leq 2.5$, Fig. 11(b) for $0.5 \leq \alpha \leq 2$, and Fig. 11(c) for $0.5 \leq \alpha \leq 1$.

While the SCMA gives satisfactory results for high temperatures and intermediate electron-phonon couplings, it deviates from the DMFT at lower temperatures [see, e.g., Fig. 11(a) for $\alpha = 2.5$ and Fig. 11(b) for $\alpha = 2$] and also for stronger coupling strengths [see, e.g., Fig. 11(a) for $\alpha > 2.5$ and Fig. 11(b) for $\alpha > 2$]. At these stronger couplings, the DMFT predicts the nonmonotonic mobility, where a region of decreasing mobility with decreasing temperature is ascribed to the hopping transport in phenomenological theories [38,62]. The strong coupling mobility is better described by the CE than SCMA, although low-temperature results are missing due to our inability to converge the results with respect to the cutoff Λ . In Appendix D, we also give mobility predictions of the MA.

VI. CONCLUSIONS AND OUTLOOK

In summary, we have presented a comprehensive analysis of the CE method in the context of the Holstein model. The second-order cumulant $C(t)$ is calculated in a broad temperature range for three vibrational frequencies $\omega_0/t_0 = 0.2, 0.5$, and 1, covering a regime from a weak to strong electron-phonon coupling. We mostly focused on the 1D system in the thermodynamic limit but some of the results are shown also in 2D and 3D. To avoid numerical instabilities and to reach high numerical precision, we derived a number of analytical expressions and we used the collocation method in calculations of the cumulant, as well as an interpolation scheme for the Fourier transform in corresponding calculations of the spectral functions. The quasiparticle properties, spectral functions, and charge mobility are shown in comparison to the DMFT and SCMA results. The DMFT, which gives close to the exact solution for the Holstein polaron throughout the parameter space [52], gave a valuable benchmark and facilitated a detailed analysis of the validity of the CE method.

At weak coupling (roughly corresponding to $m_0/m^* \gtrsim 0.9$) CE, DMFT, and SCMA give very similar spectral functions. Most of the spectral weight for $k = 0$ is in the quasiparticle peak, while even a small sideband (satellite) spectral weight is rather well reproduced in all three methods. As the interaction increases, a clear difference in the spectral functions

emerges. Nevertheless, the positions of the CE and DMFT quasiparticle and the first satellite peak at low temperatures are in rather good agreement. Furthermore, the overall spectral weight distribution is in a decent agreement even though the satellite peaks are more pronounced in DMFT for stronger electron-phonon coupling. Roughly speaking, there is a decent agreement in 1D up to the interactions corresponding to $m_0/m^* \sim 0.5$. Interestingly, the agreement between the CE and DMFT spectral functions persists also for $k = \pi$, although CE does not capture a tiny quasiparticle peak. In this case, the DMFT spectral weight almost merges to a single broad peak. We note that the difference for $k = \pi$ observed in Ref. [50] is solely due to considering a lattice of finite $N = 6$ size. The deviation of CE from the exact solution is most obvious for intermediate momenta where the CE solution merges to a single peak, while the satellite structure is seen in DMFT. At high temperatures, one might suspect that the CE would give the exact spectral functions. However, this is not the case, as we showed that the CE gives the exact spectral moments only up to the order $n = 4$. We note that in all these regimes, the CE gives slightly better results than the SCMA, while a single-shot MA is adequate only for very weak interactions.

The spectral functions were used to calculate the charge mobility from the Kubo formula without the vertex corrections. The agreement between DMFT and CE is quite good. This is the case even for stronger electron-phonon coupling where the CE even indicates nonmonotonic behavior of $\mu(T)$, with a region of increasing mobility with temperature which is usually assigned to hopping conduction in phenomenological theories. For strong electron-phonon coupling, the CE mobility results are shown only for $T \gtrsim t_0$ since a very small numerical noise at frequencies $\omega \ll E_p$ affects a precise calculation of mobility at lower temperatures. For high temperatures, the mobility assumes a universal form: For weak electron-phonon coupling $\mu \propto T^{-2}$, while for stronger coupling $\mu \propto T^{-3/2}$. These high-temperature limits can be obtained also analytically from the CE.

The CE method can be easily applied to different Hamiltonians, which makes it a particularly attractive method for the calculation of electronic properties beyond the weak-coupling limit in various systems. In particular, we argue that it will be most useful in calculations of charge mobility, as has already been done in *ab initio* calculations for SrTiO₃ [16] and naphthalene [17]. While our analysis may suggest that the DMFT appears computationally superior to CE, we note that the numerical efficiency that we achieved with DMFT is restricted to the Holstein model by virtue of the analytic solution for the impurity problem [53] and the local Green's function [52]. For predicting the properties of real materials, the numerical resources within the DMFT are vastly increased and also the issue of nonlocal correlations may emerge, while the CE remains simple and relatively inexpensive. Of course, for a definitive answer on the range of validity of CE in connection with *ab initio* calculations, one needs to perform a similar analysis for the Fröhlich model and for other models which can be used for realistic description of the electronic spectra and charge transport in real materials. A useful hint in this direction is provided by Ref. [51], which shows that the CE, around the bottom of the band, gives promising results for the spectral function even in the case when the phonons

have a dispersion [63]. Another very interesting question that we leave for further work is a possible contribution of vertex corrections to conductivity. Based on the weak coupling result [64], one might assume that their contribution is small for optical phonons, but this remains to be determined in the case of stronger coupling. Our high-temperature results for mobility may also be quite useful when analyzing a dominant type of electron-phonon coupling in real materials. Still, one needs to be cautious in such analyses since we see that at lower temperatures $\mu(T)$ does not assume a simple universal form.

ACKNOWLEDGMENTS

The authors acknowledge funding provided by the Institute of Physics Belgrade, through a grant by the Ministry of Science, Technological Development and Innovation of the Republic of Serbia. Numerical simulations were performed on the PARADOX supercomputing facility at the Scientific Computing Laboratory, National Center of Excellence for the Study of Complex Systems, Institute of Physics Belgrade.

APPENDIX A: NUMERICAL INTEGRATION SCHEME FOR THE HIGHLY OSCILLATING FUNCTIONS IN THE CE METHOD

We present a numerical integration scheme for the calculation of the cumulant function from Eq. (16). Since $C_{\mathbf{k}}(t)$ will be expressed numerically on some t -grid $[t_0 = 0, t_1 \dots t_{G-1}]$, it is much better to divide the integral \int_0^t from Eq. (16) into a sum of integrals of the form $\int_{t_{i-1}}^{t_i}$, where t_i are times from the previously defined t grid. In this manner, we do not integrate over the same interval multiple times. To shorten the notation, from now on, we denote $a \equiv t_{i-1}$ and $b \equiv t_i$. There are two different types of integrals in Eq. (16), and both of them have the following form:

$$I = \int_a^b dx g(x) e^{ir_1 x} J_0(r_2 x)^n, \quad (\text{A1})$$

where $g(x)$ is either a linear or a constant function, $r_1 = \varepsilon_{\mathbf{k}} \pm \omega_0$, and $r_2 = 2t_0$. Numerical integration of Eq. (A1) has already been studied by Levin for arbitrary r_1 and r_2 and slowly varying $g(x)$ [55]. In the rest of this Appendix, we review this method in the 1D ($n = 1$), 2D ($n = 2$), and 3D ($n = 3$) cases. The main idea is to rewrite the subintegral function as a scalar product of two columns $|\tilde{g}(x)\rangle$ and $|\tilde{J}(x)\rangle$, whose elements are functions:

$$I = \int_a^b dx \langle \tilde{g}(x) | \tilde{J}(x) \rangle. \quad (\text{A2})$$

Column $|\tilde{g}(x)\rangle$ consists exclusively of slowly varying functions, while $|\tilde{J}(x)\rangle$ contains highly oscillating functions, with the property that

$$\frac{d|\tilde{J}(x)\rangle}{dx} = \hat{A}(x)|\tilde{J}(x)\rangle, \quad (\text{A3})$$

where $\hat{A}(x)$ is a matrix of slowly varying functions. Then, the integral from Eq. (A2) can be written as

$$I = \int_a^b dx \frac{d}{dx} \langle \tilde{f}(x) | \tilde{J}(x) \rangle = \langle \tilde{f}(b) | \tilde{J}(b) \rangle - \langle \tilde{f}(a) | \tilde{J}(a) \rangle, \quad (\text{A4})$$

where $|\tilde{f}(x)\rangle$ satisfies

$$\left(\frac{d}{dx} + \hat{A}^\dagger(x) \right) |\tilde{f}(x)\rangle = |\tilde{g}(x)\rangle. \quad (\text{A5})$$

This is then, following Levin [55], solved by formally expanding $|\tilde{f}(x)\rangle = \sum_{k=1}^M u_k(x) [c_k \ d_k \ \dots]^T$ into a basis set of polynomials $u_k(x) = (x - \frac{a+b}{2})^{k-1}$ and determining the unknown polynomial coefficients c_k, d_k, \dots by imposing that Eq. (A5) is exactly satisfied at M uniformly distributed collocation points $x_j = a + \frac{(j-1)(b-a)}{M-1}$, $j = 1 \dots M$. The initial problem is thus reduced to a simple linear algebra problem.

1. 1D case

In the 1D case ($n = 1$), columns $|\tilde{g}(x)\rangle$ and $|\tilde{J}(x)\rangle$ assume the following form:

$$|\tilde{g}(x)\rangle = [g(x) \ 0]^T, \quad (\text{A6a})$$

$$|\tilde{J}(x)\rangle = e^{ir_1 x} [J_0(r_2 x) \ J_1(r_2 x)]^T, \quad (\text{A6b})$$

where $J_0(x)$ and $J_1(x)$ are the Bessel functions of the first kind, of zeroth and first order. The matrix $\hat{A}(x)$, such that Eq. (A3) holds, is given by

$$\hat{A}(x) = \begin{bmatrix} ir_1 & -r_2 \\ r_2 & ir_1 - \frac{1}{x} \end{bmatrix}. \quad (\text{A7})$$

The unknown coefficients c_k and d_k , which determine the column function

$$|\tilde{f}(x)\rangle = \sum_{k=1}^M u_k(x) [c_k \ d_k]^T, \quad (\text{A8})$$

are obtained from the following set of $2M$ linear equations:

$$\begin{bmatrix} \mathcal{C} & \mathcal{C}^d \\ \mathcal{D}^c & \mathcal{D} \end{bmatrix} \begin{bmatrix} c_1 \\ \vdots \\ c_M \\ d_1 \\ \vdots \\ d_M \end{bmatrix} = \begin{bmatrix} g(x_1) \\ \vdots \\ g(x_M) \\ 0 \\ \vdots \\ 0 \end{bmatrix}. \quad (\text{A9})$$

Here, $\mathcal{C}, \mathcal{C}^d, \mathcal{D}^c, \mathcal{D}$ are $M \times M$ matrices that read as

$$\mathcal{C}_{ij} = u'_j(x_i) - ir_1 u_j(x_i); \quad \mathcal{C}_{ij}^d = r_2 u_j(x_i), \quad (\text{A10a})$$

$$\mathcal{D}_{ij} = u'_j(x_i) - \left(ir_1 + \frac{1}{x_i} \right) u_j(x_i); \quad \mathcal{D}_{ij}^c = -r_2 u_j(x_i). \quad (\text{A10b})$$

2. 2D case

In the 2D case, the relevant quantities are given by

$$\begin{aligned} |\tilde{g}(x)\rangle &= [g(x) \ 0 \ 0]^T, \\ |\tilde{J}(x)\rangle &= e^{ir_1 x} [J_0(r_2 x)^2 \ J_0(r_2 x) J_1(r_2 x) \ J_1(r_2 x)^2]^T, \\ \hat{A}(x) &= \begin{bmatrix} ir_1 & -2r_2 & 0 \\ r_2 & ir_1 - \frac{1}{x} & -r_2 \\ 0 & 2r_2 & ir_1 - \frac{2}{x} \end{bmatrix}. \end{aligned} \quad (\text{A11})$$

The column $|\tilde{f}(x)\rangle = \sum_{k=1}^M u_k(x) [c_k \ d_k \ e_k]^T$ is determined by c_k, d_k , and e_k , which are obtained as a solution of the following system of $3M$ linear equations:

$$\begin{bmatrix} \mathcal{C} & \mathcal{C}^d & \mathcal{C}^e \\ \mathcal{D}^c & \mathcal{D} & \mathcal{D}^e \\ \mathcal{E}^c & \mathcal{E}^d & \mathcal{E} \end{bmatrix} \begin{bmatrix} c_1 \\ \vdots \\ c_M \\ d_1 \\ \vdots \\ e_1 \\ \vdots \end{bmatrix} = \begin{bmatrix} g(x_1) \\ \vdots \\ g(x_M) \\ 0 \\ \vdots \\ 0 \\ \vdots \end{bmatrix}. \quad (\text{A12})$$

Here, $\mathcal{C}, \mathcal{C}^d \dots \mathcal{E}$ are $M \times M$ matrices. Elements of \mathcal{C}_{ij} and \mathcal{C}_{ij}^d are the same as in Eq. (A10), while $\mathcal{C}_{ij}^e = \mathcal{E}_{ij}^c = 0$. All the other elements are given by

$$\begin{aligned} \mathcal{D}_{ij} &= u'_j(x_i) - \left(ir_1 + \frac{1}{x_i} \right) u_j(x_i), \\ \mathcal{E}_{ij} &= u'_j(x_i) - \left(ir_1 + \frac{2}{x_i} \right) u_j(x_i), \\ \mathcal{D}_{ij}^c &= -2r_2 u_j(x_i); \quad \mathcal{D}_{ij}^e = 2r_2 u_j(x_i); \quad \mathcal{E}_{ij}^d = -r_2 u_j(x_i). \end{aligned} \quad (\text{A13})$$

3. 3D case

The procedure that was presented so far is actually quite easily generalized to the 3D case as well. Here, the quantities of interest are easily derived and read as

$$\begin{aligned} |\tilde{g}(x)\rangle &= [g(x) \ 0 \ 0 \ 0]^T, \\ |\tilde{J}(x)\rangle &= e^{ir_1 x} [J_0(r_2 x)^3 \ J_0(r_2 x)^2 J_1(r_2 x) \\ &\quad J_0(r_2 x) J_1(r_2 x)^2 \ J_1(r_2 x)^3]^T, \\ \hat{A}(x) &= \begin{bmatrix} ir_1 & -3r_2 & 0 & 0 \\ r_2 & ir_1 - \frac{1}{x} & -2r_2 & 0 \\ 0 & 2r_2 & ir_1 - \frac{2}{x} & -r_2 \\ 0 & 0 & 3r_2 & ir_1 - \frac{3}{x} \end{bmatrix}, \\ \tilde{f}(x) &= \sum_{k=1}^M u_k(x) [c_k \ d_k \ e_k \ f_k]^T, \end{aligned} \quad (\text{A14})$$

where the coefficients c_k , d_k , e_k , and f_k satisfy

$$\begin{bmatrix} \mathcal{C} & \mathcal{C}^d & \mathcal{C}^e & \mathcal{C}^f \\ \mathcal{D}^c & \mathcal{D} & \mathcal{D}^e & \mathcal{D}^f \\ \mathcal{E}^c & \mathcal{E}^d & \mathcal{E} & \mathcal{E}^f \\ \mathcal{F}^c & \mathcal{F}^d & \mathcal{F}^e & \mathcal{F} \end{bmatrix} \begin{bmatrix} c_1 \\ \vdots \\ c_M \\ d_1 \\ \vdots \\ e_1 \\ \vdots \\ f_1 \\ \vdots \end{bmatrix} = \begin{bmatrix} g(x_1) \\ \vdots \\ g(x_M) \\ 0 \\ \vdots \\ 0 \\ \vdots \\ 0 \\ \vdots \end{bmatrix}. \quad (\text{A15})$$

Here \mathcal{C}_{ij} , \mathcal{C}_{ij}^d , \mathcal{C}_{ij}^e , \mathcal{D}_{ij} , \mathcal{D}_{ij}^e , \mathcal{E}_{ij}^c , and \mathcal{E}_{ij} are the same as in Eqs. (A10) and (A13), while $\mathcal{C}_{ij}^f = \mathcal{F}_{ij}^c = \mathcal{D}_{ij}^f = \mathcal{F}_{ij}^d = 0$. All other elements are given by

$$\begin{aligned} \mathcal{E}_{ij}^d &= -2r_2 u_j(x_i); & \mathcal{E}_{ij}^f &= 3r_2 u_j(x_i), \\ \mathcal{D}_{ij}^c &= -3r_2 u_j(x_i); & \mathcal{F}_{ij}^e &= -r_2 u_j(x_i), \\ \mathcal{F}_{ij} &= u'_j(x_i) - \left(ir_1 + \frac{3}{x_i} \right) u_j(x_i). \end{aligned} \quad (\text{A16})$$

Thus, our numerical scheme has been completely specified. We note that Eqs. (A10), (A13), and (A16) explicitly demonstrate that our numerical scheme is singular at $x = 0$. This does not pose any problems, as the subintegral function in our initial expression Eq. (A1) is not highly oscillatory around $x = 0$. Therefore, the trapezoid scheme can be applied there.

APPENDIX B: 2D SPECTRAL FUNCTIONS

We now examine the CE spectral functions in two dimensions and compare them to the results from DMFT and SCMA. We investigate the Hamiltonian from Eq. (1) on a square lattice and set \hbar , k_B and lattice constant to 1.

In the 2D case, the cumulant function is calculated from Eq. (16) by setting $n = 2$, and by exploiting the numerical integration scheme from Appendix A. The procedure for the implementation of the DMFT and SCMA is the same as explained in Sec. II B, with the only difference being that Eq. (22) no longer represents the solution for the local Green's function from Eqs. (20b) and (21). The local Green's function for the square lattice is obtained as follows. Let us introduce $B(\omega) \equiv (\omega - \Sigma(\omega))/(2t_0)$ and rewrite Eq. (21) as

$$G(\omega) = - \int_{-\infty}^{\infty} dx \hat{\rho}(x) \int_{-\infty}^{\infty} d\varepsilon \frac{e^{ix\varepsilon}}{\varepsilon - 2t_0 B(\omega)}. \quad (\text{B1})$$

The integral over ε can be solved using the residue theorem. It is thus important to note that the subintegral function has only a single pole at $\varepsilon_{\text{pole}} = 2t_0 B(\omega)$ that is situated at the upper half-plane, i.e., $\text{Im}B(\omega) > 0$ (since $\text{Im}\Sigma(\omega) < 0$). Hence

$$G(\omega) = -2\pi i \int_{-\infty}^{\infty} dx \tilde{\rho}(x) e^{2ixt_0 B(\omega)} \theta(x). \quad (\text{B2})$$

Here $\tilde{\rho}(x)$ is given by Eq. (15) for $n = 2$. Substituting this into Eq. (B2) and solving the integral gives

$$G(\omega) = \frac{K\left(\frac{2}{B(\omega)}\right)}{B(\omega)\pi t_0}, \quad (\text{B3})$$

where $K(k) \equiv \int_0^{\pi/2} d\theta / \sqrt{1 - k^2 \sin^2 \theta}$ is the complete elliptic integral of the first kind.

Results are presented in Fig. 12. We note that in Figs. 12(a)–12(d) [Figs. 12(i)–12(l)] the phonon frequency $\omega_0 = 0.2$ ($\omega_0 = 1$) is smaller (larger) than both of the temperatures $T_1 = 0.3$ and $T_2 = 0.7$ that we are considering. Therefore, we focus on Figs. 12(e)–12(h) where $T_1 < \omega_0 < T_2$, while other regimes can be analyzed analogously. We see that most of the spectral weight is concentrated in a smaller range of frequencies than in the 1D case; see Figs. 4 and 12(e)–12(h). This is a consequence of the fact that the hopping parameter is always set to unity, while the 2D bandwidth is twice as large in comparison with the bandwidth in the 1D system. Spectral functions from Figs. 12(e)–12(g) exhibit qualitatively similar behavior as results for the 1D system in Figs. 4(a)–4(d). Here, all methods are in agreement and predict that the quasiparticle peak dominates, while there is only a single tiny satellite structure that is more pronounced at higher temperatures. However, it seems that the satellites are more pronounced in the 1D spectral functions. A much more complicated multippeak structure is predicted by the DMFT in Fig. 10(h), where a large discrepancy can be observed in comparison to the CE and SCMA results. A better agreement is observed for higher temperatures.

It is interesting to note that while the DMFT frequently gave sharper peaks than other methods in 1D (see Fig. 4), here the roles are reversed. This is a consequence of the strong Van Hove singularity at the bottom of the band of a 1D system, which is highly relevant in our case when the concentration of electrons is very low, while the singularity in the 2D system is weaker and shifted to the center of the band.

APPENDIX C: A DETAILED STUDY OF THE SPECTRAL FUNCTION FOR $t_0 = \omega_0 = g = 1$ and $k = \pi$

In Sec. III, we concluded that the CE successfully captures the main features of the spectral functions both at the bottom of the band ($k \approx 0$) and at top of the band ($k \approx \pm\pi$) if the electron-phonon coupling is not too strong. Less promising results were reported in Ref. [50], where CE was examined on a finite lattice with $N = 6$ sites in the regime $t_0 = \omega_0 = g = 1$ and $k = \pi$, using the finite-temperature Lanczos method (FTLM) [44] as a benchmark. They found that the CE, in addition to the fact that it does not correctly reproduce a quasiparticle peak, predicts that the most prominent feature of the spectrum consists of only a single broad peak, whereas two distinct peaks are present in the FTLM solution. Here we show that this discrepancy between the CE and FTLM is significantly reduced in the thermodynamic limit.

Reference [50] emphasized that previous conclusions are valid only for low-temperature solutions, while CE becomes accurate for $T \geq \omega_0$. This was confirmed by the FTLM, whose spectral functions in this case look like a single broad

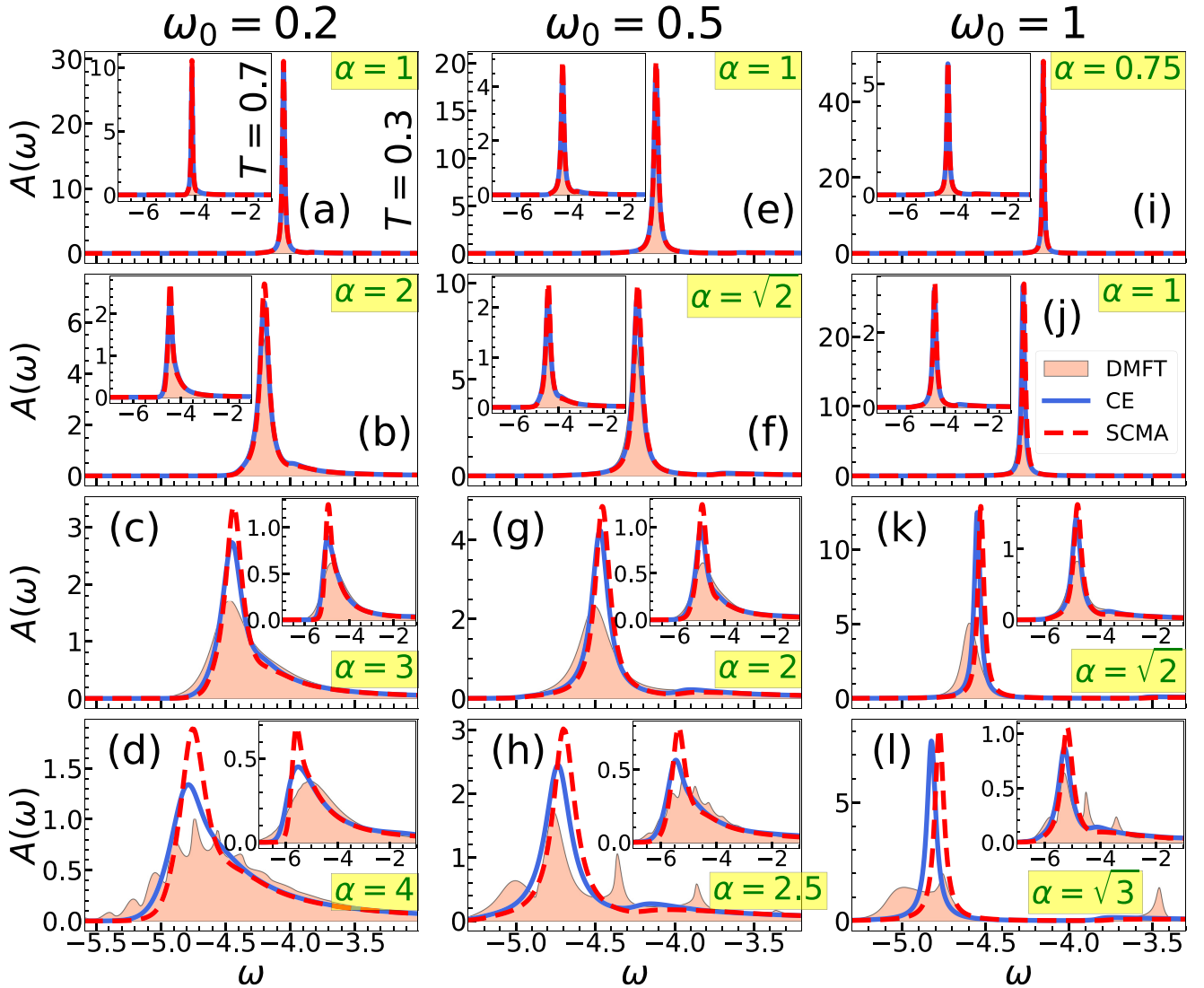


FIG. 12. (a)–(h) Comparison of the CE, DMFT, and SCMA spectral functions in 2D for $k = 0$ and $t_0 = 1$. The main panels show the results for $T_1 = 0.3$, while $T_2 = 0.7$ results are shown in the insets.

peak; see Fig. 1(c) from Ref. [50]. However, Fig. S9 in the Supplemental Material of Ref. [52] demonstrates that the spectral function in the thermodynamic limit for $t_0 = \omega_0 = g = 1$, $k = \pi$ consists of a broad single-peak structure even at $T = 0$. This conclusion was reached by carefully examining the finite-size effects using the numerically exact hierarchical equations of motion method (HEOM). It was established that the system with $N = 10$ lattice sites is representative of the thermodynamic limit, although much smaller systems are required for the $k = 0$ results. Furthermore, the same figure shows that two distinct peaks emerge for $N = 6$ and $k = \pi$, in accordance with the FTLM results. Hence, CE will provide much better results in the thermodynamic limit than previously expected. We note that for $t_0 = \omega_0 = g = 1$ and finite temperatures, one might expect that the required lattice size, representative of the thermodynamic limit, does not exceed $N = 10$, as the electron experiences much more scattering compared to the $T = 0$ case. This will be cross-checked independently (using the DMFT) in the rest of this Appendix for finite T , which satisfies the $T < \omega_0$ condi-

tion. In that case, we analyze the overall performance of the CE.

In Fig. 13(a), we show the FTLM data, (originally from Ref. [44]) used in Ref. [50], and compare them to the DMFT applied on a system of finite lattice size. We exploit the fact that the corresponding spectral functions (although certainly not as accurate in comparison with the exact solution) provide a rough estimate of how large N should be to faithfully represent the thermodynamic limit; see Sec. IV from the Supplemental Material of Ref. [52] for more details. In accordance with the FTLM results, we see that the DMFT spectral function for $N = 6$ also predicts distinct peaks around $\omega \approx 1.5$ and $\omega \approx 2.5$, although there is an additional peak around $\omega \approx 2$. Nevertheless, these results change drastically with increasing N and practically converge for $N = 10$. This is the same N as predicted by HEOM at $T = 0$. Therefore, the presented FTLM results are not representative of the thermodynamic limit. Additionally, Fig. 13(a) also shows that FTLM results for $T = 0.6$ and $T = 0.8$ are quite similar. Hence, our further analysis will be conducted for $T = 0.7$ case.

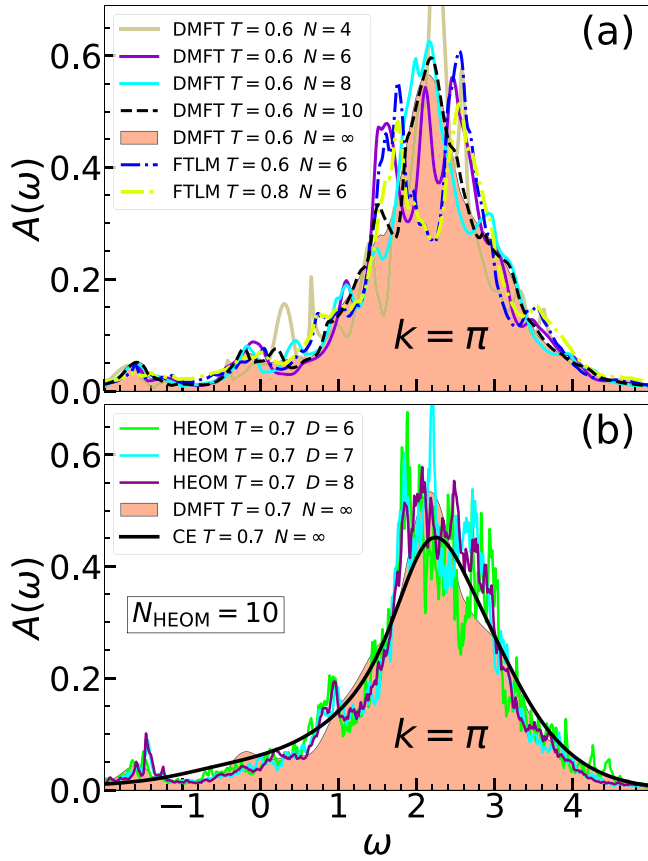


FIG. 13. CE, DMFT, FTLM, and HEOM spectral functions for $t_0 = \omega_0 = g = 1$. (a) Analysis of the finite-size effects. (b) Inspecting the convergence of HEOM data with respect to hierarchy depth D .

In Fig. 13(b), we present HEOM results for $N = 10$ and compare them to CE and DMFT. We note that HEOM has one additional parameter, the so-called hierarchy depth D . For details, we refer the reader to Ref. [47], but we only briefly mention that the numerically exact results are formally obtained in the limit $D \rightarrow \infty$. In practice, we always check whether the results converge with respect to D , which cannot be increased indefinitely, as finite computer memory presents a limiting factor. We see that the HEOM results have practically converged for $N = 10$ and $D = 8$. Here, the HEOM solution does not possess the two-peak structure predicted by the FTLM on a smaller lattice size ($N = 6$). It actually gives only a single, broad peak around $\omega \approx 2$, which is correctly reproduced by both the CE and the DMFT. Although the CE misses the quasiparticle peak around $\omega \approx -1.5$, we conclude that CE gives much more accurate results for the thermodynamic limit than for a finite system.

APPENDIX D: MOBILITY RESULTS FROM THE ONE-SHOT MIGDAL APPROXIMATION

In Sec. V, we presented and analyzed the mobility predictions from the CE, DMFT, and SCMA methods. Here, we supplement that study with the data from the one-shot MA (i.e., SCMA without self-consistency). The results are shown in Fig. 14. Since the mobility results have already been

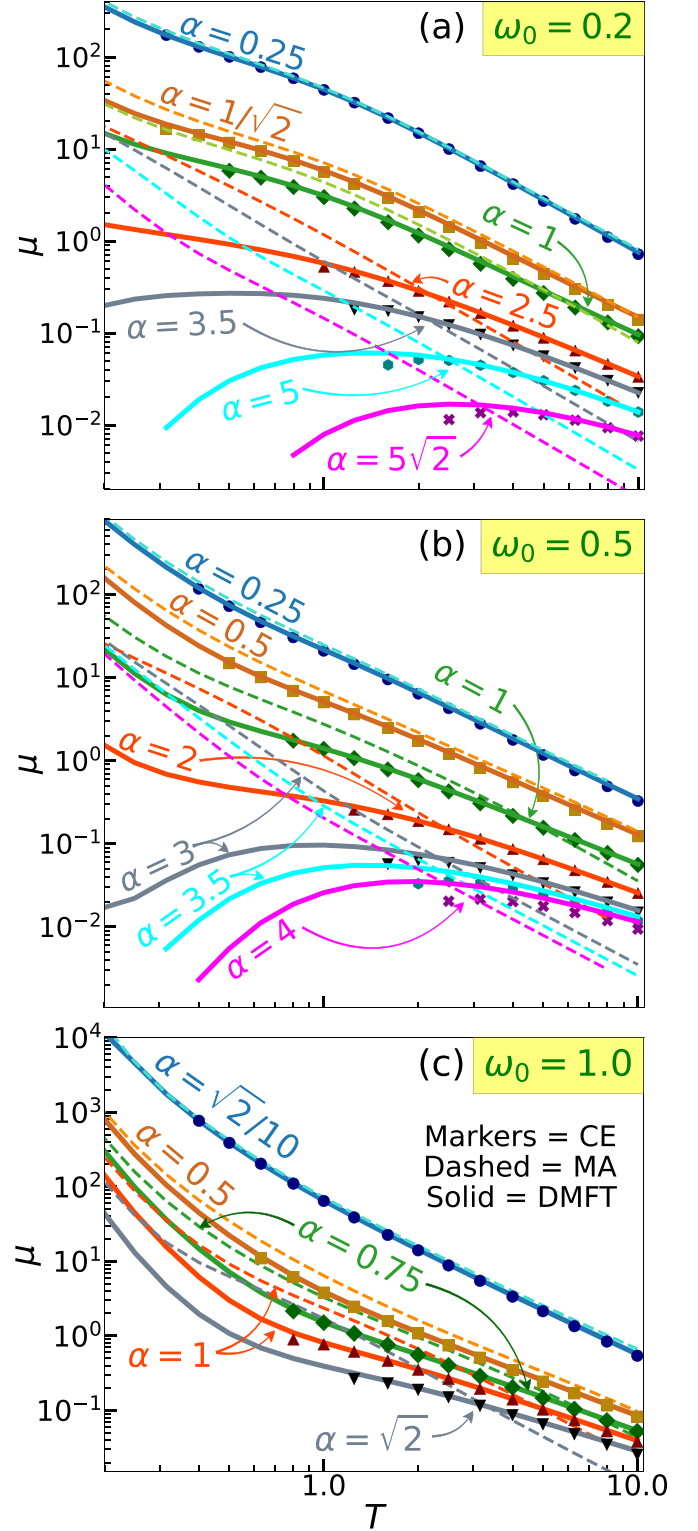


FIG. 14. Temperature dependence of the mobility within CE, DMFT, and MA. Here $t_0 = 1$.

thoroughly analyzed in Sec. V, we will here give only brief comments about the performance of the MA. Figure 14(a) shows that MA is practically useless for $\alpha \gtrsim 2.5$. Here, the results are not even qualitatively correct, regardless of the temperature. Even for $\alpha = 1$, the results are still not satisfactory:

the predictions for $T < 4$ ($T > 9$) overestimate (underestimate) the DMFT benchmark. MA proves to be reliable only for very weak interactions $\alpha \lesssim 1/\sqrt{2}$. Here, the results are better for higher temperatures. This is expected as the MA

takes into account only the lowest-order Feynman diagram, while the relevance of higher-order diagrams decreases as the temperature is increased. Similar analysis can be repeated for other phonon frequencies in Figs. 14(b) and 14(c).

-
- [1] G. Mahan, *Many-Particle Physics* (Kluwer Academic, New York, 2000).
- [2] R. Kubo, Generalized cumulant expansion method, *J. Phys. Soc. Jpn.* **17**, 1100 (1962).
- [3] B. I. Lundqvist, Characteristic structure in core electron spectra of metals due to the electron-plasmon coupling, *Phys. Kondens. Mater.* **9**, 236 (1969).
- [4] D. C. Langreth, Singularities in the x-ray spectra of metals, *Phys. Rev. B* **1**, 471 (1970).
- [5] L. Hedin, Effects of recoil on shake-up spectra in metals, *Phys. Scr.* **21**, 477 (1980).
- [6] L. Hedin, On correlation effects in electron spectroscopies and the *GW* approximation, *J. Phys.: Condens. Matter* **11**, R489 (1999).
- [7] F. Aryasetiawan, L. Hedin, and K. Karlsson, Multiple Plasmon Satellites in Na and Al Spectral Functions from *Ab Initio* Cumulant Expansion, *Phys. Rev. Lett.* **77**, 2268 (1996).
- [8] B. Holm and F. Aryasetiawan, Self-consistent cumulant expansion for the electron gas, *Phys. Rev. B* **56**, 12825 (1997).
- [9] G. D. Mahan, Phonon-broadened optical spectra: Urbach's rule, *Phys. Rev.* **145**, 602 (1966).
- [10] D. Dunn, ElectronPhonon Interactions in an insulator, *Can. J. Phys.* **53**, 321 (1975).
- [11] O. Gunnarsson, V. Meden, and K. Schönhammer, Corrections to Migdal's theorem for spectral functions: A cumulant treatment of the time-dependent Green's function, *Phys. Rev. B* **50**, 10462 (1994).
- [12] C. Verdi, F. Caruso, and F. Giustino, Origin of the crossover from polarons to Fermi liquids in transition metal oxides, *Nat. Commun.* **8**, 15769 (2017).
- [13] G. Antonius, Y.-H. Chan, and S. G. Louie, Polaron spectral properties in doped ZnO and SrTiO₃ from first principles, *Phys. Rev. Res.* **2**, 043296 (2020).
- [14] S. Moser, L. Moreschini, J. Jačimović, O. S. Barišić, H. Berger, A. Magrez, Y. J. Chang, K. S. Kim, A. Bostwick, E. Rotenberg, L. Forró, and M. Grioni, Tunable Polaronic Conduction in Anatase TiO₂, *Phys. Rev. Lett.* **110**, 196403 (2013).
- [15] F. Giustino, Electron-phonon interactions from first principles, *Rev. Mod. Phys.* **89**, 015003 (2017).
- [16] J.-J. Zhou and M. Bernardi, Predicting charge transport in the presence of polarons: The beyond-quasiparticle regime in SrTiO₃, *Phys. Rev. Res.* **1**, 033138 (2019).
- [17] B. K. Chang, J.-J. Zhou, N.-E. Lee, and M. Bernardi, Intermediate polaronic charge transport in organic crystals from a many-body first-principles approach, *npj Comput. Mater.* **8**, 63 (2022).
- [18] S. M. Story, J. J. Kas, F. D. Vila, M. J. Verstraete, and J. J. Rehr, Cumulant expansion for phonon contributions to the electron spectral function, *Phys. Rev. B* **90**, 195135 (2014).
- [19] J. J. Kas, J. J. Rehr, and L. Reining, Cumulant expansion of the retarded one-electron Green function, *Phys. Rev. B* **90**, 085112 (2014).
- [20] J. Lischner, D. Vigil-Fowler, and S. G. Louie, Satellite structures in the spectral functions of the two-dimensional electron gas in semiconductor quantum wells: A *GW* plus cumulant study, *Phys. Rev. B* **89**, 125430 (2014).
- [21] F. Caruso and F. Giustino, Spectral fingerprints of electron-plasmon coupling, *Phys. Rev. B* **92**, 045123 (2015).
- [22] J. S. Zhou, J. Kas, L. Sponza, I. Reshetnyak, M. Guzzo, C. Giorgetti, M. Gatti, F. Sottile, J. Rehr, and L. Reining, Dynamical effects in electron spectroscopy, *J. Chem. Phys.* **143**, 184109 (2015).
- [23] B. Gumhalter, V. Kovač, F. Caruso, H. Lambert, and F. Giustino, On the combined use of *GW* approximation and cumulant expansion in the calculations of quasiparticle spectra: The paradigm of Si valence bands, *Phys. Rev. B* **94**, 035103 (2016).
- [24] D. Vigil-Fowler, S. G. Louie, and J. Lischner, Dispersion and line shape of plasmon satellites in one, two, and three dimensions, *Phys. Rev. B* **93**, 235446 (2016).
- [25] J. S. Zhou, M. Gatti, J. J. Kas, J. J. Rehr, and L. Reining, Cumulant Green's function calculations of plasmon satellites in bulk sodium: Influence of screening and the crystal environment, *Phys. Rev. B* **97**, 035137 (2018).
- [26] J. Ma and J. Cao, Förster resonance energy transfer, absorption and emission spectra in multichromophoric systems. I. Full cumulant expansions and system-bath entanglement, *J. Chem. Phys.* **142**, 094106 (2015).
- [27] L. Cupellini, F. Lipparini, and J. Cao, Absorption and circular dichroism spectra of molecular aggregates with the full cumulant expansion, *J. Phys. Chem. B* **124**, 8610 (2020).
- [28] J. A. Nöthling, T. Mančal, and T. Krüger, Accuracy of approximate methods for the calculation of absorption-type linear spectra with a complex system-bath coupling, *J. Chem. Phys.* **157**, 095103 (2022).
- [29] J. P. Nery, P. B. Allen, G. Antonius, L. Reining, A. Miglio, and X. Gonze, Quasiparticles and phonon satellites in spectral functions of semiconductors and insulators: Cumulants applied to the full first-principles theory and the Fröhlich polaron, *Phys. Rev. B* **97**, 115145 (2018).
- [30] N. Kandolf, C. Verdi, and F. Giustino, Many-body Green's function approaches to the doped Fröhlich solid: Exact solutions and anomalous mass enhancement, *Phys. Rev. B* **105**, 085148 (2022).
- [31] A. S. Mishchenko, N. V. Prokof'ev, A. Sakamoto, and B. V. Svistunov, Diagrammatic quantum Monte Carlo study of the Fröhlich polaron, *Phys. Rev. B* **62**, 6317 (2000).
- [32] T. Holstein, Studies of polaron motion: Part I. The molecular-crystal model, *Ann. Phys.* **8**, 325 (1959).
- [33] I. Lang and Y. A. Firsov, Kinetic theory of semiconductors with low mobility, *Zh. Eksp. Teor. Fiz.* **43**, 1843 (1962) [*Sov. Phys. JETP* **16**, 1301 (1963)].
- [34] A. S. Alexandrov, *Polarons in Advanced Materials*, Springer Series in Materials Science, Vol. 103 (Springer, Dordrecht, 2007).

- [35] E. Jeckelmann and S. R. White, Density-matrix renormalization-group study of the polaron problem in the Holstein model, *Phys. Rev. B* **57**, 6376 (1998).
- [36] P. E. Kornilovitch, Continuous-Time Quantum Monte Carlo Algorithm for the Lattice Polaron, *Phys. Rev. Lett.* **81**, 5382 (1998).
- [37] A. H. Romero, D. W. Brown, and K. Lindenberg, Converging toward a practical solution of the Holstein molecular crystal model, *J. Chem. Phys.* **109**, 6540 (1998).
- [38] S. Fratini and S. Ciuchi, Dynamical Mean-Field Theory of Transport of Small Polarons, *Phys. Rev. Lett.* **91**, 256403 (2003).
- [39] S. Fratini and S. Ciuchi, Optical properties of small polarons from dynamical mean-field theory, *Phys. Rev. B* **74**, 075101 (2006).
- [40] C. Zhang, E. Jeckelmann, and S. R. White, Dynamical properties of the one-dimensional Holstein model, *Phys. Rev. B* **60**, 14092 (1999).
- [41] G. L. Goodvin, M. Berciu, and G. A. Sawatzky, Green's function of the Holstein polaron, *Phys. Rev. B* **74**, 245104 (2006).
- [42] M. Berciu, Green's Function of a Dressed Particle, *Phys. Rev. Lett.* **97**, 036402 (2006).
- [43] S. Ciuchi, E. Cappelluti, and S. Fratini, Optical properties of lattice/magnetic small polarons from DMFT, *J. Phys. Chem. Solids* **69**, 2164 (2008).
- [44] J. Bonča, S. A. Trugman, and M. Berciu, Spectral function of the Holstein polaron at finite temperature, *Phys. Rev. B* **100**, 094307 (2019).
- [45] N. Prodanović and N. Vukmirović, Charge carrier mobility in systems with local electron-phonon interaction, *Phys. Rev. B* **99**, 104304 (2019).
- [46] D. Jansen, J. Bonča, and F. Heidrich-Meisner, Finite-temperature density-matrix renormalization group method for electron-phonon systems: Thermodynamics and Holstein-polaron spectral functions, *Phys. Rev. B* **102**, 165155 (2020).
- [47] V. Janković and N. Vukmirović, Spectral and thermodynamic properties of the Holstein polaron: Hierarchical equations of motion approach, *Phys. Rev. B* **105**, 054311 (2022).
- [48] J. Bonča and S. A. Trugman, Electron removal spectral function of a polaron coupled to dispersive optical phonons, *Phys. Rev. B* **106**, 174303 (2022).
- [49] A. S. Mishchenko, N. Nagaosa, and N. Prokof'ev, Diagrammatic Monte Carlo Method for Many-Polaron Problems, *Phys. Rev. Lett.* **113**, 166402 (2014).
- [50] P. J. Robinson, I. S. Dunn, and D. R. Reichman, Cumulant methods for electron-phonon problems. I. Perturbative expansions, *Phys. Rev. B* **105**, 224304 (2022).
- [51] P. J. Robinson, I. S. Dunn, and D. R. Reichman, Cumulant methods for electron-phonon problems. II. The self-consistent cumulant expansion, *Phys. Rev. B* **105**, 224305 (2022).
- [52] P. Mitrić, V. Janković, N. Vukmirović, and D. Tanasković, Spectral Functions of the Holstein Polaron: Exact and Approximate Solutions, *Phys. Rev. Lett.* **129**, 096401 (2022).
- [53] S. Ciuchi, F. de Pasquale, S. Fratini, and D. Feinberg, Dynamical mean-field theory of the small polaron, *Phys. Rev. B* **56**, 4494 (1997).
- [54] See Supplemental Material at <http://link.aps.org/supplemental/10.1103/PhysRevB.107.125165> for additional figures and derivations.
- [55] D. Levin, Fast integration of rapidly oscillatory functions, *J. Comput. Appl. Math.* **67**, 95 (1996).
- [56] A. Migdal, Interaction between electrons and lattice vibrations in a normal metal, *Zh. Eksp. Teor. Fiz.* **34**, 1438 (1958) [*Sov. Phys. JETP* **7**, 996 (1958)].
- [57] A. Georges, G. Kotliar, W. Krauth, and M. J. Rozenberg, Dynamical mean-field theory of strongly correlated fermion systems and the limit of infinite dimensions, *Rev. Mod. Phys.* **68**, 13 (1996).
- [58] P. E. Kornilovitch, Photoemission spectroscopy and sum rules in dilute electron-phonon systems, *Europhys. Lett.* **59**, 735 (2002).
- [59] A. Khurana, Electrical Conductivity in the Infinite-Dimensional Hubbard Model, *Phys. Rev. Lett.* **64**, 1990 (1990).
- [60] S. Fratini, F. de Pasquale, and S. Ciuchi, Optical absorption from a nondegenerate polaron gas, *Phys. Rev. B* **63**, 153101 (2001).
- [61] W. H. Press, S. A. Teukolsky, W. T. Vetterling, and B. P. Flannery, *Numerical Recipes: The Art of Scientific Computing*, 3rd ed. (Cambridge University Press, Cambridge, 2007).
- [62] S. Fratini, D. Mayou, and S. Ciuchi, The transient localization scenario for charge transport in crystalline organic materials, *Adv. Funct. Mater.* **26**, 2292 (2016).
- [63] J. Bonča and S. A. Trugman, Dynamic properties of a polaron coupled to dispersive optical phonons, *Phys. Rev. B* **103**, 054304 (2021).
- [64] G. D. Mahan, Mobility of polarons, *Phys. Rev.* **142**, 366 (1966).

Supplemental Material: Cumulant expansion in the Holstein model: Spectral functions and mobility

Petar Mitrić, Veljko Janković, Nenad Vukmirović, and Darko Tanasković
Institute of Physics Belgrade, University of Belgrade, Pregrevaica 118, 11080 Belgrade, Serbia

Here we supplement the main text by giving an alternative derivation of the cumulant function in Sec. I, additional spectral functions and heat maps in Sec. II, and a comparison of the 1D ground state energy using DMFT, CE, SCMA, and MA in Sec. III.

I. ALTERNATIVE DERIVATION OF THE CUMULANT FUNCTION IN THE CE METHOD

In Sec. XI of the Supplemental Material in Ref. [S1], we showed that the Green's function, if there is only a single electron in the band, can be written as

$$G_{\mathbf{k}}(t) = -i\theta(t)\langle c_{\mathbf{k}}(t)c_{\mathbf{k}}^{\dagger} \rangle_{T,0}, \quad (\text{S1})$$

where:

$$c_{\mathbf{k}}(t) = e^{iHt}c_{\mathbf{k}}e^{-iHt}, \quad (\text{S2a})$$

$$H = H_{\text{el}} + H_{\text{ph}} + H_{\text{el-ph}}, \quad (\text{S2b})$$

$$H_{\text{el}} = -t_0 \sum_{\langle ij \rangle} (c_i^{\dagger}c_j + \text{H.c.}) = \sum_{\mathbf{k}} \varepsilon_{\mathbf{k}}c_{\mathbf{k}}^{\dagger}c_{\mathbf{k}}, \quad (\text{S2c})$$

$$H_{\text{ph}} = \omega_0 \sum_i a_i^{\dagger}a_i = \omega_0 \sum_{\mathbf{k}} a_{\mathbf{k}}^{\dagger}a_{\mathbf{k}}, \quad (\text{S2d})$$

$$\begin{aligned} H_{\text{el-ph}} &= -g \sum_i c_i^{\dagger}c_i (a_i^{\dagger} + a_i) \\ &= -\frac{g}{\sqrt{N}} \sum_{\mathbf{k},\mathbf{q}} c_{\mathbf{k}+\mathbf{q}}^{\dagger}c_{\mathbf{k}} (a_{\mathbf{q}} + a_{-\mathbf{q}}^{\dagger}). \end{aligned} \quad (\text{S2e})$$

Here, N is the number of sites (we take $N \rightarrow \infty$ in order to get the thermodynamic limit), while $\langle \dots \rangle_{T,0}$ denotes the thermal average over the states with no electrons

and arbitrary number of phonons

$$\langle x \rangle_{T,0} = \frac{\sum_{\{n_p\}} \langle 0, \tilde{n}_p | e^{-H_{\text{ph}}/T} x | 0, \tilde{n}_p \rangle}{\sum_{\{n_p\}} \langle 0, \tilde{n}_p | e^{-H_{\text{ph}}/T} | 0, \tilde{n}_p \rangle}. \quad (\text{S3})$$

For the rest of this section, an arbitrary state with n_p phonons and no electrons (since such state is not unique) will be denoted by $|0, \tilde{n}_p\rangle$, while $\sum_{\{n_p\}}$ represents the sum over all possible phonon configurations. We also introduce $|\mathbf{k}, \tilde{n}_p\rangle \equiv c_{\mathbf{k}}^{\dagger}|0, \tilde{n}_p\rangle$ and $Z_{\text{ph}} = \sum_{\{n_p\}} \langle 0, \tilde{n}_p | e^{-H_{\text{ph}}/T} | 0, \tilde{n}_p \rangle$.

Using the fact that $|0, \tilde{n}_p\rangle$ is an eigenstate of both the full and the phononic Hamiltonian $H|0, \tilde{n}_p\rangle = H_{\text{ph}}|0, \tilde{n}_p\rangle = n_p\omega_0|0, \tilde{n}_p\rangle$, we see how Eq. (S1) can be written in a more explicit form

$$G_{\mathbf{k}}(t) = \frac{-i\theta(t)}{Z_{\text{ph}}} \sum_{\{n_p\}} e^{i\omega_0 n_p t} e^{-n_p\omega_0/T} \langle 0, \tilde{n}_p | c_{\mathbf{k}} e^{-iHt} c_{\mathbf{k}}^{\dagger} | 0, \tilde{n}_p \rangle. \quad (\text{S4})$$

The term e^{-iHt} can be read off from

$$e^{iH_{\text{el}}t} e^{iH_{\text{ph}}t} e^{-iHt} = T_t \exp \left[-i \int_0^t dt_1 H_{\text{el-ph}}^{(I)}(t_1) \right], \quad (\text{S5})$$

which represents two different, but equivalent, forms for the evolution operator in the Dirac picture. Here, $H_{\text{el-ph}}^{(I)}$ is the electron-phonon interaction part of the Hamiltonian in the Dirac picture and T_t is the time-ordering operator. For the purely phononic part $e^{-iH_{\text{ph}}t}$ we use $\langle 0, \tilde{n}_p | e^{-iH_{\text{ph}}t} = e^{-i\omega_0 n_p t} \langle 0, \tilde{n}_p |$, while purely electronic part $e^{-iH_{\text{el}}t}$ is dealt with analogously $\langle 0, \tilde{n}_p | c_{\mathbf{k}} e^{-iH_{\text{el}}t} = e^{-i\varepsilon_{\mathbf{k}}t} \langle 0, \tilde{n}_p | c_{\mathbf{k}}$. Hence, Eq. (S4) becomes

$$G_{\mathbf{k}}(t) = -\frac{i\theta(t)}{Z_{\text{ph}}} e^{-i\varepsilon_{\mathbf{k}}t} \sum_{\{n_p\}} e^{-n_p\omega_0/T} \left\langle 0, \tilde{n}_p \left| c_{\mathbf{k}} T_t \exp \left[-i \int_0^t dt_1 H_{\text{el-ph}}^{(I)}(t_1) \right] c_{\mathbf{k}}^{\dagger} \right| 0, \tilde{n}_p \right\rangle \quad (\text{S6a})$$

$$\equiv -i\theta(t) e^{-i\varepsilon_{\mathbf{k}}t} \left\langle T_t e^{-i \int_0^t dt_1 H_{\text{el-ph}}^{(I)}(t_1)} \right\rangle_{T,\mathbf{k}}. \quad (\text{S6b})$$

The expressions of the form (S6b) have been extensively studied in the past. As shown in Eq. (6.10) of Kubo's cu-

mulant paper [S2], the expectation value with the time-ordering can be written as

$$\left\langle T_t e^{-i \int_0^t dt_1 H_{\text{el-ph}}^{(I)}(t_1)} \right\rangle_{T, \mathbf{k}} = \exp \left\langle T_t e^{-i \int_0^t dt_1 H_{\text{el-ph}}^{(I)}(t_1)} - 1 \right\rangle_{T, \mathbf{k}, c} \equiv e^{C_{\mathbf{k}}(t)}, \quad (\text{S7})$$

where we defined the cumulant function $C_{\mathbf{k}}(t)$. The notation $\langle \dots \rangle_c$ denotes the so-called cumulant average. For our present purposes, we only need to know how the first two cumulant averages are defined:

$$\langle X_1 \rangle_c = \langle X_1 \rangle \quad (\text{S8a})$$

$$\langle X_1 X_2 \rangle_c = \langle X_1 X_2 \rangle - \langle X_1 \rangle \langle X_2 \rangle. \quad (\text{S8b})$$

In general, the cumulant average is defined using the ordinary average, by formally expanding the following expression in the Taylor series with respect to ξ_i and equating, order by order, the terms on the left- and the right-hand side

$$\left\langle \exp \sum_j \xi_j X_j \right\rangle = \exp \left\langle \left(\exp \sum_j \xi_j X_j \right) - 1 \right\rangle_c. \quad (\text{S9})$$

The -1 term on the right-hand side is motivated by the fact that the expectation value of the unity operator is equal to 1. While our paper focuses on the cumulant of the second order, there is actually an analytic formula that relates the cumulant average of any order with the

ordinary average [S3].

Let us now go back to Eq. (S6b) and use Eq. (S7) to obtain

$$G_{\mathbf{k}}(t) = -i\theta(t)e^{-i\varepsilon_{\mathbf{k}}t}e^{C_{\mathbf{k}}(t)}, \quad (\text{S10})$$

where

$$C_{\mathbf{k}}(t) = \sum_{j=1}^{\infty} \left\langle T_t \frac{(-i)^j}{j!} \int_0^t \prod_{m=1}^j dt_m H_{\text{el-ph}}^{(I)}(t_m) \right\rangle_{T, \mathbf{k}, c}. \quad (\text{S11})$$

So far, everything was exact. The approximation, that we now introduce, consists of keeping only the first two terms in the previous equation ($j = 1$ and $j = 2$ terms) while neglecting everything else. This is known as the second-order cumulant expansion. In the $j = 1$ term, the cumulant average coincides with the ordinary average (see Eq. (S8a)), and hence vanishes due to Wick's theorem. As a consequence, the cumulant average can be simply replaced by the ordinary average in the case of $j = 2$ term as well; see Eq. (S8b). Therefore, the second-order cumulant function reads as

$$C_{\mathbf{k}}(t) = -\frac{1}{2} \int_0^t dt_1 \int_0^t dt_2 \left\langle T_t c_{\mathbf{k}} H_{\text{el-ph}}^{(I)}(t_1) H_{\text{el-ph}}^{(I)}(t_2) c_{\mathbf{k}}^\dagger \right\rangle_{T, 0}. \quad (\text{S12})$$

For a straightforward application of Wick's theorem, it is customary to rewrite electron creation and annihilation operators in the Dirac picture. In order not to change the already existing time ordering in Eq. (S12), the annihilation operator is expressed in the final time

$c_{\mathbf{k}} = e^{i\varepsilon_{\mathbf{k}}t} c_{\mathbf{k}}^{(I)}(t)$, while the creation operator is expressed in the initial time $c_{\mathbf{k}}^\dagger = c_{\mathbf{k}}^{\dagger(I)}(0)$. If we also use the explicit form of $H_{\text{el-ph}}^{(I)}(t)$ from Eq. (S2e), the Eq. (S12) becomes

$$C_{\mathbf{k}}(t) = -\frac{g^2}{2N} e^{i\varepsilon_{\mathbf{k}}t} \int_0^t dt_1 \int_0^t dt_2 \left\langle T_t c_{\mathbf{k}}^{(I)}(t) \sum_{\mathbf{k}_1, \mathbf{q}_1} c_{\mathbf{k}_1 + \mathbf{q}_1}^{\dagger(I)}(t_1) c_{\mathbf{k}_1}^{(I)}(t_1) A_{\mathbf{q}_1}^{(I)}(t_1) \sum_{\mathbf{k}_2, \mathbf{q}_2} c_{\mathbf{k}_2 + \mathbf{q}_2}^{\dagger(I)} c_{\mathbf{k}_2}^{(I)}(t_2) A_{\mathbf{q}_2}^{(I)}(t_2) c_{\mathbf{k}}^{\dagger(I)}(0) \right\rangle_{T, 0}, \quad (\text{S13})$$

where we introduced the shorthand notation for the phonon part $A_{\mathbf{q}} = a_{\mathbf{q}} + a_{-\mathbf{q}}^\dagger$. Eq. (S13) is now straightforwardly evaluated using Wick's theorem. Contraction between the phonon degrees of freedom gives [S4]

$$\left\langle T_t A_{\mathbf{q}_1}^{(I)}(t_1) A_{\mathbf{q}_2}^{(I)}(t_2) \right\rangle = \delta_{\mathbf{q}_1, -\mathbf{q}_2} iD(t_1 - t_2), \quad (\text{S14})$$

where $iD(t_1 - t_2) = (n_{ph} + 1)e^{-i\omega_0|t_1 - t_2|} + n_{ph}e^{i\omega_0|t_1 - t_2|}$ is the phonon propagator, while $n_{ph} = 1/(e^{\omega_0/T} - 1)$ is the Bose factor. Since we are working in the limit of vanishing electron density (single electron in a band), the contraction between the electron creation and annihilation operators does not have a hole part, and hence

reads as

$$\langle T_t c_{\mathbf{k}}^{(I)}(t_1) c_{\mathbf{q}}^{\dagger(I)}(t_2) \rangle = \delta_{\mathbf{k},\mathbf{q}} e^{-i\varepsilon_{\mathbf{k}}|t_1-t_2|} \theta(t_1-t_2). \quad (\text{S15})$$

Taking all of this into account, Eq. (S13) simplifies

$$C_{\mathbf{k}}(t) = -\frac{g^2}{2N} \sum_{\mathbf{q}} \int_0^t dt_1 \int_0^t dt_2 e^{i(\varepsilon_{\mathbf{k}}-\varepsilon_{\mathbf{q}})|t_2-t_1|} {}_iD(t_2-t_1). \quad (\text{S16})$$

We can get rid of the absolute value by noticing that the contributions for $t_2 > t_1$ and for $t_2 < t_1$ are equal. It is thus sufficient to restrict ourselves to $t_2 > t_1$ and multiply everything by 2. Also, the expression can be further simplified if we use

$$e^{i(\varepsilon_{\mathbf{k}}-\varepsilon_{\mathbf{q}}\pm\omega_0)(t_2-t_1)} = \int_{-\infty}^{\infty} d\omega e^{-i\omega(t_2-t_1)} \delta(\omega+\varepsilon_{\mathbf{k}}-\varepsilon_{\mathbf{q}}\pm\omega_0).$$

Then, the whole \mathbf{q} dependence is inside the Dirac delta function, which in combination with the summation over \mathbf{q} gives

$$\sum_{\mathbf{q}} \delta(\omega + \varepsilon_{\mathbf{k}} - \varepsilon_{\mathbf{q}} \pm \omega_0) = N\rho(\omega + \varepsilon_{\mathbf{k}} \pm \omega_0), \quad (\text{S17})$$

where ρ is the density of states. It is now straightforward to show that Eq. (S16) reduces to

$$C_{\mathbf{k}}(t) = g^2 \int_{-\infty}^{\infty} d\omega \frac{e^{-i\omega t} + i\omega t - 1}{\omega^2} \times [(n_{ph} + 1)\rho(\omega + \varepsilon_{\mathbf{k}} - \omega_0) + n_{ph}\rho(\omega + \varepsilon_{\mathbf{k}} + \omega_0)]. \quad (\text{S18})$$

This expression can be rewritten in terms of the Migdal self-energy (see Eq. (14) from the main text) as follows

$$C_{\mathbf{k}}(t) = \frac{1}{\pi} \int_{-\infty}^{\infty} d\omega \frac{|\text{Im}\Sigma^{\text{MA}}(\omega + \varepsilon_{\mathbf{k}})|}{\omega^2} (e^{-i\omega t} + i\omega t - 1). \quad (\text{S19})$$

Hence, we gave an alternative derivation of the cumulant function $C_{\mathbf{k}}(t)$, where the self-energy in the Migdal approximation emerges more explicitly than in Eq. (7) of the main text.

We note that the cumulant expansion method that we have now presented is analogous to the linked cluster expansion for the thermodynamic potential F in statistical mechanics. This is a consequence of the same mathematical form of $C_{\mathbf{k}}(t) = \ln(G_{\mathbf{k}}(t)/G_{\mathbf{k},0}(t))$ and $F = \ln(Z/Z_0)$, where Z and Z_0 are the partition function of the full and noninteracting theories.

II. SPECTRAL FUNCTIONS

In Sec. III of the main text, we presented spectral functions $A(\omega)$ and heat maps for $\omega_0 = 0.5$. Here, we present a large number of results for $\omega_0 = 1$, $\omega_0 = 0.2$, as well as some additional results for $\omega_0 = 0.5$ that are organized as follows:

1. Results for $\omega_0 = 1$:

- Fig. S1: $A(\omega)$ in the weak coupling regime for a wide range of temperatures and momenta.
- Fig. S2: $A(\omega)$ in the weak, intermediate and strong electron-phonon coupling regimes for $k = 0$ and $k = \pi$:
 - Fig. S2i: $k = 0$ at $T = 0.4$ and $T = 1$.
 - Fig. S2ii: $k = \pi$ at $T = 0.4$ and $T = 1$.
 - Fig. S2iii: $k = 0, \pi$ at $T = 2$ and $T = 5$.
- Fig. S3: $A(\omega)$ in the weak, intermediate and strong electron-phonon coupling regimes for $k = \pi/3$ and $k = 2\pi/3$:
 - Fig. S3i: $T = 0.4$.
 - Fig. S3ii: $T = 1$.
 - Fig. S3iii: $T = 2$ and $T = 5$.
- Fig. S4: Heat maps
 - Fig. S4i: $T = 0.4$.
 - Fig. S4ii: $T = 1$.

2. Results for $\omega_0 = 0.5$:

- Fig. S3: $A(\omega)$ in the weak, intermediate, and strong electron-phonon coupling regimes for $k = \pi/3$ and $k = 2\pi/3$:
 - Fig. S5i: $T = 0.3$.
 - Fig. S5ii: $T = 0.7$.
 - Fig. S5iii: $T = 2$ and $T = 5$.

3. Results for $\omega_0 = 0.2$:

- Fig. S6: $A(\omega)$ in the weak, intermediate and strong coupling regimes for $k = 0$ and $k = \pi$:
 - Fig. S6i: $k = 0$ at $T = 0.3$ and $T = 0.7$.
 - Fig. S6ii: $k = \pi$ at $T = 0.3$ and $T = 0.7$.
 - Fig. S6iii: $k = 0, \pi$ at $T = 2$ and $T = 5$.
- Fig. S7: $A(\omega)$ in the weak, intermediate and strong coupling regimes for $k = \pi/3$ and $k = 2\pi/3$:
 - Fig. S7i: $T = 0.3$.
 - Fig. S7ii: $T = 0.7$.

– Fig. S7iii: $T = 2$ and $T = 5$.

• Fig. S8: Heat maps:

- Fig. S8i: $T = 0.3$.
- Fig. S8ii: $T = 0.7$.

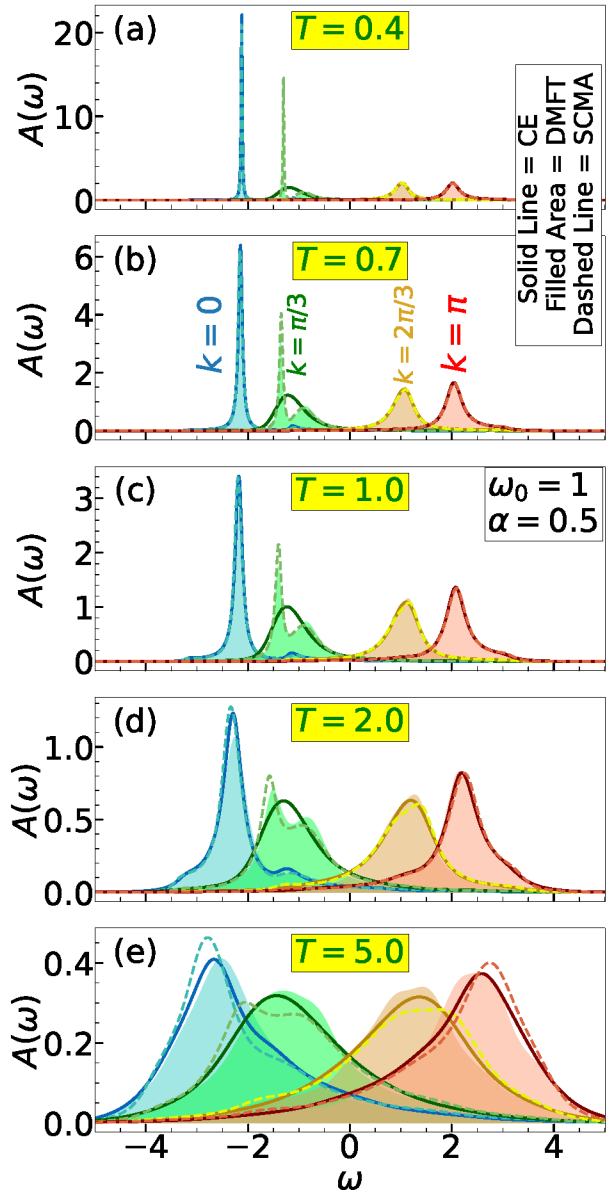
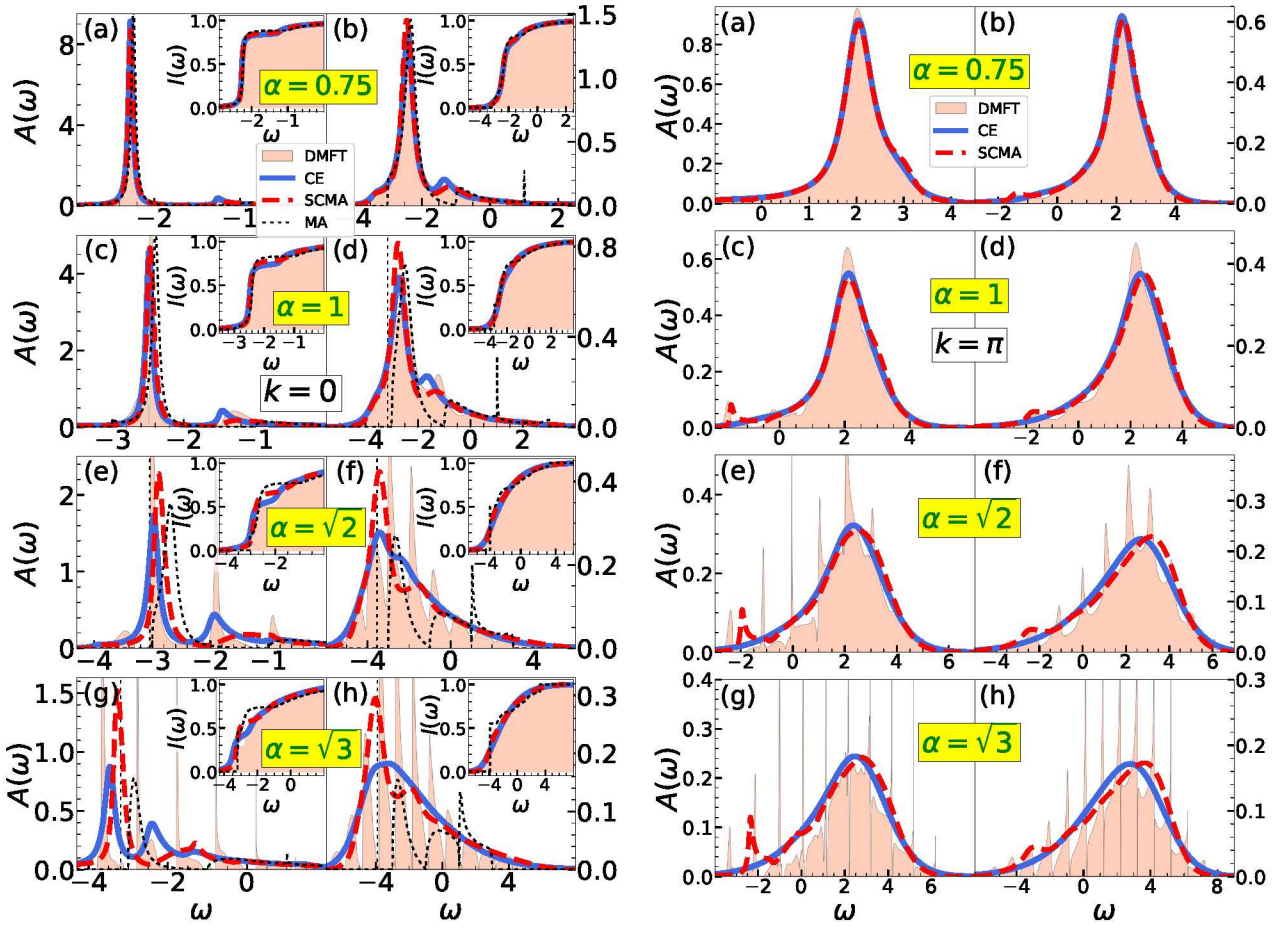
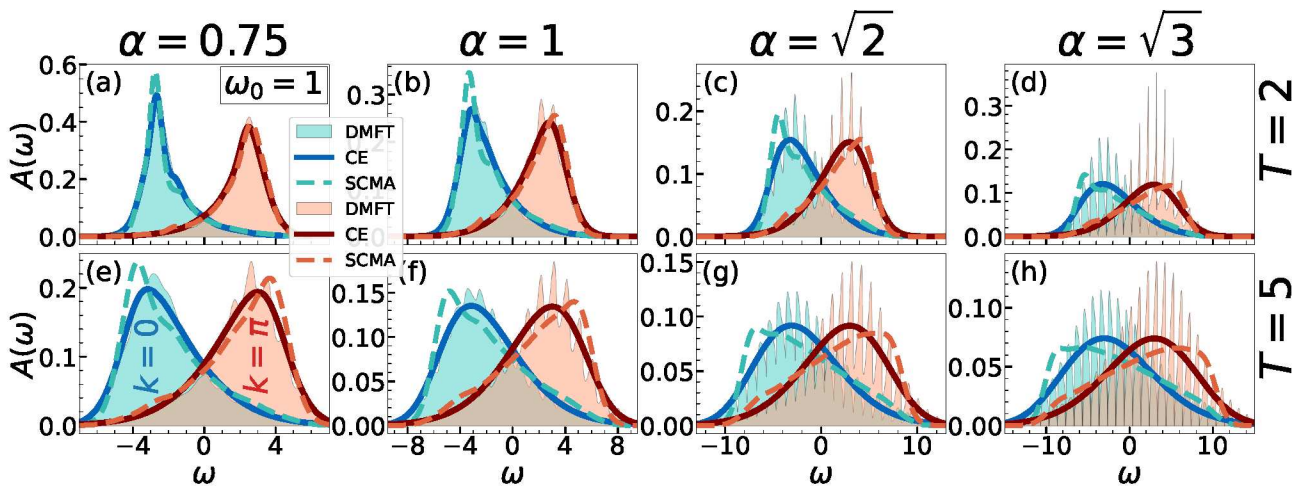


FIG. S1. (a)–(e) Comparison of CE, DMFT, and SCMA spectral functions in the weak coupling regime, for a wide range of temperatures. Here $t_0 = \omega_0 = 1$ and $\alpha = 0.5$.



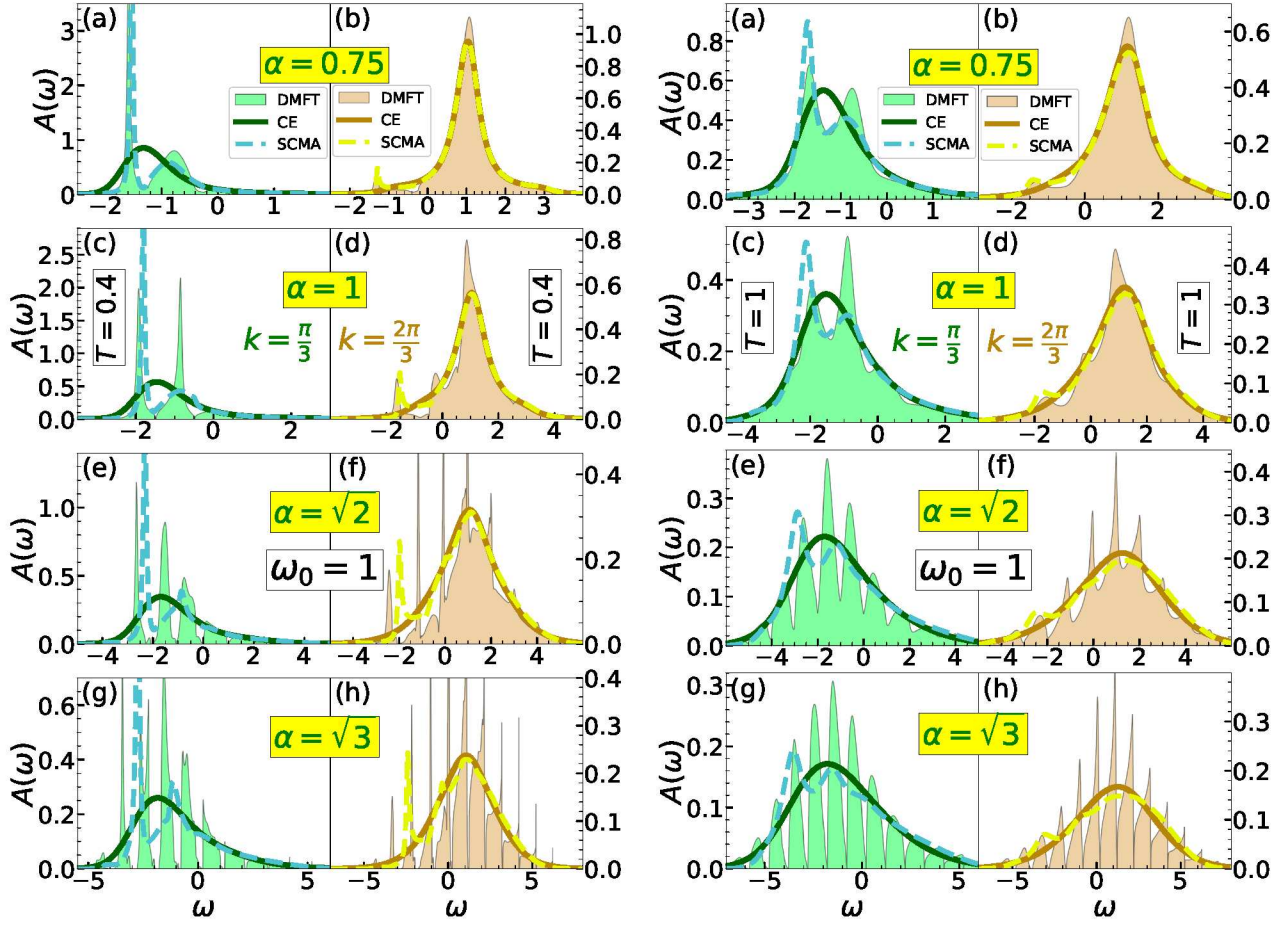
(i) (a)–(h) Spectral functions for $\omega_0 = 1$ and $k = 0$. In the left panels $T = 0.4$, while $T = 1$ in the right panels. Insets show the integrated spectral weights $I(\omega) = \int_{-\infty}^{\omega} A(\omega) d\omega$.

(ii) (a)–(h) Spectral functions for $\omega_0 = 1$ and $k = \pi$. In the left panels $T = 0.4$, while $T = 1$ in the right panels. Insets show the integrated spectral weights $I(\omega) = \int_{-\infty}^{\omega} A(\omega) d\omega$.



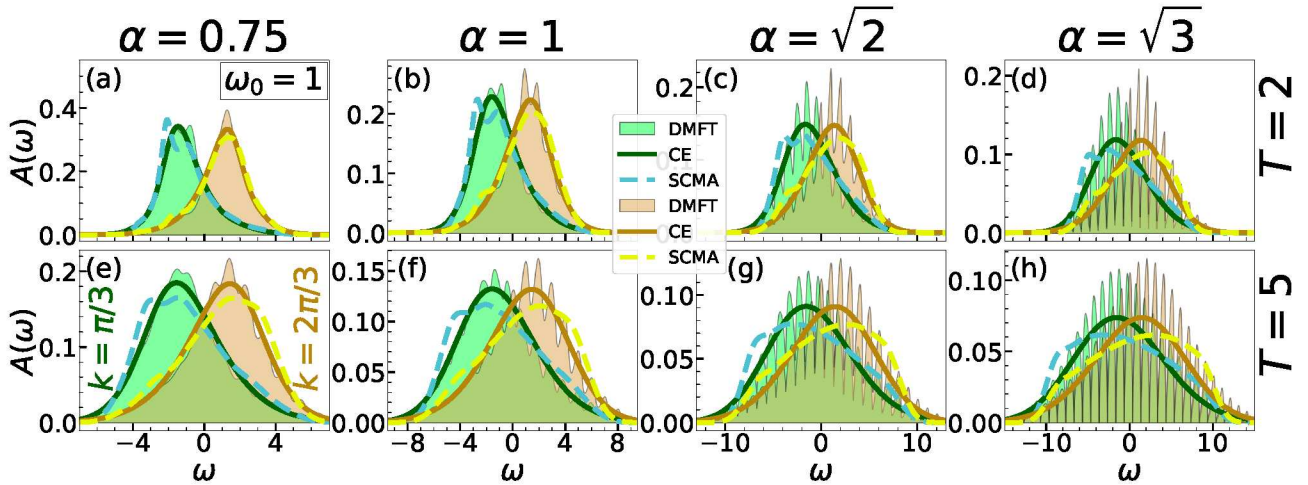
(iii) Spectral functions at higher temperatures for $\omega_0 = 1$ and $k = 0, \pi$.

FIG. S2. Comparison of the CE, DMFT, SCMA, and MA spectral functions in 1D for $t_0 = \omega_0 = 1$.



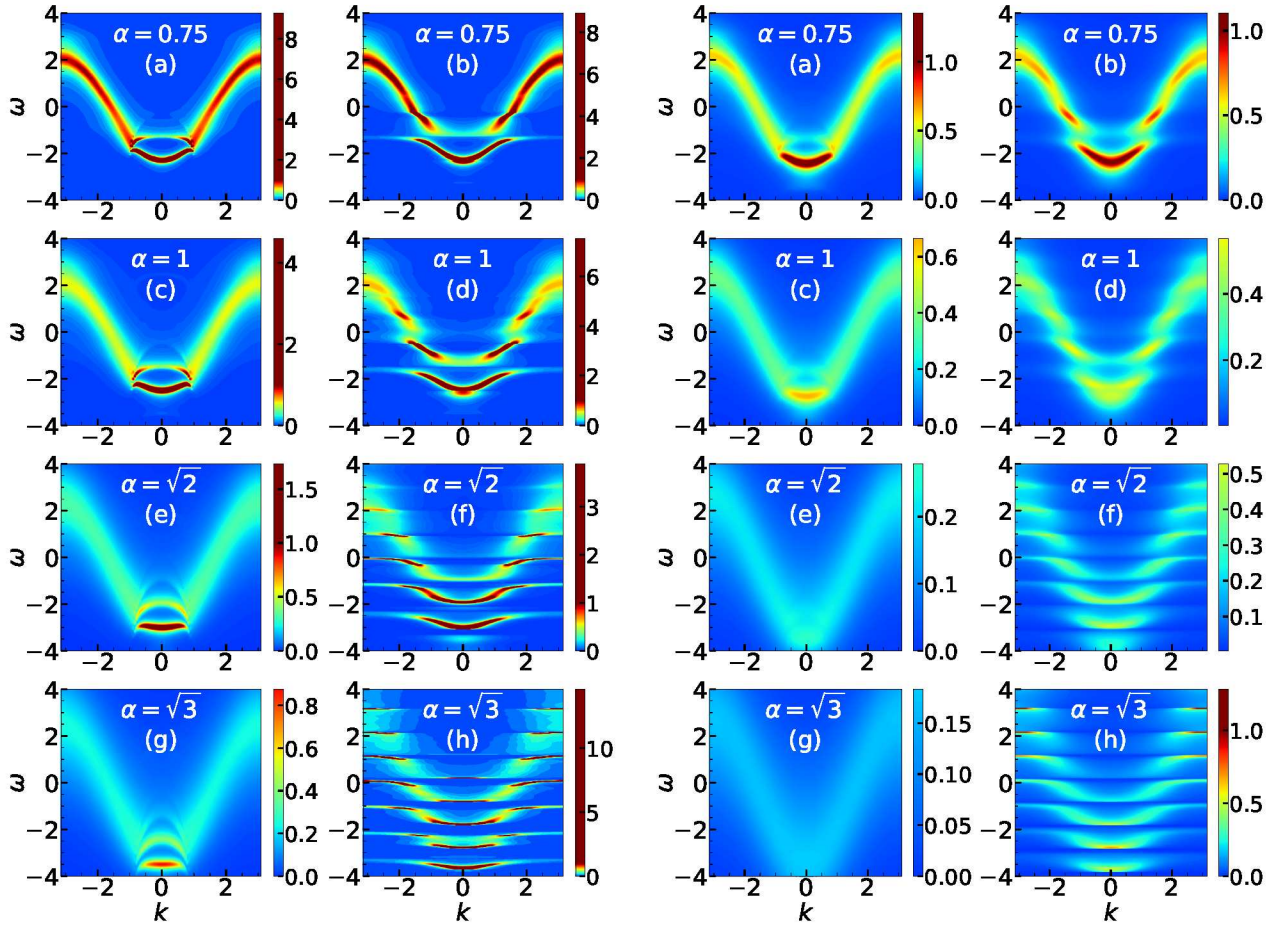
(i) (a)–(h) Spectral functions for $\omega_0 = 1$ and $T = 0.4$. In the left panels $k = \pi/3$, while $k = 2\pi/3$ in the right panels.

(ii) (a)–(h) Spectral functions for $\omega_0 = 1$ and $T = 1$. In the left panels $k = \pi/3$, while $k = 2\pi/3$ in the right panels.



(iii) Spectral functions at higher temperatures for $\omega_0 = 1$ and $k = \pi/3, 2\pi/3$.

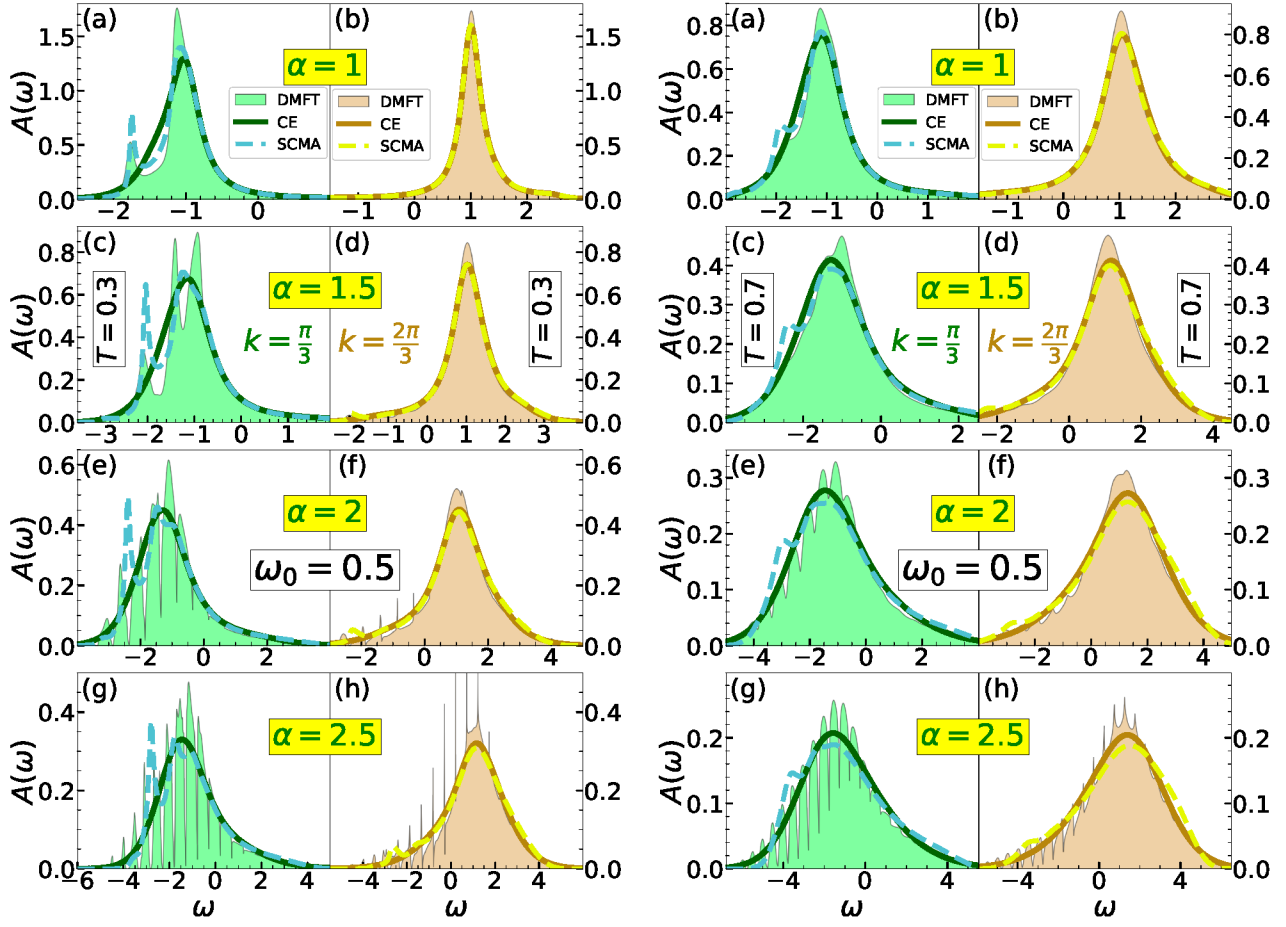
FIG. S3. Comparison of the CE, DMFT, and SCMA spectral functions in 1D for $t_0 = \omega_0 = 1$ and $k = \pi/3, 2\pi/3$.



(i) (a)–(h) Heat maps for $T = 0.4$. In the left panels, we present CE results, while the DMFT benchmark is presented in the right panels. All plots use the same color coding.

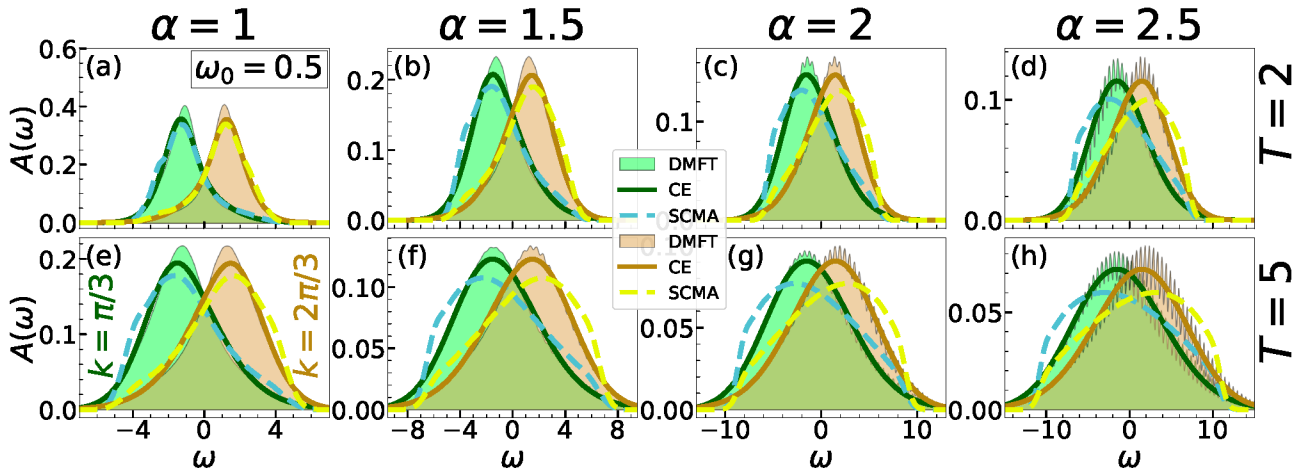
(ii) (a)–(h) Heat maps for $T = 1$. In the left panels, we present CE results, while the DMFT benchmark is presented in the right panels. All plots use the same color coding.

FIG. S4. Comparison of the CE and DMFT heat maps for $t_0 = \omega_0 = 1$.



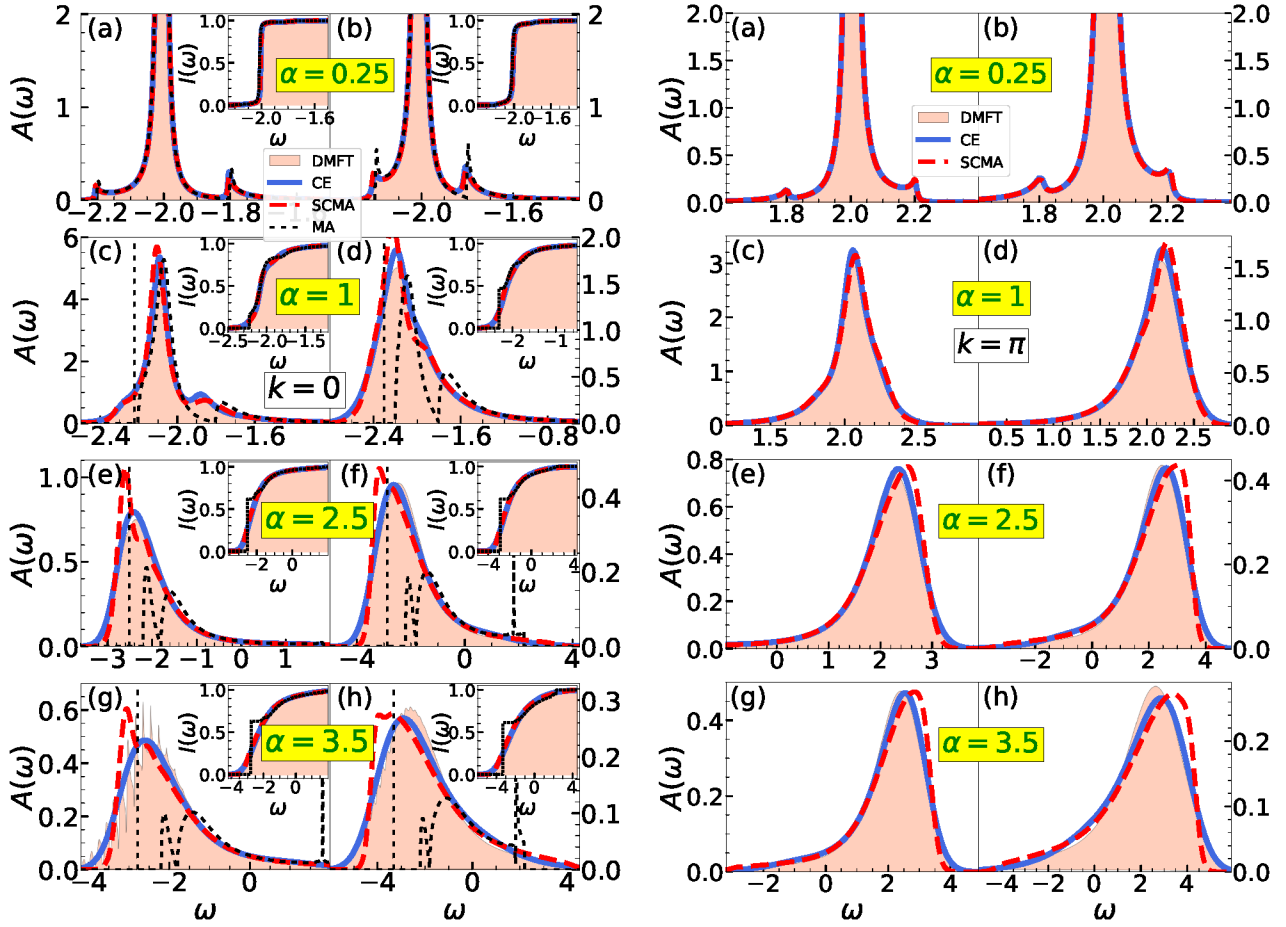
(i) (a)–(h) Spectral functions for $\omega_0 = 0.5$ and $T = 0.3$. In the left panels $k = \pi/3$, while $k = 2\pi/3$ in the right panels.

(ii) (a)–(h) Spectral functions for $\omega_0 = 0.5$ and $T = 0.7$. In the left panels $k = \pi/3$, while $k = 2\pi/3$ in the right panels.



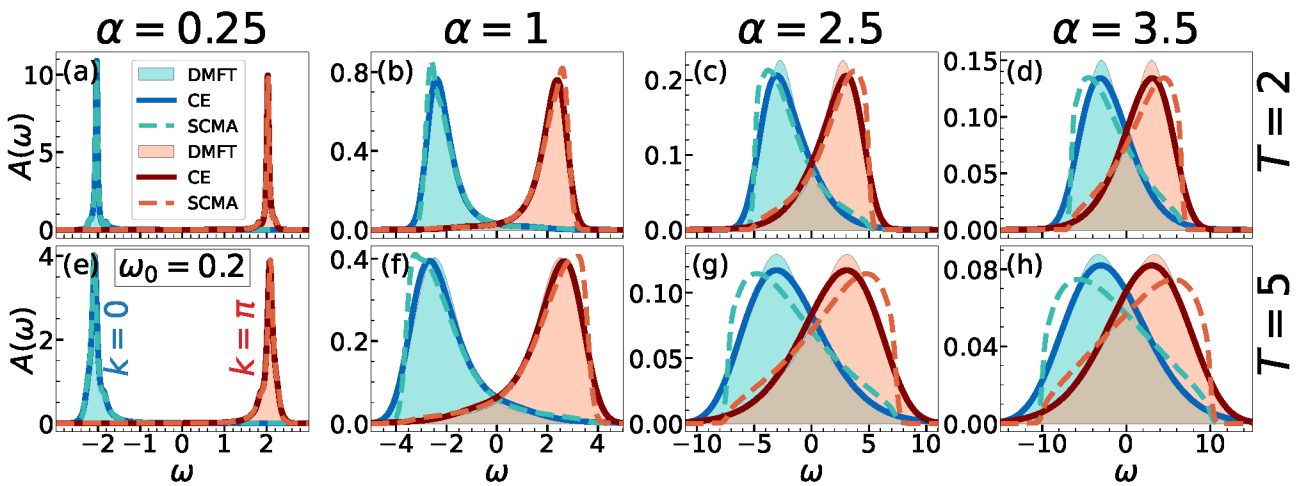
(iii) Spectral functions at higher temperatures for $\omega_0 = 0.5$ and $k = \pi/3, 2\pi/3$.

FIG. S5. Comparison of the CE, DMFT, and SCMA spectral functions in 1D for $t_0 = 1$, $\omega_0 = 0.5$ and $k = \pi/3, 2\pi/3$.



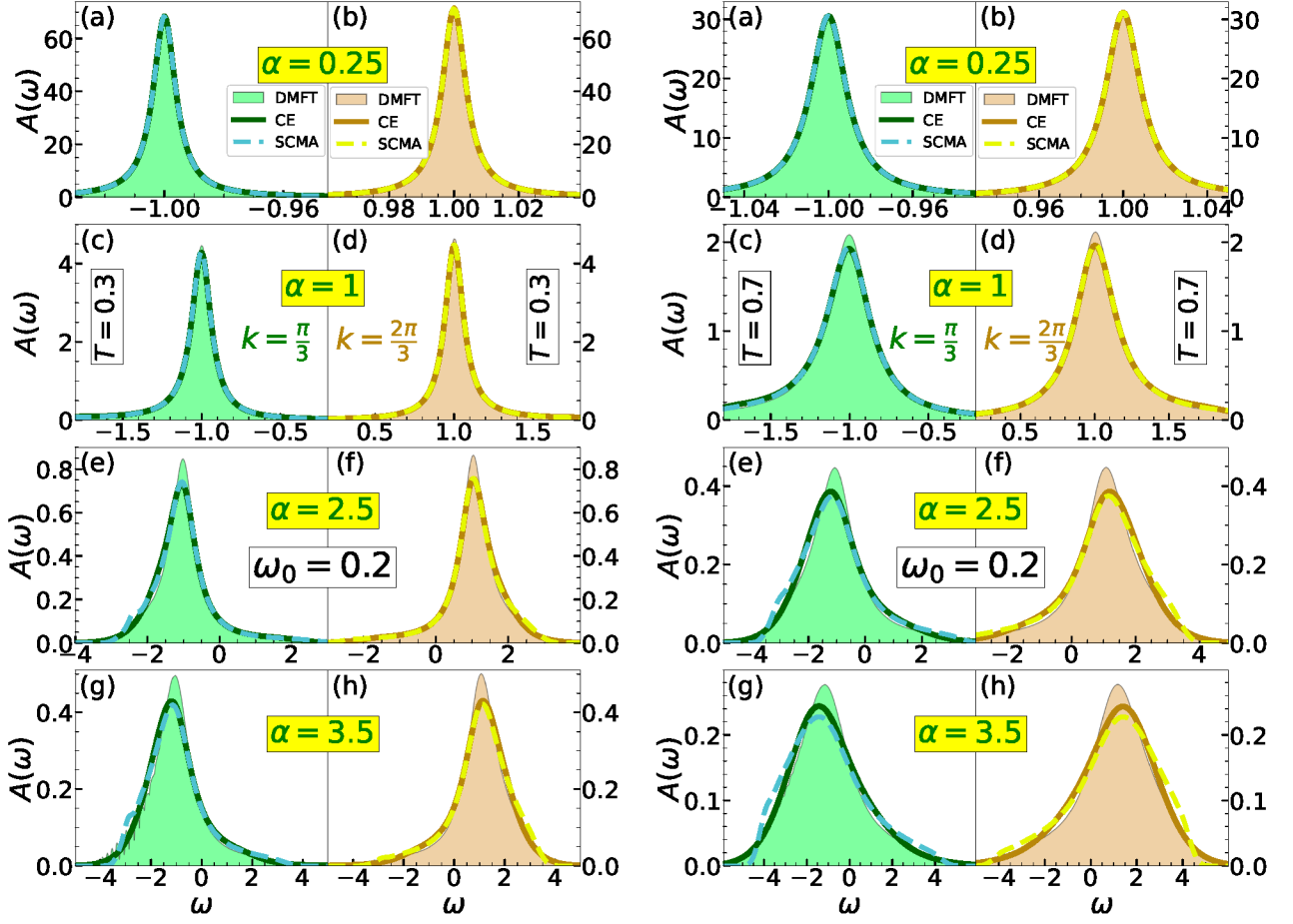
(i) (a)–(h) Spectral functions for $\omega_0 = 0.2$ and $k = 0$. In the left panels $T = 0.3$, while $T = 0.7$ in the right panels. Insets show the integrated spectral weight $I(\omega) = \int_{-\infty}^{\infty} A(\omega) d\omega$.

(ii) (a)–(h) Spectral functions for $\omega_0 = 0.2$ and $k = \pi$. In the left panels $T = 0.3$, while $T = 0.7$ in the right panels. Insets show the integrated spectral weight $I(\omega) = \int_{-\infty}^{\infty} A(\omega) d\omega$.



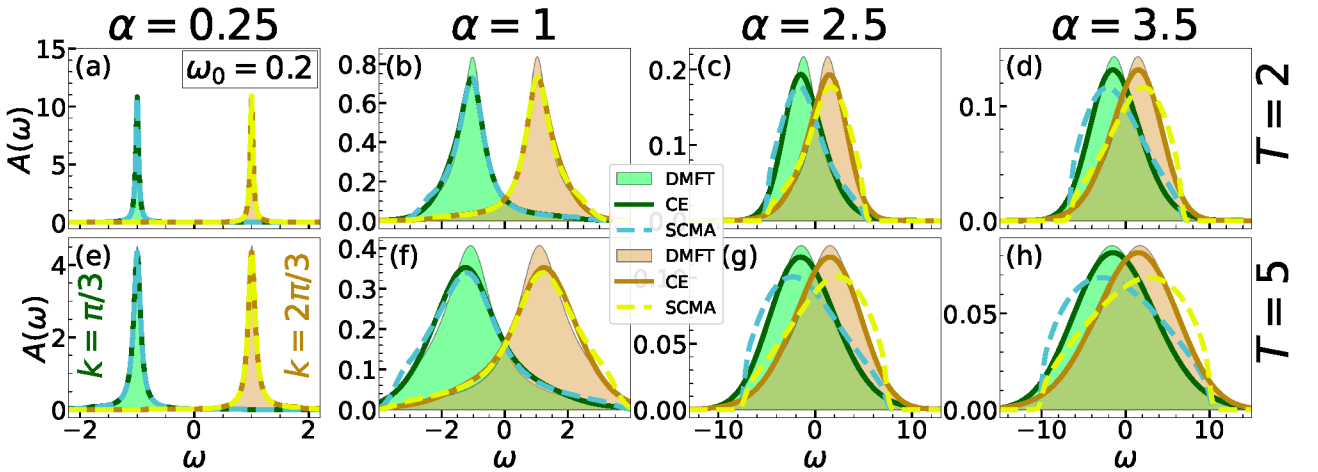
(iii) Spectral functions at higher temperatures for $\omega_0 = 0.2$ and $k = 0, \pi$.

FIG. S6. Comparison of the CE, DMFT, SCMA, and MA spectral functions in 1D for $t_0 = 1$, $\omega_0 = 0.2$, and $k = 0, \pi$.



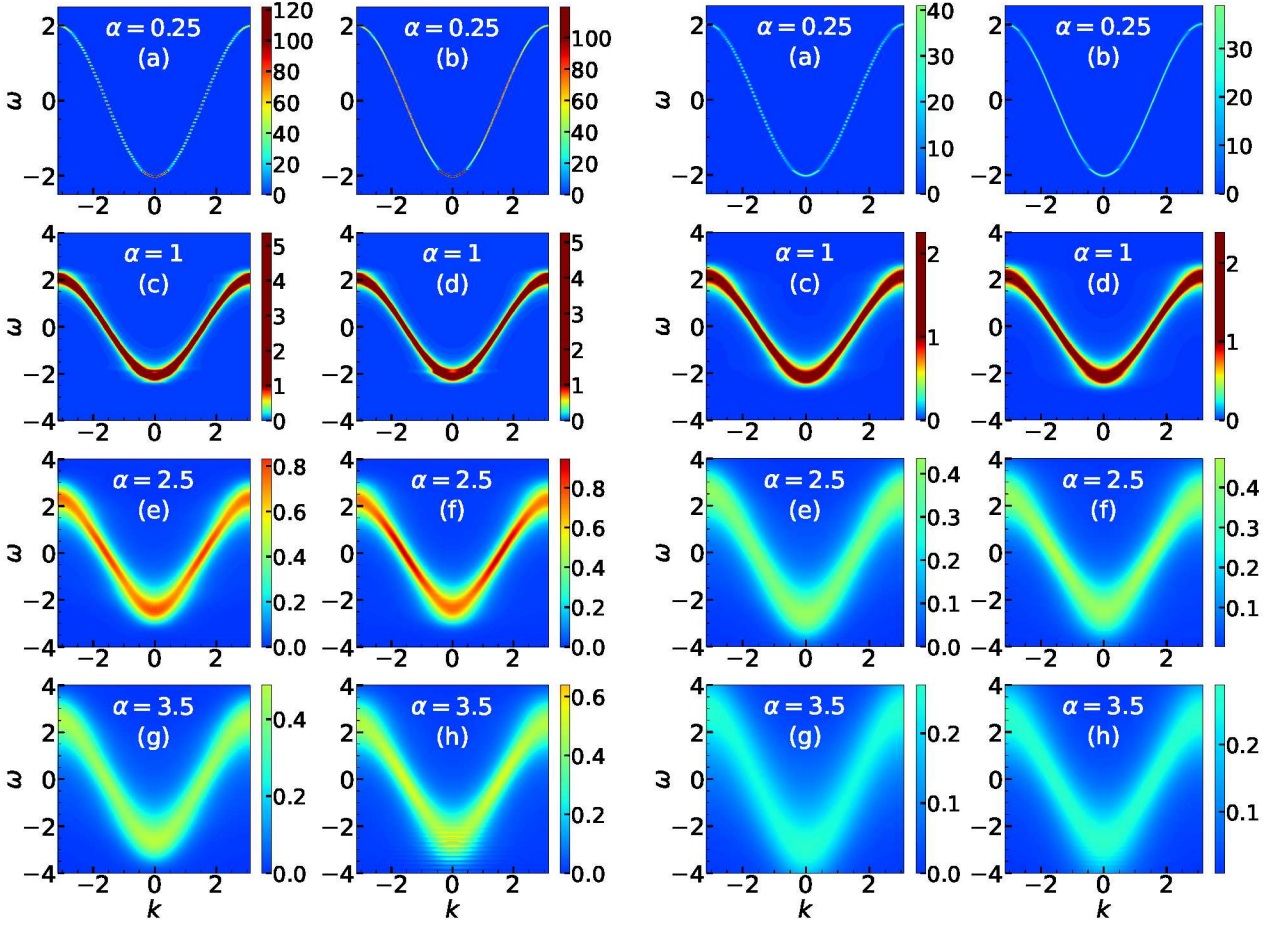
(i) (a)–(h) Spectral functions for $\omega_0 = 0.2$ and $T = 0.3$. In the left panels $k = \pi/3$, while $k = 2\pi/3$ in the right panels.

(ii) (a)–(h) Spectral functions for $\omega_0 = 0.2$ and $T = 0.7$. In the left panels $k = \pi/3$, while $k = 2\pi/3$ in the right panels.



(iii) Spectral functions at higher temperatures for $\omega_0 = 0.2$ and $k = \pi/3, 2\pi/3$.

FIG. S7. Comparison of the CE, DMFT, and SCMA spectral functions in 1D for $t_0 = 1$, $\omega_0 = 0.2$ and $k = \pi/3, 2\pi/3$.



(i) (a)–(h) Heat maps for $T = 0.3$. In the left panels, we present CE results, while the DMFT benchmark is presented in the right panels. Panels (c)–(h) use the same color coding, while panels (a) and (b) use different color coding.

(ii) (a)–(h) Heat maps for $T = 0.7$. In the left panels, we present CE results, while the DMFT benchmark is presented in the right panels. Panels (c)–(h) use the same color coding, while panels (a) and (b) use different color coding.

FIG. S8. Comparison of the CE and DMFT heat maps for $t_0 = 1$ and $\omega_0 = 0.2$.

III. QUASIPARTICLE PROPERTIES

In Sec. IV of the main text, we showed and analyzed the quasiparticle properties of CE, DMFT, and SCMA methods. Here we supplement that study by including the predictions of the Migdal approximation for the ground state energy in 1D. The results are shown in Fig. S9. We emphasize that the predictions of the DMFT benchmark are practically identical to the exact numerical results [S1]. These results readily demonstrate how much improvement to the simplest approximation (MA) is provided by including the self-consistency (SCMA) and by employing the cumulant expansion method (CE).

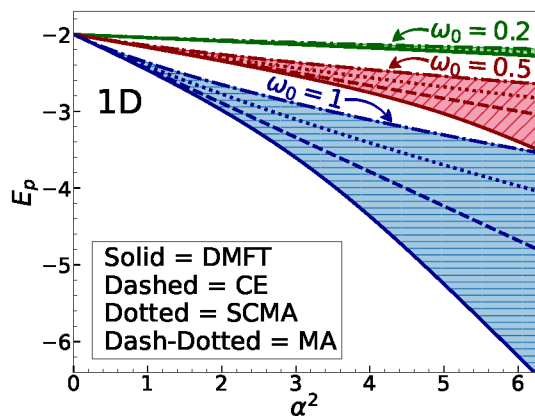


FIG. S9. Ground state energy within DMFT, CE, SCMA, and MA for the one-dimensional Holstein model with $t_0 = 1$.

- [S1] P. Mitríć, V. Janković, N. Vukmirović, and D. Tanasković, Spectral Functions of the Holstein Polaron: Exact and Approximate Solutions, *Phys. Rev. Lett.* **129**, 096401 (2022).
- [S2] R. Kubo, Generalized Cumulant Expansion Method, *Journal of the Physical Society of Japan* **17**, 1100

- (1962).
- [S3] E. Meeron, Series expansion of distribution functions in multicomponent fluid systems, *The Journal of Chemical Physics* **27**, 1238 (1957).
- [S4] G. Mahan, *Many-Particle Physics* (Kluwer Academic, New York, 2000).